

---

# **INNOVATIVE TOOLS FOR RNA INTERFERENCE: MULTIFUNCTIONAL GOLD NANOPARTICLES FOR SILENCING OF *MYC* PROTO- ONCOGENE**

---

**Valentina Marchesano**

Dottorato in Scienze Biotechnologiche XXV ciclo  
Indirizzo Biotechnologie Mediche  
Università di Napoli Federico II









---

# **INNOVATIVE TOOLS FOR RNA INTERFERENCE: MULTIFUNCTIONAL GOLD NANOPARTICLES FOR SILENCING OF MYC PROTO- ONCOGENE**

---

**Valentina Marchesano**

Dottoranda:	Valentina Marchesano
Docente guida:	Dott.ssa Claudia Tortiglione
Coordinatore di indirizzo:	Prof. Fabrizio Pane
Coordinatore:	Prof. Giovanni Sannia



*Alla mia famiglia*



## ***Index***

Riassunto	11
<i>Abstract</i>	18
<i>1. Introduction</i>	19
<i>1.1 Gene therapy by RNA interference (RNAi)</i>	19
<i>1.2 Mechanisms of RNAi-mediated gene silencing</i>	19
<i>1.3 Applications of RNA Interference</i>	21
<i>1.4 Challenges in using RNAi for therapeutic application</i>	22
<i>1.5 Nanobiotechnology and nanomaterials</i>	25
<i>1.6 Gold nanoparticles</i>	28
<i>1.6.1 Gold nanoparticles and oligonucleotides</i>	28
<i>1.7 The NANOTRUCK European project</i>	30
<i>1.7.1 The myc protooncogene as target</i>	30
<i>1.7.2 Multifunctional gold nanoparticles for myc RNAi</i>	32
<i>1.8 Hydra vulgaris as in vivo model sistem</i>	34
<i>1.8.1 Cell types in Hydra vulgaris</i>	36
<i>1.8.2 Regeneration process in Cnidaria</i>	38
<i>1.8.3 Reproduction</i>	39
<i>1.8.4 Hydra as model organism to test nanoparticles</i>	40
<i>1.8.5 Gene knock out by RNAi in Hydra.</i>	43
<i>1.8.6 Caracterization of c-myc protoncogene in Hydra vulgaris</i>	43
<i>2 Materials and methods</i>	46
<i>2.1 Animals</i>	46
<i>2.2 Nanoparticles tested</i>	46
<i>2.3 Hydra vulgaris culturing</i>	46
<i>2.4 Preparation of Artemia salina nauplii</i>	47
<i>2.5 Feeding procedure</i>	47
<i>2.6 In vivo RNA interference through small interfering RNAs</i>	47
<i>2.7 Toxicological studies with intact and regenerating animals</i>	48

2.8 <i>Hydra vulgaris</i> growth rate	48
2.9 <i>Hydra</i> cell and tissue analysis	49
2.10 Proliferation rate	49
2.11 Tissue sectioning	49
2.12 Gene and protein expression analyses	49
2.12.1 <i>in situ</i> Hybridization and Western Blot analysis	49
2.12.2 Total RNA extraction	50
2.12.3 Agarose gel electrophoresis for the evaluation of RNA integrity.	50
2.12.4 RNA reverse transcription	51
2.12.5 Quantitative Real-time reverse transcription- polymerase chain reaction (qRT-PCR)	51
2.13 Ultrastructural analysis through Transmission Electron Microscopy (TEM)	51
2.14 Sample preparation for High-Pressure Freezing Procedure (HPF)	52
2.15 Elemental analysis by Inductively coupled plasma atomic emission spectroscopy (ICP-AES)	52
3 Results	53
3.1 RNA interference mediated by free siRNA in <i>Hydra vulgaris</i>	53
3.1.1 Characterization of myc RNAi animals	57
3.2 RNA interference mediated by gold nanoparticle in <i>Hydra</i>	61
3.2 RNA interference mediated by gold nanoparticle in <i>Hydra</i>	61
3.2.1. Synthesis of Gold Nanoparticles	61
3.2.2 Biocompatibility and toxicity of AuNP on <i>Hydra</i> : impact on morphology reproduction and regenerative capabilities	62
3.2.3 AuNP impact on <i>Hydra</i> reproduction and regenerative capabilities	64
3.2.4 Internalization of AuNP in <i>Hydra vulgaris</i> : the role of the NP surface charge.	65
3.2.5 Internalization of AuNP-N <sub>3</sub> in <i>Hydra vulgaris</i>	67
3.3 Gene silencing mediated by myc siRNA functionalized AuNPs	70
3.3.1 <i>In vivo</i> assessment of uptake	70
3.3.2. Molecular assessment of Hymc1 downregulation by myc-siRNA-AuNPs	72
3.3.3 RNAi induced by myc-siRNA AuNP: a dose-response evaluation	74
3.3.4 Mechanisms of AuNP-siRNA uptake and intracellular fate	75
3.3.5 Characterization of mycRNAi animals	77

<i>3.4 Ultrastructural analysis of AuNP uptake and clearance</i>	78
<i>3.4.1 Elemental analysis confirms kinetic of uptake and clearance of AuNP</i>	83
<i>4 Discussion.</i>	84
<i>4.1 RNA interference mediated by free siRNA in Hydra vulgaris.</i>	84
<i>4.2 RNA interference mediated by gold nanoparticle in Hydra.</i>	86
<i>4.3 Ultrastructural evidence of dynamic of internalization of Au-NP-N<sub>3</sub> and Au-NP-myc-siRNA</i>	88
<i>5 Conclusion</i>	92
<i>6 Bibliography</i>	93
<i>CONFERENCE PROCEEDINGS AND COMMUNICATIONS</i>	98
<i>RESEARCH STAGE</i>	99





## Riassunto

### ***Sviluppo di tecnologie innovative di RNA interference: nanoparticelle di oro funzionalizzate per il silenziamento del proto-oncogene myc***

#### **Contesto scientifico**

La scoperta dell'RNA interference (RNAi), un importante meccanismo molecolare responsabile della modulazione trascrizionale e post-trascrizionale dell'espressione genica, ha favorito lo sviluppo di approcci terapeutici basati su modificazioni dell'espressione genica. L'RNAi è un meccanismo epigenetico mediante il quale molecole di RNA a doppio filamento (dsRNA) interferiscono con l'espressione del gene aventi sequenza complementare, mediante degradazione dell'mRNA. Dopo i primi studi dei premi Nobel Fire e Mello in *C. elegans*, che risalgono al 1998 (Fire et al., 1998), Tuschl e collaboratori hanno dimostrato che gli small interfering RNA (siRNA), frammenti di RNA a doppio filamento di 21-23 nucleotidi, sono in grado di indurre degradazione di mRNA in maniera nucleotide specifica (Schlee et al., 2006). Nonostante l'enorme potenzialità dell'RNAi, ci sono ostacoli significativi da superare prima di poter applicare tale tecnologia alla clinica, quali la scarsa stabilità dei siRNA nei fluidi biologici attraverso cui avviene la somministrazione e la possibilità di effetti aspecifici derivanti, per esempio, da una parziale omologia di sequenza in prossimità del 3' UTR, e conseguente induzione di RNAi aspecifico (Kim et al, 2009).

Con lo sviluppo delle nanotecnologie nell'ultimo decennio sono state progettate e sintetizzate numerose nanoparticelle (NP) per applicazioni biologiche, che in base alle caratteristiche specifiche sono state utilizzate con successo, come marcatori fluorescenti, sistemi di trasporto (di farmaci, proteine, acidi nucleici), agenti di contrasto per risonanza magnetica, microscopia elettronica (Giljohann et al., 2010). La natura inorganica e spesso metallica di molte classi di nanoparticelle ne ha reso necessaria un'attenta analisi tossicologica per escludere eventuali effetti citotossici legati alla composizione chimica (Rivera-Gil et al., 2012). Tali studi condotti *in vitro* in colture cellulari e *in vivo* in modelli animali hanno evidenziato l'alta compatibilità di alcune classi di nanoparticelle (per esempio quelle composte da un nucleo di oro) con la materia vivente.

Recentemente sono state sviluppate diverse strategie di RNAi che utilizzano nanoparticelle di diversa natura (dendrimeri, liposomi, quantum dots) per il trasporto di siRNA (Kim et al, 2009). In genere la loro composizione cationica media l'efficiente internalizzazione cellulare, mentre rivestimenti con specifiche molecole, come ad esempio il PEG conferiscono un'aumentata stabilità e biocompatibilità rispetto ai metodi tradizionali, che prevedono l'uso di agenti trasfettanti spesso tossici.

Negli ultimi anni le nanoparticelle di oro (AuNP) hanno ricoperto notevole interesse scientifico per studi di RNAi mediato da siRNA. Sono state sviluppate da diversi autori molteplici metodologie di sintesi e di coniugazione dei siRNA alla superficie delle AuNP, che si sono rivelate determinanti nell'induzione di silenziamento genico specifico e ad alta efficienza (Lytton-Jean et al, 2011).

## Scopo del lavoro di tesi

In questo contesto scientifico, il mio lavoro di tesi di dottorato ha avuto come obiettivo principale lo sviluppo di nuove metodologie di RNAi basate su small interfering RNA (siRNA), utilizzando nanoparticelle di oro multifunzionali.

Il mio lavoro è parte di un ampio progetto europeo (NANOTRUCK), che ha previsto la sintesi di nanoparticelle di oro (AuNP) multifunzionali ottimizzate per RNAi, la validazione di tali dispositivi in modelli cellulari e animali e una fase finale di sperimentazione preclinica in cui tali nanodispositivi sono stati utilizzati per il trattamento di un modello murino di carcinoma polmonare. Il gene selezionato per il trattamento di RNAi è il proto-oncogene *c-myc*, fattore di trascrizione coinvolto in numerosi processi cellulari (ciclo cellulare, differenziamento, crescita, apoptosi) e la cui deregolazione è associata a molteplici stati tumorali (Vita et al, 2006). La mia attività di ricerca, svolta presso l'Istituto di Cibernetica "E.Caianiello" del CNR, ha previsto la validazione di AuNP multifunzionali in un organismo invertebrato, il celenterato di acqua dolce *Hydra vulgaris*.



*Hydra vulgaris* è utilizzata dal gruppo di Nanoscienze e Biologia Molecolare come modello per lo sviluppo e la validazione di nuovi nanobiodispositivi per studio della funzione genica (trasformazione genetica, silenziamento genico), l'imaging avanzato, il delivery di molecole funzionali (Tortiglione, 2011). La semplicità strutturale anatomica (solo due strati di cellule, ectoderma ed endoderma, mancanza di organi) e l'alta plasticità tissutale (presenza di mitosi continua nei due strati cellulari e differenziamento della linea staminale interstiziale in pochi tipi specializzati) rendono *Hydra vulgaris* un modello ideale per gli studi dei processi di differenziamento cellulare e rigenerazione tissutale.

Al fine di testare in *Hydra* nuovi prodotti di coniugazione (AuNP-siRNA) e relativi intermedi di sintesi è stato necessario uno studio preliminare per definire il ruolo del gene *myc* in *Hydra* (*Hymyc1*) di recente clonato (Hartl et al., 2010). A tal fine ho validato un sistema di RNAi sviluppato nel mio laboratorio, che si basa sulla somministrazione di siRNA all'animale attraverso "soaking", ovvero per immersione in una soluzione contenente i siRNA, a concentrazioni definite. Successivamente all'identificazione del fenotipo animale e cellulare degli animali sottoposti al trattamento di RNAi, e all'avanzamento di ipotesi sul ruolo funzionale di *Hymyc1* in *Hydra*, sono iniziati gli studi con le nanoparticelle funzionalizzate, sintetizzate via via nel corso del progetto Nanotruck dal gruppo diretto dal Dr. JM de la Fuente, presso il Nanoscience Institute of Aragona, University of Zaragoza. La mia attività di ricerca ha previsto la caratterizzazione molecolare degli animali interferiti, seguita da uno studio cellulare per valutare l'effetto del silenziamento genico di *Hymyc1* sui processi di proliferazione e differenziamento delle cellule staminali, dove *Hymyc1* è espresso. Infine, grazie alle straordinarie proprietà delle AuNP di agire come agenti di contrasto per la microscopia elettronica, ho effettuato una dettagliata analisi ultrastrutturale dei tessuti trattati, per delineare i meccanismi di internalizzazione e distribuzione intracellulare delle nanoparticelle funzionalizzate. Gli interessanti risultati ottenuti mi hanno portato ad approfondire tali studi mediante analisi effettuate a vari tempi di incubazione (da 5 minuti a 48 ore) ed utilizzare altre tecniche microscopiche. A tal fine, ho completato la mia formazione nel laboratorio del Prof. Bert Hobmayer,

Institute of Zoology, University of Innsbruck, utilizzando la tecnica High Pressure Freezing Electron Microscopy. Tale metodologia ha permesso un'analisi fine della dinamica di internalizzazione ed esocitosi di AuNP in *Hydra*, definendo tali meccanismi per la prima volta a livello di animale intero. Durante lo stage nel prestigioso laboratorio del Prof. B. Hobmayer, leader riconosciuto nello studio dei processi cellulari e molecolari alla base dello sviluppo animale e del differenziamento, ed autore dell'identificazione della famiglia dei geni *myc* in *Hydra*, ho avuto modo di completare e perfezionare le mie conoscenze sui meccanismi di differenziamento di cellule staminali in *Hydra*, utilizzando metodologie per la preparazione e l'analisi morfologica di sospensioni cellulari.

### **Descrizione dettagliata del lavoro sperimentale.**

1. Sviluppo e validazione di un protocollo di RNAi mediato da free-siRNA: determinazione del ruolo del gene *Hymyc 1* in *Hydra*
2. RNAi del gene *Hymyc1* utilizzando AuNP funzionalizzate
  - a) Studio di biocompatibilità e biodistribuzione di AuNP
  - b) Valutazione dell'efficienza di RNAi: analisi molecolare, cellulare e animale.
3. Studio del meccanismo di internalizzazione, distribuzione intracellulare e turnover di AuNP: analisi ultrastrutturale.

#### **1. Sviluppo e validazione di un protocollo di RNAi mediato da free-siRNA e determinazione del ruolo del gene *Hymyc1* in *Hydra***

Sono stati progettati siRNA complementari al trascritto del gene *Hymyc1* (*myc-siRNA*) espresso in *Hydra* nelle cellule staminali in attiva proliferazione. Gli animali sono stati incubati nel loro mezzo di coltura in presenza di *myc-siRNA* e in condizioni acide, ed analizzati:

- ✓ a livello cellulare, per misurare le attività proliferative dei vari tipi cellulari e valutare quantitativamente la distribuzione dei tipi cellulari diversi (cellule staminali, cellule "committed" verso il differenziamento di neuroni, nematociti o cellule ghiandolari, morfologicamente distinguibili). L'attività di proliferazione cellulare è stata misurata mediante trattamento in vivo con BrdU, seguito da preparazione di sospensioni cellulari e immunostaining. L'analisi della distribuzione dei vari tipi cellulari è stata effettuata analizzando sospensioni cellulari di animali trattati e quantificando i vari tipi cellulari riconoscibili. Infine, l'analisi microscopica dei tentacoli degli animali interferiti ha permesso di quantizzare alterazioni nella morfologia delle cellule costituenti i tentacoli, le cellule a batteria, dovute a processi di differenziamento verso un singolo tipo cellulare, il nematocita;
- ✓ a livello molecolare, mediante analisi qualitativa e quantitativa dell'espressione del gene codificante per la proteina *Hymyc1* (*in situ* hybridization, qRT-PCR, Western blot).

### **Risultati:**

**Analisi cellulare:** caratterizzazione del fenotipo degli animali *myc-RNAi*. Nei polipi sottoposti a RNAi del gene *Hymyc1* è stato riscontrato un incremento della proliferazione delle cellule staminali interstiziali, che a sua volta ha determinato un aumento dei tipi cellulari (intermedi e definitivi) derivanti dal loro differenziamento.

**Analisi molecolare:** è stata dimostrata una riduzione dei livelli di trascrizione del gene *Hymyc1* pari al 60% rispetto ai livelli di espressione dei polipi non trattati, dimostrando la validità della metodologia di RNAi mediata da siRNA.

Dall'analisi funzionale condotta mediante RNAi è emerso che una riduzione dell'espressione del gene *Hymyc1* provoca un aumento dell'attività di proliferazione delle cellule staminali della linea interstiziale di *Hydra*, che si traduce in un aumento dei tipi cellulari derivati dal loro differenziamento. Analogamente al ruolo svolto da c-myc nei vertebrati, gli studi funzionali in *Hydra* suggeriscono un coinvolgimento del gene omologo (*Hymyc1*) nei processi che regolano l'equilibrio tra proliferazione e differenziamento delle cellule staminali, suggerendo il ruolo chiave di questa famiglia di fattori trascrizionali nell'evoluzione del regno animale.

## **2. RNAi del gene *Hymyc1* utilizzando AuNP funzionalizzate**

La capacità dei siRNA di attraversare le membrane cellulari di *Hydra* e raggiungere le cellule bersaglio (i nematoblasti) dove *Hymyc1* è espresso ha supportato lo sviluppo di nuovi approcci volti a migliorare l'efficienza di silenziamento genico. A tal scopo, nell'ambito di un progetto europeo, sono state utilizzate nanoparticelle di oro come veicoli per il trasporto dei siRNA da testare in diversi modelli animali, tra cui *Hydra*. Al fine di valutare l'assenza di potenziali effetti tossici dovuti alla natura metallica di tali vettori, sono state condotte analisi tossicologiche preliminari.

### **a) Studio di biocompatibilità e biodistribuzione**

Sono stati utilizzati diversi protocolli, precedentemente sviluppati dal gruppo di Nanoscienze e Biologia Molecolare per valutare la tossicità di nanoparticelle metalliche in Cnidari (Ambrosone et al., 2012; Ambrosone and Tortiglione, 2013). Tali protocolli si basano su valutazioni degli effetti del trattamento di nanoparticelle sugli animali, effettuate a diversi livelli:

- ✓ analisi morfologica dell'animale, *in vivo*;
- ✓ analisi delle capacità rigenerative
- ✓ analisi della velocità di accrescimento della popolazione mediante riproduzione asessuata.

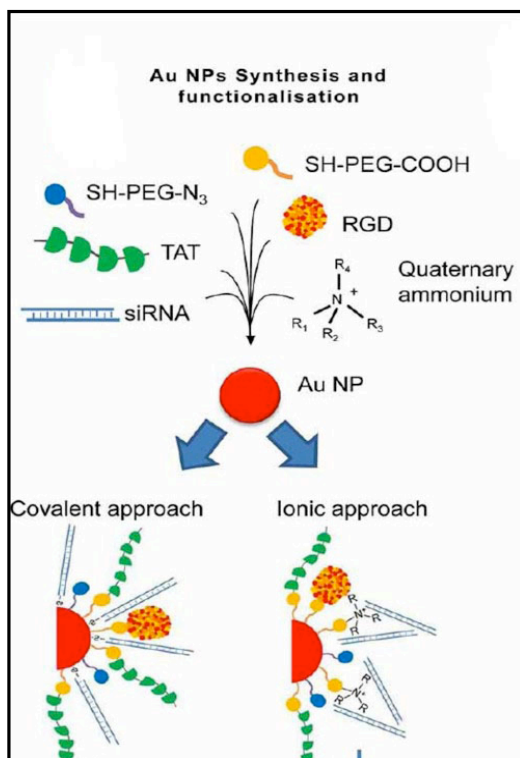
### **Risultati:**

Non sono state riscontrate alterazioni morfologiche negli animali trattati con dosi crescenti di AuNP. Non sono state riscontrate anomalie nei processi di rigenerazione degli animali sottoposti a trattamento acuto e cronico. Infine, gli individui trattati mostrano capacità riproduttive paragonabili a quelle degli individui non trattati, generando popolazioni secondo normali ritmi di accrescimento.

### **b) Valutazione dell'efficienza di RNAi: analisi molecolare, cellulare e animale**

In questa fase di lavoro, il protocollo di RNAi sviluppato con i siRNA è stato applicato a nanoparticelle di oro funzionalizzate con *myc-siRNA*. Tali nanoparticelle sono state sintetizzate nel laboratorio del Dr. Jesus M. de La Fuente (Nanoscience Institute of Aragona, University of Zaragoza), seguendo due differenti strategie di legame dei siRNA al nucleo di oro, covalente e ionico. Inoltre per aumentare l'efficienza di internalizzazione cellulare, per ciascuna strategia di legame è stato caricato sulla

superficie delle AuNP un peptide noto per favorire la penetrazione cellulare, il peptide di origine virale TAT.



Per studiare gli effetti delle strategie di coniugazione sull'efficienza del gene silencing, i polipi sono stati incubati con le singole AuNPs ed analizzati dopo 48 h di incubazione mediante:

- ✓ analisi molecolare (qRT-PCR) per valutare e confrontare i livelli di espressione genica di *Hymyc1* ottenuti in seguito a trattamento con 8 classi di nanoparticelle diverse, funzionalizzate secondo diverse strategie e recanti diversi gruppi attivi di superficie.
- ✓ analisi cellulare e tissutale per valutare l'effetto *myc-RNAi* sulla velocità di proliferazione e differenziamento delle cellule staminali

## Risultati

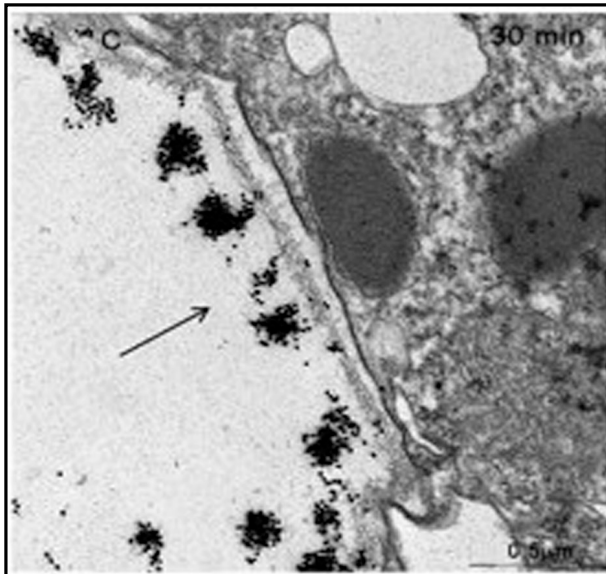
**Analisi molecolare:** dall'analisi quantitativa (via qRT-PCR) dei livelli di espressione del gene *Hymyc1* eseguita dopo trattamento con

ognuno dei prodotti di sintesi è stata selezionata una nanoparticella ottimale coniugata in maniera covalente a siRNA, capace di indurre una riduzione dell'espressione genica molto più efficace (80%) rispetto agli altri prodotti di sintesi derivanti da ambedue le strategie, covalente e ionica. Come atteso, le AuNP utilizzate controllo, prive di siRNA, non hanno indotto riduzione dell'espressione genica indicando l'assenza di effetti aspecifici provocati dal trattamento delle NP sui processi trascrizionali endogeni. Inaspettatamente, AuNP funzionalizzate con siRNA e TAT si sono dimostrate inefficaci nell'induzione di silenziamento genico, suggerendo un possibile ruolo inibitorio del TAT sul meccanismo di RNAi.

**Analisi cellulare:** dall'analisi della distribuzione dei tipi cellulari e della velocità di proliferazione delle cellule staminali negli animali sottoposti a trattamento con AuNP-siRNA (selezionata dai test molecolari) è emerso un fenotipo che riproduce completamente quello ottenuto utilizzando siRNA in soluzione e ne aumenta la severità. Le cellule interstiziali staminali di tipo 1s e 2s, in attiva proliferazione, presentano cicli di divisione più rapidi rispetto agli animali non trattati e la distribuzione dei tipi cellulari conferma un aumento delle popolazioni cellulari (nematoblasti, cellulare ghiandolari e nematociti) derivati dal differenziamento delle cellule dove *Hymyc 1* è espresso. Il numero dei nematociti analizzato sui tentacoli di animali interirisulta analogamente aumentato.

## 3. Studio del meccanismo di internalizzazione, distribuzione intracellulare e turnover di AuNP: analisi ultrastrutturale.

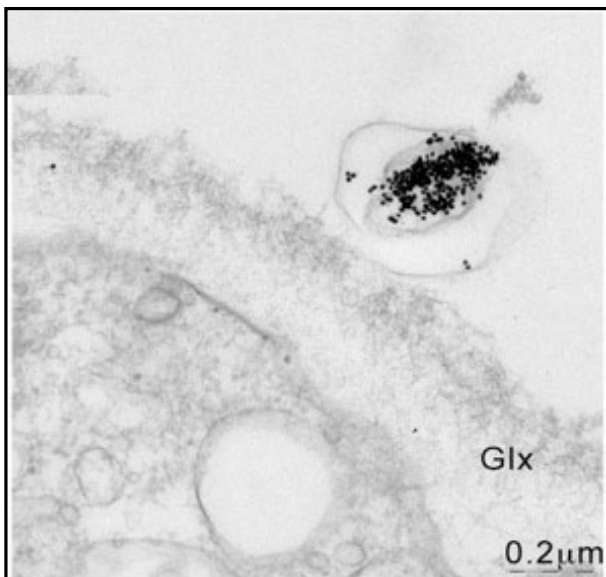
Lo studio dei meccanismi di internalizzazione, traffico cellulare e turn-over delle AuNP nei tessuti degli animali trattati è stato condotto attraverso una dettagliata analisi di microscopia elettronica su polipi trattati con AuNP-siRNA e AuNP-N<sub>3</sub>, funzionalizzate rispettivamente con siRNA e catene PEG-azide. La carica positiva di



queste ultime è stata dimostrata (utilizzando anche altri approcci, quali microscopia *in vivo* e analisi del contenuto in oro dei tessuti trattati) responsabile dell'elevata efficienza di internalizzazione (Tortiglione et al., 2009) rispetto a AuNP funzionalizzate con gruppi carichi negativamente (come nel caso di cargo siRNA). L'analisi condotta a tempi diversi di incubazione (5min, 30', 4h, 8h, 14h, 24h, 48h) ha dimostrato l'influenza della carica di superficie delle AuNP sull'efficienza di internalizzazione, e rivelato l'induzione alla membrana cellulare di diversi meccanismi che affiancano i noti

processi di endocitosi a meccanismi di trasporto attraverso la membrana e legame a vescicole nanometriche (esosomi). Le osservazioni a tempi crescenti di incubazione hanno rivelato all'interno della cellula la presenza di AuNP in endosomi e poi lisosomi, nei quali si accumulano in maniera massiva dopo 48h. Infine è stato possibile visualizzare i processi di esocitosi che determinano l'eliminazione delle AuNP dall'animale. Durante il mio stage presso il lab. diretto dal Prof. Hobmayer

(Istituto di Zoologia, University of Innsbruck) sottoponendo gli animali a trattamenti pulse and chase ed utilizzando la tecnologia HP-cryoTEM (Holstein et al., 2010), è stato possibile visualizzare l'esocitosi delle AuNP via fusione diretta dei lisosomi con la membrana o estroflessione di regioni estese di membrana. Di grande interesse la presenza anche a 48h di vescicole nanometriche contenenti AuNP al di fuori della membrana cellulare, probabilmente identificabili come esosomi che potrebbero quindi essere coinvolti nei meccanismi di entrata e di uscita delle AuNP. La conservazione evolutiva dei meccanismi



di endocitosi nel regno animale rende i risultati di tutti gli studi ultrastrutturali di grande valore per tutta la comunità scientifica che sviluppa nuovi nanomateriali e dispositivi per applicazioni diagnostiche e terapeutiche.

## **Conclusioni**

Il mio lavoro di tesi ha previsto lo sviluppo di nuove metodologie di RNAi, basate sull'uso di siRNA per lo studio della funzione del gene *Hymyc1* in *Hydra*. Accanto ad approcci già esplorati in altri sistemi animali mediati da siRNA somministrati in soluzione, la metodologia mediata da nanoparticelle di oro si è dimostrata capace di aumentare l'efficienza di silenziamento genico, determinando un abbassamento dei livelli trascrizionali pari all'80%. L'analisi fenotipica e molecolare degli animali interferiti ha confermato la specificità della metodologia ed ha delineato il ruolo del gene *Hymyc1* nei processi che controllano l'equilibrio proliferazione/differenziamento delle cellule staminali. Di particolare rilievo nell'ambito del progetto Nanotruck la scoperta che una singola particella multifunzionale prodotta con una specifica metodica, si sia rivelata efficace nell'indurre silenziamento genico specifico in tre sistemi biologici a diversi gradi di complessità: colture cellulari umane, *Hydra* e topo, dimostrando la validità generale del nanodispositivo prodotto nell'indurre RNAi. Al di là dell'impatto che tale tecnologia potrà dare in ambito terapeutico, il mio lavoro all'interfaccia tra le nanoscienze e la biologia, ha contribuito a validare *in vivo* nuovi nanodispositivi per RNAi, a delineare i meccanismi di interazione AuNP cellula vivente (dall'internalizzazione all'esocitosi), a elucidare mediante tale approccio il ruolo funzionale di un protooncogene, coinvolto nella cancerogenesi negli organismi superiori, con ovvie ricadute applicative nel campo della terapia basate sull'RNAi. I risultati del mio lavoro di tesi hanno contribuito in parte o completamente alla realizzazione di tre lavori scientifici su riviste specializzate ad alto impatto, pubblicati nel 2012 e 2013: Ambrosone et al., 2012, Conde et al., 2012, Marchesano et al., 2013.



## **Abstract**

### ***Innovative tools for RNA interference: multifunctional gold nanoparticles for silencing of myc proto-oncogene***

Despite its simple body plan and structural anatomy, the Cnidaria *Hydra vulgaris*, a diploblastic animal at the base of metazoan evolution, is an excellent model system to investigate the mechanisms controlling stem cell proliferation and differentiation and the balance between the two phenomena. In vertebrates one of many genes that participate in regulating cell homeostasis is the protooncogene *c-myc*. The MYC family of transcription factors controls disparate aspects of cell physiology including cell growth, cell cycle progression, biosynthetic metabolism, and apoptosis. As expected *c-myc* deregulated expression occurs in the majority of human cancers, making it a seemingly attractive target for therapeutic inhibition. In order to develop effective strategies of *c-myc* gene silencing, two methodologies based on small interfering RNAs (siRNA) were developed in this work, using *Hydra* as model organism and targeting the *Hydra c-myc* orthologue gene *Hymyc1*. The first methodology, based on free *myc-siRNA* supplied to the polyps by soaking under acidic condition was shown to induce specific RNAi and to affect proliferation of stem cells and derived cell types. The ability of *Hydra* cells to uptake double stranded RNA and to trigger a RNAi response laid the foundations for the second methodology, developed in the frame of a European project and based on the use of gold nanoparticles (AuNP) as innovative shuttles for safe and successful delivery of siRNA. AuNPs were conjugated to *Hymyc-siRNA* using different chemical strategies and tested for functionality in *Hydra* by molecular analysis, followed by measurement of cell cycling activity and quantitative estimation of cell ratios between stem and differentiated cells. Among eight different *myc-siRNA*-AuNP conjugates, a single nanodevice (presenting siRNA covalently conjugated to the gold core) was shown able to induce 80% gene silencing. The biological effect of *Hymyc1* downregulation was elucidated as a strong impairment of the balance between stem cell self-renewal/differentiation, as shown by the accumulation of stem cell intermediate and terminal differentiation products in RNAi animals. The confirmation also in other model systems of the bioactivity of such nanodevice to induce efficient and specific gene silencing strongly supports its feasibility to be broadly used for therapeutic RNAi.

In addition to the gene silencing performance, and thanks to the unique contrast agent behaviour of the gold nanoparticle core for Electron Microscopy, a detailed investigation of the mechanisms of internalization of AuNPs was performed by comparing different chemical functionalities (siRNA and positively charged groups) present on AuNP surface.

The dynamic and kinetic of the whole journey of gold nanoparticles within a whole animal was reported, from the first interaction nanoparticle/cell membrane, to the intracellular trafficking and final extracellular clearance. Beside classical routes, new portals of entry/exit were captured by imaging *Hydra* treated tissue, including exosome-like structures as novel undescribed nanoparticle shuttles inward and outward the cell membrane. The conservation of the endocytic/secretory machinery through evolution extends the value of our finding to mammalian systems providing new clues to take into account when designing nanomaterials to interface with biological entities.



## **1. Introduction**

### **1.1 Gene therapy by RNA interference (RNAi)**

Most of the diseases for which a genetic base has been demonstrated and discovered, are theoretically, suitable for treatments based on gene therapy. This approach, that is diffusing more and more, is mainly applicable both for rare genetic syndromes or cancer. The idea behind is the manipulation of gene expression in both the directions (overexpression or gene knock down). For gene therapy by overexpression it is necessary to target to specific cell types a transgene that, once integrated into the genome, can replace the lacking or inactive gene. However this approach is not free from negative effects; indeed, the wrong integration of the transgene could also led to adverse outcomes. This is the reason why many research efforts are focusing on transient gene therapy treatments. Dereglulation (often upregulation) in gene expression levels has been found in several types of cancer, thus that an ideal therapeutic treatment would consists in downregulation the expression of those genes (oncogenes) through exploitation of endogenous cell processing, i.e. RNA interference (RNAi).

The knowledge about this pathway has expanded at a remarkable rate since the initial characterization of RNAi in the nematode *Caenorhabditis elegans*. In fact in 1998, Fire, Mello and colleagues discovered the ability of double stranded RNA molecules to silence gene expression in *C.elegans*. Soon after this, RNAi was shown to occur in mammalian cells in response to double-stranded small interfering RNAs (siRNAs), i.e. ~21 long dsRNA molecules that serve as the effector molecules for sequence-specific gene silencing. Three years later, Tuschl and co-workers, demonstrated that synthetic small interfering RNA (siRNA) could achieve sequence specific gene knockdown in a mammalian cell line. Mechanistic insights followed rapidly during the ensuing years, increasing the possibility to use RNAi pathways for the therapeutic intervention of human diseases, at least those in which an alteration of gene expression is documented. The principle of RNAi is sequence-specific degradation of mRNA induced by a double-stranded RNA (dsRNA) homologues to the target sequence. RNAi is shared by a wide variety of eukaryotes, including yeast, fungi, plants, and animals (Elbashir et al., 2001), (Gheysen et al., 2007), (Hamlin et al., 2003)

### **1.2 Mechanisms of RNAi-mediated gene silencing**

RNAi pathways are guided by small RNAs that include siRNAs and microRNAs (miRNAs), which derive from imperfectly paired hairpin RNA structures naturally encoded in the genome. RNAi effector molecules induce gene silencing in several ways: they direct sequence-specific cleavage of perfectly complementary mRNAs and translational repression and transcript degradation for imperfectly complementary targets. The general mechanism is triggered when dsRNA is introduced into cells and is processed by the RNase III-like protein Dicer in 21- to 23-bp RNA fragments with 2-nt 3'-overhangs. Once siRNA is present in the cytoplasm of the cell, it is incorporated into a protein complex called the RNA- inducing silencing complex (RISC). The RISC-siRNA complex targets complementary mRNA, leading to a shutdown of gene expression in a sequence-specific manner. Tuschl's group was the first to demonstrate that synthetic double-stranded 21-bp siRNAs transfected into mammalian cell lines mimic the effects of Dicer products, thereby introducing a

powerful tool to manipulate gene expression selectively in adult mammalian cells. Exogenous siRNAs target complementary mRNAs for transcript cleavage and degradation in a process known as post-transcriptional gene silencing (PTGS). In nematodes, insects and plants, this pathway functions as an innate antiviral defence mechanism, in which viral double-stranded RNA (dsRNA) molecules are processed by the RNase III enzyme Dicer into siRNAs that mediate the RNAi response. Whether or not siRNA-mediated PTGS exists in mammalian cells for intrinsic immunity against viral infections is unclear, and remains an area of further investigation. Effective PTGS requires perfect or near-perfect Watson–Crick base pairing between the mRNA transcript and the antisense or guide strand of the siRNA, and results in cleavage of the mRNA by the RNA induced silencing complex (RISC). The endonuclease Argonaute 2 (AGO2) is responsible for the cleavage mechanism of RISC, and AGO2 is the only member of the Argonaute subfamily of proteins with observed catalytic activity in mammalian cells. RISC activation is initially thought to involve AGO2-mediated cleavage of the sense or passenger strand of the double-stranded siRNA, generating the single-stranded antisense strand that serves to guide RISC to complementary sequences in target mRNAs. The cleavage of targeted mRNA takes place between bases 10 and 11 relative to the 5' end of the siRNA guide strand, leading to subsequent degradation of the cleaved mRNA transcript by cellular exonucleases. On activation by the siRNA guide strand, RISC can undergo multiple rounds of mRNA cleavage to mediate a robust PTGS response against the target gene. PTGS by mRNA cleavage has been exploited as the method of choice for potential therapeutic applications of RNAi because of the potency of this catalytic gene-silencing pathway (Figure 1) (S.-S. Kim et al., 2009)

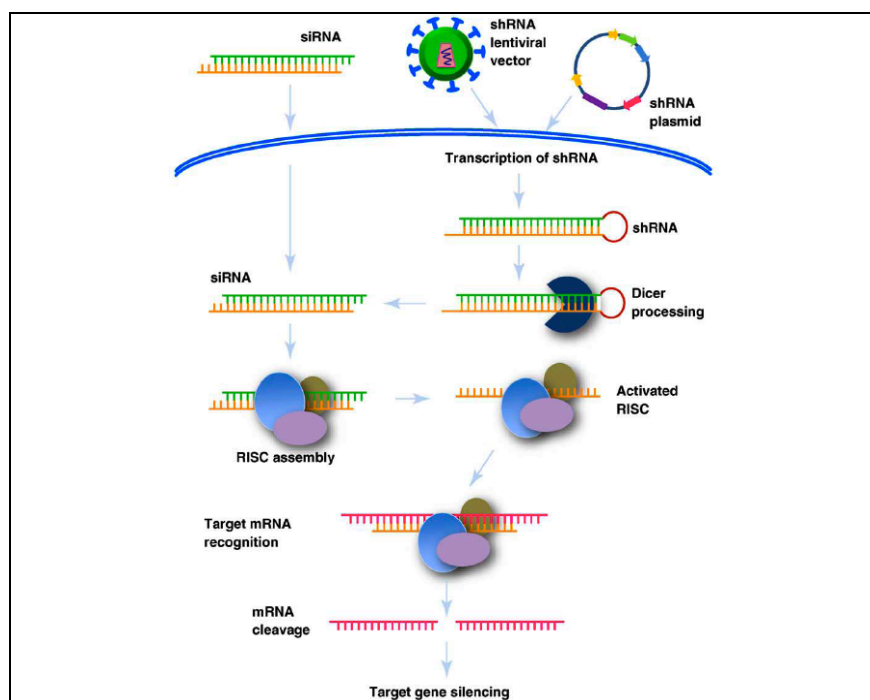


**Figure 1. Mechanisms of RNA interference.** Short hairpin or long double-stranded RNA (dsRNA) are introduced into the cytoplasm, where they are cleaved by Dicer enzyme into a small interfering RNA (siRNA). siRNA can be introduced also directly into the cell. Then the siRNA is incorporated into the RNA-induced silencing complex (RISC), resulting in the cleavage of the sense strand of RNA by argonaute 2 (AGO2). The activated RISC-siRNA complex seeks out, binds to and degrades complementary mRNA, which leads to the silencing of the target gene. Figure 1 adapted from Kim et al., 2009.

### 1.3 Applications of RNA Interference

RNAi technology represents now day the most widely used tool to investigate gene function, both on cell culture and in model organisms. RNAi can regulate several biological processes, such as signal transduction, cell cycle, macromolecular synthesis and degradation, development, cell motility, cell death and viral replication. The most obvious clinical use of RNAi targets diseases in which selective depletion of one or a few specific proteins is expected to slow or halt the disease process in the affected cells, i.e cancer.

There are two general abnormalities in cancer cells: the deregulation of the cell cycle that results in uncontrolled growth and the resistance to death as a result of abnormalities in one or more proteins that mediate apoptosis (Nam & Parang, 2003). The RNAi approaches for cancer therapy are therefore to knock out the expression of a cell cycle gene and/or an anti-apoptotic gene in the cancer cells thereby stopping tumor growth and killing the cancer cells. To selectively eliminate cancer cells without damaging normal cells, the RNAi would be targeted to a gene specifically involved in the growth or survival of the cancer cell, or the siRNAs would be selectively delivered into the cancer cells. For many years antisense oligodeoxynucleotide technology was pursued in preclinical studies of cancer therapies but with discouraging results overall (Jansen & Zangemeister-Wittke, 2002). Recent studies have clearly demonstrated advantages of RNAi methods for the growth suppression and killing of cancer cells. In one study, siRNA was shown to be greater than an order of magnitude more potent than antisense DNA in suppressing gene expression in human hepatoma and pancreatic cancer cell lines. Clinical trials using RNAi based strategies are under way for viral, ocular neurodegenerative diseases and cancer (table 1). (D. H. Kim et al., 2007; Pecot et al., 2011).

Company	Product	Target	Disease	Delivery	Status
Acuity Pharmaceuticals	Bevasiranib	VEGF	Age-related macular degeneration	Intravitreal	Phase II
Acuity Pharmaceuticals	Bevasiranib	VEGF	Diabetic macular edema	Topical	Phase II
Aegera Therapeutics	AEG35156	X-linked inhibitor of apoptosis protein	Chronic lymphocytic leukemia, non-small cell lung cancer, pancreatic cancer	Systemic	Phase I/II
Allergan/Merck	AGN211745	VEGF receptor-1	Age-related macular degeneration	Intravitreal	Phase II
Alnylam Pharmaceuticals	ALN-RSV01		Respiratory syncytial virus	Intranasal or inhalation	Phase II
Benitec/City of Hope	sidrZT		HIV/AIDS	Lentiviral vector	Phase I
Calando Pharmaceuticals	CALAA-01	Ribonucleotide reductase M2	Solid tumors	Systemic	Phase I
Merck/Sirna Therapeutics	Sirna-027		Age-related macular degeneration		Phase II
Nudeonics	NUC B1000		Hepatitis B virus	Systemic	Phase I
Quark Pharma./Pfizer	RTP801i-14	RTP801	Age-related macular degeneration	Intravitreal	Phase I/II
Quark Pharma./Pfizer	RTP801i-14	RTP801	Diabetic macular edema	Topical	Phase II
Quark Pharmaceuticals	AKli-5	p53	Acute renal failure	Systemic	Phase I
Santaris Pharmaceuticals	SPC3649		Hepatitis C virus		Phase I
Senetek PLC	ATN-RNA		Glioblastoma multiforme		Phase I
TransDerm Inc.	TD101	Keratin 6a (K6a) N171K mutant	Pachyonychia congenita	Intradermal	Phase Ib
Duke University	Proteasome siRNA and tumor antigen RNA	Proteasome/ dendritic cells	Metastatic melanoma	Transfection of autologous dendritic cells ex vivo	Phase I
Silence therapeutics AG	Atu027	Protein kinase N3	Advanced Solid Tumors	IV infusion	Phase I
Tekmira Pharmaceuticals Corporation	PRO-020401	ApoB	Hypercholesterolemia	IV infusion	Phase I

Table 1. siRNA therapeutics in clinical trials.

## **1.4 Challenges in using RNAi for therapeutic application**

Small interfering RNAs (siRNA) show significant potential in new molecular approaches to down-regulate specific gene expression in cancerous or viral-infected cells. However, there are still lots of critical points to resolve before their use as anticancer agents in clinical applications (Kim et al, 2007). This is because free siRNAs, delivered into the bloodstream, may undergo enzymatic degradation. A still open field is the mechanism of internalization of siRNA. In *Drosophila* cell cultures it has been shown that dsRNA is taken up by an active process involving receptor-mediated endocytosis (Saleh et al., 2006). Pharmacological inhibition of endocytic pathways disrupted exogenous dsRNA entry and the induction of gene silencing. This dsRNA uptake mechanism seems to be evolutionarily conserved, as knockdown of orthologues in *Caenorhabditis elegans* inactivated the RNA interference response. Another crucial point is the correct delivery of siRNAs. To induce gene-silencing, intact double-stranded siRNAs have to reach the cell cytoplasm and be loaded onto RISC. Although small compared to nucleic acid standards, siRNAs are molecules much larger compared to typical small-molecule drugs that can enter easily cells. Moreover, siRNAs also have a strong negative charge due to phosphate groups and thereby cannot readily cross biological membranes to be taken up by cells. Thus, poor cellular uptake is the first major barrier for the use of siRNA, which limits its use even for local administration. In some cases siRNA can be taken up spontaneously by some cells at a very low efficiency via caveolin-mediated endocytosis. In addition, in complex systems, many tissues *in vivo* can only be reached through the systemic administration of siRNA via the blood stream. For an effective systemic delivery, the siRNA has to remain intact in the blood stream, extravasate through the vessels, diffuse through the extracellular matrix (ECM), penetrate the cellular membranes and be released into the cytoplasm. Thus, besides the poor cellular uptake, a series of other biological barriers are interposed between siRNAs and their target sites inside the cells. Since it is extremely necessary that after its correct delivery, the siRNA has to be still intact and active, the stability of siRNA in the extracellular and intracellular environments is crucial. Naked siRNAs have a very short half-life, few minutes in serum due to degradation by ribonucleases (RNases), rapid renal excretion, uptake by the reticuloendothelial system (RES) and sequestration by serum proteins, thus lowering its bioavailability. Some of these issues, such as degradation by ribonucleases, can be avoided introducing chemical modifications such as a phosphorothioate backbone and 2'-sugar modifications that resist nuclease degradation, although their actual benefit for therapy has yet to be demonstrated (Lewis et al., 2002). Even if, with the mentioned modifications, siRNA can survive a while in the plasma, the next major barrier of siRNA delivery is the tight vascular endothelial wall. In general, molecules larger than 5 nm in diameter are not able to easily cross the capillary endothelium. However, liver, spleen and some tumors have enhanced the vascular permeability that allows the exit of macromolecules and nanoparticles up to approximately 200 nm in diameter, known as the enhanced permeation and retention (EPR) effect. Once overcome this barrier siRNA must diffuse through the ECM, which is a dense network of polysaccharides and fibrous proteins that can slow down or block siRNA complex diffusion. Finally, when the siRNA complex reaches the target cells, they have to be uptaken via endocytosis and, inside the cells they should escape the endosome and reach the cytoplasm (figure 2) (Akhtar et al., 2007).

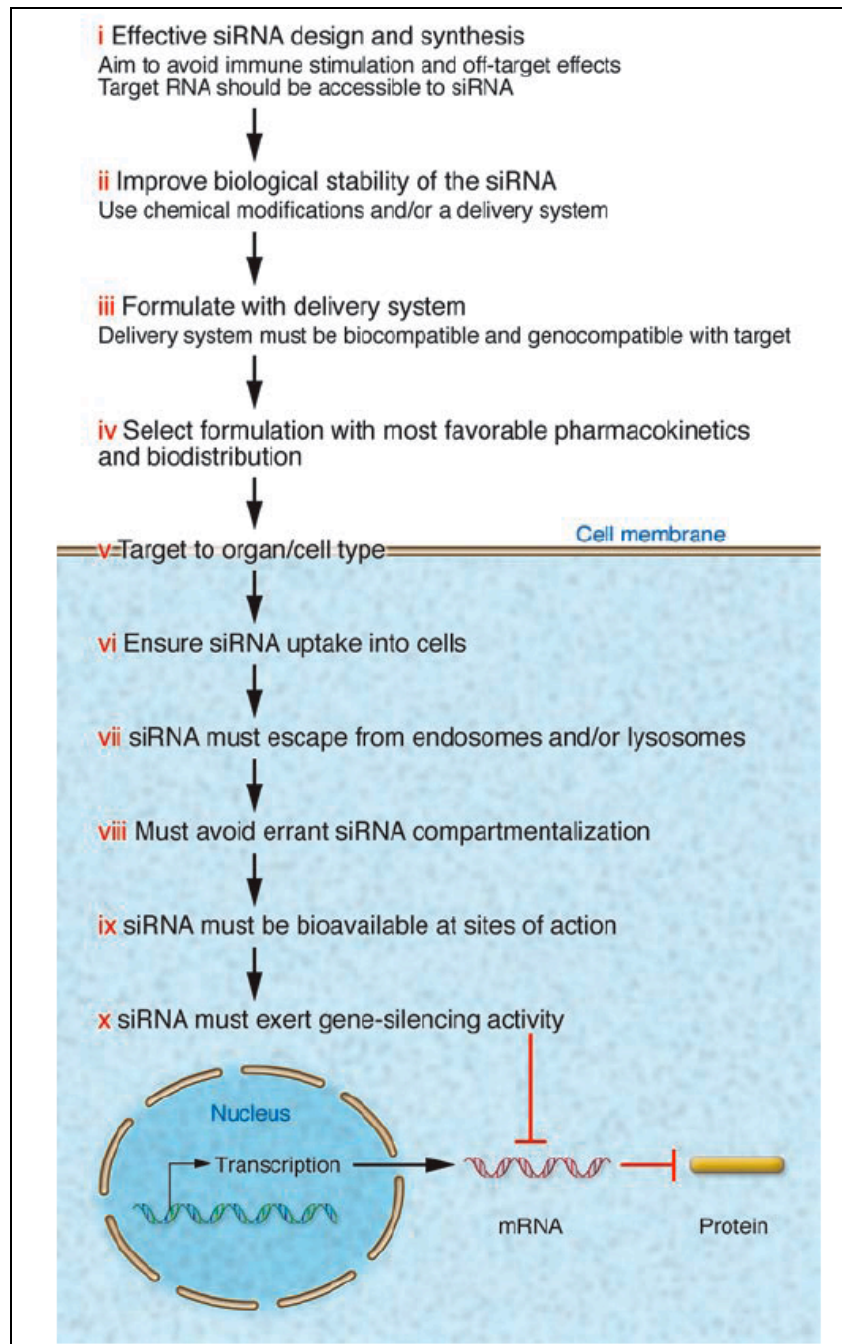


**Figure 2. The pharmaceutical challenges to effective siRNA delivery and activity *in vivo*.** The challenges for effective siRNA delivery and activity *in vivo* range from the effective empirical or *in silico* design and selection of an effective siRNA sequence to its chemical modification or formulation with delivery vectors to improve biological stability and pharmacokinetics (steps i–iv). Optimally designed and formulated siRNA should then efficiently enter target cells and escape endosomal and other intracellular compartments to become highly bioavailable inside the cells so as to exert sequence-specific gene-silencing activity with no or minimal effects on nontargeted genes or inadvertent stimulation of the immune system (steps v–x). Figure 2 adapted from Akhtar et al., 2007.

Although siRNAs are, in many cases, designed to exert therapeutic effects, they can also induce toxic side effects, such as the activation of the innate immunity through the induction of interferon responses as well as off-target gene silencing. siRNAs can potentially induce interferon responses either through the cytosolic dsRNA-activated protein kinase PKR or binding to toll-like receptors (TLRs). It has been shown (Bridgeet al., 2003; Reynolds et al., 2006), that the interferon and interleukin

production by plasmacytoid dendritic cells seems to be induced by some particular nucleotide motifs such as 5'-UGUGU-3' or 5'-GUCCUUCAA-3' within siRNAs. Apart from immunostimulation, siRNAs can also induce off-target effects. The majority of off-target effects are caused by small regions of seed sequence homology to the 3' UTR of cellular mRNAs. Exogenous siRNA in large amounts can also potentially affect the activity of cellular microRNA by saturating the RISC. Furthermore, nonselective systemic siRNA delivery approaches result in their nonspecific distribution, thereby significantly decreasing the local concentration in the desired tissue and requiring large amounts of siRNA for gene silencing *in vivo*. To minimize toxicity, off target effects, excessive immunostimulation and to increase the specificity of delivery and targeting, in the last years there has been a great deal of interest in developing targeted delivery systems that reduce the effective dose as well as toxicities.

To this aim many carriers have been developed in the last years, such as macromolecules based on nonviral lipids or protein carriers, including cholesterol, liposomes, antibody protomer fusions, cyclodextrin nanoparticles, fusogenic peptides, aptamers, biodegradable polylactide copolymers, and polymers. Positively charged cationic liposomes and polymers, such as polyethyleneimine, are currently the two major carriers used to complex with negatively charged siRNA for systemic delivery (Table 2, Kim et al., 2009).

Formulation	Targeting moiety	Target gene product	Delivery route	Disease model
<b>Liposomes</b>				
Cationic liposome	Antibody to transferrin receptor	Her-2	Intravascular	Breast cancer, pancreatic cancer
PEGylated liposome	Antibody to insulin and transferrin receptor	Luciferase, EGF receptor	Intravascular	Brain cancer
Stabilized liposome	Antibody to beta7 integrin	Cyclin D1	Intravascular	Gut inflammation
DOTAP:chol liposome	Transferrin	Cy3-siRNA, Luciferase	Intracerebellar	-
<b>Polymers</b>				
PEI nanoparticle	Folate	Survivin	Cell-mediated	Nasopharyngeal epidermal carcinoma
Cyclodextrin nanoparticle	Transferrin	<i>Ews-Fli1</i>	Intravascular	Ewing's sarcoma
<b>Peptides</b>				
Protamine	HIV envelope gp160, ErbB2 antibody Fab	<i>c-myc</i> , VEGF, MDM2, Ku70	Intratumoral, intravascular	gp160-expressing melanoma cells, breast cancer
Protamine	LFA-1 antibody scFv	Cy3-siRNA	Intravascular	K562 xenograft
Nona-D-arginine	RVG	JEV envelope	Intravascular	JEV infection
Nona-D-arginine	CD7 antibody scFv	<i>vif</i> , <i>tat</i> , <i>ccr5</i>	Intravascular	HIV infection
<b>Aptamers</b>				
Aptamer	PSMA	<i>Plk1</i> , <i>Bcl-2</i>	Intratumoral	Prostate cancer

Table 2. siRNA formulations employed for RNAi in different disease models. Table 2 from Kim et al., 2009.

The strategies employed for the delivery of siRNA into cells can be broadly classified as either viral or nonviral-based. For the former, lentivirus, adeno-associated viruses and retro-viruses have all been used successfully as delivery vehicles of siRNA into cells (Morris et al., 2006). However, though effective, there are safety and toxicity concerns associated with using viral vectors that prevent their use in humans *in vivo*. On the other hand, nonviral methods of delivering siRNA have also been investigated. These include the use of lipid-based vectors such as liposomes, peptides, and cationic polymers as well as nanoparticles. Most importantly, tracking and monitoring the delivery of siRNA into cells are hard to accomplish without the help of a suitable tracking agent. As such, there is an impetus for finding a safe, nonviral, highly efficient and self-tracking vehicle for delivering siRNA into mammalian cells.



Nevertheless, all these systems have several disadvantages: they are difficult to synthesize; their composition is not easy to control; they often have low stability in biological fluids.

The spreading of the nanotechnologies over the last decade, and the capability to control material size, shape and physical properties at the nanoscale, allowed us to use also nanoparticle to increase siRNA delivery and efficiency.

As the term nanoparticle is generally used to indicate materials with very different chemico-physical properties, a brief introduction on different nanomaterials is reported below for clarity.

### **1.5 Nanobiotechnology and nanomaterials**

Nanotechnologies use materials or engineered nanosized devices, usually from 1 to 100 nm, with properties depending on their size, shape, chemical composition. Nanotechnology include the design, synthesis and characterization of nanomaterials and nanodevices. Chemistry, an integral component of nanotechnology deals with the manipulation of matter at the nanoscale leading to products with specific intrinsic properties that affect their interaction with the environment. Nanomaterials are being employed in several fields such as electronics, textiles, construction, sensors, chemical industry, automotive industry, medicine and many others. Nanobiotechnologies are widely recognized as one of the most interesting areas of application of nanotechnology. They use tools, materials and technologies to measure the chemistry and physics of nanosystems thought to investigate the properties and function of biological systems. The great potential of these methods is to reveal the function of biological systems at the molecular level, considering even a single (bio) molecule as a machine. The impacts of this research in the biomedical field are already evident and hold great potential in drug delivery, imaging and cell tracking. Manifold nanoparticle (NP) types have been produced, different in their chemical composition, shape, dimension, chemical-physical properties, which make each type best suited for a specific purpose. For example, the fluorescent NP with a semiconductor core are chosen for fluorescence imaging in biology, the magnetic NP for diagnostic (MRI) or hyperthermia applications, the gold nanoparticles provide best contrast for electron microscopy and, given the non-toxic nature, for drugs delivery. This highlights the need to consider not only the usefulness of NPs but also the potentially unpredictable and adverse consequences of human exposure to them. In this context, NP toxicity refers to the ability of the particles to adversely affect the normal physiology as well as to directly interrupt the normal structure of organs and tissues of humans and animals. It is widely accepted that toxicity may be related to physicochemical parameters (size, shape, surface charge and chemistry, composition, stability). However the exact underlying mechanism is yet unknown, and recent literature suggests manifold pathways possibly involved, from oxidative stress to pro-inflammatory gene activation (Ambrosone et al., 2012; Tino et al., 2011; Alarifi et al., 2013).

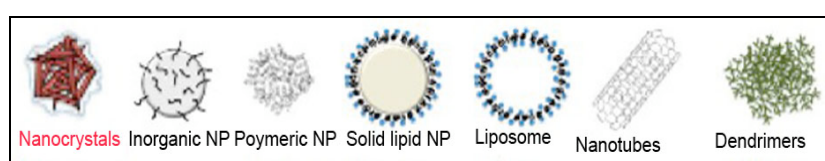


**Figure 3. Overview on nanoparticles.** Different types of nanoparticles are presented.

Among the main properties of nanoparticles suitable for nanomedicine, there is the capability to bind to their surface a large plethora of molecules and functional groups. NPs functionalization can be designed to achieve better targeting efficiency, better cellular internalization and higher bioavailability. It is also possible to add on NP surface drugs, bioactive compounds, in order to build nanomachines that can reach the target tissue and cells (figure 4).

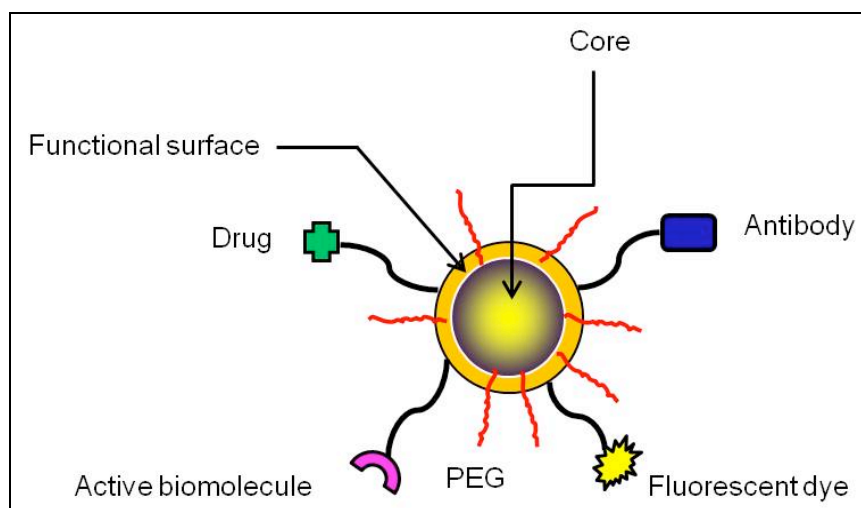


**Figure. 4. Scheme of a general nanoparticle structure.** Schematic representation of the multiple functional groups that can be linked to NP surface. The core confers physical, electrical and magnetic properties; the surface confers the stabilization in aqueous medium, and finally the functionalization of NPs is important for specific targeting or the delivery.

Iron oxide nanoparticles present magnetic properties. By applying an intense external magnetic field, the particles of iron oxide begin to resonate releasing heat. This effect, known as magnetic hyperthermia, can be used for selective cell ablation of tumor cells, in view of their high susceptibility to heat (Huang et al., 2010).

Ag nanoparticles are known for their antibacterial properties and are present in many products, from fabrics for sportswear. Although the antimicrobial properties of silver are known for thousands of years, the increase in the area of engineered silver nanoparticles (1-100 nm) makes them more chemically active and increases the therapeutic properties (Stanić et al., 2011).

Fullerenes are molecules composed entirely of carbon, which may take the form of a hollow sphere, of an ellipsoid or a tube. They can be single-walled SWNT (single-walled nanotube), if constituted by a single sheet or multiple wall, MWNT (multiwalled nanotube), if formed from sheets positioned as concentric cylinders inserted one inside the other. In recent times, the fullerenes have attracted attention for many properties they possess: they are six times lighter, but a hundred times stronger than steel, yet flexible. Are extremely resistant to high temperatures and can be conductors, semiconductors or insulators, depending on the method of production (Zinchenko et al., 2013).

Carbon nanotubes are also finding application in regenerative medicine. In particular, in the neurological field, they could be used to reestablish the intricate connections between nerve cells. The organic structure, characterized by a remarkable ability to conduct electricity makes it possible the transfer of action potentials between nerve cells (Yildirimer et al., 2011)



The Dendrimers are branched polymers with 3-8 or more branches, starting from a central core. The dendrimers have emerged as one of the best vectors for drugs due to their biocompatibility, the nanosized dimension and the structure resembling certain biomolecules. Specific drugs targeting through dendrimers is based on the fact that if a receptor is specifically expressed or is in excess on the surface of a cell, the dendrimer carrying the drug (together with the ligand receptor) can travel in the blood stream, bind specifically to the cell and release the drug (Gareth et al., 2005).

The Quantum Dots are fluorescent nanoparticles made of metals semiconductors, with singular chemical-physical properties, such as high luminescence, photostability, absorption spectra and emission dependent on the composition and size. Compared to organic fluorophores the QDs have different optical properties, as evidenced by the emission and absorption spectra (Figure 5c) The traditional organic dyes are characterized by asymmetric emission spectra and narrow absorption spectra, which means that they can only be excited within a narrow window of wavelengths. The QDs instead have broad absorption spectra, allowing excitation in a wide range of wavelengths and their emission spectra are symmetrical and narrow. They have dimensions between 2 and 40 nm in diameter, and after UV excitation, emit at different wavelengths ranging from 400 to 800 nm (from near UV to infrared). The characteristics of absorption and emission of light are dictated both by the size that the chemical composition. Consequently multicolored nanocrystals of different sizes can be excited by a single wavelength. In general the QDs structure present: a core of semiconducting material such as CdSe and CdTe, a shell of CdS, ZnS, PbS to greatly increase the fluorescence properties and an outer capping important for biocompatibility (Younes et al., 2009).

The Quantum Rods, have rod-shaped and in addition to the properties described for the QDs, are endowed with superior brilliance, having intervals of absorption wider, making them fluorescent probes of election (Figure 5d).

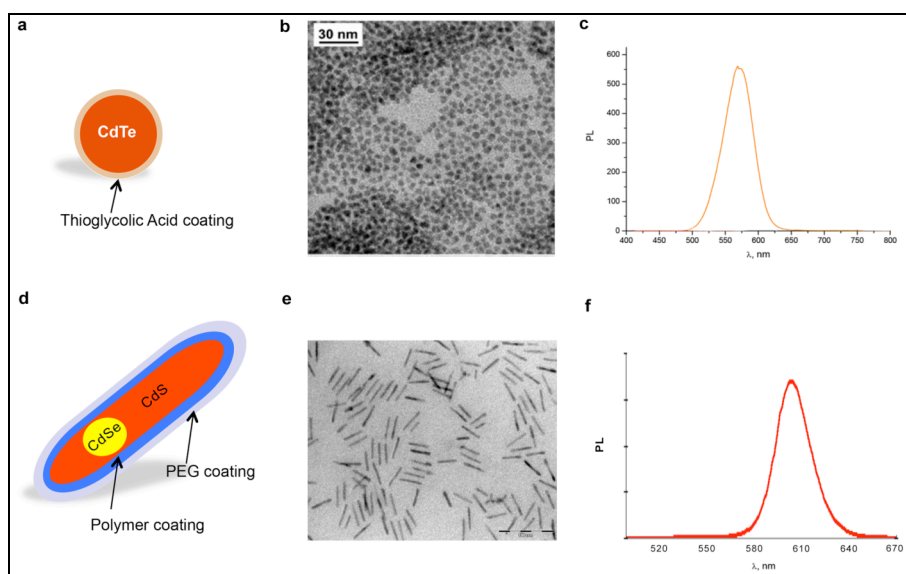


**Figure 5. General scheme of QD and QR.** a) schematic representation of the CdTe quantum dot. QDs present a dimension between 2 and 4 nm in diameter b) TEM images of QDs; c) emission spectra d) schematic representation of the CdSe/CdS rods, highlighting the asymmetrical shape derived from the synthesis procedure. The rod samples present an average of 35nm in length and 4 nm in diameter as confirmed by e) the TEM image. f) emission spectra of QR (From Ambrososne et al, submitted)

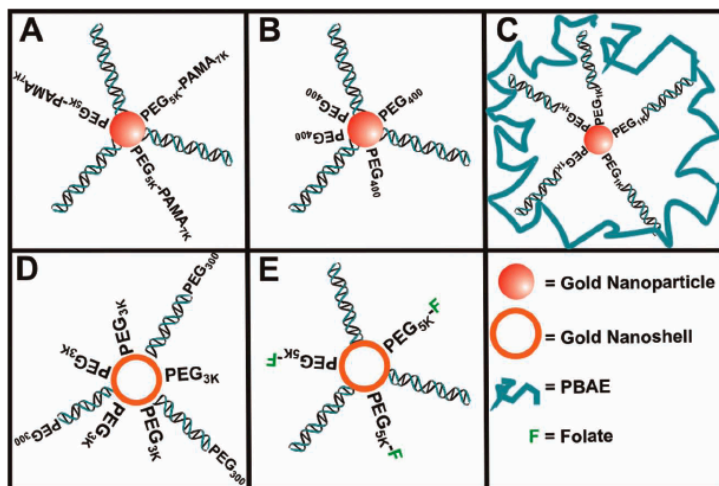
## **1.6 Gold nanoparticles**

Gold nanoparticles are produced with easy and mild conditions by chemical reduction of gold salts. They possess, as other types of metal particles, particular properties of absorption of visible light (plasmonic absorption) that make them particularly suitable for the development of diagnostic tools. Spherical gold nanoparticles exhibit an intense red color due to the surface plasmonic absorption, while triangular shaped nanocrystals show blue colour. Changes in their shape reflect also changes in their property of emitting heat, because of the plasmon resonance. Indeed, some nanoparticles, for instance those with a triangular or rod shapes are excellent nanoheaters (heat development and emission after NIR light excitation), while the spherical NP do not present this property. Another important feature common to other nanocrystal is the possibility to functionalize their surface with various molecules, such as PEG to prevent aggregation or bioactive molecules (peptide, nucleic acid, carbohydrates) to add functionality. The possibility to modify the surface of those nanodevices by linking it to drugs or to molecules and release them at destination has opened new doors on the development of molecular and macromolecular therapies. The highly tunable and multivalent surface architecture of gold nanoconjugates offers the potential to incorporate multiple therapeutic agents as well as to target and protect molecules on the surface of a single nanoparticle, and thus are expected to improve the delivery and efficacy of therapeutic payloads.

### **1.6.1 Gold nanoparticles and oligonucleotides**

In the recent years several research groups succeeded in the synthesis, characterization and production of DNA-functionalized gold nanoparticles able to enter a wide variety of cell types. Their uptake by cells was not predicted, given that these structures contain a densely functionalized shell of polyanionic DNA (ca. 100 DNAs on the surface of each 13 nm gold particle), and that strategies for the introduction of oligonucleotides typically require that DNAs are complexed with positively charge agents to effect cellular internalization. Indeed, because of their high negative charge, most researchers at the time would have predicted that the nanoparticles would not enter cells (Niidone et al., 2002). The importance of the polyvalent arrangement of oligonucleotides to cellular uptake can be further emphasized when comparing DNA-AuNPs to other types of AuNPs. Oligonucleotide functionalized gold nanoparticles uptake resulted to be cell type independent since several cell lines resulted able to take those particles from the media. This property has been used to modulate gene expression by means of antisense oligonucleotide or siRNA conjugated NPs. The first siRNA delivery paper was published in late 2006. In this work 15 nm AuNPs were co-decorate with SH-PEG<sub>5000</sub>-PAMA and SH-siRNA (A). PAMA is a poly ethil methacrylate polymer bearing terminal amines. In this complex, the siRNA is roughly the same size as the coloaded PEG-PAMA. Then, 13 nm AuNPs were loaded with SH-PEG400 and SH-siRNA (B). In this system the PEG is smaller than siRNA thus that the particle surface exposed to the cells displays almost entirely siRNA, (Lytton-Jean et al., 2011). This reviews shows the work on siRNA-gold nanoparticles delivery for the first 5 years of its existence, mainly based on cell culture systems and on the downregulation of reporter genes (beta-gal, GFP). In vivo studies targeting physiological important genes are needed to assess the applicability of these materials as delivery agents for new therapies. On 2010 Davis and coworkers, tested for the first time the systemic administration of siRNA to

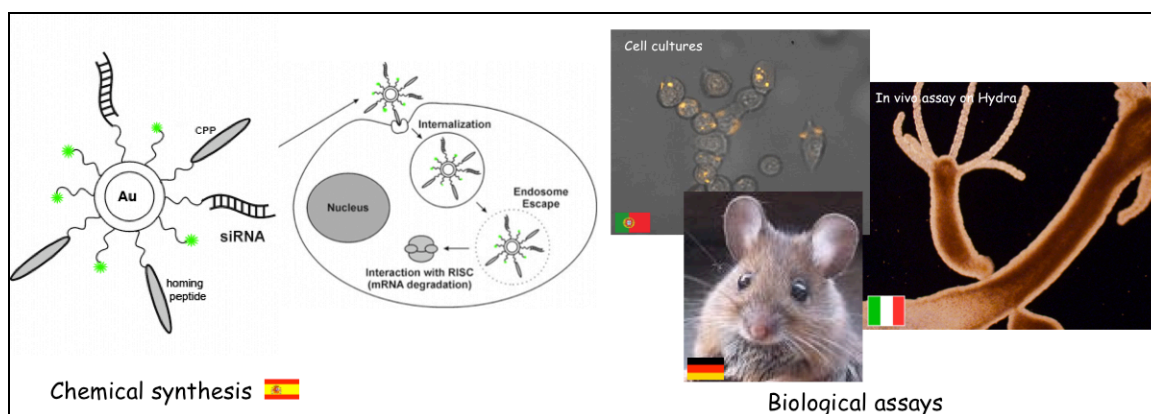
patients with solid cancers using a targeted nanoparticle delivery system. Tumor biopsies of treated patients, showed the intracellular localization of particles, and a reduction in both the specific messenger RNA and protein levels, demonstrating the feasibility of using this nanodevice for translation in clinical trials (Davis et al., 2010).








**Figura 6. Gold nanoparticle conjugates used for siRNA delivery formed via a gold-thiol bond.** Gold nanoparticles are decorated with siRNA and varying lengths of PEG. Adapted from Lytton-Jean et al., 2011.

## 1.7 The NANOTRUCK European project

The work presented in this PhD thesis is part of the European project “Multifunctional gold nanoparticles for gene therapy” (NANOTRUCK), aimed to develop gold nanoparticles functionalized with multiple bioactive molecules triggering, in a cell type specific manner, gene silencing by RNA interference. The idea is to produce new tools for lung cancer treatment, by targeting a gene frequently deregulated in this disease: the **protooncogene *c-myc***. This new nanoplatform emerged from the collaboration of 5 research groups spread all over Europe, presenting complementary expertises in Chemistry, Biology, Medicine. The project intends to develop an innovative kind of multifunctional gold nanoparticles loaded with fluorescent and tumoral markers, cell penetrating peptides and siRNA complementary to the proto-oncogene *myc*. These biofunctional products were tested in different biological systems, ranging from *in vitro* cultured human cells to *in vivo* animal models (primitive *Hydra* and complex vertebrate mouse).



-  Partner 1 (Coordinator): *Instituto de Nanociencia de Aragón* Zaragoza (Spain): Prof. R. Ibarra; Dr. JM. de la Fuente
-  Partner 2: Centre for Cell Engineering. University of Glasgow (UK): Dr. Catherine Berry
-  Partner 3: Istituto di Cibernetica “E. Caianiello” ,Pozzuoli (Italy): Dr. Claudia Tortiglione
-  Partner 4: Helmholtz Zentrum München. München (Germany): Dr. Furong Tian
-  Partner 5: Faculdade de Ciências e Tecnologia. Universidade Nova de Lisboa. Caparica (Portugal): Dr. P.V. Baptista

My PhD thesis contributed to achieve the objectives expected for the Italian Research Unit, testing AuNP-siRNA conjugates on *Hydra vulgaris*.

### 1.7.1 The *myc* protooncogene as target

Most of the genes involved in neoplastic transformation and cancer, namely the oncogenes, encode for proteins devoted either to transcription or to control DNA integrity/cell cycle progression. Among them, the *MYC* family of transcription factors controls disparate aspects of cell physiology including cell growth, cell cycle progression, biosynthetic metabolism, and apoptosis. As expected, its deregulated expression occurs in the majority of human cancers (Figure 7), as reported in Dans et al., 2012. Activation or upregulation of *c-myc* is known to cause numerous biological effects including cell proliferation and paradoxically induction of apoptosis, cell differentiation and stem cell self-renewal. Thus the main rationale for selecting

*myc* as a target for cancer therapy is two fold; (1) the gene is involved in a wide variety of human tumors and thus therapies could potentially have an impact on the treatment of a broader range of malignancies; (2) *myc* is involved in both proliferation and apoptosis, thus strategies aimed at targeting *myc* might lead to either inhibition of tumor cell proliferation and/or increase in cell apoptosis.

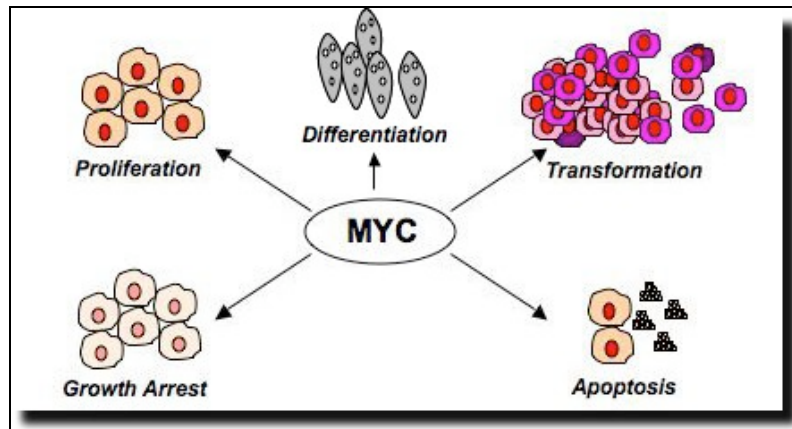


Figure 7. Cellular processes controlled by *myc* during normal conditions and during tumorigenesis.

The MYC protein consists of an N-terminal domain (TAD) required for transcriptional activation, a central region and a C-terminal domain (CTD), critical point for DNA binding and protein interactions. Furthermore, MYC has four conserved region, called Myc boxes (MB) that are important for different functions. The TAD domain contains MBI, that contributes to gene activations and protein degradation, and MBII, that is critical for the several *myc* functions. The central regions contains the conserved domain, MBIII, involved in transcriptional repression, apoptosis, trasformation, and lymphomogenesis, and MBIV, that regulates DNA binding, apoptosis, transformation and G2 arrest (Figure 8, Cowling et al., 2006).

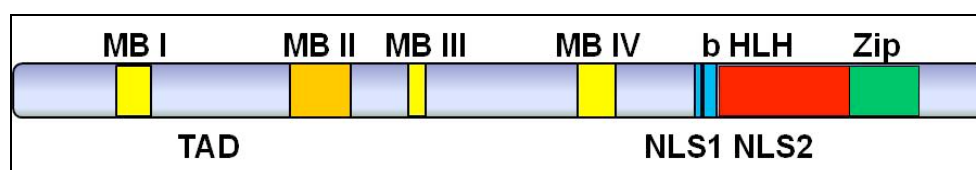


Figure 8. Scheme of the *c-myc* transcription factor structure. MYC is characterized by the presence of four Myc boxes (MBI to MBIV), at the N terminus there is the TAD domain involved in transcriptional activation. At the C terminus there is the DNA binding domain and the two sequences of nuclear localization.

*Myc* expression is regulated by external signals, such as growth factors, but also by internal cell cycle control. In the normal cells, *myc* levels are low, instead they increase upon entry into the cell cycle, and then decline to remain at a basal level in cycling cell as described in Amati et al., 1998 and Edgar et al., 2001. Oncogenic alterations of *myc* gene are induced by mutations, gene amplification, translocation, over-expression, enhanced translation and increased protein stability. The role of *c-myc* in cancer has been extensively examined in many studies for the past decade; breast cancer, for example is generated by overexpression of *c-myc* (Liao et al., 2000).

### **1.7.2 Multifunctional gold nanoparticles for myc RNAi**

In the frame of the Nanotruck project, in the laboratory headed by dr. Jesus de la Fuente, (University of Zaragoza, Spain) stable gold nanoparticles (AuNPs) with a diameter of 14 nm were synthesized by reduction of sodium tetrachloraurate hydrate with sodium citrate dehydrate. The whole synthesis procedure is reported in the manuscript by Conde et al, 2012 and the main rationale is here briefly described. To improve the stability, biocompatibility, and chemical functionality, AuNPs were functionalized with two types of thiolated polyethylene glycol (PEG) spacers: a commercial carboxylated spacer, SH-EG (8)-(CH<sub>2</sub>)<sub>2</sub>-COOH, and an azide-containing spacer custom synthesized, SH-(CH<sub>2</sub>)<sub>3</sub>-CONH-EG(6)-(CH<sub>2</sub>)<sub>2</sub>-N<sub>3</sub>. The first spacer provides the anchoring moieties for the covalent binding of amine-containing molecules through carbodiimide chemistry, while the azide spacer confers positive zeta potential values, which is important for cell uptake. With the aim to elucidate the most efficient strategy to bind siRNA molecules to AuNPs, two types of AuNPs stabilized by different degrees of PEG chains were selected: 1) NP-ionic with 100% PEG coverage (25% azide-containing spacer and 75% carboxylated spacer); 2) NP-covalent with 25% PEG coverage (composed by 50% of either spacer). These AuNP formulations represented the basic nanoparticles for downstream functionalization with c-myc siRNA, using either ionic approach (ion) or covalent (cov) approach. The moieties selected for AuNP functionalization were the following: cell penetrating peptides, to overcome the lipophilic barrier of the cellular membranes and improve cell delivery; Quaternary ammonium: to introduce stable positively charged on gold nanoparticles surface; small interfering RNAs, to achieve gene silencing. All AuNP bioconjugates presenting at the surface siRNA and other groups, TAT peptide, RGD, and quaternary ammonium (R<sub>4</sub>N<sup>+</sup>), in different combinations, were characterized by transmission electron microscopy (TEM), UV/vis spectroscopy, surface plasmon resonance (SPR) shift, and Zeta potential, as showed in Figure 9. The ionic and covalent synthetic strategies are showed in Figure 10. In the covalent approach thiolated siRNAs were used given their ability to be conjugated to a non saturated PEG layer. Whereas the ionic approach took advantage of the negative charge of siRNAs that allows the interaction with quaternary ammonium loaded on the surface of the AuNPs.



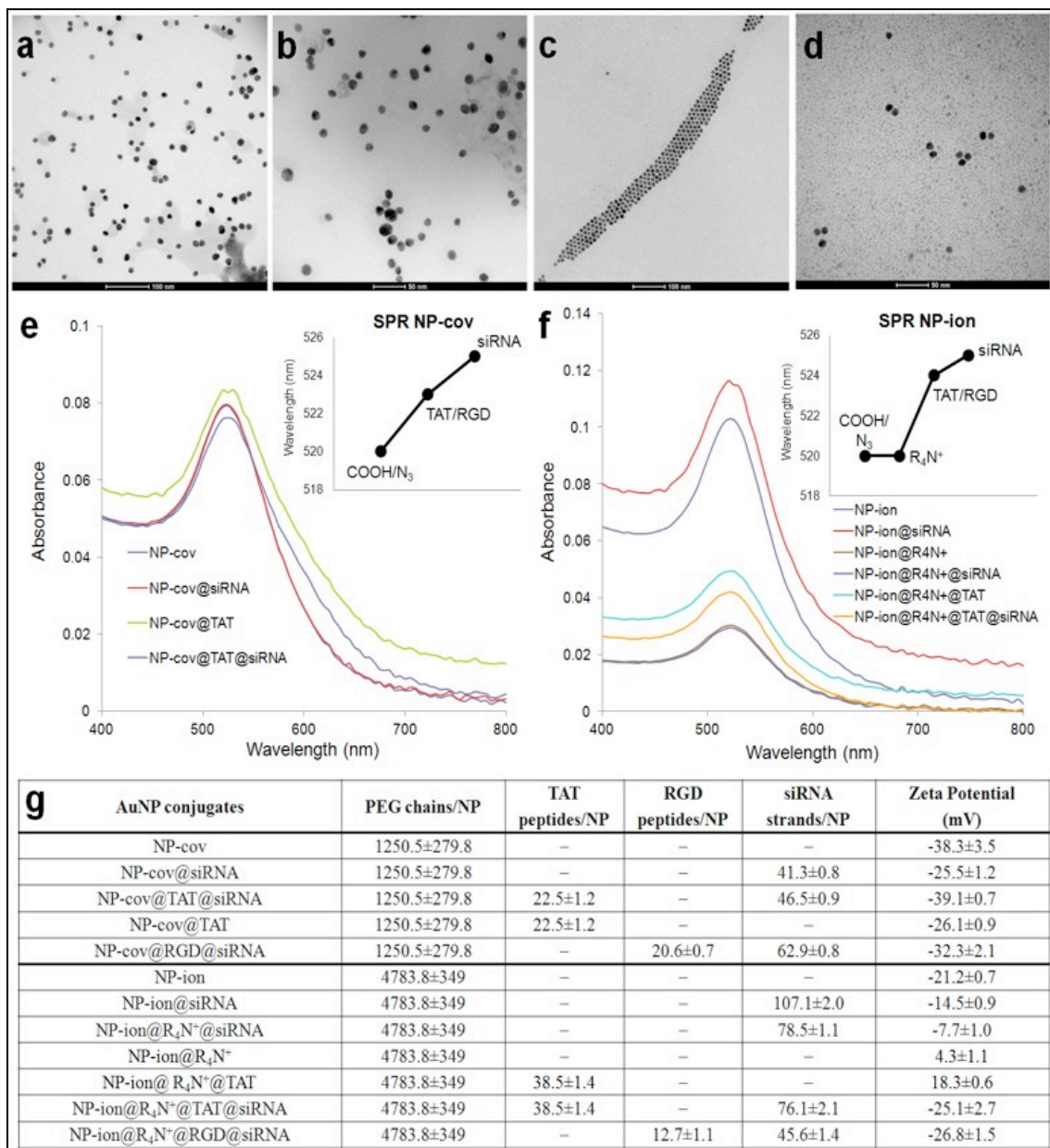


**Figure 9. Characterization of AuNPs.** TEM analysis of (a-b) NP-cov approach, (c-d) NP-ion approach. The stabilization effect of the different functional groups can be observed the optical properties by UV-vis spectroscopy (e-f). The absorption band appear at 550 nm due to the surface plasmon resonance of the AuNPs. The SPR shown in e and f insets exhibited a red shift from 520 to 525 nm. In g is showed the quantification of the PEG chains, TAT and RGD peptides and siRNA for all AuNPs, together their Z-potential measurements. (Figure from Conde et al., 2012)

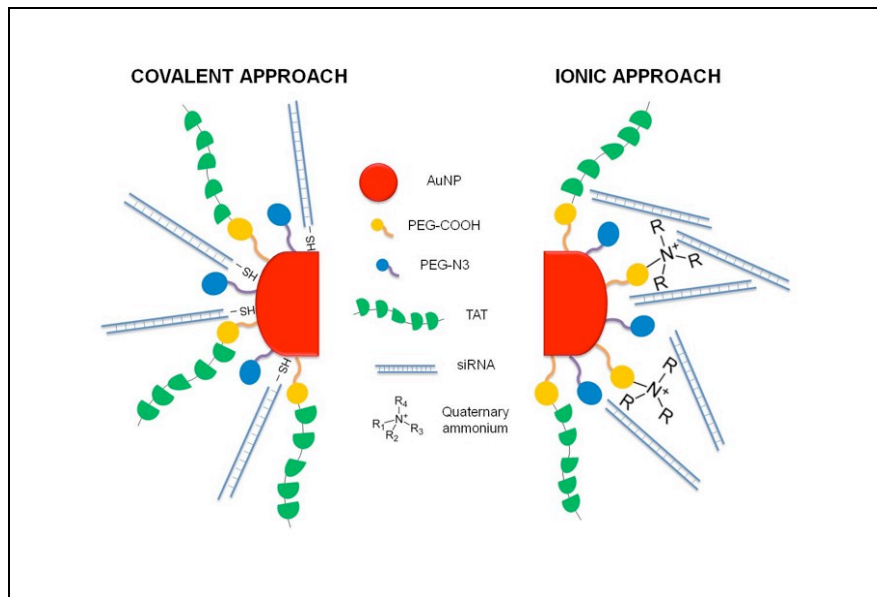


**Figure 10. Covalent and Ionic synthetic approach employed to bind siRNA on AuNPs.** Covalent approach, use of thiolated siRNA for gold-thiol binding to the nanoparticle; Ionic approach: interaction of the negatively charged siRNA to the modified surface of the AuNP through ionic interactions

In the frame of this project my experimental thesis aimed to test biocompatibility and efficiency of functional nanoparticles determining *in vivo*, a whole animal level the capability of functional NPs to induce specific gene silencing. Below, a description of the animal model I used is reported.

### 1.8 *Hydra vulgaris* as *in vivo* model sistem

The freshwater coelenterate *Hydra vulgaris* represents an interesting model system to investigate basic cellular mechanisms. Among the wide range of molecular tools available to dissect gene function in model organisms, in *Hydra* only very few have been found efficient. *Hydra vulgaris* belongs to the animal phylum Cnidaria that arose almost 600 million years ago (Figure 11) (Lenhoff et al., 1968).

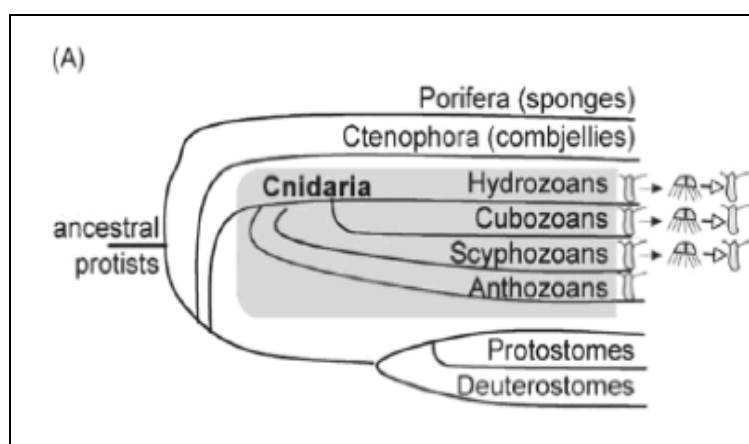


**Figure 11. Cnidaria position in Metazoan phylogeny.**

Its body plan is very simple, consisting of a single oral-aboral axis with radial symmetry. The structures along the axis are a head, a body column and a foot to



anchor to a substrate. It is shaped as a tube, about 5-20 mm long and 0.3-1.0 mm wide. The head is divided in two structures, the hypostome or mouth at the apex, and the tentacles in number of six-eight (Figure 12).

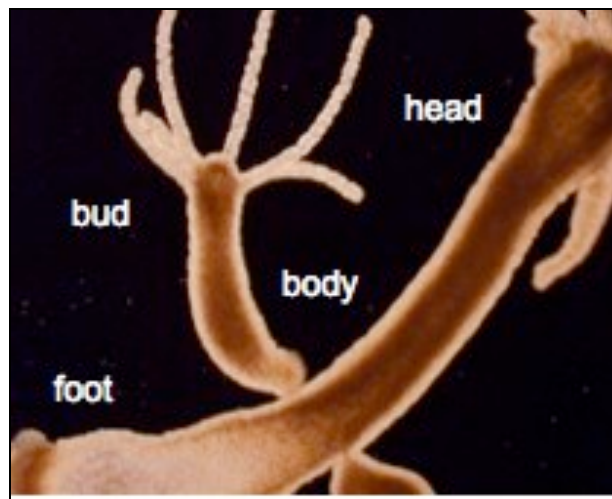


**Figure 12. *Hydra vulgaris*.** An adult animal with a bud emerging from gastric region.

The body consists of two concentric epithelia, the ectoderm and endoderm separated by an acellular basement membrane, the mesoglea. This bilayer structure extends throughout the entire body column, tentacles and buds. A third cell lineage, the interstitial stem cells lineage, is located in the interstices, among the epitheliomuscular ectodermal cells (Figure 13). Most of *Hydra* body is occupied by the gastric region, where the digestion takes place. In the lower part of the body the budding of new animals occurs, and this process accounts for the rapid asexual reproduction, which enable massive culturing of the animal in laboratory conditions.

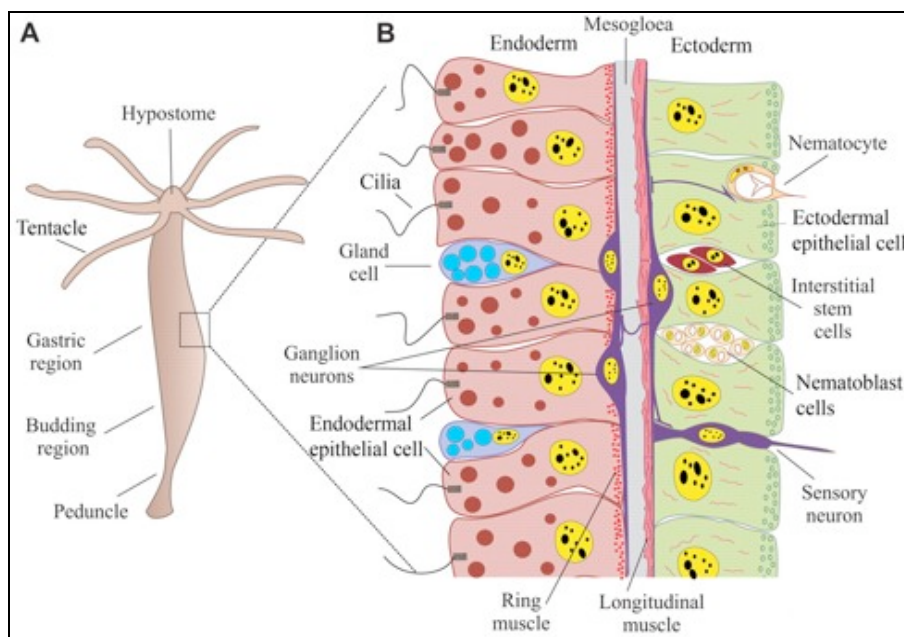


**Figure 13. Anatomical structure of *Hydra vulgaris*.** The body wall is composed of two self-renewing cell layers, an outer ectoderm and an inner endoderm, separated by mesoglea. Along the body the two epithelial layers are composed by epitheliomuscular cells, while the interstitial cells and their differentiated products are located in the interstices between the cells.

### 1.8.1 Cell types in *Hydra vulgaris*

Of 15-20 identified cell types in *Hydra*, most can be placed in one of three cell lineages. Each lineage contains a population of self-renewing stem cell and differentiated cell derived from those stem cells.

The ectoderm and endoderm contain the major epithelial cell type, called the ectodermal and endodermal epitheliomuscular cells, or simply epithelial cells. Epithelial cells divide continuously although after an injury such as a cut or after feeding, the duplication rate is slowed down (Holstein, Hobmayer, & David, 1991). These epithelial cells are large, vacuolated and usually cuboidal or columnar (Figure 14, Hobmayer et al., 2012). The epithelial cell in the tentacles develop into battery cells.

Interstitial stem cells (i-cells): the i-cells are multipotent stem cells, with a fast-cycling activity, evenly distributed along the body and absent in the regions of the head and foot (David et al., 1980). They are characterized by a large nucleus and a small cytoplasm and occur either as single or as pairs, thus for this reason they are named 1s and 2s (Figure 15). They are able to differentiate into nematocytes, secretory cells, gland cells, neurons and gametes. The interstitial stem cell system constitutes an independent cell lineage in *Hydra* that contributes about 75% of all cells in the organism (David 1987 et al., Genetic regulation of development). In Figure 15 the proliferation and differentiation pathways of the Interstitial stem cell lineage are shown.

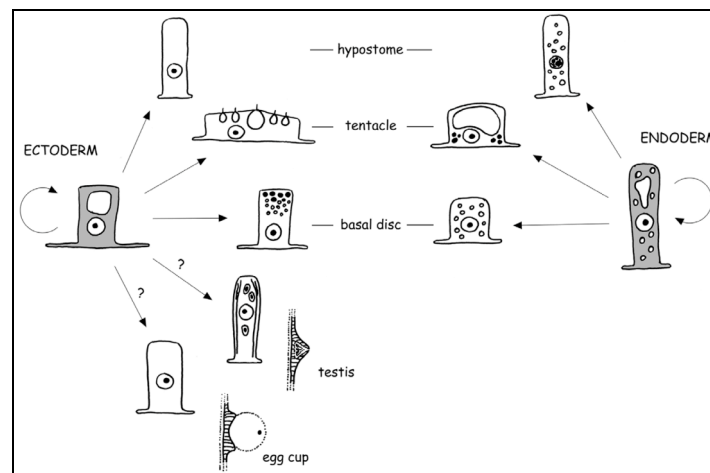


**Figura 14.** Scheme of the proliferation and differentiation pathways of ectodermal and endodermal epitheliomuscular cells. Hobmayer et al., 2012

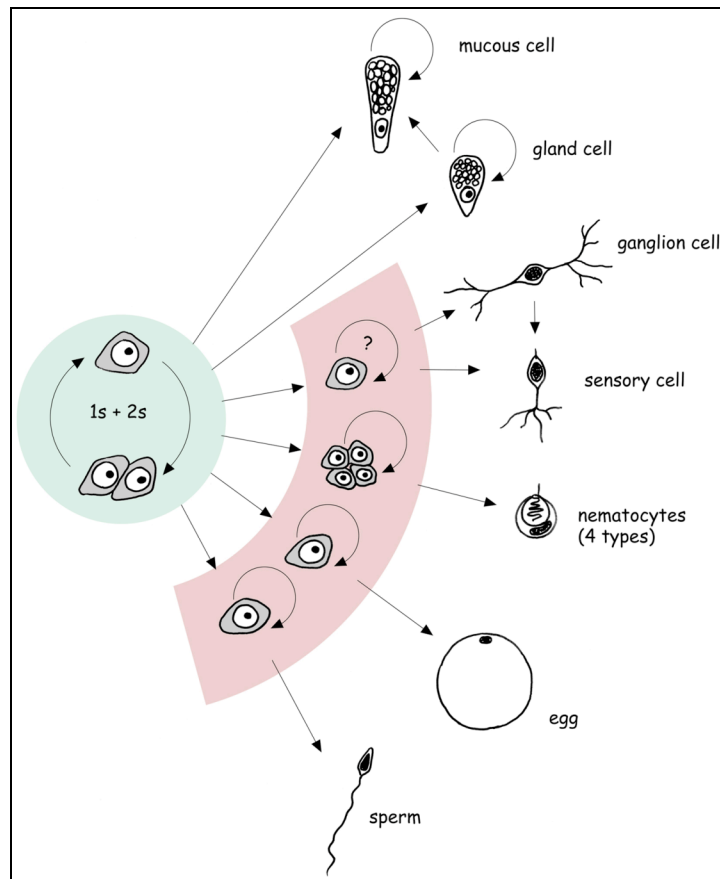


**Figura 15.** Scheme of the proliferation and differentiation pathways of the interstitial stem cell lineage. Blue, stem cells; pink, transit amplifying cells. From Hobmayer et al., 2012.

Nematoblasts include all intermediate cells between the stage of 1s interstitial cell and mature nematocyte. They occur in nests or clusters of cells ranging from 4 to 32 cells. Nematoblast in nest of 4 cells resemble small interstitial cells and can divide further. Nest of 8, 16, 32 cells are conspicuously smaller; in fact when isolated and viewed with phase microscopy they have a granular appearance and inconspicuous nucleolus. These 8-32 nest stage have been often called dividing nematoblasts.

The nematocytes, cells involved in the capture of prey, are located in the ectodermal layer and are concentrated in the tentacles. There are 4 different types of nematocytes, which differ in the type of secretory vacuole, called nematocyst capsule. In general the nematocytes appears as a tube wrapped reversed, able to release its contents during the process of prey capture (Holstein T., 1981). Once differentiated nematocytes migrate into the tentacles, where they are incorporated as aggregates of 10 to 20 units to form battery complexes (Figure 16). The battery cells consists of a modified ectodermal epithelial cell and do not undergo mitosis. These cells are characterized by several cell type embedded into a single giant cells: sensory neurons and nematocytes (Campbell R.D. 1987). In a previously work, using the monoclonal antibody NV1 as a marker for tentacle-specific nerve cells (Hobmayer et al, 1990) have been investigated formation of tentacle tissue on a cellular level. Formation of a NVI-battery cell complex occurs during head formation and is stimulated by treatment with the neuropeptide head activator (HA), which has been shown to stimulate tentacle (Schaller, 1973) and nerve cell formation (Holstein et al., 1986) in *Hydra*.

Other endodermal cells: the basal cells, found near the mesoglea; gland cells which divided in two classes: zymogen cell and mucous cell. The zymogen cell is characterized by large and dense secretory vesicles. Zymogen cells occur throughout the body column, but not in the hypostome or basal disk regions. Mucous cells are small granules found in the hypostome. In Figure 17 the different cell types isolated from macerated *Hydra* tissue are shown.

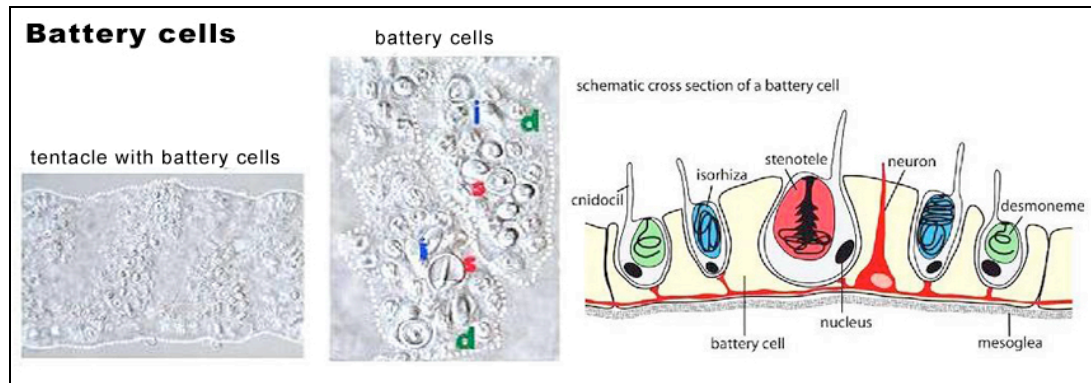


**Figure 16. Structure of battery cell in *Hydra vulgaris*.** Three types of nematocytes, a sensory cell and cnidocil form the battery cell.

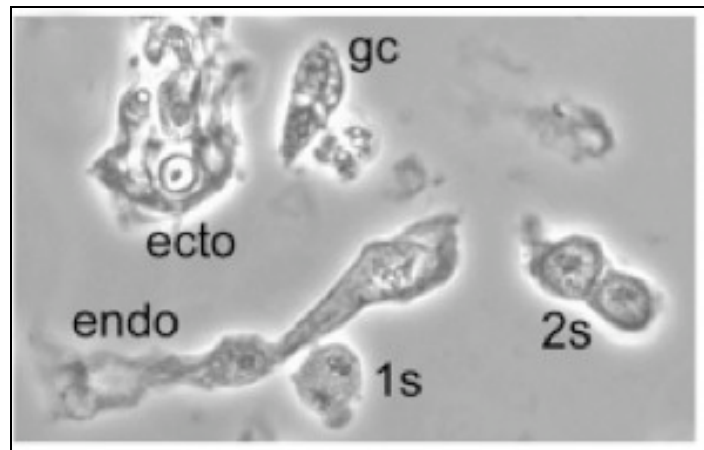


**Figure 17. Isolated cells from macerated *Hydra* tissue as viewed using phase microscopy.** The cell types illustrated are: ectodermal epitheliomuscular cell from body column (ecto); endodermal epitheliomuscular cell (endo); single interstitial cell (1s); interstitial cell in nest of two (2s); basal disc gland cell (gc). Kind courtesy from B. Hobmayer.

### 1.8.2 Regeneration process in Cnidaria

Regenerative capability of Cnidaria is one of the most interesting aspects of this phylum. The regeneration in *Hydra* species enable amputated polyps, to reform a new head from the body and a new body from the head (Figure 18). Morphogenetic processes take place during the first 48 h post amputation, followed by cell proliferation to restore adult size (Bode et al., 2003); (Holstein et al., 2003).

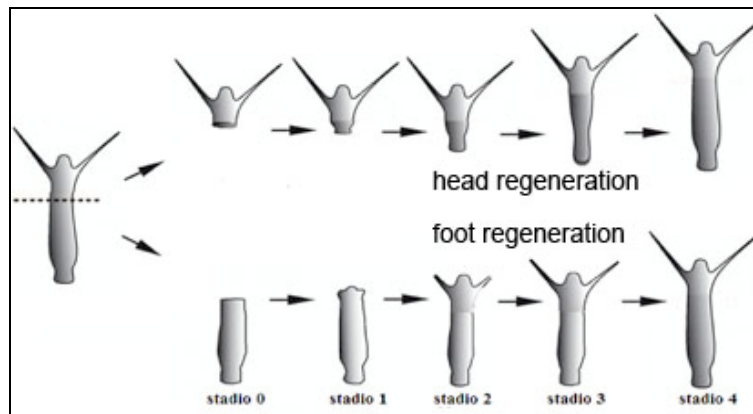


**Figure 18. The regeneration process in *Hydra vulgaris*.** After amputation, the two polyps start immediately an asymmetric process at the wound site: the upper half undergoes foot regeneration in about two days, while the lower half initiates the head regeneration process, which is completed in three days.

This ability to self-organization is due to the continuous production of adult tissue cells and signaling factors. The tissue regeneration shows a directional property called polarity, which confers the capability to regenerate a head in the apical part, and a foot in the basal extremity. The polarity depends on a gradient of molecules, which provide positional information (Bosch et al., 2007). In contrast to vertebrates, in which the morphogenetic signal is active only during embryogenesis, in *Hydra* it is continuously active (Holstein et al., 2003).

In summary radial symmetry, and high capacity for regeneration make *Hydra* an excellent model organism to study of stem cell proliferation, differentiation and regenerative processes

### 1.8.3 Reproduction

The biological cycle of *Hydra*, unlike other cnidarians, includes only one stage of polyp that can reproduce by both asexual and sexual means. The epithelial cells structuring the body continuously divide and contribute to the formation of new individuals, budding of the gastric region, and detaching from the mother in about 3 days (Galliot et al., 2006). The *Hydra* in their natural habitat typically reproduce by budding during the regular feeding regime, but they produce male gametes and / or female in autumn (Figure 19). In laboratory condition, the main method of reproduction is budding. Growth rate of *Hydra* tissue is normally regulated by a balance between epithelial cell cycle length, phagocytosis of ectodermal cells and bud formation (Bosch et al., 1984). Environmental factors, such as the presence of the pollutants or the feeding regime, can affect this balance.

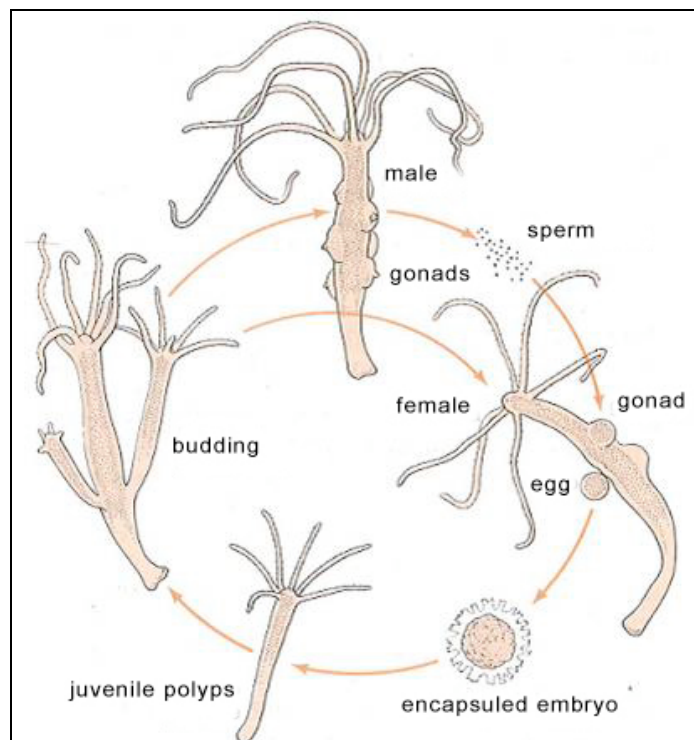


**Figure 19. Biological cycle of *Hydra*.** The eggs are kept in glass on the epidermal surface of the polyp. After fertilization, they undergo segmentation and surround themselves with a protective chitinous capsule. Encapsulated embryos (with a diameter of 0.5 / 1 mm), which end up by turning away are able to survive periods of drought and winters. The young *hydra* emerges when environmental conditions become favorable.

#### **1.8.4 *Hydra* as model organism to test nanoparticles**

*Hydra* offers several potential advantages as investigation target by means of NPs, such as 1) the simplicity of the body structure, which allows easy detection of fluorescent probes, 2) the dynamics of the two epithelia, which continuously divide, migrate and are eliminated at the apical and basal ends of the polyp, allowing cell migration and tracking studies, and 3) the regenerating capability, involving extensive remodelling and plasticity phenomena, whose temporal dynamics can be best approached by using photostable fluorescent probes.

In a recent work, QDs functionalized with glutathione (GSH) were synthesised and shown able to evoke a particular behavior of the animal, consisting in the opening of the mouth: the QDs-GSH reach the gastric region and are uptaken by endodermal cells (Tortiglione et al., 2007), Figure 20



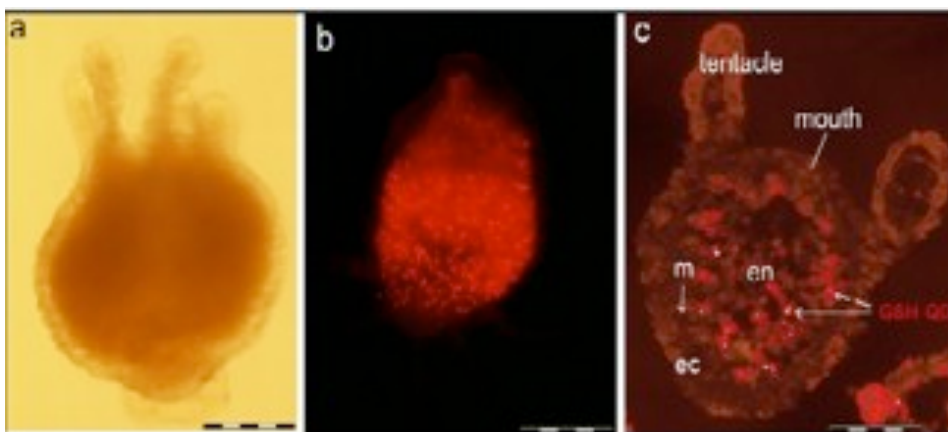


**Figure 20. In vivo fluorescence imaging of *Hydra* polyps treated with GSH-QDs.** a) Bright field image of *Hydra* showing the animal structure. b) Image of 24 hours after treatment shows an intense fluorescence along the gastric region. c) cell localization of QDs in *Hydra* cross section. Endodermal cells (en) , mesoglea (m) and ectodermal cells (ec) are indicated by arrows. Adapted from Tortiglione et al., 2007.

GSH-functionalized nanoparticles represent the first example of fluorescent and bioactive abduct used by the NanoBiomolecular group (Istituto di Cibernetica, CNR, Pozzuoli) for staining of a specific tissue in *Hydra*. The remarkable results opened the road to following studies with nanoparticles of different size, composition and shape on living *Hydra*. For example, it was demonstrated that QRs with CdSe core and shell of CdS, in nanomolar concentrations, induce in *Hydra* a particular tentacle writhing, similar to that observed during feeding or induced by GSH (Figure 21). The results of these experiments led to the identification of a target cell, the sensory neuronal cells of the tentacle. The induction of tentacle writhing activity was explained by assuming electric fields generated by permanent dipole moments of the nanoparticles, of sufficient intensity to stimulate voltage-gated channels on tentacle neurons, and therefore capable of triggering the sprawling activity. It was also demonstrated that the presence of calcium in solution is a necessary condition for the induction of that activity (Malvindi et al., 2008)

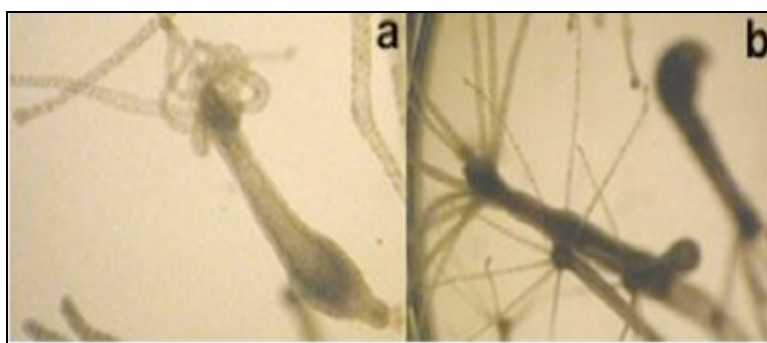


**Figure 21. Elicitation of tentacle writhing by QRs.** *Hydra* polyps were incubated with QRs and motor activity was monitored by video recording. a) *Hydra* polyp after addition of QRs to culture medium. The tentacles begin to writhe immediately. b) *Hydra* polyps in physiological condition, with extended tentacles. Adapted from Malvindi et al., 2008.

Another example of interaction of NP and *Hydra vulgaris* is provided by the use of the same CdSe/CdS quantum rods at acidic conditions. (Tortiglione et al., 2009). Indeed, at acidic pH, the QRs present positive charge and interact with the negative charge of the plasma membrane, stimulating the endocytosis process. At neutral pH, QRs present a negative charge and exhibit a low efficiency of internalization. Images of

labelled polyps at different time post incubation with nanomolar amount of QRs are shown in Figure 22, while in Figure 23 the QR tissue localization is shown.

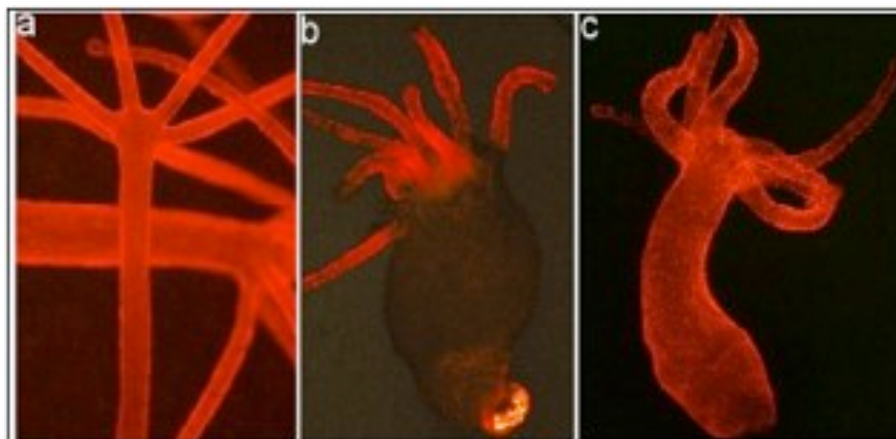


**Figure 22. In vivo fluorescence imaging of *Hydra vulgaris* exposed to QRs.** a) *In vivo* image of *Hydra* 30 minutes post incubation: QRs labels all the body regions. b) *In vivo* image of polyp 2h post incubation: QRs label the mouth, the tentacles and the foot. c) 24h post incubation QRs are evident also in the body column. Adapted from Tortiglione et al., 2009.

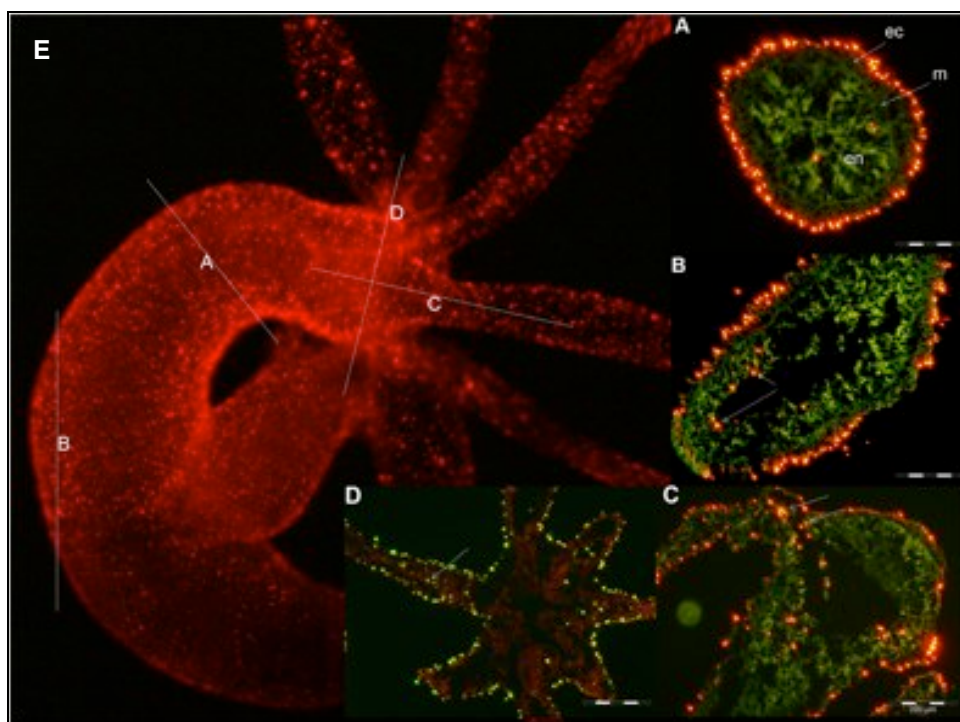


**Figure 23. Localization of QRs in *Hydra* tissue sections.** *Hydra* were treated with QRs at acidic pH for 4h, and 24 h later fixed and processed for cryosectioning. The green color is the auto fluorescence of tissue, while the red staining indicate the QRs presence. A, B, C) Serial longitudinal cross sections of head and D) of body, show QRs into the ectodermal layer, but also inside endodermal cells. On the right part of the image the labeling pattern before cryosection is shown. Scale bar A-D 200  $\mu$ m, E 500  $\mu$ m. Adapted from tortiglione et al., 2009.

Another advantage offered by *Hydra* as model organism to be targeted by metal based NP is the possibility to evaluate the potential toxicity of the NPs. *Hydra* is sensitive to a range of pollutants and has been used as a biological indicator of water pollution (Pollino and Haldway, 1999). Bioassays measuring *Hydra* population growth by asexual reproduction are rapid, sensitive, and precise when



measuring the effect of environmental pollutants. Large numbers of *Hydra* can be cultured due to their small size and rapid reproductive rate (Loomis, 1954). We showed the toxic effect displayed by CdTe QDs on *Hydra* morphology, reproductive and regenerative capabilities (Ambrosone et al., 2012) and identified also the activation of apoptotic pathways by biochemical and biomolecular approaches.

### 1.8.5 Gene knock out by RNAi in *Hydra*.

In recent years the number of methodologies to induce gene silencing in *Hydra* is increasing. In fact using electroporation, particle gun and embryo injection is possible to introduce into *Hydra* cell nuclei a green fluorescent protein (GFP) expression under the control of both homologous and heterologous promoters (Böttger et al., 2002); (Miljkovic et al., 2002); (Bosch, 2006). Gene silencing mediated RNA interference has been successfully obtained in a number of cases and using different delivery methods by both double strand RNA producing plasmids or oligonucleotides (Lohmann et al., 1999); (Chera et al., 2006); (Amimoto et al., 2006). In the first case bacteria carrying plasmid producing RNA are taken up into the body cavity upon mouth chemically opening, and many cycles of exposure are needed to knock out a specific gene. In the second case, a LEP procedure (Localised electroporation) has been developed to allow oligonucleotides to enter cells of a restricted body region. These techniques present several disadvantages, as the invasiveness of electroporation and the introduction of massive bacteria doses into animal cavity. For these reasons, it would be necessary to develop alternative strategies for study of RNAi.

### 1.8.6 Characterization of *c-myc* protooncogene in *Hydra vulgaris*

A *c-myc* homologue (*Hymyc1*), has been recently characterized in *Hydra magnipapillata* (Hartl et al., 2010), and by genomic analysis three additional *myc* related genes have been predicted. Among them, HyMYC1 and HyMYC2 protein sequences, displayed the principal topography of MYC proteins. The bHLH-Zip domains and MYC boxes I to III are orthologues of vertebrate *myc*, while the other two proteins HyMYC3 and HyMYC4, present the bHLH zip domains with a difference in the N-terminal region (Figure 24). *Hymyc1* is expressed in proliferating interstitial stem cells and gland cells. In Figure 25 was showed the amino acid sequences of *Hymyc1* and alignment with their vertebrate homologs.



Figure 24. The *Hydra* protooncogene *Hymyc1*

			MB I	
hu c-Myc	MPLNVSFTNRNYLDYDSVQPYFYCDEEE-NFYQQQQQ--SELQPPAPSEDIWKKFELLPTPLSPSRRLGLCSPSYVAVTPFSLRGDNDGGGGSFSTAD	97		
ck c-Myc	MPLSASLPSKNYDYDYDSVQPYFYFEDEEENFYLAQQRGSELQPPAPSEDIWKKFELLPTPLSPSRRLSAAASC-----FP-----STAD	83		
hy Myc1	MYFEKTF-NTDI-----E-----LETPTMTPSFGE-----TMFEFG-FDAELLSFNFA-	42		
			MB II	
hu c-Myc	QLEMVTELLGGDMVNQSFICDPDDETFIKNIIIQDCMWSGFSAAAKL---VSEKLASYQAARKDSG---S---PN---PARGHSVCSTSSLYLQDLGA	183		
ck c-Myc	QLEMVTELLGGDMVNQSFICDPDDES FVKSI IQDCMWSGFSAAAKLEKVVSEKLATYQASRREGGPAAASRPGPPPSGPPPPAGPAASAGLYLHDLGA	183		
hy Myc1	-LQ---D-LA-DGLIISV-----FPSEVLRDDCMW-GESDF-KF---SNSLDS---RH-SR---S-----LLVT	89		
			MB IIIa	MB IIIb
hu c-Myc	AASECIDPSVVFPPPLNDSSSPKSCASQDSSAFSPSSDLSSTESSPOGSPEPLVLHEETPPTTSSDSEEEQDEEEDVVSVEKRQAPGKRSESGSPS	283		
ck c-Myc	AAADCIDPSVVFPPPLSER-APR-----AAPPGANPAALLGVDTPTTSSDSEEEQDEEEDVVTILAEANESESTESTEA	260		
hy Myc1	PINFALNPS---PFPTNDD--P-----CCDTSNEYSIILTPVDTESEDEVVVGISDGSVLCGN-EDNSLE	148		
			MB IV	
hu c-Myc	AGGHSKPPHSPVLVLRCHV-----STHQHNYAAPSTRKDYPAAKRVKLDVSVRLRQISNNRKCTSPRSSDTEENVKRRTHNVLERQRRNELKRS	373		
ck c-Myc	SEEHCKPHHSPVLVLRCHV-----NIHQHNYAAPSTKVEYPAAKRLKLDVSVRLRQISNNRKCSPTSDSEENDKRRTHNVLERQRRNELKLS	360		
hy Myc1	RNSSFLPPFDNICSQTNNTESCFATSFFAEHFLFDKRRKDLTKRMKTS-RSKAKRFNNCYSSDDNSNGSLSPRL-E-N--RKTHNHLERKRDELKRS	243		
			bHLH-Zip	
hu c-Myc	FFALRDQIPELENNEKAPKVILKATAYILSVQAEQKLISEEDLLKRREQLKHKLEQLRNSCA	439		
ck c-Myc	FFALRDQIPEVANNEKAPKVILKATEYVLSIQSDEHRLIAEKEQLRRRREQLKHKLEQLRNSRA	416		
hy Myc1	FDDLRLKSLPELELHEKAPKVIILTKGIDHIKQLENEDEKLLTIQKNLLKSINSMLSKKLKMILTRQEEMKFRF	314		
			*	*

**Figure 25. Amino acid sequences of *Hydra myc1* and alignment with their vertebrate homologs.** (A) Alignment of human (Hu) c-Myc, chicken (Ck) c-Myc, and Hydra (Hy) Myc1 sequences (GenBank accession nos.: hu c-Myc, NP\_002458; ck c-Myc, NP\_001026123; hy Myc1, GQ856263). Identical residues are shaded in Blue, gaps are indicated by Dashes. The positions of the Myc boxes (MB) I–IV in the transactivation domains of the vertebrate proteins and of the bHLH-Zip region in the Myc are indicated. Conserved heptad repeat residues in the leucine zipper regions are marked by Asterisks. The positions corresponding to exon-exon junctions are indicated by Arrows above (HU, CK) and below (HY) the alignments. Figure from Heartl 2010.

## **1.9 Aim of PhD thesis**

In the frame of NANOTRUCK project my thesis work was aimed to test and validate effective protocols of RNAi using *Hydra vulgaris* as model system. In order to achieve this goal, I developed two strategies, one based on free myc-siRNA administration to living polyp by soaking, the other based on the incubation with *myc-siRNA* conjugated gold nanoparticles (AuNP). As a *myc* homologue gene has been identified in *Hydra*, I determined its functional role on cell proliferation and differentiation through downregulation by RNAi. In addition to the gene silencing studies, I also investigated the mechanisms of AuNPs internalization, intracellular trafficking and clearance by means of transmission electron microscopy, uncovering new dynamics and inward and outward routes, which should be taken into account when designing NP based devices for biomedical application

## **2 Materials and methods**

### **2.1 Animals**

*Hydra Vulgaris* (strain Zurich, originally obtained from Pierre Tardent), Figure 1.



Figure 1. Adult *Hydra vulgaris*

### **2.2 Nanoparticles tested**

Stable gold nanoparticles (AuNPs) with a diameter of 14 nm were synthesized by reduction of sodium tetrachloroaurate hydrate with sodium citrate dehydrate by the group of Jesus M. De la Fuente at Institute of nanoscience in Zaragoza, according to Turkevich et al, 1951. To improve the stability, biocompatibility, and chemical functionality, these AuNPs were functionalized with two types of thiolated polyethylene glycol (PEG) spacer: a commercial carboxylated spacer, SH-EG (8)-(CH<sub>2</sub>)<sub>2</sub>-COOH, and an azide-containing spacer custom synthesized in laboratory, SH-(CH<sub>2</sub>)<sub>3</sub>-CONH-EG(6)-(CH<sub>2</sub>)<sub>2</sub>-N<sub>3</sub>. The first spacer provides the anchoring moieties for the covalent binding of amine-containing molecules through carbodiimide chemistry, while the azide spacer confers positive zeta potential values, which is the principal factor for cell uptake.

### **2.3 *Hydra vulgaris* culturing**

Sea salt Solution (for shrimp hatching): sea salt 4% and deionized water. The solution was filtered and sterilized

*Hydra* medium (Sol Hy): 1 mM di CaCl<sub>2</sub> and 0.1 mM NaHCO<sub>3</sub> in di H<sub>2</sub>O Milli Q (bidistilled water) adjusted to pH 7.

Components	Work solution	Stock solution	Volume (1L)
Tris-HCL	1mM	1M	1mL
NaHCO <sub>3</sub>	0,1mM	0,1M	1mL
KCL	0,1mM	0,1M	1mL
MgCl <sub>2</sub>	0,1mM	0,25M	0,4mL
CaCL <sub>2</sub>	1mM	0,5M	2mL

NaHCO<sub>3</sub> Solution: 0.1mM NaHCO<sub>3</sub> in 1mM Tris HCl a pH 7.4

CaCl<sub>2</sub> Solution in 1mM Tris HCl a pH 7.4

Tris HCl Solution: 1mM Tris HCl a pH 7.4

## 2.4 Preparation of *Artemia salina* nauplii

The freeze-dried cysts were stored at +4°C. To get their hatching they were put in suspension in a beacker containing saline solution until the convergence of the *Artemia salina* nauplii towards the center. Then the beacker was illuminated in order to obtain greater convergence of artemia and thus facilitating their harvesting. At room temperature, the eggs hatch in about 48 hours. The collected artemia, were washed with double-distilled water, to remove salts which are toxic for the freash water polyp *Hydra vulgaris*.

## 2.5 Feeding procedure

Artemia were collected, transferred to filter meshed and after rinsing in fresh water, were added to the polyps. The removal of residual larvae, occurred after 4-6 hour of feeding. If the containers are clean enough just rinse and change a couple of times a *Hydra* solution, otherwise you need to transfer the animals into new containers with fresh solution. To avoid losing too many animals during the rinsing a filter mesh (about 0.4 mm) has been used to retain the hydras and eliminate the artemia residues. To handle both the brine shrimp and *Hydra* glass Pasteur pipettes were used.

## 2.6 In vivo RNA interference through small interfering RNAs

For RNA interference groups of 25 polyps were collected in plastic multiwells, allowed to equilibrate at room temperature in 1mL of *Hydra* medium at pH 4. The test was initiated by adding 70nM siRNA to each well containing the animals, since then continuously exposed to the siRNA oligonucleotides, under normal feeding regime. After the washing new siRNA oligonucleotides were supplied. 21 bp long siRNA targeting Hymyc1 were designed using on line siRNA design service and purchased by QIAGEN. Both unlabelled and 3' – Alexa fluor 488 siRNA were designed on the Hymyc1 DNA target sequence: 5' – AAGATGCTCACGCGTCAAGAA – 3'. As control of silencing specificity, siRNA oligonucleotides targeting the Luciferase GL2 gene

were purchased by QIAGEN. siRNA uptake was monitored *in vivo*, using a Camedia-digital camera (Olympus) connected to a stereomicroscope (Olympus ZSX-RFL2). *In vivo* imaging was accomplished at several magnification by using both a stereomicroscope and an inverted microscope (Axiovert 100, Zeiss) equipped with a digital colour camera (Olympus, DP70). For imaging acquisition and analysis the software system Cell F (Olympus) was used.

## **2.7 Toxicological studies with intact and regenerating animals**

Groups of 20 animals were collected in plastic multiwells, allowed to equilibrate at room temperature in 300 µl of *Hydra* medium. The test was initiated by adding gold nanoparticles (AuNPs) and *Hymyc1* to each well containing 20 polyps and incubating as necessary. AuNPs and *Hymyc1* uptake was monitored *in vivo*, unless otherwise stated, by continuous video recording using a Camedia-digital camera (Olympus) connected to a stereomicroscope (Olympus ZSX-RFL2). Following extensive washes, *in vivo* imaging was accomplished at several magnification by using both a stereomicroscope and an inverted microscope (Axiovert 100, Zeiss) equipped with a digital colour camera (Olympus, DP70). For imaging acquisition and analysis the software system Cell F (Olympus) was used. For regeneration experiments, treated polyps were bisected in the gastric region and *in vivo* imaged at various time points post amputation. The number of regenerating tentacles was monitored every 24hr. Experiments were performed in air-conditioned environment at 22°C, and repeated three times for each condition tested. In order to evaluate acute toxicity, the morphological changes induced by AuNPs treatment were monitored, by using a scoring procedure of the progressive changes in structure. This procedure allows examining the ability of animals to recover from NP-induced damage. Every day, using a stereomicroscope, recognizable physical changes in response to different NP ranges were recorded, according to score values (ranging from 1-10) described by Wilby (Wilby, 1988; Wilby and Tesh, 1990).

## **2.8 *Hydra vulgaris* growth rate**

The determination of the *Hydra* growth rate has allowed us to determine the following parameters:

- Duplication time of the population (T)
- Bud detachment
- Constant population growth (K), determined by:

$$K = \ln(n/n^0)/T$$

where:

$n^0$ : the initial number of individuals

$n$ : the number of individuals at time T

T: the time expressed in days taken for the population to switch from  $n$  to  $n^0$

*Hydra* polyps were exposed to a chronic treatment with sub-lethal concentrations of nanoparticles, to study the possible effects on population growth rate. Subsequently they were arranged in groups of 4 in 3 24 well-plates in *Hydra* solution (0.1 mM NaHCO<sub>3</sub>, 1 mM CaCl<sub>2</sub>) and incubated at +18°C and fed with artemia salina.

On day 0 the growth rate measurements initiated by marking with A1, A2, A3, A4 animals treated with AuNP-N<sub>3</sub> which have undergone a treatment of 100 nM; B1, B2, B3, B4 animal treated with AuNP-COOH with a concentration of 100 nM; C1, C2, C3 and C4 the control animals. Starting from the founder population, each time a bud detached from an adult it was transferred to a new well and let grow and reproduce. This process was repeated daily for two weeks and at the end all the adults were counted.

## **2.9 Hydra cell and tissue analysis**

Analysis of treated animals was done both on whole animals and isolated fixed cells. Animals were anaesthetized in 2% urethane in *Hydra* medium for 2 minutes. Then the animals were fixed with Lavdowsky's fixative (ethanol-formalin-acetic acid-water 50:10:4:40), rehydrated and mounted on microscope slides in Glycerol 50% in PBS 50% (8 g/l NaCl; 0.2 g/l KCl; 1.44 g/l Na<sub>2</sub>HPO<sub>4</sub>·7H<sub>2</sub>O; 0.24 g/l KH<sub>2</sub>PO<sub>4</sub>). For analysis of cell type distribution whole animals were macerated into a suspension of fixed single cells as described in David et al., 1973. Five polyps for condition were macerated at the indicated time of treatment and scored for single and pairs of interstitial cells (1s+2s), nests of four-sixteen proliferating or differentiating nematoblasts (4s-16s), zymogen and mucous cells, epithelial cells (EPI).

## **2.10 Proliferation rate**

For analysis of proliferation rate, animals were incubated with 5 mmol/l bromodeoxyuridine (BrdU) (Sigma) for 1, 12, 24, 48 and 72 hr, immediately fixed and macerated. BrdU, an analogue of nucleotides is incorporated in proliferating cells and detected by immunolocalization using mouse anti BrdU monoclonal antibody (1:500, Sigma) and Novolink Polymer detection System (Novocastra Laboratories Ltd).

## **2.11 Tissue sectioning**

For tissue sectioning, test animals were soaked overnight in 30% sucrose in PBS and then embedded in the frozen section medium Neg-50 (Richard-Allan Scientific). Cryo-section of 10µm thickness were obtained by a cryostat. Collected on adhesion microscope slides (SuperFrost Plus, Menzel) slides and mounted in D.P.X (Sigma) before imaging.

## **2.12 Gene and protein expression analyses**

### **2.12.1 *in situ* Hybridization and Western Blot analysis**

Whole mount *in situ* Hybridization using DIG-labelled RNA probe was carried out as described previously in Grens et al., 1996, using NBT/BCIP (Roche) as substrate for staining. The myc riboprobe was synthesized using the plasmid *Hymyc1* as template and used at a concentration of 0.1 ng/mL for hybridization. The *Hymyc1* plasmid was produced as described in Hartl M et al. 2010.

For Western Blot analysis, total protein were extracted from groups of 25 polyps, using the triple detergent buffer according to Sambrook et al. 1989. The homogenate was centrifuged for 15 min at 14000 g and the proteins continued into the

supernatants collected and quantified by the Bradford method using BioRad reagent with BSA as standard. The proteins were separated on 12% SDS- polyacrylamide gel and transferred onto nylon membranes (BioRad, San Diego, CA). MYC protein levels were detected using anti HyMYC1 antibody (1:500, kindly provided by Innsbruck University) and compared to actin proteins using an anti-actin primary antibody (1:100, sigma) to probe an identical blotted gel.

### **2.12.2 Total RNA extraction**

RNA extraction is a very delicate multi step procedure because of RNases that would degrade RNA molecules. The use of gloves, pipette tips, Eppendorf and falcon sterile (autoclaved), together with the decontamination of work areas and equipment used with alcohol and water previously treated with diethylpyrocarbonate (DEPC), can greatly reduce the presence and enzymatic activity of RNase. RNA was extracted from treated and untreated animals by purification in TRIZOL (Invitrogen) according to protocol recommended by the manufacturer: 25 *Hydras* were homogenized in 500 µl of Trizol and left for 5 minutes at room temperature (RT); to each tube 100 µl of chloroform were added. The samples were then incubated for 2-3 minutes at RT and then centrifuged at 12,000 g for 15 minutes at 4°C, thus allowing the separation of the phases. Subsequently, the aqueous phase containing the RNA was collected and 250 µl of isopropanol were added. In order to precipitate the RNA molecules, the samples were centrifuged at 12,000 g for 10 min at 4 ° C; the RNA pellet was then washed with 200 µl of 75% ethanol, centrifuged again (at 7500 g for 5' at 4 ° C) and finally resuspended in an appropriate volume of sterile water (30 µl). The concentration of RNA samples extracted was determined by reading in a spectrophotometer. The absence of any contaminants, such as proteins, polysaccharides and phenol, was estimated by measurement of the ratio Absorbance O.D.<sub>260</sub>/Absorbance OD<sub>280</sub>. The samples were considered for further analysis when the ratio  $A_{OD_{260}} / A_{OD_{280}}$  had a value between 1.7 and 2.0.

### **2.12.3 Agarose gel electrophoresis for the evaluation of RNA integrity.**

The RNA samples were analyzed by electrophoresis on agarose gel (1.2%) to verify the absence of any degradation and contamination of residual genomic DNA.

#### **Buffer MOPS 10X**

3-(N-morpholino)propanesulfonic acid pH 7 0,2 M  
Sodium acetate 80 mM  
EDTA 10 mM

#### **Denaturing buffer**

Formamide 750 µl  
10X MOPS 120 µl  
37% formaldehyde 250 µl  
10 µg/µl Etidium Bromide 1 µl

Samples resuspended in denaturing buffer were incubated at 65°C for 5 min and then loaded onto 1.2% denaturing agarose gel and the migration was at 70 V in



MOPS 1X buffer. RNA integrity was then evaluated by checking the presence of rRNA 28S and 18S that in a non degraded RNA are in a 2:1 ratio.

#### **2.12.4 RNA reverse transcription**

Before starting the reverse transcription RNA samples were treated with DNaseI (*Amplification Grade, Invitrogen*) according to manufacturer's instruction. The RNA, now without any DNA contamination was subjected to a reaction in which a reverse transcriptase is able to copy a complementary DNA strand (cDNA) using RNA as template. To selectively target mRNA, oligodT were used as primers for the Superscript II DNA polymerase (Invitrogen). The reaction was set up as follows: 1µg RNA, 1X RT Buffer, 0.5 mM di dNTPs, 10 mM di DTT, 1,5 µM Oligo(dT)12-18 (*Invitrogen*), 50 uL di Superscript II, DEPC treated H<sub>2</sub>O to 20 uL. The thermocycler profile used was 42°C 1h, 95°C for 5'. The cDNA obtained was then used for further analysis.

#### **2.12.5 Quantitative Real-time reverse transcription- polymerase chain reaction (qRT-PCR)**

A specific pair of primers has been designed for each gene using the Primer3 program (<http://frodo.wi.mit.edu>). These primer pairs were chosen to amplify products of 100–200 bp in length. Blast searches against the whole *Hydra* genome were performed to verify primers specificity. The Real Time PCR (qRT-PCR) experiment measures the number of cycles needed to attain a threshold concentration of Q-PCR product (Ct). The threshold value is chosen to fall within the exponential amplification phase, before limiting reagents become a factor in the efficiency of each cycle.

This method requires a known reference gene with constant expression in all tested samples and whose expression is not changed by the treatment under study. A pair of primers for *Hydra Elongation 1 alpha (HyEF1α)* housekeeping gene has been used as standard reference. The number of cycles needed for the standard to reach a specified Ct is used to normalize the Ct for the selected genes. A higher Ct for the gene of interest implies a lower initial concentration in the sample, and vice versa.

To capture intra-assay variability all qRT-PCR reactions were carried out in triplicate. For triplicate samples, Ct is calculated as the average value among the replicates.

Diluted cDNA was used as template in a reaction containing a final concentration of 0.3 µM for each primer and 1x FastStart SYBR Green master mix (total volume of 25 µl). PCR amplifications were performed in triplicate in a *Step One (Applied Biosystem)* using the following thermal profile: 95°C for 2 min, one cycle for cDNA denaturation; 95°C for 15 sec and 60°C for 1 min, 40 cycles for amplification. The expression of the following genes was assessed by Real time PCR: *c-myc 1 (Hymyc1)* and *Hydra Elongation 1 alpha (HyEF1α)* as control. Gene sequences were obtained from the Hydrazome database (<http://Hydrazome.metazome.net>).

The expression profiles were analyzed by applying the  $\Delta\Delta C_t$  method where the values of the gene of interest (*Hymyc1*) were normalized for the values of reference control gene (*HyEF1α*).

#### **2.13 Ultrastructural analysis through Transmission Electron Microscopy (TEM)**

*Hydra* polyps were treated with 2% urethane in *Hydra* medium (1 mM CaCl<sub>2</sub>, 0.1 mM NaHCO<sub>3</sub>, pH 7.0) to prevent contractions during fixation and then fixed for 2hrs in 2%

glutaraldehyde in SolHy. Samples were then washed at least four times with SolHy and postfixed for 45' with 1% buffered OsO<sub>4</sub>. After a series of four washes in SolHy, animals were dehydrated in a graded ethanol series (30%-50%-70%-90%-100%). Samples were incubated 2x15' with Propylene oxide and then over-night in a 1:1 mixture Propylene oxide/Epon 12 Resin. Before flat embedding, animals were incubated 2 x 2 h in Epon 12 Resin. Sample serial thin (70nm) section of tentacles and hypostoma were cut with a diamond knife and mounted onto 150-200 mesh hexagonal tem grid (G200TT-Ni, Electron Microscopy Sciences). Thin sections were stained with uranyl acetate and lead citrate. Ultrathin sections were examined with Leo 912 AB transmission electron microscope operating at 80 kV.

#### **2.14 Sample preparation for High-Pressure Freezing Procedure (HPF)**

*Hydra* polyps immersed in SolHy were dissected into appropriate pieces to fit into cup-shaped HPF specimen carriers. Tissue pieces were pipetted with SolHy into a 0.2 or 0.3 mm deep carrier and covered with an additional carrier. Finally, the obtained sandwiches were cryo-immobilized by HPF. Frozen sandwiches were transferred into appropriate containers for storage in Liquid N<sub>2</sub> for later use or subjected to freeze substitution (FS). The frozen samples were transferred under liquid N<sub>2</sub> into cryovials containing frozen FS cocktails (anhydrous acetone plus 1% OsO<sub>4</sub> and 0.1–0.2% uranyl acetate). Subsequently, the lids were screwed loosely onto the vials to permit safe evaporation of excess N<sub>2</sub> gas. The vials were placed into the precooled FS device and after about 1 h the lids tightened and FS was performed for at least 8 h at -80 to -90°C; warming up to -55°C at a rate of 5-10°C per hour, subsequent post-fixation and staining at -55°C for 6 h, followed by warming up to -30°C at a rate of 5–10°C per hour where samples were left for an additional 3 h 36. Finally the samples were washed 3x with acetone (10 min each), 16 h in 10% epoxy resin (epon) in acetone, 6 h in 30% epon in acetone, 16 h 70% epon in acetone, 6h 100% epon in acetone, 16 h 100% epon in acetone. Then the samples were placed in fresh resin and placed in oven at 60° C overnight. Sample serial thin (70nm) section of tentacles and body regions were cut with a diamond knife and mounted onto 150-200 mesh Hex grids. Ultrathin sections were examined with transmission EM Libra 120 EFTEM (Zeiss, Oberkochen, Germany) at 80 eV (Holstein et al., 2010)

#### **2.15 Elemental analysis by Inductively coupled plasma atomic emission spectroscopy (ICP-AES)**

To estimate the extent of endocytosis and exocytosis of AuNP-N<sub>3</sub> in *Hydra*, living polyps were treated 24h with AuNP, washed, and processed for elemental analysis to evaluate the amount of Au present inside the animals and released in the medium. 1500 *Hydra* polyps were incubated in 3 ml of *Hydra* medium with 25 nM AuNP-N<sub>3</sub> for 24h. At this time point 150 polyps were extensively rinsed and homogenized for ICP-AES. The remaining animals were kept in fresh medium and saved at 24h and 48h post washing. For each time point the same amount of polyps (150) and incubation media were saved. Experiments were done in duplicate. For ICP-AES measurements, all the samples were treated with 400 µl of aqua regia overnight and then diluted with MilliQ water to 20 ml to reach a final concentration of acid 2% (v/v).

### 3 Results

#### 3.1 RNA interference mediated by free siRNA in *Hydra vulgaris*

With the aim to downregulate *Hymyc1* gene we tested the possibility to perform RNA interference mediated by small interfering RNAs (siRNA). 21 bp long RNA oligonucleotides with symmetric 2nt 3' overhangs targeting the coding region of the *Hymyc1* gene (*myc*-siRNA) were designed according to specific rules determined to enhance the silencing effect of siRNA, and chemically synthesized (in Figure 1 the sequence selected on the mRNA sequence is shown) (Elbashir SM et al., 2001, Naito et al., 2009; Reynolds A. et al., 2004). Recently, specific rules for siRNA design have been developed to improve siRNA efficiency. These algorithms combine specific rules (low GC content, lack of internal repeats, an A/U-rich 5' end) and other features enhancing the silencing effect of siRNA. The sequence of the *Hymyc* siRNA selected was used to BLAST *Hydra* genome (<http://hydrazome.metazome.net/cgi-bin/gbrowse/hydra/>) to identify possible off-targets. Selected siRNA duplex were synthesised by one of the several commercial entities involved in siRNA manufacturing. The addition of an organic fluorophore to either the 3' or the 5' of the protruding RNA strand allowed monitoring its uptake and cell targeting, *in vivo*.

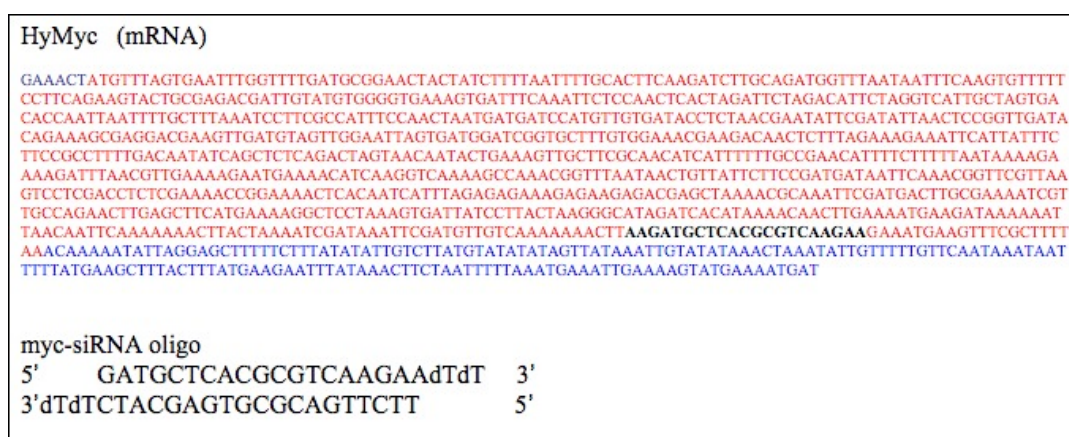


**Figure 1.** *Hydra* specific siRNA duplex (*Hymyc*-siRNA) composed of 21-nt sense and 21-nt antisense strands, paired in manner to have 2-nt 3' overhang, were designed on both coding- non coding *HyMyc* DNA sequence with the help of specific on line tools to overcome hurdles such as the correct target identification and the minimization of potential off target effect. In red are shown the coding nucleotides, in blu the 3' untranslated region and in black the siRNA nucleotides.

Given the capability of *Hydra* polyps to uptake at high efficiency positively charged compounds, we performed an estimation of siRNA surface charge by Zeta potencial measurement, and showed that they present positive net charge at pH 4 in *Hydra* culture medium, while at physiological pH they are negatively charged (Figure 2) The silencing effect was tested at pH 4, soaking the animal in culture medium in presence of 70 nM siRNA. Alexa fluor 488 end-labeled *myc*-siRNAs were used to track internalization by mean of *in vivo* fluorescence microscopy. The capability of siRNAs to penetrate *Hydra* cell membrane was higher at pH 4 than at pH 7, as showed in Figure 3, indicating that siRNA delivery was enhanced by acidic conditions.

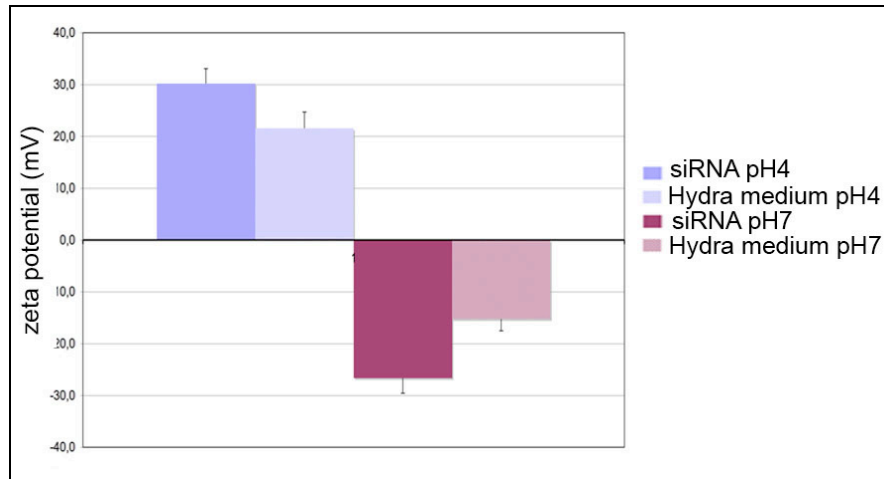


**Figure 2. Zeta potential measurement of siRNA duplexes in *Hydra* medium at different pH.** They present positive net charge at pH 4 in *Hydra* culture medium, while at physiological pH, as expected, they are negatively charged. From Ambrosone et al., 2012

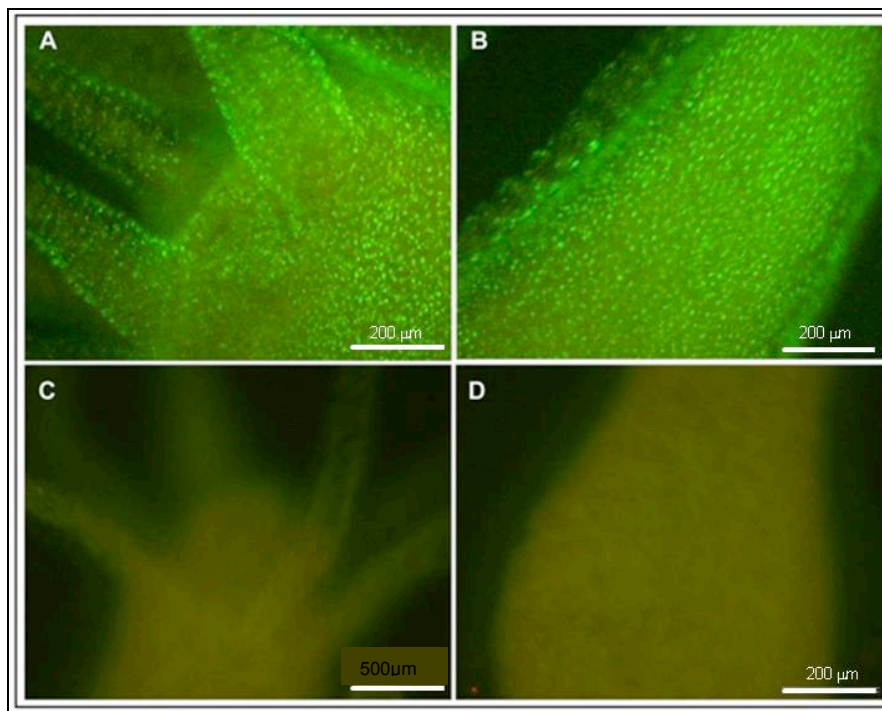


**Figure 3. *In vivo* imaging of siRNA uptake.** Living polyps were challenged with 70 nm Alexa fluor 488 end-labelled *myc-siRNA*, in *Hydra* medium either at pH 4 (A-B) or at pH 7 (C-D). After 24 hrs of incubation with *myc-siRNA* a strong punctuated fluorescence labels uniformly the whole animal, from the head (A) along body (B) of animal treated at acidic pH, indicating the siRNA uptake. In C and D are shown the same regions of animals treated at neutral pH. The absence of signals indicates that the acid pH enhances siRNA delivery in *Hydra*. Scale bars 200  $\mu$ m. From Ambrosone et al., 2012.

Confocal microscopy analysis confirmed siRNA presence within nests of nematoblasts, which represent the cell type where *Hymec1* is expressed (Figure 4).

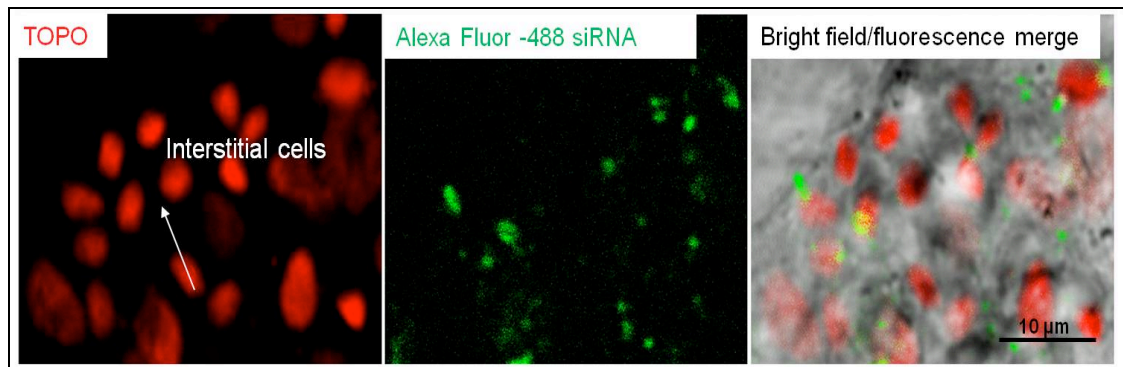


**Figure 4.** Confocal laser scanning imaging (A–C) of living *Hydra* treated 24 hr with Alexa488-labelled *myc*-siRNA revealed localization of oligonucleotides into interstitial cells. In (A), nuclear staining of interstitial cell nest with TOPO; in (B) siRNA green fluorescence appears as faint staining or more evident granules; in (C), the overlay of bright field and fluorescence images revealed that siRNAs localize prevalently into the cytoplasm of interstitial cells. Scale bars: 10 µm.

The silencing effect was evaluated at molecular level by quantitative Real time PCR (qRT-PCR). When *Hydra* polyps were treated with *myc*-siRNA for two days a significant reduction of *Hymyc1* transcript levels at pH 4, but not at pH 7, was observed. This suggested that the acidic condition enhanced siRNA uptake enabling silencing. About 60% of downregulation of *Hymyc1* was observed in siRNA treated animals after two days of incubation at pH 4 (Figure 5A). Increasing the period of treatment up to 9 days did not enhance the gene silencing, probably due to the fast cell turnover of the interstitial cell lineage (Figure 5B), renewing the healthy cells repertoire, reestablishing normal transcripts levels and saturation of silencing machinery. The post-transcriptional silencing induced by *myc*-siRNA was confirmed also at protein level by Western Blot analysis. Using polyclonal antibodies raised in rabbit against HyMYC1 recombinant protein (kindly provided by B.Hobmayer, University of Innsbruck), a drastic decrease of HyMYC1 protein was detected in *myc* RNAi animals (two days treatment), compared to endogenous levels of *Hydra* actin (Figure 6). The specificity of the RNAi approach was assessed by testing unrelated siRNAs, such as *Luciferase* siRNA (*luc*-siRNA), designed on the firefly luciferase *GL2* gene, not present in the *Hydra* genome. Results showed that *Hymyc1* transcription and translation were unaffected in *luc*-siRNA treated animals (Figure 5), demonstrating the specificity of the RNAi approach.

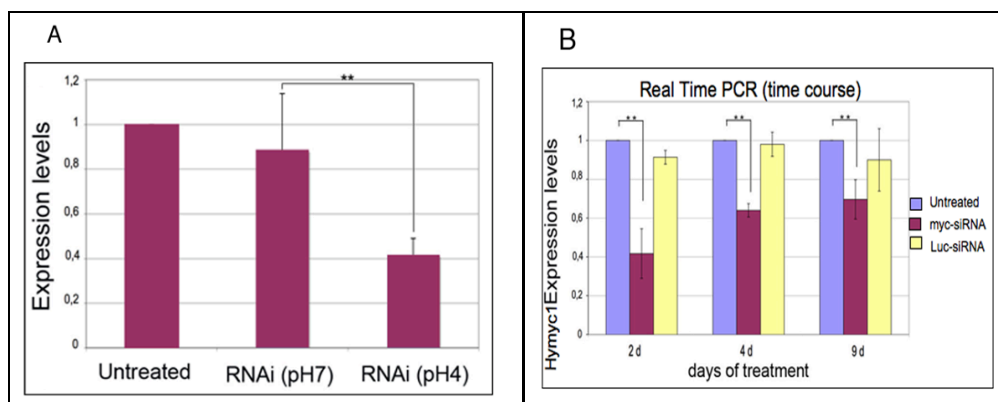


**Figure 5. Molecular characterization of *Hymyc1* RNAi.** Quantitative RT-PCR show *Hymyc1* downregulation under acidic condition. *Hydra* polyps treated with *myc*-siRNA at pH 4 showed 60% decrease of *Hymyc1* transcript levels compared to *Hydra* elongation factor *HyEF1α* mRNA, used as control. The treatment at pH 7 was not effective. **(B) Kinetics and specificity of *Hymyc1* downregulation.** qRT-PCR was performed on total RNA extracted from 25 animals either untreated or incubated with the indicated siRNA for different periods. The most effective downregulation is detected at 48h and it is specific for *myc*-siRNA oligonucleotides. Adapted from Ambrosone et al., 2012.



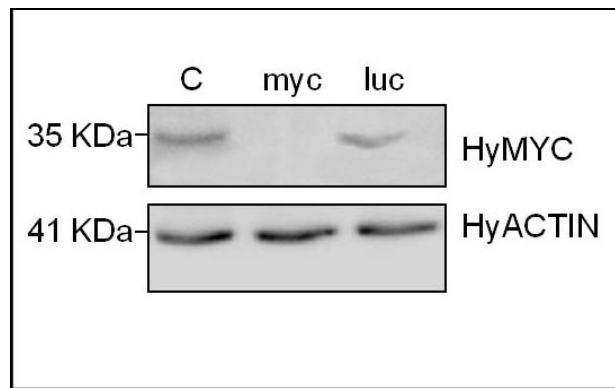


**Figure 6. Post-transcriptional silencing induced by *myc*-siRNA was confirmed by Western Blot.** (B) *Hymyc1* RNAi affect also MYC protein levels. MYC protein levels were detected using anti-HyMYC1 antibody (1:500, Kindly provided by Innsbruck University) and compared to actin proteins, using an anti-actin primary antibody (1:100, Sigma) to probe an identical blotted gel. Adapted from Ambrosone et al., 2012.

In order to detect differences in the expression pattern of *myc* RNAi polyps, whole mount *in situ* hybridizations using a Digoxigenin-labelled *Hymyc1* RNA probe were performed.

Despite the downregulation of *Hymyc1* detected at molecular level, we did not observe a significant difference in the expression pattern between untreated and RNAi animals (Figure 7A), probably due to the methodology, which does not detect quantitative differences. Cryosection of stained animals confirmed the expression pattern in proliferating interstitial cells, i.e. single and pairs of interstitial cells (1s+2s), nest of nematoblasts (4s-16s) and gland cells, according to previous reports (Hartl M et al. 2010), as showed in Figure 7C.

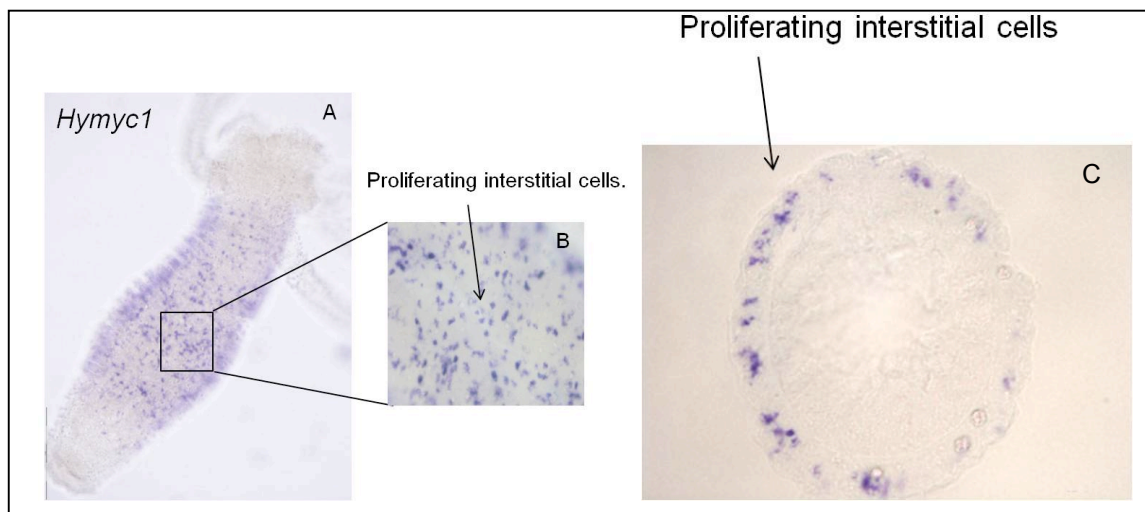


**Figure 7. *Hymyc* expression pattern.** *in situ* Hybridization on healthy animals shows the expression of *Hymyc1* in proliferating interstitial cells, distributed along the gastric region (fig. A). (B) Higher magnification of whole mount gastric region. C) Cryosection confirms the expression pattern in pairs of interstitial cells (1s+2s) and nest of nematoblasts (4s-16s). Adapted from Ambrosone et al., 2012.

### 3.1.1 Characterization of myc RNAi animals

- **Analysis of cell proliferation**

A morphological analysis both at cellular level and in intact animals was performed to investigate the effect induced by gene silencing on the cell proliferation activity and cell type relative distribution. In Figure 8 different cell types present in *Hydra* tissues are shown: epitheliomuscular cell (ectodermal and endodermal cells), gland cell (gc), single interstitial cell (1s), pairs of interstitial cell (2s). The analysis of the different cell types may be performed by macerating animals in single cell suspension, which are morphologically distinguishable and that can be quantified.

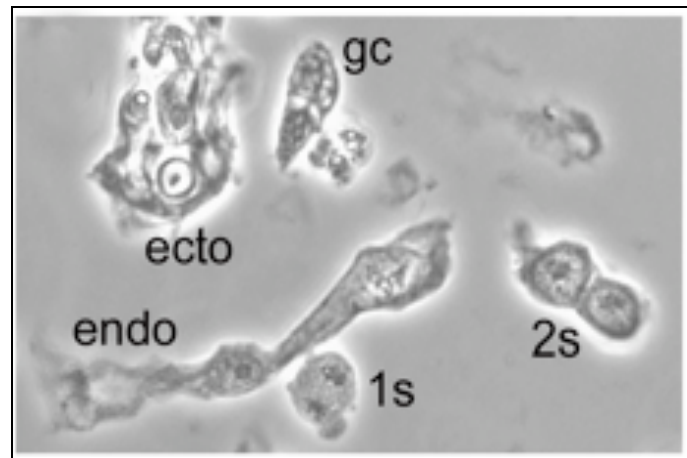


**Figure 8. Isolated cells from macerated *Hydra* tissue as viewed using phase microscopy.** The cell types illustrated are: ectodermal epitheliomuscular cell from body column (ecto); endodermal epitheliomuscular cell (endo); single interstitial cell (1s); interstitial cell in nest of two (2s); basal disc gland cell (gc). ). From Ambrosone et al., 2012.

**Evaluation of cell proliferation activity:** As *Hydra* epithelial cells proliferate with a cell cycle of 3,5 days (David et al. 1972, Holstein et al. 1991) and interstitial cells much faster with a cell cycle of 1 day, the cycling activity of cells was assayed by BrdU-labelling, over 3 and 2 days respectively. BrdU, an analog of nucleotide, is incorporated instead of Thymine in the DNA of proliferating cells, and detected by immunostaining using anti-BrdU antibody. Cell cycling activity of epithelial and 1s+2s cells were obtained in control and treated animals by continuous incubation with BrdU, for 1, 12, 24, 48 and 72 hours, followed maceration at the indicate time points and immunostaining. In Figure 9A the proliferation rate of epithelial cells appears not affected by myc-siRNA, while the proliferation of interstitial cells 1s+2s was enhanced in myc RNAi animals, indicating an effect of myc on the stem cell cycling activity (Figure 9B).

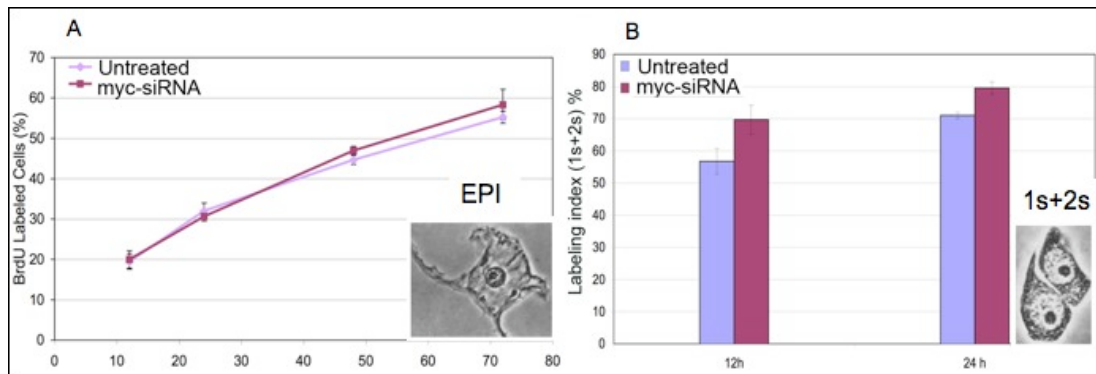


**Figure 9. Effect of *myc* siRNA on cell cycling activity.** Cell cycling activity of epithelial cells (A) and 1s+2s stem cells (B) were obtained in control animals and in treated animals by continuous incubation with BrdU, followed maceration of ten animals at indicated time point and immunostaining.

### • Analysis of cells type distribution

To investigate the effect of *Hymyc1* downregulation on the whole interstitial cell lineage, the cell type distribution was analyzed in macerates at two time points, i.e. at day 4, to ensure that treated polyps completed a whole cell cycle, and at day 9 to observe eventual effects also on later differentiation processes. As shown in Figure 10A, after 4 days of treatment we observed an increase both in proliferating and differentiating cell types, thus 1s+2s, nematoblasts (4s-16s), zymogen and mucous cells were found more abundant in *myc* RNAi animals compared to control untreated animals. At day 9 no further increase in 1s+2s population was observed compared to untreated and also compared to the *myc*-siRNA treated cell after 4 days, meaning that the effect of *myc* silencing on the proliferative rate of 1s+2s was not constant throughout the treatment. Altogether these evidence suggest a *Hymyc1* specific role in nematocyte and gland cell differentiation pathways (Figure 10B).

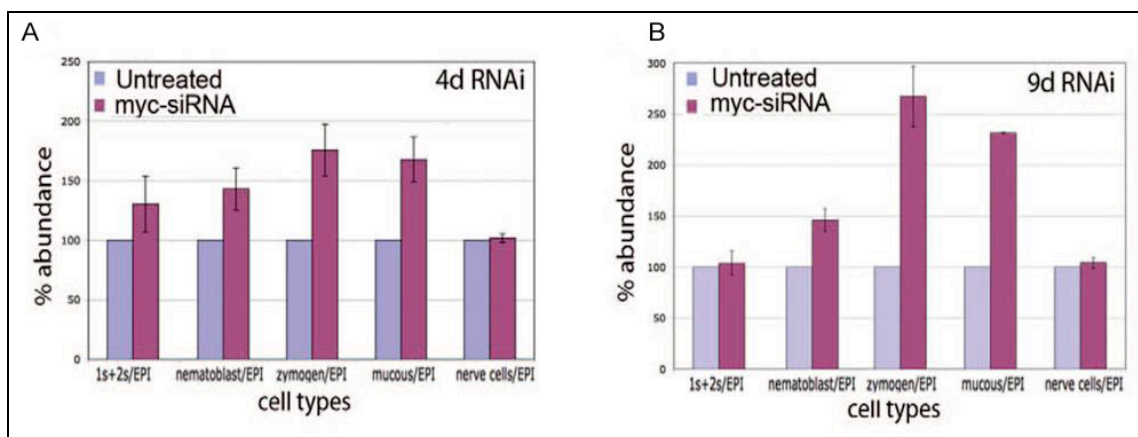


**Figure 10. Effect of *myc* siRNA on differentiation activity after 4 and 9 days.** In A and B the distribution of different cell types was assayed after 4 and 9 days of *myc* RNAi, respectively. Bars indicate standard errors. 1s+2s= single and pairs of interstitial cells; nematoblast = nest of 4s-16s proliferating and differentiating nematoblast; EPI= epithelial cells. Adapted from Ambrosone et al., 2012.

A schematic model of the effect of *Hymyc1* gene silencing on proliferation/differentiation rate is showed in Figure 11. These results suggested a role of *Hymyc1* in the negative regulation of the stem cells where it is expressed: the



decreased expression enhances stem cell proliferation and turn the differentiation of intermediates and terminal derivatives.

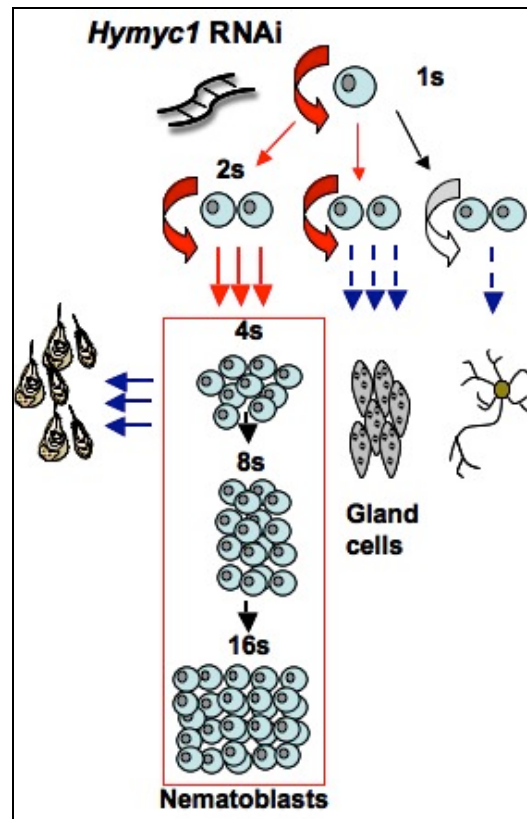


**Figure 11. Effect on stem cell proliferation/differentiation induced by *Hymyc1* downregulation.** *Myc* siRNA treatment induce a moderate increase in the 1s and 2s stem cell self-renewal and proliferation activity (red arrows). This in turn generates a higher number of both differentiating intermediates (nematoblast) and terminal differentiated products such as nematocytes and gland cells (blue arrows). Dashed arrows indicate the absence of morphological distinct cellular intermediates. *Hymyc1* downregulation does not affect the nerve differentiation pathways, consistent with the absence of *Hymyc1* expression in this cell type. Adapted from Ambrosone et al., 2012.

- **Whole mount analysis of tentacles morphology**

Populations of mature nematocytes embedded in the battery cells were analysed in tentacles of intact fixed animals. Battery cells are large modified tentacle epithelial cells containing embedded in the cytoplasm different type of nematocytes (stenothele, desmoneme and isorhiza), and are easily recognizable by phase contrast optical microscopy. For this experiment I analyzed 5 battery cells located on 5 tentacles of 5 different animals, for a total of 125 battery cells. As shown by the graph of Figure 12 *myc* RNAi animals presented an increase in the number of nematocytes per battery cell, compared to untreated and siRNA (luc-siRNA) treated *Hydra*, which confirm the enhanced nematoblast differentiation in mature nematocytes.

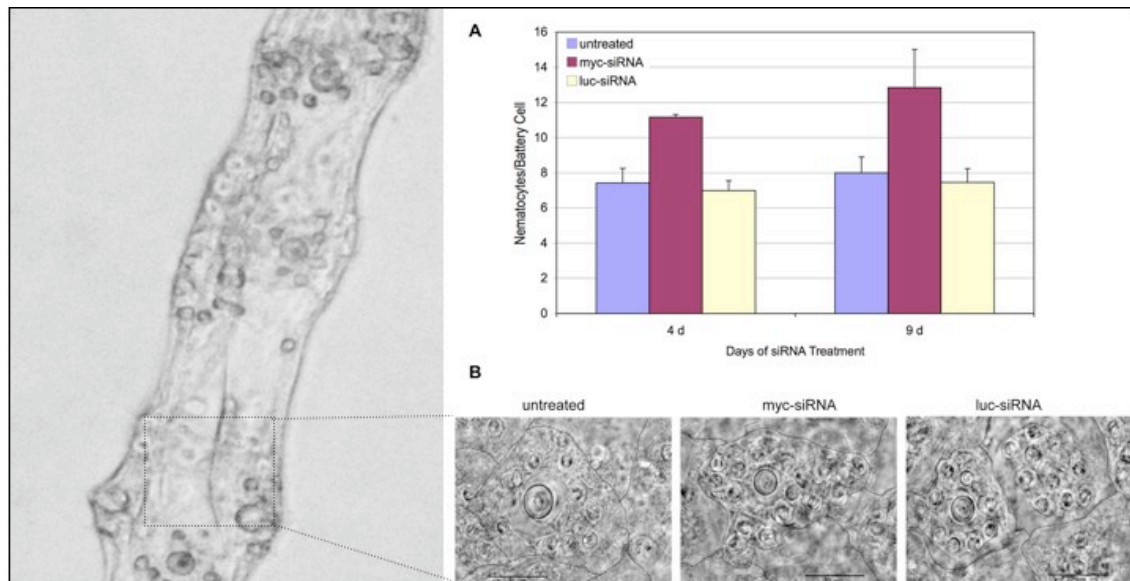


**Figure 12. *Hymyc1* induces an increase in the nematocyte content per battery cell.** (A) At time 4 d and 9 d of treatment with the indicated siRNA, the number of nematocytes embedded in the battery cells was counted by microscopic observations obtained from the same focus plane. (B) Representative battery cells imaged from untreated, *myc-siRNA* and *luc-siRNA* treated animals, on whole mounts. Scale bars 20  $\mu$ m.

This part of the study, focused on *Hymyc1* silencing through a novel RNAi strategy, describe how *Hymyc1* knockdown affects the developmental dynamics of stem and interstitial cell in polyps (Ambrosone et al., 2012), causing a clear cellular and molecular phenotype. The approach we employed, based on free siRNA supplied by soaking under acidic condition, represents a new tool to study gene function in *Hydra*.

In the second part of my experimental work a nanoparticle mediated approach of RNAi will be described, and the effects analysed at whole animal, cell and molecular level. Moreover, the uptake mechanism, cell trafficking and final clearance of nanoparticle in *Hydra* cells, extensively characterized by electron microscopy, will be presented.

## 3.2 RNA interference mediated by gold nanoparticle in Hydra

### 3.2.1. Synthesis of Gold Nanoparticles

Stable gold nanoparticles (AuNP) with an average diameter of  $14 \pm 1$  nm were synthesized by Dr. Jesus de la Fuente (University of Zaragoza) by the reduction of sodium tetrachloroaurate (III) hydrate with sodium citrate dehydrate, following a standard protocol (Turkevich et al., 1951). The functionalization of AuNP was carried out using bifunctional PEG spacers, i.e. PEG chains carrying a carboxyl group for the binding of molecules containing amine groups, and PEG chains ending with an azide group for the binding of molecules with alkyne groups. A combined functionalization of the nanoparticles with a single or both bifunctional chains generated two kinds of AuNP: AuNP-COOH/N<sub>3</sub> coated by 25% PEG chains (50% PEG COOH and 50% PEG-N<sub>3</sub>) and AuNP-N<sub>3</sub>, surface saturated by PEG-N<sub>3</sub> chains (figure 13).

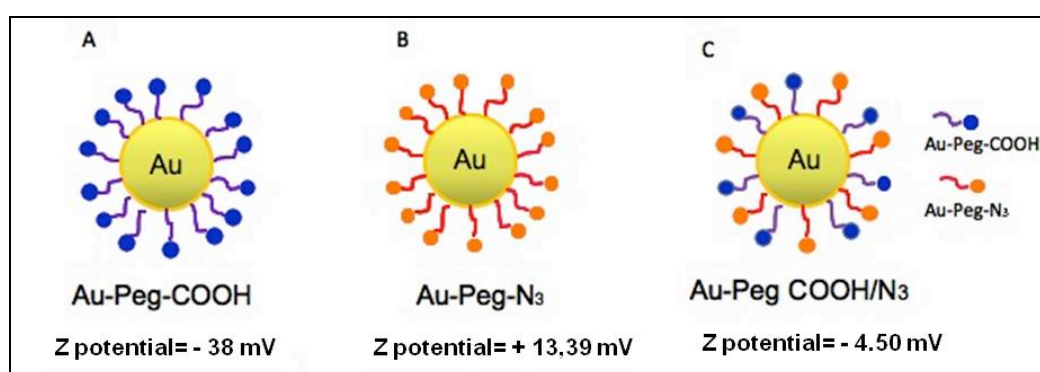


**Figure 13. Schematic illustration of the AuNPs.** A) a schematic illustration of the AuNPs shows the nanoparticle structure, coated by PEG-COOH.; B) Nanoparticle scheme illustrating the homogeneous PEG-azide coating the Au core. C) A nanoparticle scheme shows the nanoparticles structure coated by two different PEG spacers (PEG-COOH, and PEG-N<sub>3</sub>).

### 3.2.2 Biocompatibility and toxicity of AuNP on *Hydra*: impact on morphology reproduction and regenerative capabilities

- **AuNP impact on *Hydra* morphology**

*Hydra* is a suitable *in vivo* model system to study the biological response to nanoparticles. Here, this model was used to assess the potential toxicity of AuNP before the addition of functional groups on the surface.

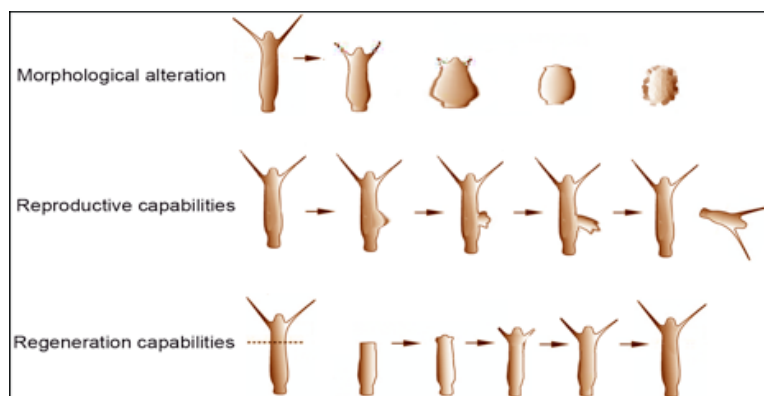
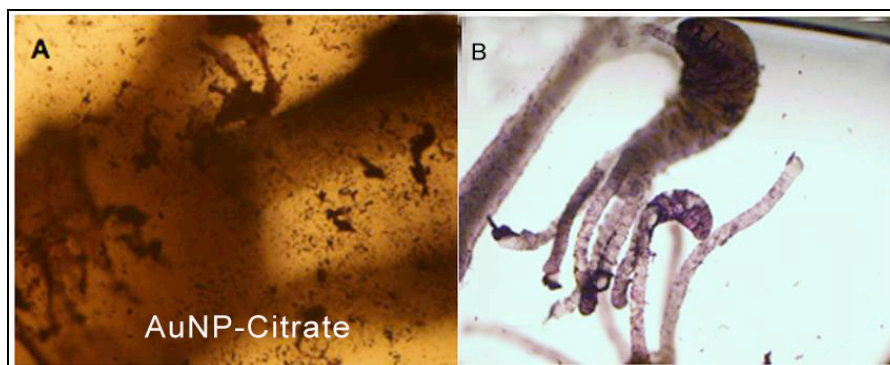
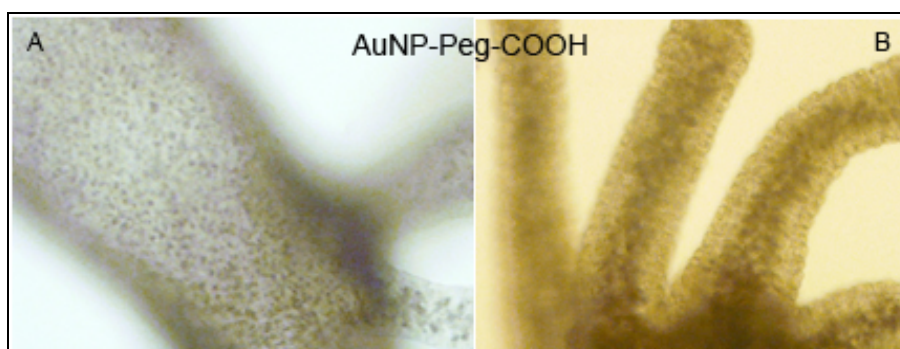


Figure 14. Representative scheme of physiological process of *Hydra* allowing estimating the toxicological impact of any medium suspended compounds: morphology alteration, impairment of reproductive and regeneration capabilities.

Groups of animals were independently incubated with AuNPs either uncoated (i.e. exposing citrate on the surface) or functionalized with either PEG-COOH or PEG-N<sub>3</sub> chains, at different concentration from 50 up to 100 nM. According to *Hydra* Health Index (HHI) based on distinguishable morphological alterations induced by medium suspended compounds supplied in homeostatic or regenerative conditions, there was not induction of any significant morphological change in animals treated with the highest possible concentration of AuNP PEG-COOH (100 nM). Low dosage (18 nM) of citrate-coated AuNPs, by contrast, manifested aggregation and precipitation in *Hydra* medium (Figure 15). They were shown attached to the animal outer surface, forming a film-like structure enveloping the whole animal. In light of this instability, Au-citrate NPs were not further used. AuNP-PEG-COOH, appeared instead well dispersed in *Hydra* medium but showed a low efficiency of internalization, probably due to the negative charge, Z potential - 38 mV (Figure 16). As expected AuNP-PEG-N<sub>3</sub> showed a strong internalization (Figure 17), mediated by their positive Zeta potential (+13,39 mV). This behaviour is in line with previous study by our group (Tortiglione et al., 2009), demonstrating the high rate of internalization of positively charged CdSe/CdS quantum rods. In Figure 18 the similar behaviour of the two positive NPs respect to the uptake by *Hydra* cells is shown.



**Figure 15. Interaction of AuNP-citrate and *Hydra*.** A) Au citrate capped NPs aggregate into *Hydra* medium, and appear as dark precipitates into the well. B) after several washes, *Hydra* ectoderm appears labelled (pink staining), but this interaction is not strong, as big patches of materials detaches progressively from the animal.



**Figure 16. *In vivo* imaging of *Hydra* polyps treated with 100 nM AuNP-PEG- COOH.** In A) body and B) tentacles of *Hydra vulgaris* exposed to AuNP-PEG-COOH. After 24 h of incubation no NP labelling was detected.

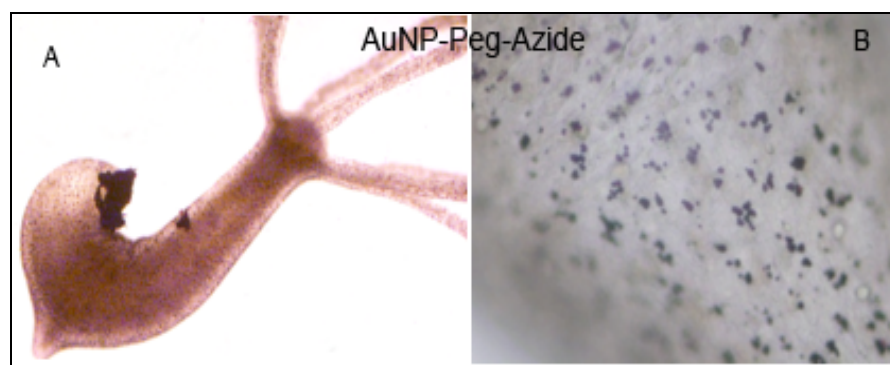


**Figure 17. *In vivo* imaging of *Hydra* polyps treated with 100 nM Au NP-N<sub>3</sub>.** (A) Bright field imaging of *Hydra vulgaris* exposed to AuNP-PEG-N<sub>3</sub>. After 24 h of continuous incubation, a dark punctuated staining due to gold nanoparticles labelled uniformly the whole animal. B) A Higher magnification of (A) indicates AuNP-N<sub>3</sub> located in the outer epithelial cell layer.

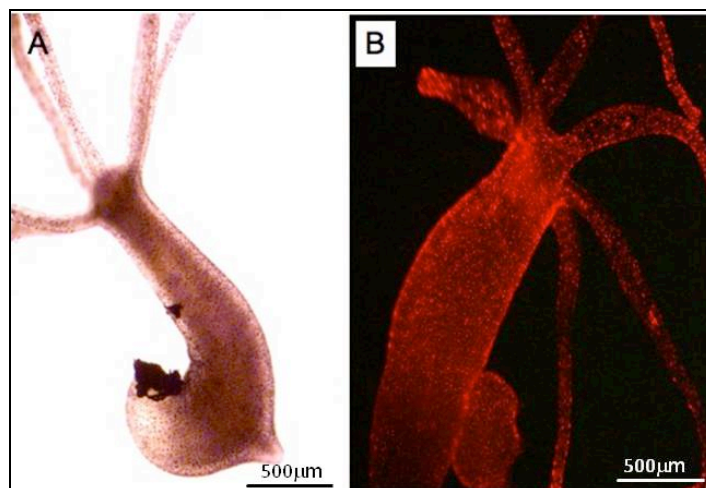


**Figure 18. Internalization Pattern of AuNP-N<sub>3</sub> and CdSe/CdS QRs.** These pictures showed the same pattern of internalization for both types of NPs.

### **3.2.3 AuNP impact on *Hydra* reproduction and regenerative capabilities**

In *Hydra*, the growth rate is normally regulated by a balance between epithelial cell cycle length, phagocytosis of ectodermal cell in excess, and bud formation (Bosch et al., 1984). Environmental factors, such as the presence of pollutants, the feeding regime, can affect this balance. Thus, the population growth rate is an indirect measure of the *Hydra* tissue growth rate and cell viability.

The growth rate of polyps treated with AuNP was compared to untreated animals. Four adult Hydras (the population founders), were treated for 24 hrs and then the medium was changed to allow a complete removal of the AuNPs. The sample were considered the founder generation and were then transferred into a new multiwell plate. Their reproductive capability was monitored for three weeks, to estimate the impact of internalized NP on the reproduction rate. As shown in the graph in Figure 19 the growth rate of the two populations were not significantly different, suggesting that the NP treatment did not affect the animal reproductive potential. Interestingly, 3 weeks after treatment the NPs were still detected, although rarely, in the endodermal tissue of founder individuals. Nevertheless, reproduction rate were not affected. This indicates an active proliferation of NPs containing cells and preservation of the budding process.



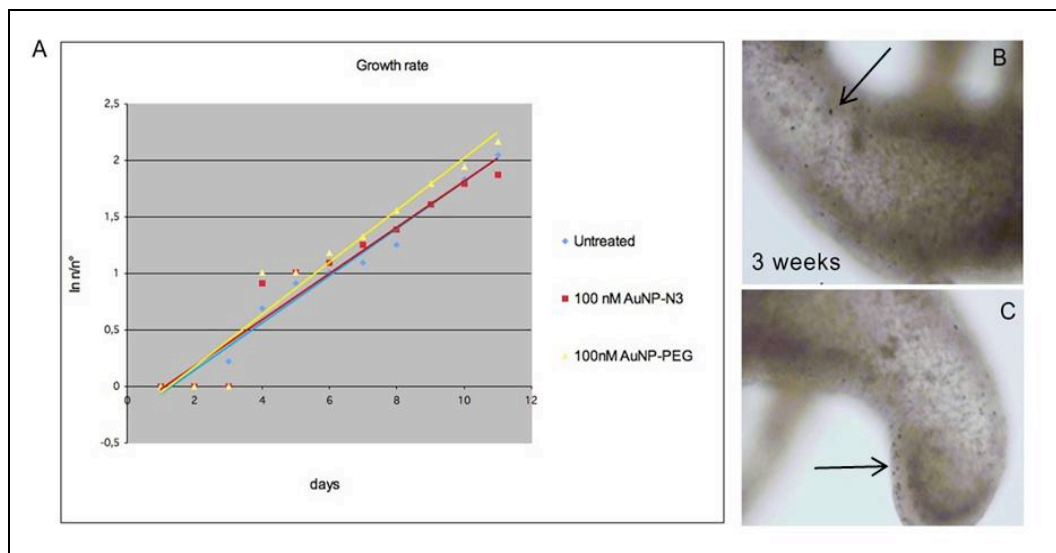


**Figure 19. Influence of AuNP treatment on *Hydra* population growth rate.** (A) Population growth test started with a population of four full-grown *Hydra*, incubated 24 h with 100nM AuNPs, rinsed and monitored every day for bud detachment. The individuals were inspected daily and counted under a stereomicroscope. There are not significant differences between Untreated (blue line) and treated (red and yellow lines) population growth rates. The logarithmic growth rate constant ( $k$ ) is the slope of the regression line using the standard equation of logarithmic growth:  $\ln(n/n_0) = kt$ . *In vivo* imaging 3 weeks post-incubation revealed the presence of AuNP(arrowed) in the body of founder animals (B, C).

Next, the toxicological impact on the regenerative capability of *Hydra* was analyzed. The head regeneration is a critical process of *Hydra* biology and the development of new tentacles can be monitored by a stereomicroscope to assess the effects of toxic agents. Regeneration efficiency was estimated by cutting the animals under the hypostoma after 24 hrs of incubation with AuNPs and analysing the efficiency of the regeneration process. Polyps incubated with AuNP-PEG-N<sub>3</sub> were shown regenerating head and tentacles with the same efficiency as untreated animals, suggesting that there were not adverse effects played by AuNPs on the regeneration process.

### 3.2.4 Internalization of AuNP in *Hydra vulgaris*: the role of the NP surface charge.

- **Analysis at whole animal, tissue and cellular levels**

In order to evaluate the efficiency of internalization of AuNPs, polyps were incubated for 24 hrs with AuNP-COOH/N<sub>3</sub> and AuNP-N<sub>3</sub> (70 nM). The two NPs present different surfaces, being the first functionalized with 25% of the maximum possible loadable Peg chain amount (in turn composed by half PEG COOH chains and half PEG N<sub>3</sub> chains), and representing the starting NP for siRNA functionalization; the second, AuNP-N<sub>3</sub>, presenting the surface completely saturated by PEG-N<sub>3</sub> chains (Figure 20 A and 21 A). The analysis under an optical microscope revealed that AuNP-N<sub>3</sub> were internalized at high rate into ectodermal cells, while AuNP-COOH/N<sub>3</sub> showed a less efficient uptake (Figure 20B-C-D). Under bright field observation a strong punctuated labeling all over the animal (head, body and tentacles) was detected, while AuNP-COOH/N<sub>3</sub> (Figure 21 B-C-D) showed a weak punctuated pattern over the body and tentacles. To deeper investigate the NP uptake mechanism, the animals were incubated for 24 h with AuNPs, fixed, cryosectioned and macerated into single-cell suspensions. Cryosections of polyps treated with AuNP-N<sub>3</sub> showed that the uptake

occurs rapidly and efficiently in the ectodermal cells, while 24h after treatment, groups of nanoparticles were found also in the endodermal layer (Figure 21 E). The same analysis on animals treated with AuNP-COOH/N<sub>3</sub> did not revealed any evident staining (Figure 20 E). Maceration of treated polyps confirmed the presence of Au NPs in the cytosol (Figure 20-21 F). These data suggest that the positive charge of AuNP-N<sub>3</sub> allows a high efficiency of internalization and confirms the crucial role played by the NP net charge in the interaction with the cell membrane (Tortiglione et al. 2009) and driving of the uptake process.

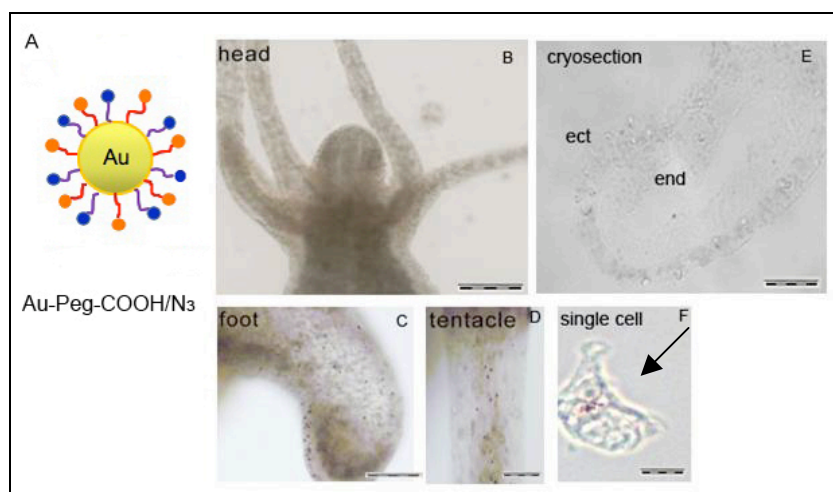


**Figure 20. *In vivo* uptake and biodistribution of AuNP-COOH/N<sub>3</sub> in *Hydra*:** in A) a schematic illustration of the AuNPs shows the nanoparticle structure, coated by two different PEG spacers (PEG-COOH, and PEG-N<sub>3</sub>). B) Bright field image of a living *Hydra*, treated 24h with 70nm AuNP-PEG-COOH/N<sub>3</sub>. Internalized nanoparticles are hardly detectable by whole animal imaging. Zooming into C) foot and D) tentacle regions show nanoparticle as dark granules located on ectodermal cells E) tissue cryosections prepared from treated animals. AuNPs are not detectable on such preparation, while on F) single cells preparations AuNPs are visible (arrowed) into the cytosol of ectodermal cells. Scale Bars: 200  $\mu$ m in B-C-E, 100  $\mu$ m in D, 50  $\mu$ m in F.

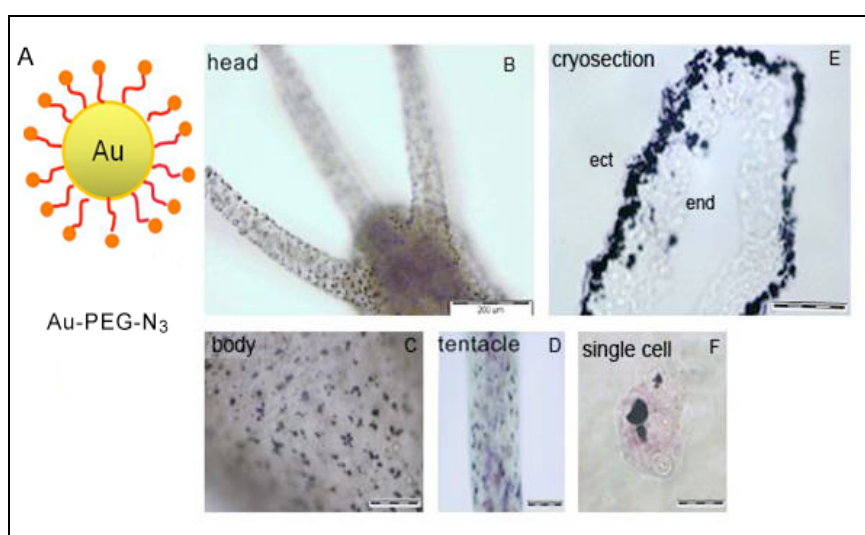


**Figure 21. *In vivo* uptake and biodistribution of AuNP-N<sub>3</sub> in *Hydra*:** in A) Nanoparticle scheme illustrating the homogeneous PEG-azide layer coating the Au core. B) Bright field image of a living *Hydra* treated 24h with 70nm AuNP-PEG-N<sub>3</sub> shows a strong punctuated dark labeling present uniformly all over animal. The pattern is clearly evident on separate imaging of C) foot and D) tentacles of treated polyps. E) Cryosections from labeled polyps show massive AuNP-N<sub>3</sub> accumulation into the ectoderm (ect) and the endoderm (end). F) Fixed single cell suspension reveal AuNP-N<sub>3</sub> location into vesicle-like structures of different sizes. Scale Bars: 200  $\mu$ m in B-C-E, 100  $\mu$ m in D, 50  $\mu$ m in F.



### 3.2.5 Internalization of AuNP-N<sub>3</sub> in *Hydra vulgaris*

- **Analysis at ultrastructural level**

In order to investigate the mechanisms of internalization an ultrastructural study by mean of transmission electron microscopy (TEM) was performed on animals treated with AuNP-N<sub>3</sub>, showing highest internalization rates, at different incubation times. The histological semithin section (Figure 22) of *Hydra* tissue, stained with toluidine blue, shows the structure of animal tissue. In the picture are visible the ectoderm and endoderm, separated by mesoglea. The black spot in the epitheliomuscular layers are gold nanoparticles accumulated into large vacuoles. Figure 23 shows that after 5 minutes of incubation AuNP-N<sub>3</sub> are bound to the glycocalix, a cuticle layer of mucopolisaccarids covering the animal outer surface. In a recent paper the molecular components of the cuticle were identified, as glycoproteins and glycosaminoglycans (Bottger et al., 2012). The strong interaction between the positive azide group of NPs and the negative cuticle components caused, within 30 minutes, the massive accumulation of nanoparticles all around the animal tissue. In fact, after 30 minutes of incubation, NPs were found at the level of the glycocalyx, surrounding the ectoderm, but even within large vacuoles, also containing the glycocalyx, as showed in figure 24 and 25. Furthermore, the nanoparticles were found in the act of moving outside these structures, reaching the cytosol. Finally, at 24 h time point, AuNPs were found accumulated in large cytoplasmic vesicles, mixed to glycocalix/subcellular debris components, probably originating from multiple fusion events (Figure 26), and giving rise to micrometer sized granular structures, visible also in semithin section (figure 22).

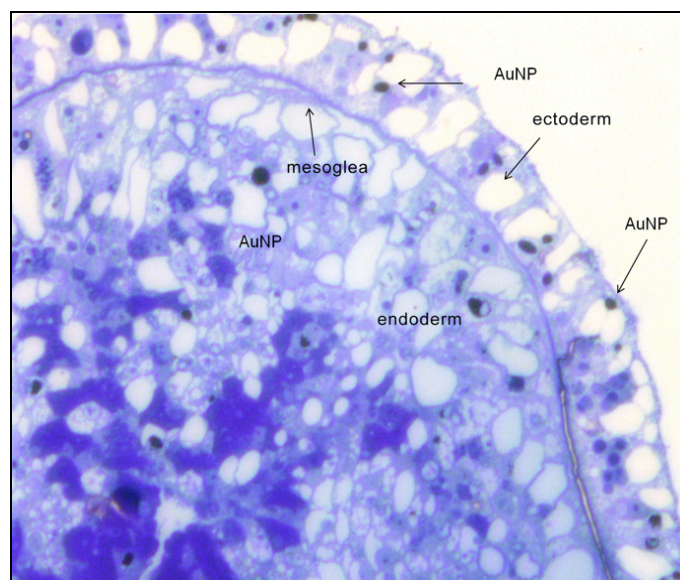


**Figure 22. Semithin cross section of *Hydra* treated with AuNP-N<sub>3</sub>.** NP appeared accumulated as micro-sized granules within both the ectoderm and endoderm.

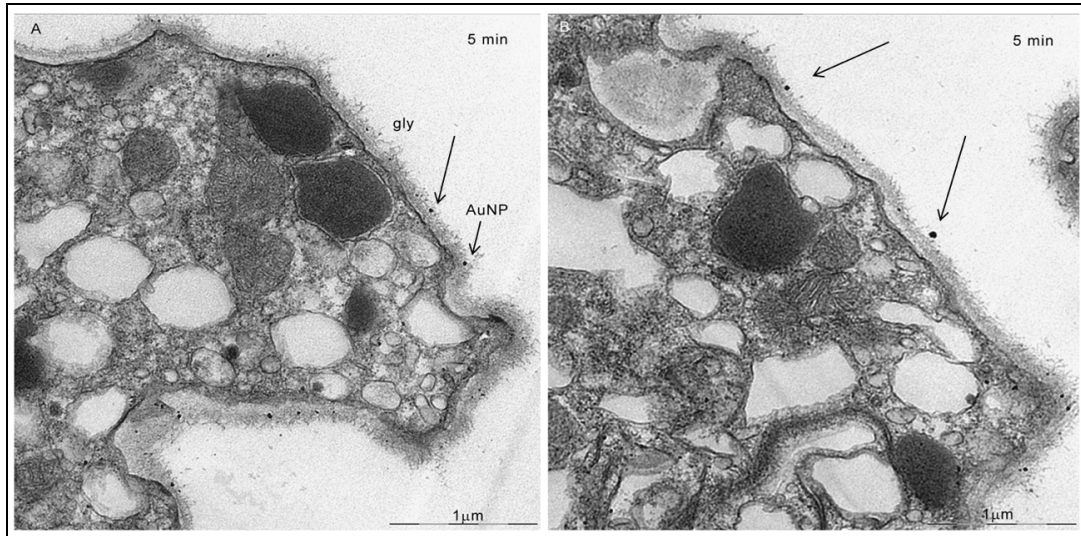


**Figure 23. Ultrastructural analysis of *Hydra* tissue treated with AuNP-N<sub>3</sub>.** *Hydra* polyps were exposed to AuNP-N<sub>3</sub> for 5 min, then extensively washed and processed for TEM. A-B) At 5 min time points, AuNP-N<sub>3</sub> were found attached to the glycocalix, uniformly decorating the animal outer surface (black arrows).

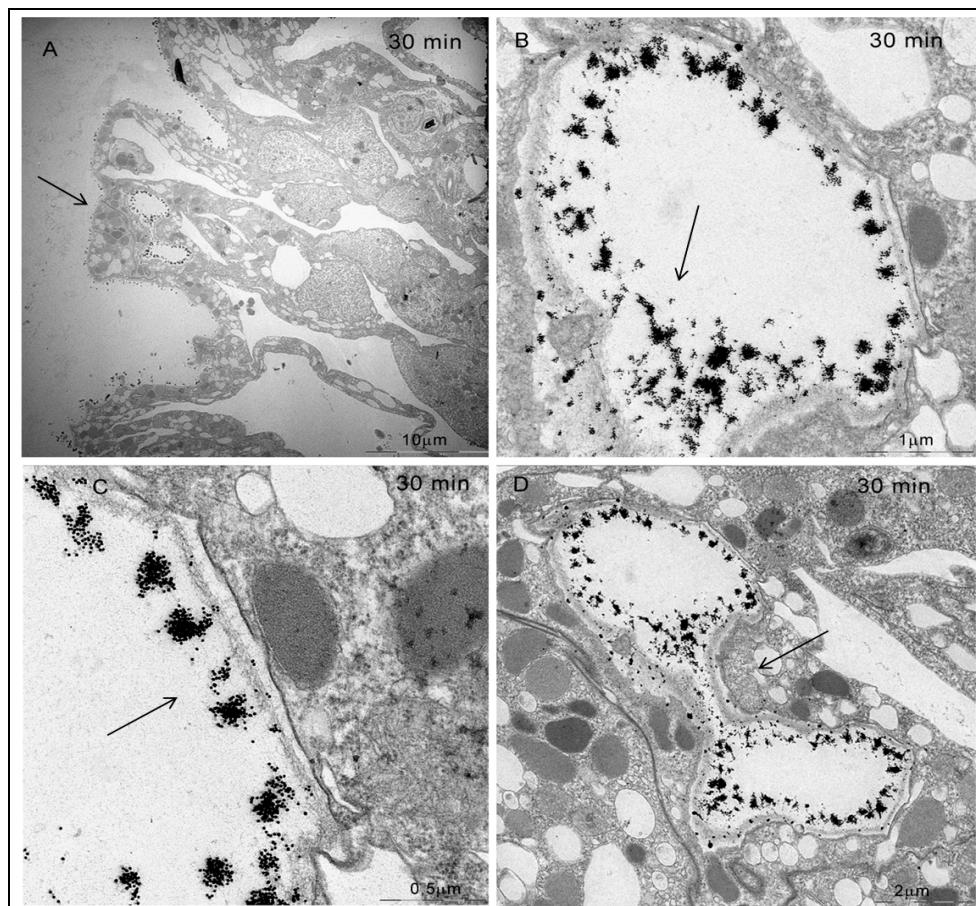


**Figure 24. Ultrastructural analysis of *Hydra* tissue treated with AuNP-N<sub>3</sub>.** *Hydra* polyps were exposed to AuNP-N<sub>3</sub> for A-B-C-D) 30 min, then extensively washed and processed for TEM. A) At 30 min time point, AuNP-N<sub>3</sub> were found attached to the glycocalix, uniformly decorating the animal outer surface (black arrows), but also inside large vacuoles. B-C-D). At higher magnifications the inner side of this structure appears lined by the glycocalix layer, suggesting the origin from membrane invagination (black arrows). C) A close view of the AuNP-N<sub>3</sub> entrapped into the vacuoles together with the glycocalix components.



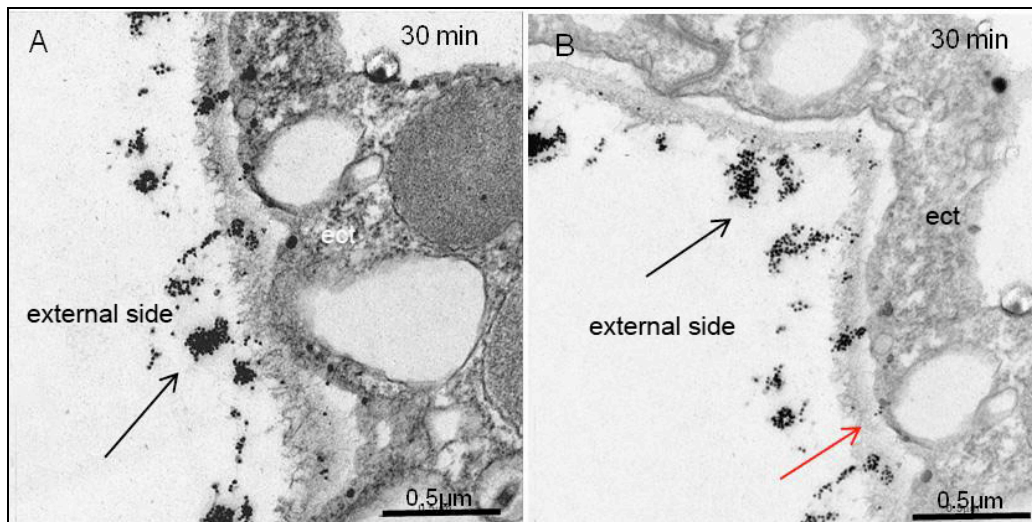


**Figure 25. Ultrastructural analysis of *Hydra* tissue treated with AuNP-N<sub>3</sub>.** *Hydra* polyps were exposed to AuNP-N<sub>3</sub> for 30 min. In the figure is showed NPs surrounding ectodermal layer, attached to the glycocalix (Black arrows) and some of them freely crossing the plasma membrane (red arrows).

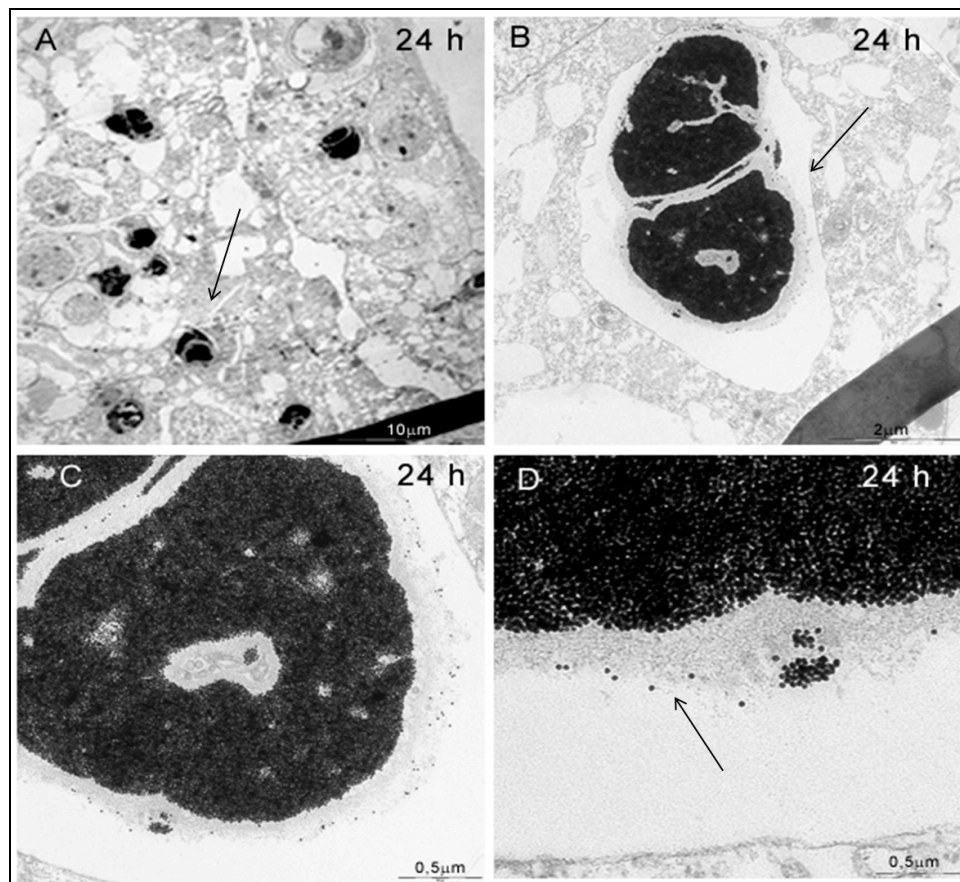


**Figure 26. Ultrastructural analysis of *Hydra* tissue treated with AuNP-N<sub>3</sub>.** *Hydra* polyps were exposed to AuNP-N<sub>3</sub> for A-B-C-D) 24 hrs, then extensively washed and processed for TEM. A) At 24h time point a massive accumulation of AuNP-N<sub>3</sub> into micrometer-sized vesicles was found. In B-C and D, higher magnifications of such structures clarify the presence of membrane components in between the packed NPs, suggesting multiple self-fusion and invagination events.

### 3.3 Gene silencing mediated by myc siRNA functionalized AuNPs

#### 3.3.1 In vivo assessment of uptake

The following bioactive molecules were selected for AuNP functionalization:

1) 21-nt siRNA oligonucleotides (*Hymyc*-siRNA) were designed on the sequence coding for *Hymyc1* (Figure 1 of Results section) .

2) the TAT peptide (GRKKRRQRRRPQ), a virus derived peptide known to increase the cellular uptake. This peptides can bind through N-terminal group the PEG-COOH moieties by mean of a EDC coupling reaction.

In order to bind the siRNA, two methodologies were applied: the binding of the negatively charged siRNA through ionic interaction to positively charged group present on the NP surface (i.e quaternary ammonium groups), or the binding of thiolated siRNA to the gold nanoparticles through covalent bond gold-thiol (Figure 27). For each approach four different AuNP abducts were synthesized, carrying either the siRNA (siRNA-AuNP), or the TAT peptide (TAT-AuNP), or both functionalities (siRNA-TAT-AuNP), and compared to the unfunctionalized AuNP, used as starting material. In this way the specificity of the RNAi effect could be analysed, together with TAT effect, which has not been reported in *Hydra*, to date.

Polyps were challenged *in vivo* with all Au NPs types reported in Figure 28 and the level of *Hymyc1* expression was monitored after 48 h of continuous incubation using qRT-PCR. This incubation time was selected as inducing the highest downregulation by using free siRNA.

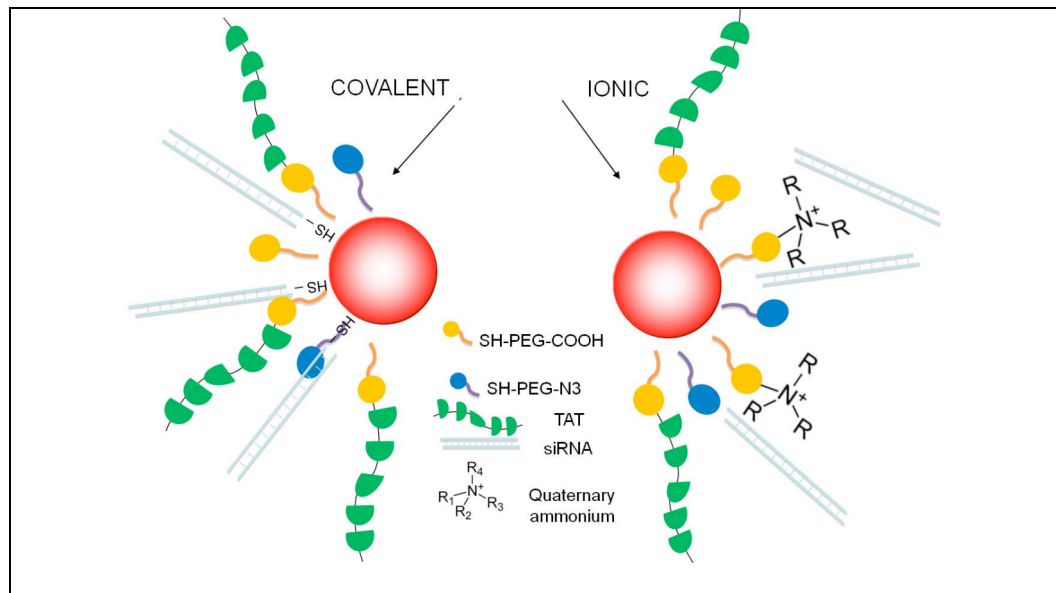
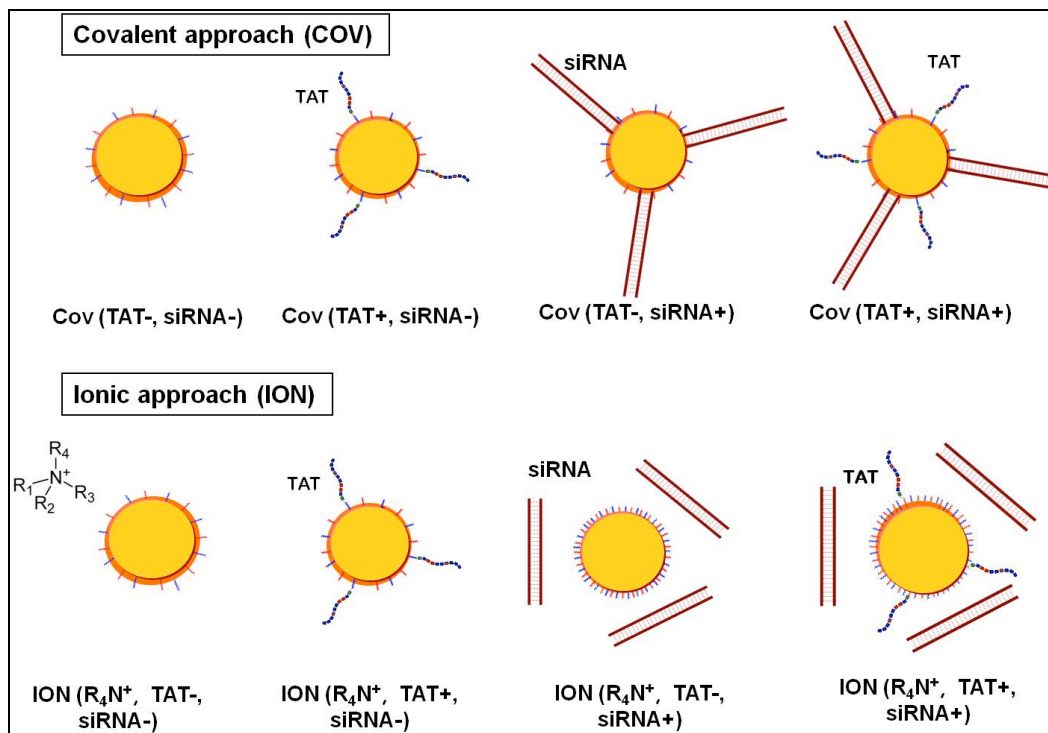
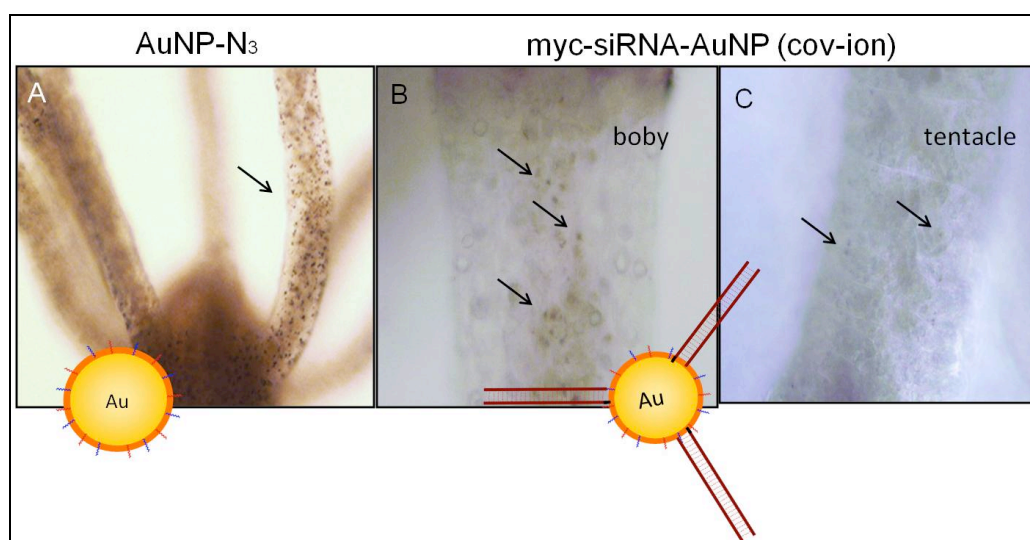


Figure 27. (A) Ionic and (B) Covalent approaches employed to bind siRNA to the Au core.



**Figure 28. Scheme of multifunctional nanoparticles synthesized by using two different approaches.** Upper panel: siRNA molecules were covalently conjugated to PEG-COOH/N<sub>3</sub> coated Au NPs. Lower panel: siRNA duplexes were attached to R<sub>4</sub>N<sup>+</sup> present on NP surface by electrostatic interaction. The TAT peptides were added by covalent binding.

The optical microscopy analysis showed that myc-siRNA-AuNPs displayed a low efficiency of internalization compared to AuNP-N<sub>3</sub>. As shown in Figure 29B-C, body and tentacles of animals displays only few dark granular staining (indicated by arrows) suggesting that siRNA functionalization decreases the efficiency of cell uptake in *Hydra*.



**Figure 29. Differential uptake of AuNP.** (A) Polyps treated with AuNP-N<sub>3</sub> show a strong internalization. (B-C) Body and tentacles of animals treated with myc-siRNA- AuNP appeared not efficiently labelled, indicating that siRNA functionalization decreases the efficiency of cell uptake in *Hydra vulgaris*.

### 3.3.2. Molecular assessment of *Hymyc1* downregulation by myc-siRNA-AuNPs

*Hymyc1* expression levels were assessed by qRT-PCR in polyps treated independently with each type of nanoparticle. The effects of myc-siRNA-AuNPs were compared to those produced by free siRNA under acidic or neutral conditions, TAT-AuNP and siRNA-TAT-AuNP (Figure 30). Among this NP series (produced by using the covalent approach) myc-siRNA-AuNP (COV) conjugate induced a 80% decrease of *Hymyc1* expression level (Figure 30), while the other NPs were shown unable to induce effective gene silencing. Remarkably TAT-AuNPs, produced with the aim to increase cell penetration and in turn RNAi efficiency, were shown ineffective, suggesting either toxicity of the viral derived TAT peptide in *Hydra* cells, or potential activity of TAT to suppress the RNAi machinery, as reported for other systems (Qian et al, 2009). The other set of AuNPs, synthesised by using the ionic approach to bind siRNA on the gold core, were also analysed for their activity to induce myc RNAi by qRT-PCR, following 48h of incubation. Results, reported in Figure 31, show the capability of siRNA-AuNP (ION) to induce a significant repression of *Hymyc1* (about 50%), while the other AuNP conjugates were ineffective. Once again the TAT peptide was shown to repress the RNAi effect, confirming results obtained by the same conjugates (produced by the COV approach). A Summary of the results obtained, using the two approaches is presented in Figure 32.

Of considerable importance is the evidence that all the sets of particles not carrying siRNA did not produce alterations of *Hymyc1* expression, indicating the absence of non-specific effects caused by NP.

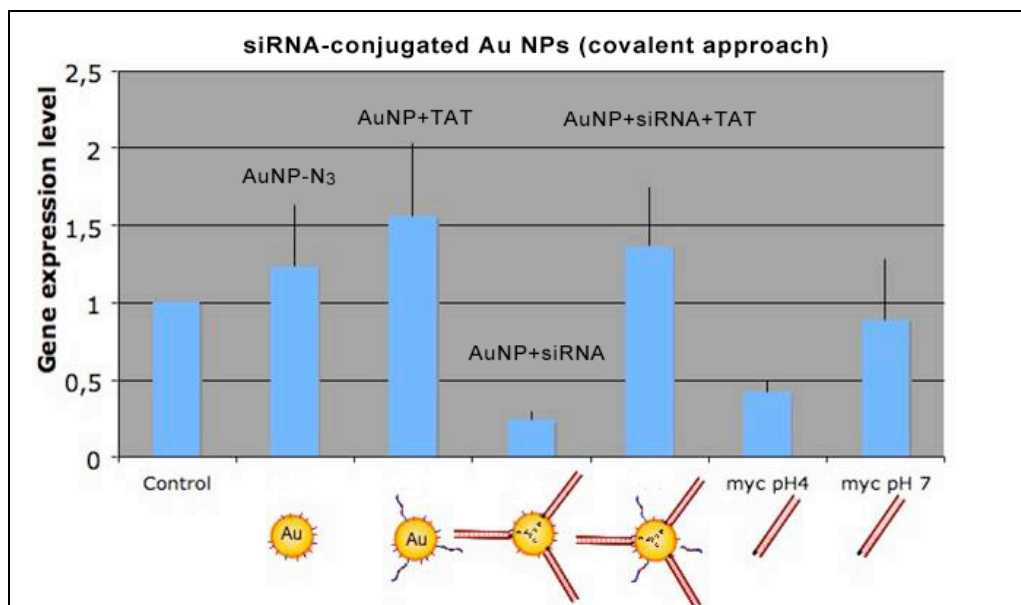


**Figure 30. Molecular analysis of *Hymyc* downregulation by siRNA-conjugated Au NPs (covalent approach)** To quantify silencing efficiency, 50 nM siRNA Au NPs were added to groups of 25 polyps in 100  $\mu$ l hydra medium. After 24 h the medium was replaced and the NP treatment refreshed. Total RNAs were extracted 48 h post-incubation and the mRNA levels of *Hymyc* were determined using qPCR and Elongation Factor 1 $\alpha$  (EF1 $\alpha$ ) as internal reference gene. *HyMyc1* relative expression upon incubation with covalent conjugated NPs and ionic conjugated NPs were reported. Unfunctionalized NPs were used to check undesired effects of AuNP on myc expression. Naked siRNA were administered at pH4 and pH 7 to compare silencing efficiency.



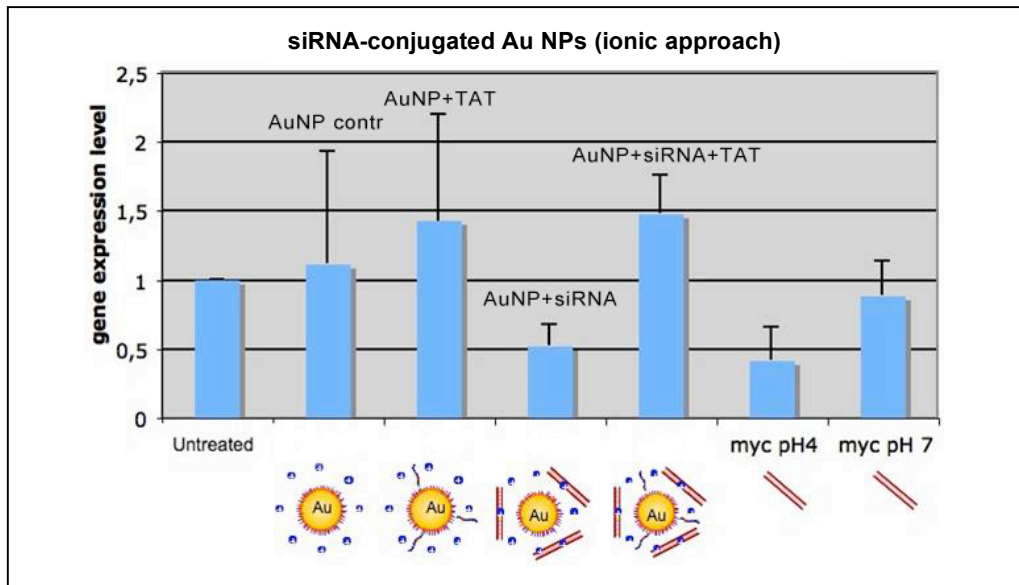


**Figure 31. Molecular analysis of *Hymyc* downregulation by siRNA-conjugated Au NPs (ionic approach)** To quantify silencing efficiency, 50 nM siRNA e Au NPs were added to groups of 25 polyps in 100 ul hydra medium. After 24 h the medium was replaced and the NP treatment refreshed. Total RNAs were extracted 48 h post-incubation and the mRNA levels of *Hymyc* were determined using qPCR and Elongation Factor 1 $\alpha$  (EF1 $\alpha$ ) as reference gene. Unfunctionalized NPs were used to check undesired effects of AuNP on *myc* expression. Naked siRNA were administered at pH4 and pH 7 to monitor silencing efficiency.

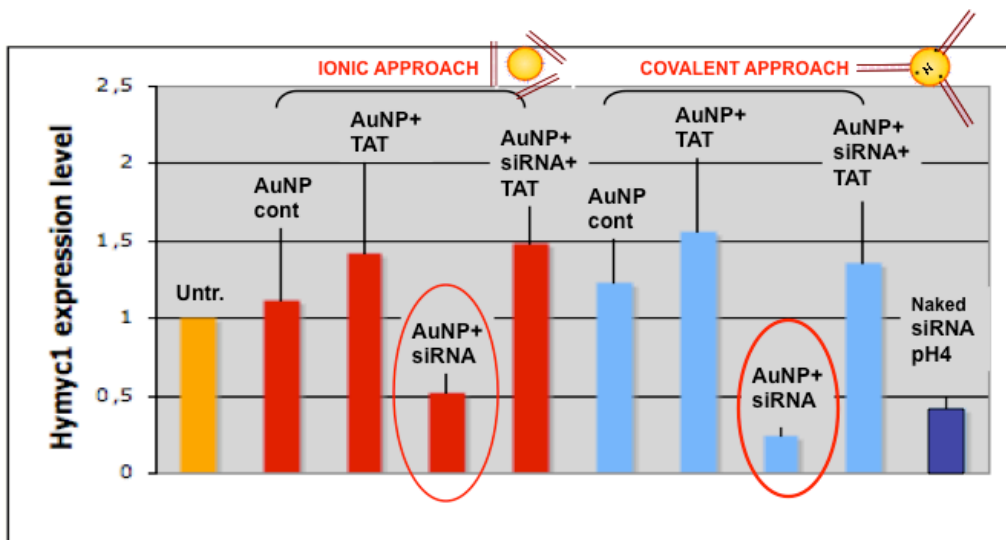


**Figure 32. Molecular assessment of RNAi efficiency by qRT-PCR using 50 nM AuNPs and 25 polyps in 100 ul hydra medium.** *Hymyc1* relative expression upon treatment with NP ion an NP cov, was compared to naked siRNA. Among all the NPs tested the best in *Hymyc1* silencing were the ion AuNP-siRNA without TAT and cov AuNP-siRNA without TAT.

### 3.3.3 RNAi induced by myc-siRNA AuNP: a dose-response evaluation

Since the covalent approach produced the most efficient *Hymyc1* downregulation a dose response was determined by treating the animals with increasing concentrations (0, 5, 25, 50 nM) of *myc*-siRNA AuNP for 48 h and then analyzing by qRT-PCR the *Hymyc1* expression levels. Results showed efficient RNAi induced by 25 nM and 50nM NP dose, while 5 nM dose was ineffective (Figure 33).

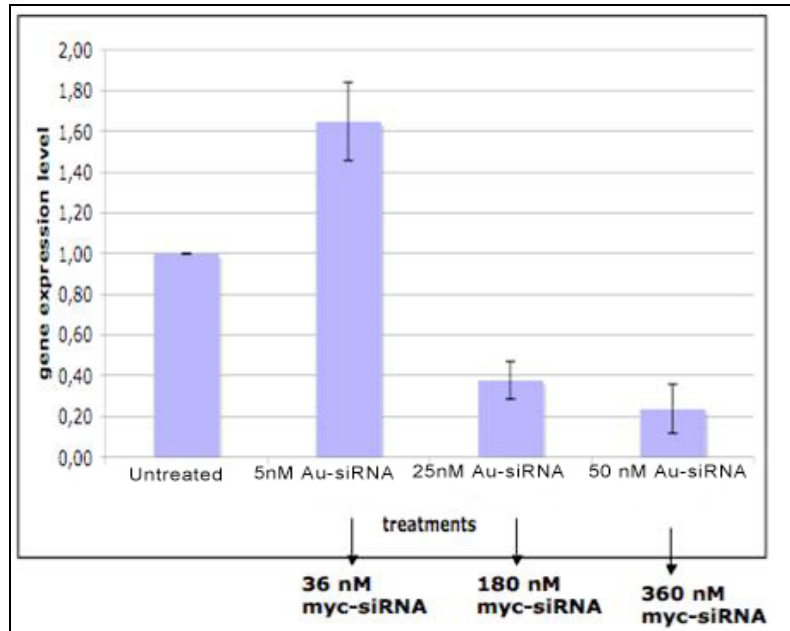


**Figure 33. RNAi induced by AuNP-*myc*-siRNA: a dose response evaluation.** To characterize the silencing efficiency of *myc* siRNA-AuNP conjugated NPs, 5nM, 25nM and 50 nM AuNP-siRNA were added to groups of 25 polyps in 100 ul of *Hydra* medium. After 24 h the media was replaced and the NP treatment refreshed. *Hymyc1* gene expression levels were determined upon 2 days of incubation using qRT-PCR and *Elongation Factor 1 $\alpha$*  (*EF1 $\alpha$* ) as reference gene.



### 3.3.4 Mechanisms of AuNP-siRNA uptake and intracellular fate

Ultrastructural analysis was performed to investigate the mechanism of internalization employed by siRNA-AuNP to enter Hydra cells and reach the cytoplasm, the site where RNAi occurs. A time course analysis over different incubation times was performed, to capture the interaction of siRNA-AuNP nanoparticle with the cell membrane, the intracellular distribution and the final clearance. TEM analysis showed that after five minutes of incubation no appreciable interactions occur between NPs and cell membranes, while after 30 min, single NPs or in cluster of a few units were found close to the plasma membrane or in the act of passing through it (Figure 34A, 34B). After 24 hours of treatment, siRNA-AuNPs were detected within a dense region cytosolic likely representing a late endosome/lysosome structure (Figure 35A, 35B, 35C). Remarkably, free nanoparticles were also found on membranes of interstitial cells, laying in the interstices between ectodermal cells, proving the capability of NP to deliver their siRNA cargo far from the administration site to the interstitial cell, where *Hymyc1* is expressed (Figure 35D).

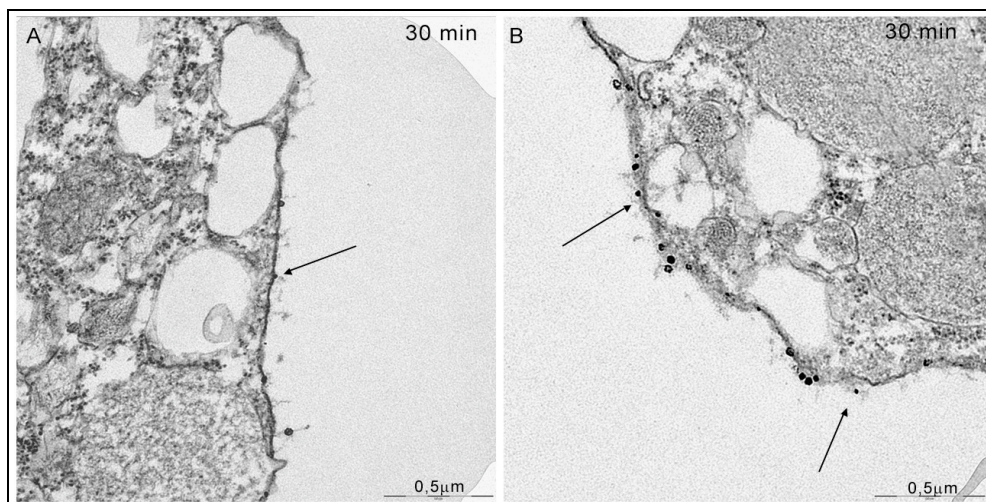


**Figure 34. Ultrastructural analysis of AuNP-siRNA uptake.** Polyps were treated with *myc*-siRNA-AuNP for 30 min, then carefully washed and processed for TEM. Thin sections were obtained cutting the animal at the mid gastric or sub-hypostomal (below the mouth) level. After 30min, single NPs or clusters of 2-3 units are detected in close proximity of the plasma membrane or within it (indicated by black arrows).

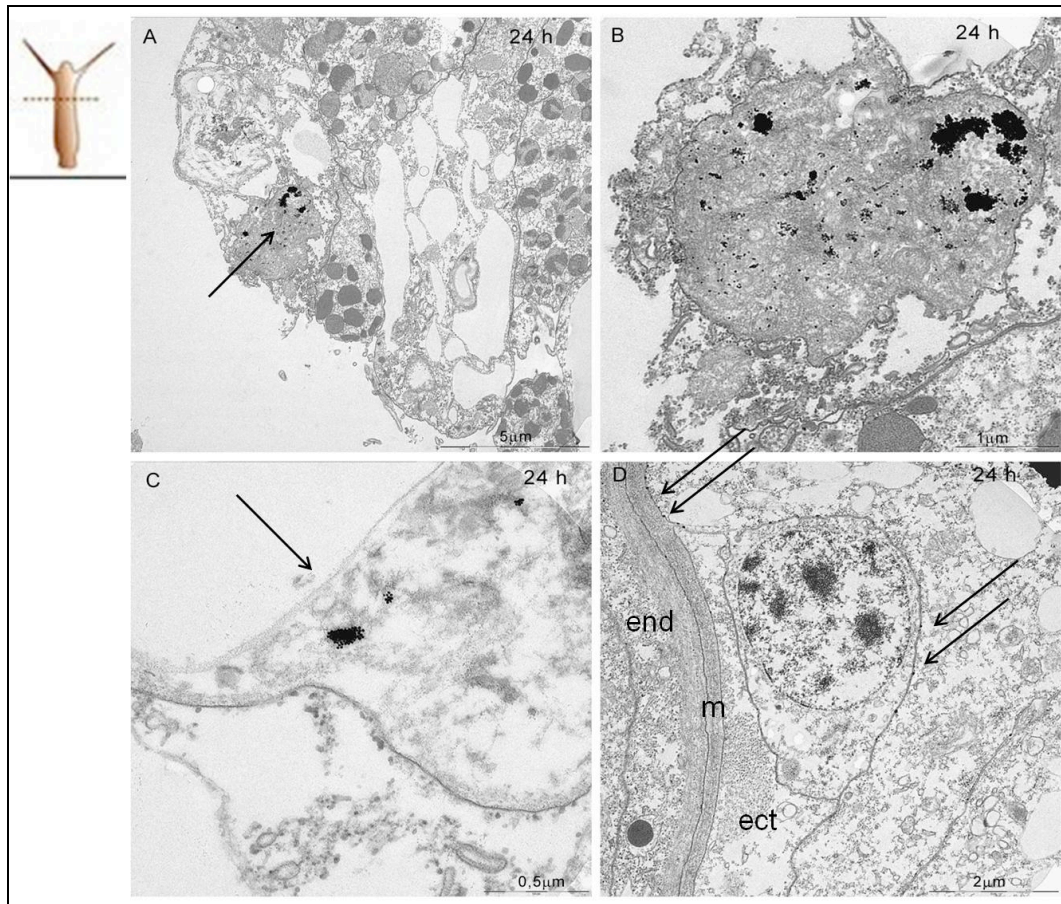


**Figure 35. Intracellular distribution of siRNA-AuNP after 24 h of incubation.** Polyps were treated with *myc*-siRNA-AuNP for 24h, then carefully washed and processed for TEM. Thin sections were obtained cutting the animal at the mid gastric or sub-hypostomal (below the mouth) level, as shown schematically in the upper part of image A. In A, B and C images at increasing magnification show AuNP located within a dense cytosol region, likely representing a lysosome. In this environment, NPs are not degraded. D) AuNP-siRNA are detected after 24hr of incubation on membrane of interstitial cells (is). This single stem cell is located in the interstices between ectodermal cells close to the mesoglea (m), which separates ectoderm (ect) from the endoderm (end). AuNP-siRNA are found also on the mesoglea (indicating the capability of the NP to reach districts distant from the original delivery site, which is the ectoderm).

### 3.3.5 Characterization of mycRNAi animals

- **Exploring the balance between proliferation and differentiation in myc-siRNA-AuNPs treated animals.**

By using free siRNA administered to living animals by soaking, we previously showed that *Hymyc1* downregulation impairs the balance between stem cell proliferation and differentiation, promoting proliferation and in turn the differentiation of nematocytes and gland cells. In order to evaluate similar effects induced by *myc*-siRNA-AuNP, cell suspensions obtained from treated animals were analysed for the content in the different cell types.

As result of a single experiment, we found in treated animals an increase in the population of nematoblasts (4s-16s), gland and mucous cells, suggesting an alteration in the stem cell population self renewal capability and a corresponding boost in the differentiation pathways leading to abnormal intermediate and terminal differentiated population sizes (Figure 36). As these phenotypical traits mirror the results obtained by using free *myc*-siRNA we showed i) the specificity of the RNAi methods, ii) the functional role of the *Hymyc 1* in the control of the stem cell proliferation.

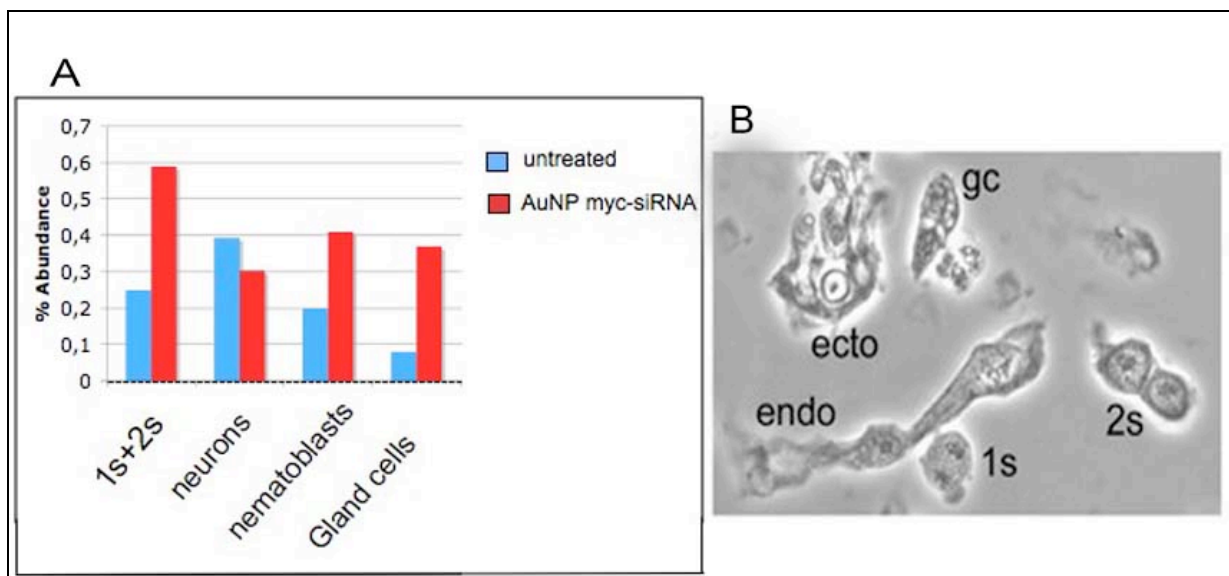


**Figure 36. A) Effect of AuNP-mycRNAi on cell type distribution.** An increase in the cell population where the *Hymyc1* gene is expressed is shown. **B) Isolated cells from macerated *Hydra* tissue as viewed using phase microscopy.**



### 3.4 Ultrastructural analysis of AuNP uptake and clearance

To get deeper insights in the mechanisms characterizing the uptake and the fate of NPs in *Hydra vulgaris*, we performed an electron microscopy study using the AuNP-N<sub>3</sub> nanoparticles, shown to be uptaken at high efficiency by ectodermal cells. The concentration of AuNP was lowered from 70 to 25 nM, avoiding massive accumulation of nanoparticle on the cell glycocalyx and allowing detection of single nanoparticle dynamics. High-Pressure cryo TEM was selected as innovative methodology for these studies. The advantages of this technique are the lack of ice crystals and of artifacts of fixation, enabling best preservation of cell and tissue structures. The experiments were performed at University of Innsbruck, where I was hosted in the laboratory of Prof. Bert Hobmayer, and assisted by Dr. Willi Salvemonser. The animals were incubated with the AuNP from 4h to 48h to widen the temporal window respect to previous studies and better understand the dynamics of internalization.

In figure 37 TEM images show at 4h of incubation single nanoparticles attached to nanosized vesicles outside the cell membrane, within the glycocalyx. Later on, after 8h-14h of incubation, vesicles are found traversing the cell membrane to reach the cytoplasm (figure 38A-B-C-D). At 24h and 48h time points most of the AuNP-N<sub>3</sub> are detected inside lysosomes (figure 39A-B). Surprisingly, at 48h nanosized vesicles loaded by NPs are also found outside cell membrane (Figure 39C-D), making it not clear wheather these nanovesicle are in the act of moving in or out the cell. This finding opened the possibility that beside their role as carriers of AuNP from the external medium inside the cell, those vesicles could also represent endosome recycled material brought back to the cell membrane (Figure 40). An estimation of the lysosome containing NPs (recorded from five different animals (and an average of twenty observations) show their increase from 8h to 48h time points (Figure 41), indicating that most of uptaken NPs are delivered to lysosomes for degradation.

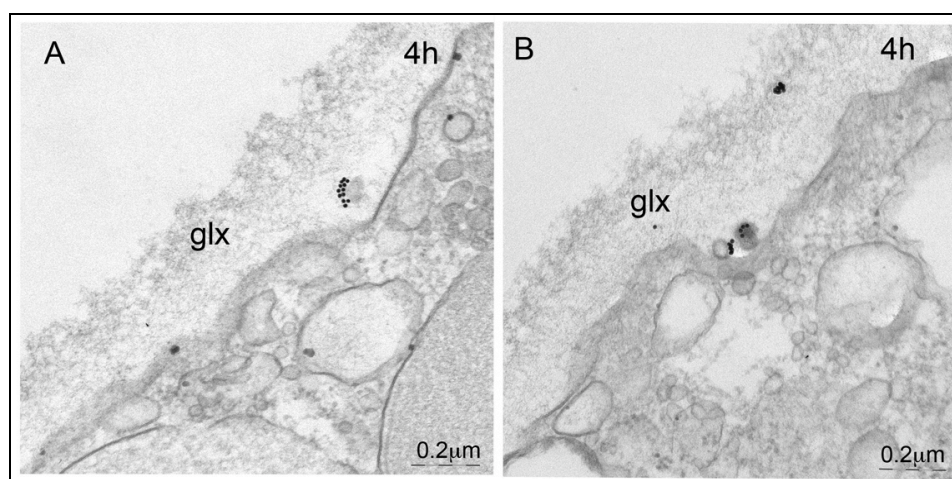


**Figure 37. High-pressure cryo-TEM of *Hydra* tissue treated with AuNP-N<sub>3</sub> (4h time points).** In A and B single distinguishable AuNP-N<sub>3</sub> appear attached to nano-sized vesicles outside the cell membrane, within the glycocalyx (Glx)

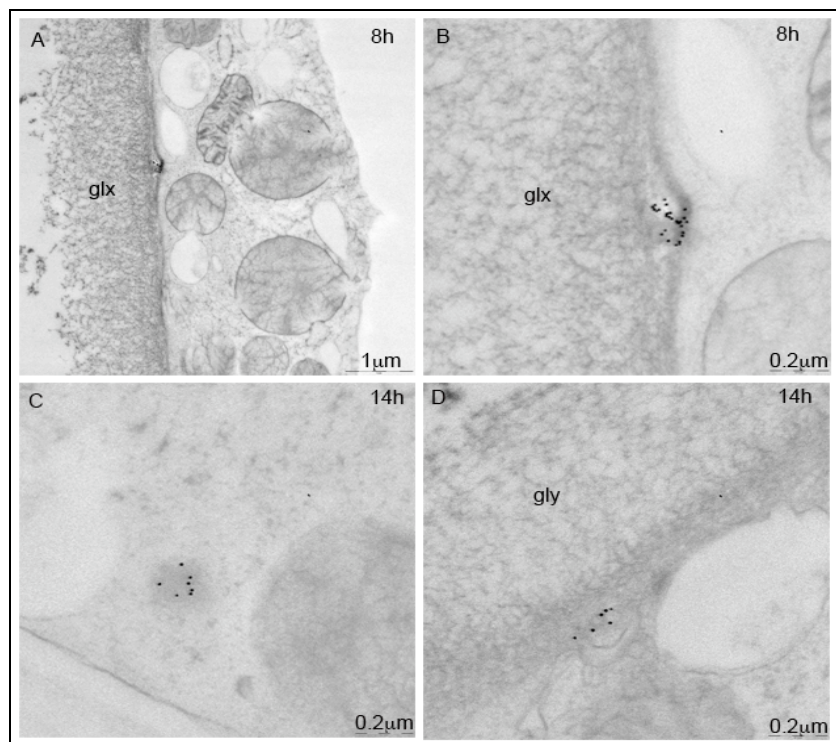


**Figure 38. High-pressure cryo-TEM of *Hydra* tissue treated with AuNP-N<sub>3</sub> (8h - 14h time points).** A-B) after 8h of incubation vesicles are found traversing the cell membrane to reach later (C-D) the cytoplasm.

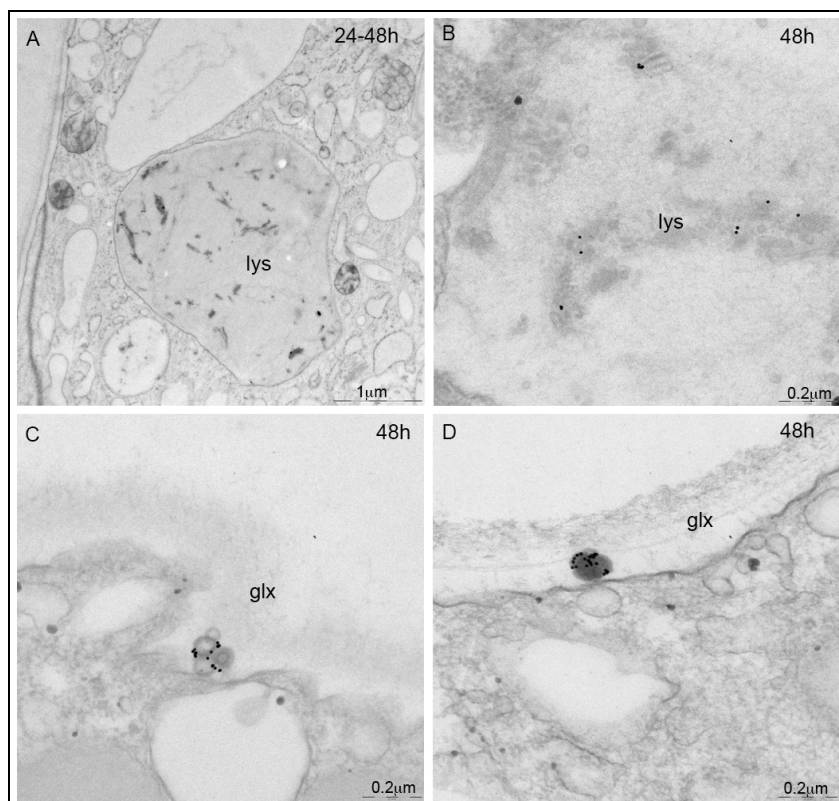


**Figure 39. High-pressure cryo-TEM reveals additional internalization pathways.** Polyps were incubated for the indicated periods with 25nM AuNP-N<sub>3</sub>. A-B) At 24h and 48h time points most of the AuNP-N<sub>3</sub> are detected inside lysosomes (Lys). C-D) At 48h nanosized vesicles loaded by NPs are also found outside cell membrane. Scale bars: 1μm in A, 0.2μm in B, C, D.

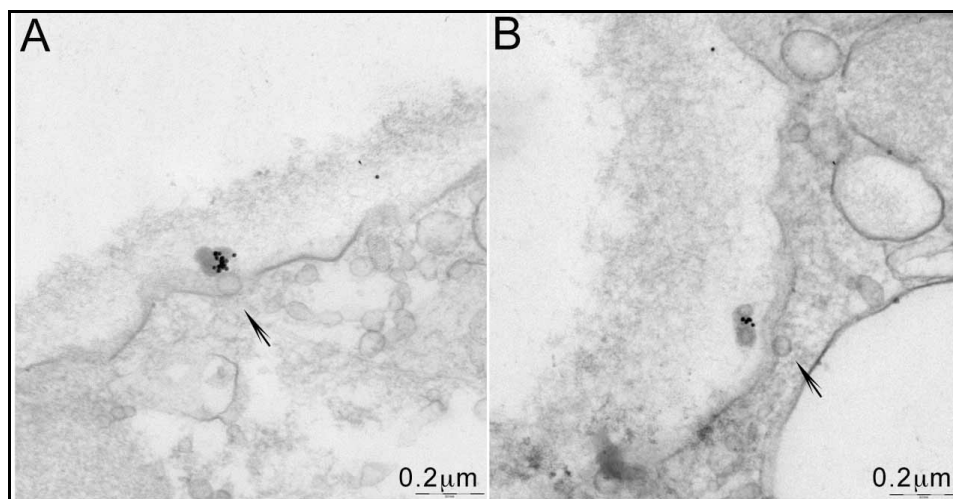


**Figure 40. Nanovesicle-mediated exocytosis of AuNP-N<sub>3</sub>** A) Nanovesicles underlying the cell membrane may release their content outside upon fusion with the phospholipid layer. Gold nanoparticles may be shuttled in and out the membrane through binding to these nanovesicles. The membrane appears interrupted on different regions to enable cell release, and empty vesicles (arrowed) are clearly detected on the cytosolic region below the external electron dense material. B) Another example of an empty nanovesicle in close proximity of external one decorated by gold nanoparticle.

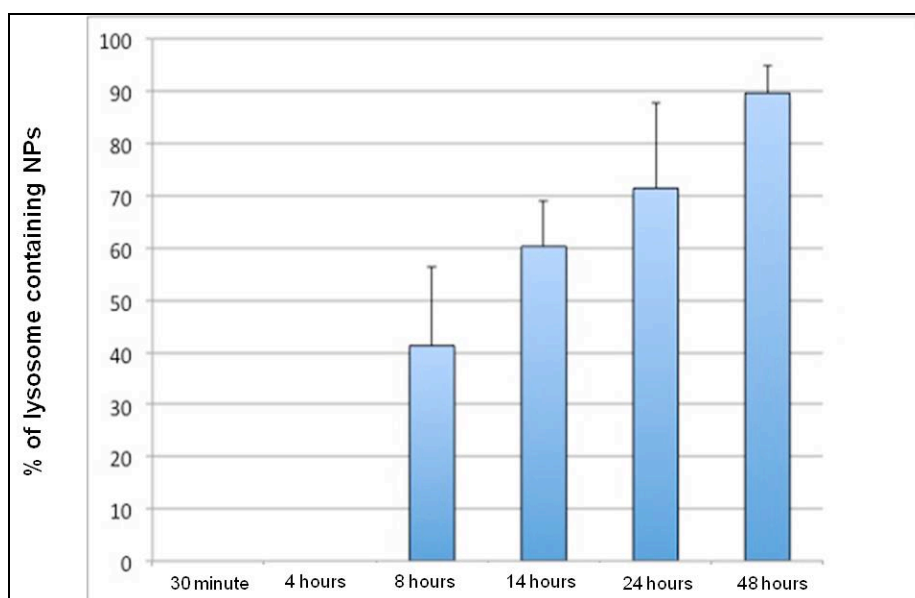


**Figure 41.** An estimation of the lysosome containing NPs (expressed as percentage  $\pm$  SE) show that they increase from 8h to 48h of incubation, when most of up taken NPs are delivered to lysosomes for degradation. The estimation was done at each time point on 20 TEM images collected from three different animals

To further confirm the exocytosis pathway, a “pulse and chase” experiment was carried out. Living animals were incubated 24h with AuNP-N<sub>3</sub>, extensively washed and incubated in fresh medium for further 24h and 48h before processing for TEM and elemental analysis. TEM images in Figure 42A show that 24h post incubation, vesicles containing NP are in the apical part of the cell, underneath the cell membrane, embedded into the glycocalyx layer and in the act being released outside the cell (Figure 42B-C-D). In Figure 43A a low magnification image shows the whole animal tissue section in the act of AuNP-N<sub>3</sub> clearance. Other images showed exocytosis by shedding vesicles densely packed with AuNPs or mediated by multiple vesicle release through larger membrane areas (Figure 43B-C-D).



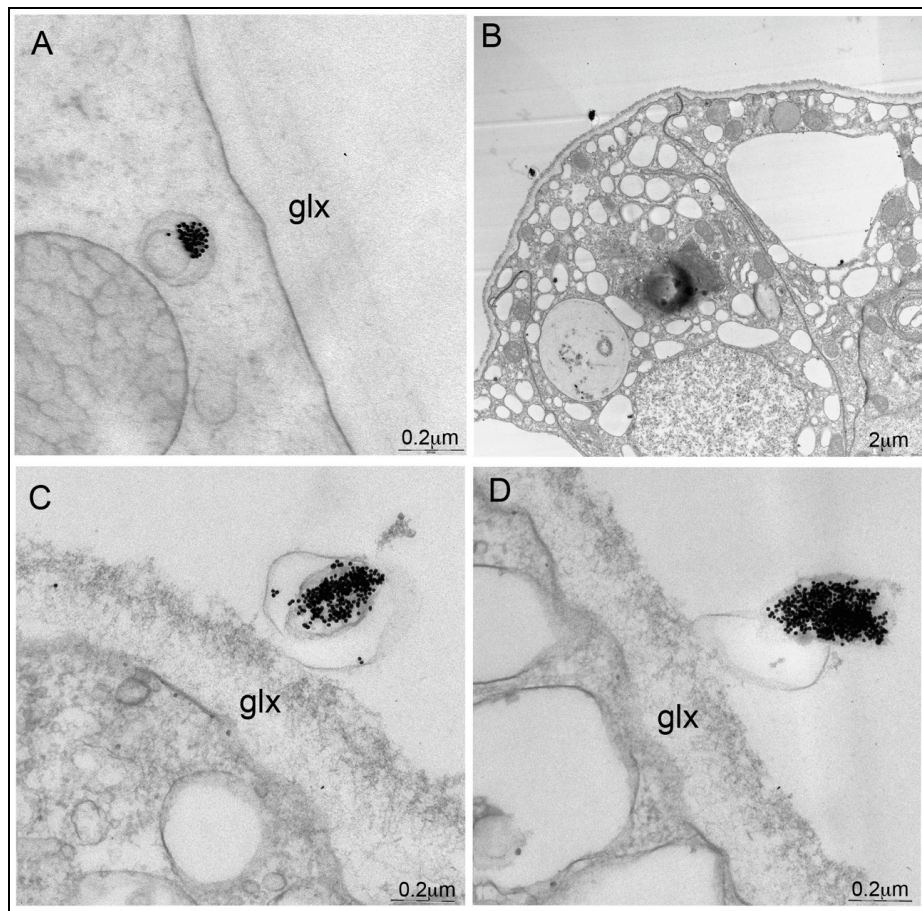


**Figure 42. Exocytosis of AuNP-N<sub>3</sub>.** Polyps were “pulsed” 24h with AuNP-N<sub>3</sub>, extensively washed and “chased” by incubation for additional 48h in fresh medium, before processing for TEM analysis. A) AuNP-N<sub>3</sub> are found on the apical part of the cell, entrapped into nanosized vesicles that are released out of the animal (B C and D).



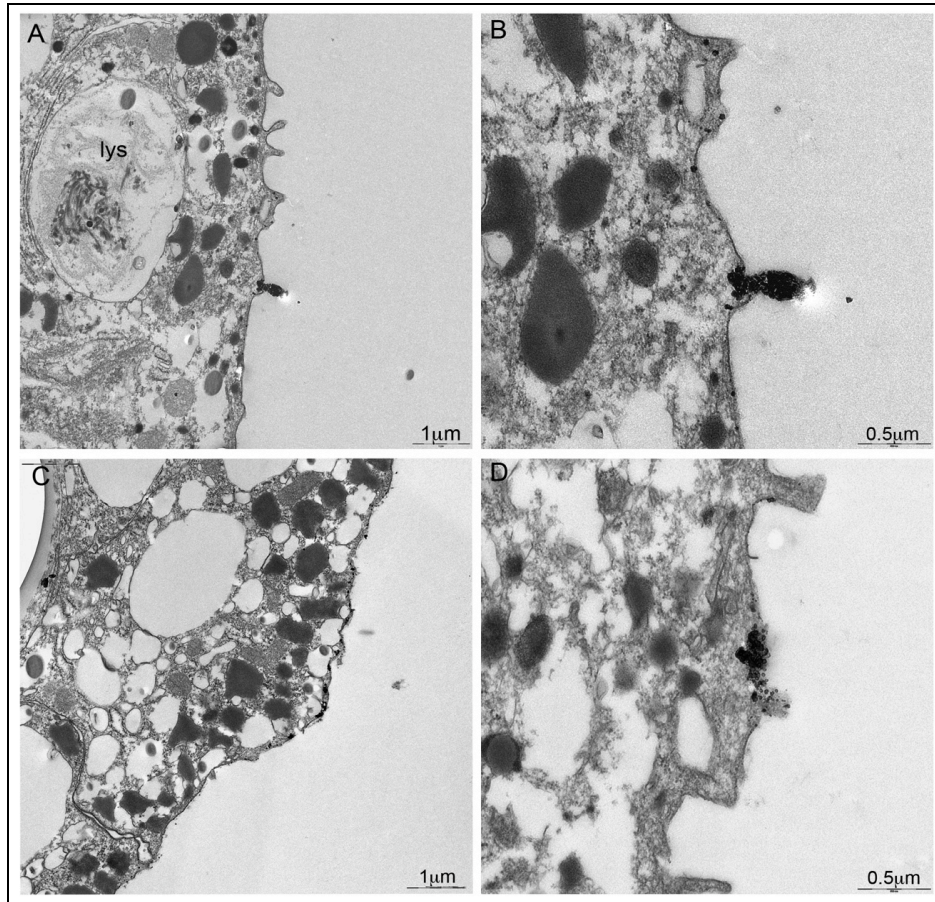


**Figure 43. Exocytosis of AuNP-N<sub>3</sub>.** Polyps were “pulsed” 24h with AuNP-N<sub>3</sub>, extensively washed and “chased” by incubation for additional 48h in fresh medium, before processing for TEM analysis. In A a low magnitude image shows the whole animal tissue section in the act of AuNP-N<sub>3</sub> clearance. Other similar membrane sheddings without NP are present on the animal surface, proving the normal occurrence of this phenomena. The same region at higher magnification is shown in B. In C and D) Other tissue regions showing NP clearance. In this case a larger membrane area is involved, probably reflecting lysosome exocytosis.

### 3.4.1 Elemental analysis confirms kinetic of uptake and clearance of AuNP

In order to calculate the amount of AuNP-N<sub>3</sub> internalized by *Hydra vulgaris*, elemental analysis by ICP-AES (Inductively coupled plasma atomic emission spectroscopy) was performed on animals pulsed 24h with 25 nM AuNPs (corresponding to 1.25 mg), then washed and chased in fresh medium for 24h and 48h. The Au content (calculated on 150 treated animals) at the end of the pulse (24h) was estimated as 93,7 µg, namely 7.5% of the total dose used for treatment.

After 24hrs of incubation in fresh medium, the Au content decreases down to 26,1 µg and 23,1 µg, respectively at 24h and 48h time points, indicating a 75% release of the internalized material.

From analysis of the supernatants collected during the chase phase, a low but appreciable amount of Au (0,8 µg) was found only at 24h post washing, confirming AuNP exocytosis mainly occurring within this temporal window (Table 1). Overall these findings confirm the kinetics of AuNP entry/exit suggested by the TEM images: AuNPs are moderately recruited into vesicles within the first 24h of incubation, and then sorted out 1) to lysosomes for external release during the following 24h, 2) to more stable structures, possibly representing storage vacuoles, discharging their content over a longer period. The unavailability of molecular markers specific for different types of *Hydra* storage vesicles makes it impossible to further characterize the nature of such structures.

h post washing	Intracellular Au content (µg)	Extracellular Au (µg)
0 h	93,74 ± 1.55	0
24 h	26,14 ± 1.20	0,819 ± 0.012
48 h	23,14 ± 0.42	0

**Table 1. ICP-AES analysis.** ICP-AES was performed on animals pulsed 24h with 25 nm AuNPs(1,25 mg), then washed and chased in fresh medium for 24 h and 48 h. At each time point 15 animals (and 1ml of their incubation medium) were collected and processed for ICP AES analysis. Experiments were performed in triplicate.

## **4 Discussion.**

In 1998, Fire and Mello uncovered the mechanisms of RNA interference opening the new fascinating research field on gene silencing. For this groundbreaking discovery they were awarded the 2006 Nobel Prize in Physiology and Medicine. Very soon it became clear that beside its profound effect on the study of gene function, RNAi could provide a new class of therapeutic agents based on dsRNAs (Kim et al., 2007). The progression from basic discovery to applications in medicine ran really fast; nowadays, few years later its discovery, there is a growing interest to exploit RNAi as a therapeutic strategy for degenerative diseases and cancer (Davis et al., 2010), which led to a dozen of phase I to III clinical studies. Despite this promising potential, some hurdles must be overcome before RNAi technology can be widely employed in clinical practice. In particular, physicochemical features of siRNA molecules such as small size, hydrophilicity, net negative charge and high sensitivity to nuclease activities pose severe challenges to gene silencing. More in detail, one of the most critical points to achieve an effective gene silencing concerns the safe and efficient delivery of siRNA into the cytoplasm, where the RNAi process takes place. In fact, cell membranes and endosomal compartments may represent a stumbling block for siRNA entrance into the cytoplasm limiting or even inhibiting RNAi-based approaches (Akhtar et al., 2007). To facilitate intracellular delivery of siRNAs many biochemical and biotechnological strategies have been developed, including the use of transfection agents or viral systems. In addition, recent technological tools have also facilitated cell-specific targeting of RNAi reagents through the use of ligands such as, receptor-targeting aptamers or ligand-coated nanostructures (Davis et al., 2010) driving specific delivery to desired cell population. Although these significant advances contributed notably to enhance gene silencing efficacy, the design of forefront strategy to further improve RNAi methodologies is of outstanding importance in biological research as well as for therapeutic purposes.

### **4.1 RNA interference mediated by free siRNA in *Hydra vulgaris*.**

The possibility to perform gain or loss of function approaches to analyze gene function may add new values to the widespread use of *Hydra vulgaris* as model organism. While the generation of transgenic polyps by embryo microinjection has been exploited by several groups as a feasible methodology to study gene function by overexpression in *Hydra* tissues, the development of reliable and reproducible RNAi methodologies was faced for many years by several groups by using different approaches including: embryo microinjection (Wittlieb et al., 2006), whole animal electroporation (Lohmann et al. 1999), localized electroporation (Smith KM et al. 2006). Subsequently, new milder strategies for dsRNAs delivery were introduced. *Hydra* was fed with dsRNA producing bacteria (Chera S. et al, 2006), allowing the silencing of both endodermal and ectodermal genes. The soaking method using long dsRNA has been employed for efficient RNAi of key developmental genes in the marine hydroid *Hydractinia echinata* (Duffy DJ. et al. 2010). Despite these efforts, RNAi is not yet a robust, widely used technology for functional studies in *Hydra*. During the first part of my PhD thesis, I studied the possibility to downregulate the expression of the protooncogene *c-myc*, introducing a new approach of RNA interference in *Hydra vulgaris*, based on soaking adult polyps with siRNAs. As the net negative charge of siRNA molecules may prevent them from interaction with biological membranes and cell internalization, we established conditions to improve

siRNA uptake. Previous study from our group showed that the positive net charge of colloidal nanoparticles influences the cell uptake (Tortiglione et al, 2009). Thus we used mildly acidic condition to soak *Hydra* with siRNA. Under these conditions we showed that siRNA undergo charge reversal and cell uptake was greatly enhanced. Alexa fluor 488-labelled myc-siRNAs, indeed, were detected at pH 4, but not at pH 7, into the cytoplasm of *Hydra* ectodermal cells, within both epitheliomuscular and interstitial cells, as granular structures of different sizes, confirming the role of the positive surface charge for cell delivery (Tortiglione et al., 2009, Howard et al., 2009). *Hymyc1* is the *Hydra* homologue of the *c-myc* proto-oncogene, a gene conserved throughout the animal kingdom (de la Cova C. et al. 2006), which governs key cellular processes such as cell growth, proliferation, apoptosis. Although *Hymyc1* showed a structural conservation in bHLH-Zip domain and myc-boxes I to III, as in the vertebrates, its physiological role in *Hydra* has not been fully elucidated.

By challenging living *Hydra* polyps with myc-siRNA, *Hymyc1* mRNA and protein levels were downregulated. At cellular level, an analysis of single cells prepared by maceration revealed abnormal distribution between cellular types of the interstitial cell lineage. *Hymyc1* downregulation did not affect epithelial cell rate, while it induced an increase in stem cell proliferation rate, which produced dramatic effects on the related cell population sizes. These results are in line with previous studies relating stem cell self-renewal to the cell density, and showing that nematocyte commitment increases as stem cell concentration increase (David et al., 1980). In particular David and coworkers demonstrated using cell aggregates, that the rate of nematocyte differentiation increases as the concentration of stem cells increases; under the same conditions the rate of nerve differentiation remains essentially constant. Here, by *myc* RNAi, the 1s+2s amount was increased after 4 days. This lead to a huge increase in the zymogen, mucous cell and nematocyte population. After 9 days of treatment, the stem cell density was restored to physiological levels, suggesting a negative feedback between stem cell, as elsewhere suggested (Holstein et al., 1990). Holstein and coworkers demonstrated, using *Hydra oligactis*, for the first time, changes in the cell cycle parameters of interstitial cells associated with altered population growth rates.

The specificity of the phenotype induced by myc-siRNAi was confirmed by Tortiglione and coworkers by treating animals with a biochemical c-MYC inhibitor, the thioxothiazolidinone 10058-F4, that affects also the myc gene transcription level. Treatment of living polyps with 10058-F4 for 2 days induced 50% reduction of *Hymyc1* expression levels, as assayed by qRT-PCR (Figure 1A). Cell type distribution analysis revealed increased proliferation of stem cells, and increased amounts of intermediates and terminal differentiation products (nematoblasts, nematocytes, secretory cells), Figure 1B. As detected in *Hymyc1* RNAi polyps, also the phenotype of the battery cells was affected, containing an abnormal number of nematocytes (Figure 1C), indicating the specificity of the *Hymyc1* downregulation effects. Taken together, these findings suggest that *Hymyc1* conditional knock down enhanced stem cell proliferation, and in turn unbalances the differentiating products.

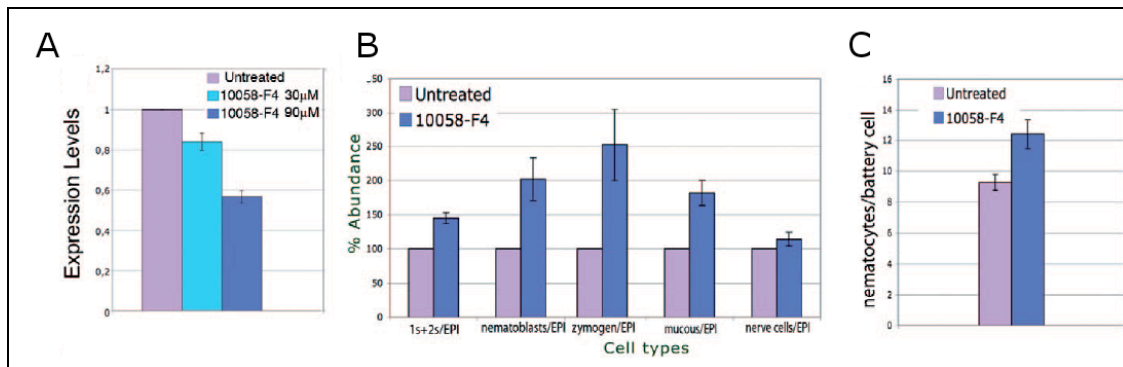


**Figure 1. Molecular and morphological alteration induced by the *c-myc* inhibitor 10058-F4.** A) Living polyps were treated with the *c-myc* inhibitor 10058-F4 for 48 h at two different concentrations (30 mM and 90 mM) before RNA extraction for qRT-PCR analysis. Expression levels, relative to *HyEF1α*, indicate *Hymyc1* silencing in a dose dependent manner, reaching 47% downregulation at the higher dose tested. Error bars indicate standard deviations calculated from three independent experiments, each performed in triplicate. B) Single cell suspensions were prepared from polyps treated as in A and the relative cell types counted by phase contrast microscopy. C) Polyps treated with the *c-myc* inhibitor as in A were fixed and whole mounted for analysis of the nematocyte content into the tentacles (as described in Figure 12, chapter Results).

The involvement of *c-myc* in controlling cell proliferation and differentiation processes has been shown in many systems, by both gain and loss of function approaches. For example in murine hematopoietic stem cells (HSC), it was showed that *c-myc* depletion resulted in the accumulation of HSCs *in situ* due to their failure to initiate normal stem cell differentiation (Laurenti et al., 2009) (Wilson et al., 2008). In human pancreatic endocrine cell lines *c-myc* downregulation by siRNAi induces the exit of the cell from proliferating phase and to enter in the differentiation pathways, thus *c-myc* plays a role in the switch mechanism that controls the inverse relationship between proliferation and differentiation (Demeterco et al., 2002). In *Hydra* we showed for the first time the role of *myc* proto-oncogene in controlling the balance between stem cell renewal/differentiation suggesting that in the ancient progenitor of animal evolution the *myc* factor was already at work to control crucial processes of stem cell biology.

On the top of the elucidation of the functional role played by *Hymyc1* in the maintainement of the cell homeostasis, the development of an efficient tool to downregulate gene expression demonstrates the conservation in *Hydra* of the RNAi cell machinery and the conserved role of siRNA. Although the molecular mechanisms underlying RNAi have not been exhaustively elucidated in Cnidaria, we provide evidences that siRNAs enter *Hydra* cells and trigger a RNAi response, similarly to many metazoans (Ambrosone et al., 2012). The strong molecular downregulation observed in siRNA treated animals suggest that the RNAi response may result from both direct delivery to interstitial cells and spreading effect of the RNAi response, similarly in other vertebrates (Timmons et al., 2003). This hypothesis is supported by the presence in *Hydra* genome of predicted genes encoding for components required for amplification and systemic spread of an RNAi signal.

#### 4.2 RNA interference mediated by gold nanoparticle in *Hydra*.

Gold nanoparticles (AuNP) have attracted much interest over the last decade owing to excellent physicochemical properties such as their reduced sizes, rendering them capable of interacting with biomolecules in a one to - one scale, and the high surface-to-volume ratio allowing for surface functionalization with a plethora of molecules for specific targeting and drug payloads. Noteworthy, among the array of nanomaterials designed to improve biomolecule delivery, Au NPs have shown to be safe in *in vitro*

and *in vivo* tests minimizing the risks of their use in biomedical research (Giljohann et al., 2010).

Therefore, in the second part of this study, we developed and tested a new RNAi method, based on siRNAs conjugation to AuNPs. More in detail, stable gold nanoparticles were synthesized and functionalized with two different PEG spacers. These PEGylated AuNP formulations represented the basic nanoparticles for downstream functionalization with *c-myc* siRNA, using either ionic interaction (ION) or covalent binding (COV). In the ION method, electrostatic interactions between the negatively charged siRNA backbone and both the azide and quaternary ammonium positively charged groups ensured binding of siRNA onto the NP surface for the whole pH range. In the COV method, thiolated siRNA was bound via a thiol bond to AuNPs with a nonsaturated PEG layer. Further functionalization of these AuNPs with the HIV-derived TAT peptide was performed to increase the cell penetration of functional NPs. Considering the possible combinations of different chemical groups on the nanoparticle surface, we tested in total 8 different functionalised NPs.

Multiparametric analysis of AuNP toxicity showed that this kind of NPs has no or negligible effects on animal morphology, reproduction and regeneration indicating their safe use in *Hydra*, even at high concentrations (4 mg/ml).

Molecular analysis by qRT-PCR showed that in terms of RNAi, the best performing nanovector, the AuNP harboring *Hymyc1* siRNA covalently bond to the NP surface (cov approach), markedly reduces (80%) the expression level of myc protooncogene. Interestingly, the functionalization with TAT, initially added to enhance the cell permeability, caused probably an inhibition of RNAi, confirming that TAT may exert a conserved RNAi suppressor activity, as reported in Qian et al., 2009.

In this work, in fact, it has been demonstrated that both in human and plant cells the underlying mechanism of RNA silencing suppression by human virus HIV-1 TAT peptide and plant virus P19 are related. TAT and P19 resulted not to be able to reduce maturation of dsRNA duplexes but they exert their effects downstream, indicating a common mechanism to prevent guide strand programming of RISC.

Furthermore, our results proved that siRNA conjugation through ionic approach provides nanovectors with a lower silencing efficiency. This could be explained considering the different release mechanisms of covalently and ionically produced AuNP-myc-siRNA. Indeed the ionic approach, relying on the interaction of positively charged AuNPs and negatively charged siRNA, could be affected by changes of the chemical physical properties of environment, that could weak the electrostatic interaction between the siRNA and the AuNP core. The lower downregulation efficiency compared to the corresponding covalent conjugates could suggest that siRNA molecules might be released from NP surface before reaching the cytoplasm. By contrast the AuNPs-myc-siRNA functionalized by covalent approach might efficiently deliver siRNA to the cytoplasm. With this method siRNA could not be released before their cellular uptake because they are linked to the AuNPs surface through a thiol bond. The breakdown of this kind of covalent bonds could be achieved only in reducing environments, such as the cytoplasm. However, besides the mentioned release mechanism of siRNA duplexes, another way through which cov AuNPs-myc-siRNA can induce myc downregulation is by releasing only the antisense strand with the sense strand permanently linked to the AuNP surface. The chemical basis of NPs production could thus provide an explanation of the different silencing efficiencies. We argued whether RNAi may be triggered also by siRNA still linked to NPs. In the case of ion AuNPs we do not have data that can allow us neither to accept or refuse this possibility. For the cov AuNPs, as they have been

produced in this work, it is quite impossible that the silencing may be induced with the siRNA attached to NPs because the sense strand is bound to the NP with the antisense free to be released. To better investigate this issue we should produce AuNPs with the antisense strand covalently bound to the surface, with a bond insensitive both to pH and reducing environments. In conclusion, we demonstrated that Au NPs function as a safe and potent tool for siRNA delivery in living animals. Moreover, our data successfully contributed to optimize the design of smart nanodevices which are currently employed in pre-clinical studies focused on lung cancer treatment in murine models.

#### **4.3 Ultrastructural evidence of dynamic of internalization of Au-NP-N<sub>3</sub> and Au-NP-myc-siRNA**

Beyond the important goal to achieve advanced functional materials designed for RNAi, it is of great interest in nanomedicine to gain knowledge on mechanisms controlling the uptake of nanoparticles in living organisms, in order to control the delivery of nanotools into living targeted cells. Thanks to their well-known biocompatibility and their large use as contrast agent in transmission electron microscopy, Au NPs are excellent candidate to understand the routes followed by nanomaterials to enter the cells (Chithrani et al., 2010; Kim et al., 2009). For these reasons, we investigated the dynamics and kinetics of events occurring at the bio/non-bio interface, from the early NP/cell membrane interactions to the intracellular trafficking and the final extracellular clearance. To this aim, we analyzed the positively charged AuNP-N<sub>3</sub>, and the AuNP-myc-siRNA and performed a time course analysis to track step by step their cell internalization. By optical microscopy polyps treated with these AuNP-N<sub>3</sub> showed a punctuated staining throughout the animal body (Marchesano et al., 2013), confirmed also by tissue cryosections and by analysis of isolated cells. Tissue sectioning showed internalized AuNPs both within the ectoderm and few endodermal cells, confirming previous evidence on dynamic processes occurring between the two cell epithelia, causing displacement or migration of labeled cells or free NPs from ectoderm to the endoderm (Tortiglione et al., 2009). Indeed, optical microscopy observations showed that covalent and ionic AuNP-myc-siRNA were internalized at low rate by *Hydra* ectodermal cells compared to positively charged AuNP-N<sub>3</sub>.

To investigate the events that characterized the NPs uptake and fate, we performed a transmission electron microscopy study following two different methodologies: standard TEM and High pressure cryo TEM, which avoids ice crystal formation and potential fixative artifact, enabling ultrastructure description as close as possible to the living state (Holstein et al., 2010).

Transmission electron microscopy analysis was performed to understand the subcellular distribution of AuNP-myc-siRNA. TEM observations showed that in the treated animals the AuNPs bound the glycocalyx after few minutes while later, after 24 hours of incubation, NPs localised in the cytoplasm, clustered or monodispersed, demonstrating their capability to cross cell membrane and deliver siRNA into the cytoplasm. On the other hand, standard TEM analysis of AuNP-N<sub>3</sub>, showed that NPs bound to the glycocalyx after 5 min of incubation. The strong interaction between the positive azide group of the AuNP and the negative cuticle components caused in 30 minutes the massive accumulation of nanoparticles all around the animal tissue. Interesting, large vacuoles containing NP were often found in the apical part of the



ectodermal cells, whose probable origin from membrane invagination and fusion is indicated by the presence of the glycocalix in the inner side of the limiting membrane. These data are supported by previous study from Brust et al., 2011. In this work Hela cells were incubated with TAT modified AuNPs and ultrastructure analysis showed NPs to freely negotiate intracellular barriers, moving from vesicles to cytoplasm in either ways by direct membrane translocation. Noteworthy, datum was found at 24h time point analysis, where AuN-N<sub>3</sub> were found packed into micrometer sized granular structure, mixed to glycocalix/subcellular debris components. These structures are responsible for the punctuated pattern observed by optical microscopy and are very similar to granules obtained after the interaction of QRs with *Hydra vulgaris* (Tortiglione et al., 2009), suggesting that the mechanism of internalization is the same and that the positive charge of Au azide and QRs determine the high efficiency of uptake by *Hydra* ectodermal cells.

To better understand the mechanisms that govern the uptake of AuNP, the nanoparticles with a positive charge (AuNP-N<sub>3</sub>) were chosen and supplied to Hydra at a concentration of 25 nM, lower than the former, in order to avoid massive NP accumulation on the cell glycocalix. Moreover, thin section were analysed by a different technique of electron microscopy, which provides, through a cold sealing, an extremely fast fixation: High-Pressure cryo TEM (Serp et al., 2002). High pressure time course analysis (from 4h to 48h) showed that NPs cross cell membrane within vesicles-like structure after 4-8h; later on the AuNP-N<sub>3</sub> reach the cytoplasm and finally after 24-48h time points, NPs were found in lysosomal compartment, as single units or cluster, suggesting that the lysosomal compartmentalization is the main intracellular fate of Au NPs. Surprisingly, the presence of nanosized vesicles loaded with NPs outside the cell membrane at 48h post-incubation opened the possibility that beside their role as carriers of AuNP from the external medium inside the cell, they could also represent endosome recycled material brought back to the cell membrane.

This results might support what occurs in mammals, where the fusion of multivesicular bodies with the cell membrane, may induce the release of exosomes in the extracellular space (Keller et al., 2006). However from the deep analysis of all images taken by HPF, we could not find any MVB containing AuNP, thus at moment this remain an hypothesis and the nature of these nanosized vesicles able to load AuNP and shuttle them into the cells remain to be elucidated.

“Pulse and chase” experiment confirmed that the exocytosis take place within 48 h post incubation mainly through two mechanisms: by shedding of vesicles densely packed with AuNPs or mediated by multiple vesicle release through larger membrane areas.

Our data are perfectly in agreement with a previous study (Krpetić et al., 2011), where it has been demonstrated that TAT modified gold nanoparticles after internalization in Hela cells can rapidly escape from the endocytic system and be distributed in other cell compartments by direct translocation across the intracellular membranes, before membrane rupture as showed in figure 2.

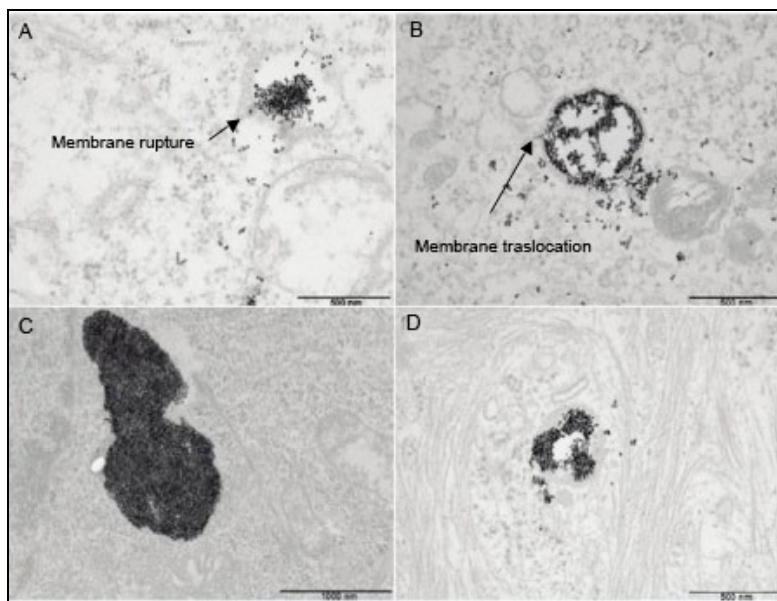


**Figure 2. TEM images of HeLa cells incubated for different times with TAT-modified gold nanoparticles:** TEM images showed that particles are found after 10-24 h in a dense vesicles, releasing particles by membrane rupture (A) and by direct membrane translocation (B), and massively packed vesicles found after 24 h (C) and after 48 h (D).

Comparing the TEM images of this previous work with ours (chapter 3, par 3.2.5) we observed the same patterns, suggesting the presence of a conserved mechanism exploited by eukariotic cells to sort out foreign materials, by accumulating them in vacuoles. In *Hydra* they may represent storage/garbage vacuoles, possibly due to the saturation of the lysosome machinery unable to sort out high NP concentration.

To summarize, in Figure 3 we report a schematic representation of inwards and outwards trafficking routes of AuNPs observed in our study. Briefly, NPs internalization in *Hydra* can occur through different mechanisms: direct membrane translocation, loading on nanovesicles, endocytosis (macropynocytosis) of large membrane invaginations. These processes occur within 30 min-24h, when the NP are localized into a vesicle/vacuole in the cytoplasm. From 24h to 48 h were found in different cell compartment, such as late endosome/phagosome or lysosome. After 48 h of incubation NP were localized into lysosomes, but also secreted chiefly by secretory vesicles, exosomes-like structures (Keller et al., 2006) or sorted by direct membrane exocytosis.

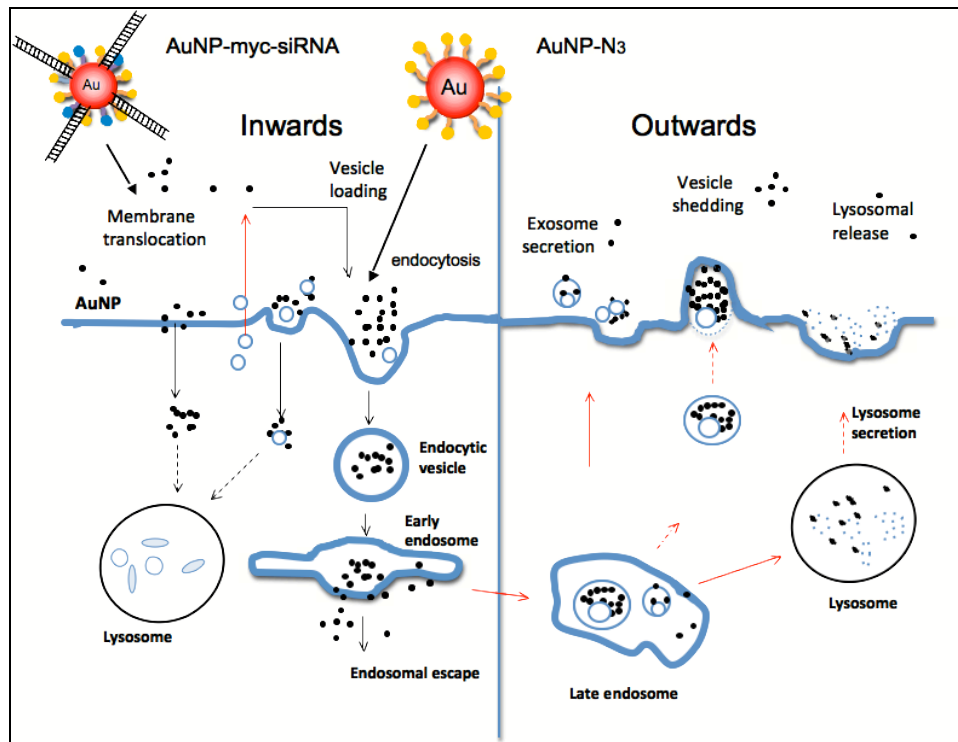


**Figure 3. Schematic representation summarising inwards and outwards trafficking routes of AuNPs.** Following AuNP exposure to *Hydra*, several inwards routes may be exploited by ectodermal cells, leading to AuNP internalization, illustrated on the left panel: i) direct membrane translocation ii) loading on nanovesicles iii) endocytosis (macropynocytosis) through large membrane invaginations. These processes occur within 30min-24h, when a massive recruitment of particles from different cytoplasmic districts into vesicle/vacuole structures is observed. From 24h to 48h a dynamic exchange of particles between different cell compartments (late endosome/phagosome -lysosome) takes place and AuNPs appear also moving out vesicle membranes. After 48h of incubation AuNPs are found at a great extent into lysosomes, but also on exosome-like vesicles. We suggest that following endosomal recruitment several outward routes may take place, i) through exosomes (possibly derived by late endosomes) ii) direct membrane exocytosis of NP-loaded vesicles iii) fusion of lysosomes with cell membrane. In the scheme the black and red arrows indicate the inward and outward routes, respectively, the dotted arrows indicate possible intracellular trafficking.

## 5 Conclusion

In conclusion, the work presented here shows the development of new methods of siRNA mediated RNAi. The approach that took advantage of the use of functionalized gold nanoparticles resulted to be much more efficient than the other based on free siRNA administration. siRNA functionalized AuNPs lead to a 80% *Hymec1* downregulation, allowing to better dissect the functional role played by this gene in *Hydra vulgaris*. *Myc* has been highlighted as a gene deeply involved in the processes controlling the homeostasis of stem cells, regulating thus the balance between self-renewal and differentiation. The elucidation of its role in *Hydra*, could provide new insights in the definition of *myc* role in physiological and pathological condition of higher vertebrates.

The great impact of this work relies on the potential translation of the new nanodevice to preclinical models. The screening of the AuNP-siRNA through cell culture and *Hydra* led to select a *myc* siRNA-AuNP conjugate that is currently used to rescue the lung tumor of a mouse lung xenograft.

This nanodevice, able to induce RNAi in three biological systems, represents an excellent platform on which therapeutic strategies could be modeled. Of course by changing the specificity of siRNA it would be possible to target different genes for treatment of different pathologic conditions. Beside the new RNAi methodologies, this PhD project led also to the fine dissection and characterization of the mechanism of internalization, trafficking and exocytosis of AuNPs in *Hydra*. These data, along with the molecular evidences confirming *myc* silencing, suggest that the siRNA-AuNPs, once uptaken, are able to reach the cytoplasm, elicit their function, and then reach the lysosomes for degradation and final excretion outside the cells.

The results obtained by this PhD work wants to stress the importance of using simple model systems as valuable tool for applied and basic research: while the *Hydra* high reproductive rate and fast life cycle allow analysis of statistically relevant specimens for each experimental condition, the conservation in this species of key regulatory cell and developmental pathways, make our results of general value for higher organisms.

The results obtained by this PhD thesis contributed to the realization of three scientific papers, published on high impact specialized journal, in 2012 and 2013.

## 6 Bibliography

- Akhtar, S., & Benter, I. F. (2007). Nonviral delivery of synthetic siRNAs in vivo. *Journal of Clinical Investigation*, 117(12), 3623–3632. doi:10.1172/JCI33494.following
- Ambrosone, A., Marchesano, V., Tino, A., Hobmayer, B., & Tortiglione, C. (2012). Hymyc1 downregulation promotes stem cell proliferation in *Hydra vulgaris*. *PLoS ONE*, 7(1), e30660. doi:10.1371/journal.pone.0030660
- Ambrosone, A., Mattera, L., Marchesano, V., Quarta, A., Susa, A. S., Tino, A., Rogach, A. L., et al. (2012). Mechanisms underlying toxicity induced by CdTe quantum dots determined in an invertebrate model organism. *Biomaterials*, 33(7), 1991–2000. doi:10.1016/j.biomaterials.2011.11.041
- Bode, H. R. (2003). Head regeneration in *Hydra*. *Developmental dynamics an official publication of the American Association of Anatomists*, 226(2), 225–236.
- Bosch, T. C., & David, C. N. (1984). Growth regulation in *Hydra*: relationship between epithelial cell cycle length and growth rate. *Developmental Biology*, 104(1), 161–171.
- Bode, H.R., The interstitial cell lineage of hydra: a stem cell system that arose early in evolution. *J Cell Sci*, 1996. 109 ( Pt 6): p. 1155-64
- Bosch, T. C. G. (2007). Why polyps regenerate and we don't: towards a cellular and molecular framework for *Hydra* regeneration. *Developmental Biology*, 303(2), 421–33. doi:10.1016/j.ydbio.2006.12.012
- Bridge, A. J., Pebernard, S., Ducraux, A., Nicoulaz, A.-L., & Iggo, R. (2003). Induction of an interferon response by RNAi vectors in mammalian cells. *Nature Genetics*, 34(3), 263–264.
- Böttger, A., Alexandrova, O., Cikala, M., Schade, M., Herold, M., & David, C. N. (2002). GFP expression in *Hydra*: lessons from the particle gun. *Development Genes and Evolution*, 212(6), 302–305.
- Conde, J., Ambrosone, A., Sanz, V., Hernandez, Y., Marchesano, V., Tian, F. R., Child, H., et al. (2012). Design of Multifunctional Gold Nanoparticles for In Vitro and In Vivo Gene Silencing. *Acs Nano*, 6(9), 8316–8324.
- David, C. N., & Plotnick, I. (1980). Distribution of interstitial stem cells in *Hydra*. *Developmental Biology*, 76(1), 175–184.
- Davis, M. E., Zuckerman, J. E., Choi, C. H. J., Seligson, D., Tolcher, A., Alabi, C. a, Yen, Y., et al. (2010a). Evidence of RNAi in humans from systemically administered siRNA via targeted nanoparticles. *Nature*, 464(7291), 1067–70. doi:10.1038/nature08956
- Davis, M. E., Zuckerman, J. E., Choi, C. H. J., Seligson, D., Tolcher, A., Alabi, C. A., Yen, Y., et al. (2010b). Evidence of RNAi in humans from systemically administered siRNA via targeted nanoparticles. *Nature*, 464(7291), 1067–70. doi:10.1038/nature08956
- Demeterco, C., Itkin-Ansari, P., Tyrberg, B., Ford, L. P., Jarvis, R. A., & Levine, F. (2002). c-Myc controls proliferation versus differentiation in human pancreatic endocrine cells. *The Journal of Clinical Endocrinology & Metabolism*, 87(7), 3475–3485.
- Galliot, B., Miljkovic-Licina, M., De Rosa, R., & Chera, S. (2006). *Hydra*, a niche for cell and developmental plasticity. *Seminars in cell developmental biology*, 17(4), 492–502.
- Giljohann, D. A., Seferos, D. S., Daniel, W. L., Massich, M. D., Patel, P. C., & Mirkin, C. A. (2010). Gold nanoparticles for biology and medicine. *Angewandte Chemie International Edition*, 49(19), 3280–3294.
- Grens, A., Gee, L., Fisher, D. A., & Bode, H. R. (1996). CnNK-2, an NK-2 homeobox gene, has a role in patterning the basal end of the axis in *hydra*. *Developmental Biology*, 180(2), 473–488.

- Hamlin, B. J., Rong, J., & Tan, M.-W. (2003). Systematic dissection of *Caenorhabditis elegans* innate immunity using RNAi. *International Worm Meeting*.
- Harborth, J., Elbashir, S. M., Bechert, K., Tuschl, T., & Weber, K. (2001). Identification of essential genes in cultured mammalian cells using small interfering RNAs. *Journal of Cell Science*, 114(Pt 24), 4557–4565.
- Hartl, M., Mitterstiller, A.-M., Valovka, T., Breuker, K., Hobmayer, B., & Bister, K. (2010). Stem cell-specific activation of an ancestral myc protooncogene with conserved basic functions in the early metazoan Hydra. *Proceedings of the National Academy of Sciences of the United States of America*, 107(9), 4051–4056. doi:10.1073/pnas.0911060107
- Hobmayer, B., Jenewein, M., Eder, D., Eder, M.-K., Glasauer, S., Gufler, S., Hartl, M., et al. (2012). Stemness in Hydra - a current perspective. *The International journal of developmental biology*, 56(June), 509–517. doi:10.1387/ijdb.113426bh
- Hobmayer, E., Holstein, T. W., & David, C. N. (1990). Tentacle morphogenesis in hydra II . Formation of a complex between a sensory nerve cell and a battery cell. *Development*, 109(4), 897–904.
- Holstein, T W, & David, C. N. (1990). Cell cycle length, cell size, and proliferation rate in hydra stem cells. *Developmental Biology*, 142(2), 392–400.
- Holstein, T W, Hobmayer, E., & David, C. N. (1991). Pattern of epithelial cell cycling in hydra. *Developmental Biology*, 148(2), 602–611.
- Holstein, Thomas W, Hess, M. W., & Salvenmoser, W. (2010). Preparation techniques for transmission electron microscopy of Hydra. *Methods In Cell Biology*, 96(10), 285–306.
- Huang, J., Bu, L., Xie, J., Chen, K., Cheng, Z., Li, X., & Chen, X. (2010). Effects of nanoparticle size on cellular uptake and liver MRI with polyvinylpyrrolidone-coated iron oxide nanoparticles. *ACS nano*, 4(12), 7151–7160.
- Jacob, J., Vanholme, B., Haegeman, A., & Gheysen, G. (2007). Four transthyretin-like genes of the migratory plant-parasitic nematode *Radopholus similis*: members of an extensive nematode-specific family. *Gene*, 402(1-2), 9–19.
- Jansen, B., & Zangemeister-Wittke, U. (2002). Antisense therapy for cancer—the time of truth. *The lancet oncology*, 3(11), 672–683.
- Johnson, A. B., Lewis, A. J., & Et Al. (2002). An Overview of Gene Control. *Molecular Biology of the Cell*. Garland Science.
- Keller, S., Sanderson, M. P., Stoeck, A., & Altevogt, P. (2006). Exosomes: from biogenesis and secretion to biological function. *Immunology Letters*, 107(2), 102–108.
- Kim, D. H., & Rossi, J. J. (2007). Strategies for silencing human disease using RNA interference. *Nature Reviews Genetics*, 8(3), 173–184.
- Kim, D. H., & Rossi, J. J. (2009). Overview of gene silencing by RNA interference. *Current protocols in nucleic acid chemistry edited by Serge L Beaucage et al, Chapter 16*(March), Unit 16.1.
- Kim, S.-S., Garg, H., Joshi, A., & Manjunath, N. (2009). Strategies for targeted nonviral delivery of siRNAs in vivo. *Trends in Molecular Medicine*, 15(11), 491–500. doi:10.1016/j.molmed.2009.09.001
- Krpetić, Z., Saleemi, S., Prior, I. A., Sée, V., Qureshi, R., & Brust, M. (2011). Negotiation of intracellular membrane barriers by TAT-modified gold nanoparticles. *ACS nano*, 5(6), 5195–5201.
- Laurenti, E., Wilson, A., & Trumpp, A. (2009). Myc's other life: stem cells and beyond. *Current Opinion in Cell Biology*, 21(6), 844–854.
- Liao, D. J., & Dickson, R. B. (2000). c-Myc in breast cancer. *Endocrinorelated cancer*, 7(3), 143–164.

- Lohmann, J. U., Endl, I., & Bosch, T. C. (1999). Silencing of developmental genes in Hydra. *Developmental Biology*, 214(1), 211–214.
- Loomis, W.F., and Lenhoff, H. M., Growth and sexual differentiation of Hydra in mass culture. . J. Exp. Zool., 1956. 132: p. 555-574
- Lytton-Jean, A. K. R., Langer, R., & Anderson, D. G. (2011). Five years of siRNA delivery: spotlight on gold nanoparticles. *Small Weinheim an der Bergstrasse Germany*, 7(14), 1932–1937. doi:10.1002/sml.201100761
- Malvindi, M. A., Carbone, L., Quarta, A., Tino, A., Manna, L., Pellegrino, T., & Tortiglione, C. (2008). Rod-shaped nanocrystals elicit neuronal activity in vivo. *Small Weinheim an der Bergstrasse Germany*, 4(10), 1747–1755.
- Miljkovic, M., Mazet, F., & Galliot, B. (2002). Cnidarian and bilaterian promoters can direct GFP expression in transfected hydra. *Developmental Biology*, 246(2), 377–390.
- Montgomery, M. K., Xu, S., & Fire, A. (1998). RNA as a target of double-stranded RNA-mediated genetic interference in *Caenorhabditis elegans*. *Proceedings of the National Academy of Sciences of the United States of America*, 95(26), 15502–15507.
- Morris, K. V., & Rossi, J. J. (2006). Lentiviral-mediated delivery of siRNAs for antiviral therapy. *Gene Therapy*, 13(6), 553–558.
- Naito, Y., Yoshimura, J., Morishita, S., & Ui-Tei, K. (2009). siDirect 2.0: updated software for designing functional siRNA with reduced seed-dependent off-target effect. *BMC bioinformatics*, 10, 392. doi:10.1186/1471-2105-10-392
- Nam, N.-H., & Parang, K. (2003). Current targets for anticancer drug discovery. *Current Drug Targets*, 4(2), 159–179.
- Pascoe D, Karntanut W, Muller CT. Do pharmaceuticals affect freshwater invertebrates. A study with the cnidarian *Hydra vulgaris*. *Chemosphere* 2003; 51(6):521e8.
- Pecot, C. V., Calin, G. A., Coleman, R. L., Lopez-Berestein, G., & Sood, A. K. (2011). RNA interference in the clinic: challenges and future directions. *Nature Reviews Cancer*, 11(1), 59–67.
- C. A. Pollino and D. A. Holdway, "Potential of two hydra species as standard toxicity test animals," *Ecotoxicology and Environmental Safety*, vol. 43, no. 3, pp. 309–316, 1999
- Qian, S., Zhong, X., Yu, L., Ding, B., De Haan, P., & Boris-Lawrie, K. (2009). HIV-1 Tat RNA silencing suppressor activity is conserved across kingdoms and counteracts translational repression of HIV-1. *Proceedings of the National Academy of Sciences of the United States of America*, 106(2), 605–610.
- Reynolds, A., Anderson, E. M., Vermeulen, A., Fedorov, Y., Robinson, K., Leake, D., Karpilow, J., et al. (2006). Induction of the interferon response by siRNA is cell type– and duplex length–dependent. *Rna New York Ny*, 12(6), 988–993.
- Rivera-Gil, P., Jimenez De Aberasturi, D., Wulf, V., Pelaz, B., Del Pino, P., Zhao, Y., De La Fuente, J. M., et al. (2012). The Challenge To Relate the Physicochemical Properties of Colloidal Nanoparticles to Their Cytotoxicity. *Accounts of Chemical Research*, XXX(Xx). doi:10.1021/ar300039j
- Schlee, M., Hornung, V., & Hartmann, G. (2006). siRNA and isRNA: two edges of one sword. *Molecular therapy the journal of the American Society of Gene Therapy*, 14(4), 463–470. doi:10.1016/j.ymthe.2006.06.001
- Serp, D., Mueller, M., Von Stockar, U., & Marison, I. W. (2002). Low-temperature electron microscopy for the study of polysaccharide ultrastructures in hydrogels. I. Theoretical and technical considerations. *Biotechnology and Bioengineering*, 79(3), 243–52. doi:10.1002/bit.10286



- Stanić, V., Janačković, D., Dimitrijević, S., Tanasković, S. B., Mitrić, M., Pavlović, M. S., Krstić, A., et al. (2011). Synthesis of antimicrobial monophasic silver-doped hydroxyapatite nanopowders for bone tissue engineering. *Applied Surface Science*, 257(9), 4510–4518. doi:10.1016/j.apsusc.2010.12.113
- Timmons, L., Tabara, H., Mello, C. C., & Fire, A. Z. (2003). Inducible Systemic RNA Silencing in *Caenorhabditis elegans*. (M. Wickens, Ed.) *Molecular Biology of the Cell*, 14(7), 2972–2983.
- Tino, A., Ambrosone, A., Mattera, L., Marchesano, V., Susa, A., Rogach, A., & Tortiglione, C. (2011). A new in vivo model system to assess the toxicity of semiconductor nanocrystals. *International journal of biomaterials*, 2011, 792854. doi:10.1155/2011/792854
- Tortiglione, C., Quarta, A., Malvindi, M. A., Tino, A., & Pellegrino, T. (2009). Fluorescent nanocrystals reveal regulated portals of entry into and between the cells of *Hydra*. *PloS one*, 4(11), e7698. doi:10.1371/journal.pone.0007698
- Tortiglione C. An ancient model organism to test in vivo novel functional nanocrystals. In: Fazel-Rezaei R, editor. Biomedical Engineering: from theory to application. InTech - Open Access Publisher; 2011. p. 225e52.
- Tortiglione, C., Quarta, A., Tino, A., Manna, L., Cingolani, R., & Pellegrino, T. (2007). Synthesis and biological assay of GSH functionalized fluorescent quantum dots for staining *Hydra vulgaris*. *Bioconjugate Chemistry*, 18(3), 829–835.
- Turkevich, J., Stevenson, P. C., & Hillier, J. (1951). A study of the nucleation and growth processes in the synthesis of colloidal gold. *Discussions Of The Faraday Society*, 11(c), 55. doi:10.1039/df9511100055
- Vita, M., & Henriksson, M. (2006). The Myc oncoprotein as a therapeutic target for human cancer. *Seminars in Cancer Biology*, 16(4), 318–330.
- Wilson, A., Laurenti, E., Oser, G., Van Der Wath, R. C., Blanco-Bose, W., Jaworski, M., Offner, S., et al. (2008). Hematopoietic stem cells reversibly switch from dormancy to self-renewal during homeostasis and repair. *Cell*, 135(6), 1118–1129.
- Wittlieb, J., Khalturin, K., Lohmann, J. U., Anton-Erxleben, F., & Bosch, T. C. G. (2006). Transgenic *Hydra* allow in vivo tracking of individual stem cells during morphogenesis. *Proceedings of the National Academy of Sciences of the United States of America*, 103(16), 6208–6211.
- Yildirim, L., Thanh, N. T. K., Loizidou, M., & Seifalian, A. M. (2011). Toxicology and clinical potential of nanoparticles. *Nano Today*, 6(6), 585–607. doi:10.1016/j.nantod.2011.10.001

## SCIENTIFIC PUBLICATIONS

**Marchesano V**, Hernandez Y, Salvenmoser W, Ambrosone A, Tino A, Hobmayer Bert, De la Fuente JM. and Tortiglione C.

***Imaging inwards and outwards trafficking of gold nanoparticles in whole animals***

ACS Nano. 2013 Mar 12

CondeJ, Ambrosone A, Sanz V, Hernandez Y, **Marchesano V**, Tian F, Child H, Berry CC, Ibarra MR, Baptista PV, Tortiglione C, de la Fuente JM.

***Design of Multifunctional Gold Nanoparticles for In Vitro and In Vivo Gene Silencing.***

ACS Nano 2012, 6 (9), 8316–8324.

Ambrosone A, **Marchesano V**, Tino A, Hobmayer B, Tortiglione C.

***Hymc1 Downregulation Promotes stem Cell Proliferation in Hydra vulgaris.***

Plos one 2012, (1): e30660

Ambrosone A, Mattera L, **Marchesano V**, Quarta A, Susha AS, Tino A, Rogach AL, Tortiglione C.

***Mechanisms underlying toxicity induced by CdTe quantum dots determined in an invertebrate model organism.*** Biomaterials. 2012 Mar;33(7):1991-2000.

Tino A, Ambrosone A, Mattera L, **Marchesano V**, Susha A, Rogach A, Tortiglione C. (2011)

***A new in vivo model system to assess the toxicity of semiconductor nanocrystals.***

International Journal of Biomaterials. Vol 2011, Article ID 792854, 8 pages, doi:10.1155/2011/792854

Ambrosone A, **Marchesano V**, Mattera L, Tino A, Tortiglione C (2011)

***"Bridging the fields of nanoscience and toxicology: nanoparticle impact on biological models"***

Proc. SPIE 7909, 79090B (2011); doi:10.1117/12.874494

## CONFERENCE PROCEEDINGS AND COMMUNICATIONS

V.Sanz, J.Conde, A.Ambrosone, Y.Hernández, **V.Marchesano**, G. Estrada, M.R. Ibarra, P. Baptista, F.Tian, C.Tortiglione and J.M. de la Fuente.

***Multifunctional Gold Nanoparticles for Gene Silencing.***

243<sup>rd</sup> ACS National Meeting & Exposition. March 25- 29 2012, San Diego, California

V.Sanz, J.Conde, A.Ambrosone, Y.Hernández, **V.Marchesano**, G. Estrada, M.R. Ibarra, P. Baptista, F.Tian, C.Tortiglione and J.M. de la Fuente.

***Multifunctional Gold Nanoparticles functionalized with cell penetrating peptides and siRNA for Gene Silencing.***

13th Naples workshop on "Bioactive peptide" 7-10 June 2012 , Naples, Italy, p. 22

Y. Hernández-García, J. Conde. A. Ambrosone, V. Sanz, **V. Marchesano**, F. Tian, H. Child, C. C. Berry, M. R. Ibarra, P. V. Baptista, C. Tortiglione, J. M. de la Fuente.

***Multifunctional AuNPs for gene therapy***

MRS Fall Meeting November 25-30 2012, Boston.

Ambrosone A., Mattera L., **Marchesano V.**, Tino A. and Tortiglione C.

***Cnidarian models for nanotoxicology;***

Oral communication, AISAL-ICSU meeting: Biomaterials in medicine and animal models. 22-23 September 2011. Naples

**Marchesano V**, Ambrosone A, Pellegrino T, de la Fuente J, and Tortiglione C.

***An Ancient Model Organism to Test in Vivo advanced materials for biomedical application.*** AISAL-ICSU meeting: Biomaterials in medicine and animal models. 22-23 September 2011. Naples – Italy

Ambrosone A, **Marchesano V**, Tino A. and Tortiglione C.

***Elucidating the role of Hymc1 protooncogene in Hydra by RNA interference;*** International Workshop "Searching for Eve: basal metazoans and the evolution of multicellular complexity" 12-15 September 2011, Tutzing - Germany.

Ambrosone A, **Marchesano V**, Tino A. and Tortiglione C.

***Hydra vulgaris for nanoecotoxicology: from in vivo studies to the molecular pathways.***

International Workshop "Searching for Eve: basal metazoans and the evolution of multicellular complexity", 12-15 September 2011, Tutzing - Germany.

**Marchesano V**, Ambrosone A, Mattera L, de La Fuente JM, and Tortiglione C.

***Probing membrane dynamics in Hydra at single-nanoparticle level.***

International Workshop "Searching for Eve: basal metazoans and the evolution of multicellular complexity", 12-15 September 2011, Tutzing - Germany.

Ambrosone A, Mattera L, **Marchesano V**, Tino A. and Tortiglione C.

***Interfacing nanocrystals with living organisms: uptake, biodistribution and***

***toxicological impact;*** Oral communication, Bionano conference, Spring Meetings E-MRS, 9-13 Maggio 2011- Nice (France)

**Marchesano V**, Ambrosone A, and Tortiglione C.

***Fluorescent nanotechnology tools for in vivo labelling of Nematostella vectensis***;

E-MRS 2011 SPRING MEETING. Nanobiotechnology Symposium (OP5-98), 9 · 13 May 2011. Nice - France

### **RESEARCH STAGE**

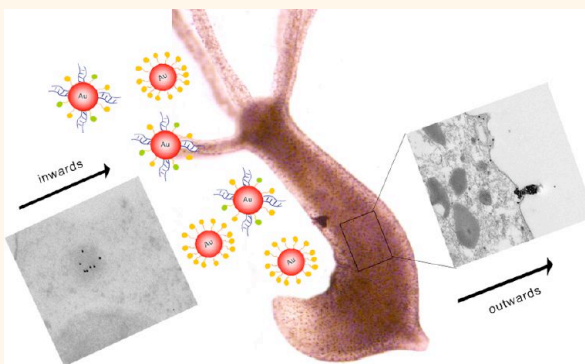
From April 2012 to May 2012 – Institute of Zoology, University of Innsbruck, Austria, Laboratory headed by Prof. Bert Hobmayer. This group is world's recognised leader in studying the mechanisms of cell differentiation in Cnidaria. Moreover, historically, it developed the know how and technical skills to analyse hydra cell morphology by Electron Microscopy. This stage was aimed to acquire expertise of 1) Hydra cell Biology, by preparing and analysing single cell suspensions 2) Electron Microscopy, by using several fixation procedures. The availability of High pressure freezing Electron Microscopy enabled to acquire new knowledge on the mechanism of internalization of gold nanoparticles in *Hydra vulgaris*.

# Imaging Inward and Outward Trafficking of Gold Nanoparticles in Whole Animals

Valentina Marchesano,<sup>†</sup> Yulan Hernandez,<sup>‡</sup> Willi Salvenmoser,<sup>§</sup> Alfredo Ambrosone,<sup>†</sup> Angela Tino,<sup>†</sup> Bert Hobmayer,<sup>§</sup> Jesus M de la Fuente,<sup>‡</sup> and Claudia Tortiglione<sup>†,\*</sup>

<sup>†</sup>Istituto di Cibernetica "E.Caianiello", Consiglio Nazionale delle Ricerche, Via Campi Flegrei, 34, 80078, Pozzuoli, Italy, <sup>‡</sup>Instituto de Nanociencia de Aragon, University of Zaragoza, C/Mariano Esquillor s/n, Zaragoza, Spain, and <sup>§</sup>Institute of Zoology, University of Innsbruck, A-6020 Innsbruck, Austria

**ABSTRACT** Gold nanoparticles have emerged as novel safe and biocompatible tools for manifold applications, including biological imaging, clinical diagnostics, and therapeutics. The understanding of the mechanisms governing their interaction with living systems may help the design and development of new platforms for nanomedicine. Here we characterized the dynamics and kinetics of the events underlying the interaction of gold nanoparticles with a living organism, from the first interaction nanoparticle/cell membrane, to the intracellular trafficking and final extracellular clearance. By treating a simple water invertebrate (the cnidarian *Hydra* polyp) with functionalized gold nanoparticles, multiple inward and outward routes were imaged by ultrastructural analyses, including exosomes as novel undescribed carriers to shuttle the nanoparticles in and out the cells. From the time course imaging a highly dynamic picture emerged in which nanoparticles are rapidly internalized (from 30 min onward), recruited into vacuoles/endosome (24 h onward), which then fuse, compact and sort out the internalized material either to storage vacuoles or to late-endosome/lysosomes, determining almost complete clearance within 48 h from challenging. Beside classical routes, new portals of entry/exit were captured, including exosome-like structures as novel undescribed nanoparticle shuttles. The conservation of the endocytic/secretory machinery through evolution extends the value of our finding to mammalian systems providing dynamics and kinetics clues to take into account when designing nanomaterials to interface with biological entities.



**KEYWORDS:** gold nanoparticles · cell uptake · intracellular trafficking · exocytosis · transmission electron microscopy · model organism

The plasma membrane is a dynamic structure that functions to separate the cytoplasm from the extracellular environment by regulating and coordinating the entry and exit of small and large molecules. Small molecules, such as amino acids, sugars, and ions, can traverse the plasma membrane through the action of integral membrane protein pumps or channels. Macromolecules must be carried into the cell in membrane-bound vesicles derived by the invagination and pinching-off of pieces of the plasma membrane in a process termed endocytosis. The endocytic pathways (phagocytosis, (macro)pynocytosis) differ with regards to the size of the endocytic vesicle and the chemistry of the cargo triggering either membrane proteins (hormone

mediated-signal transduction, cell–cell communication, immune surveillance, cell motility)<sup>1</sup> or cytosolic compartments. Within the endosome the cargos are sorted to distinct destinations, being either recycled back to the plasma membrane or sorted into intraluminal vesicles for lysosomal destruction *via* multivesicular bodies.<sup>2</sup> The macromolecular nature of the material transported by endocytosis makes this route one of the most important targets for nanomedicine.<sup>3–5</sup> Indeed, many nanoparticle formulations are customized to bypass cell membranes and deliver the cargo within the cell.<sup>6–8</sup> However, not much is known about the intracellular trafficking and fate of nanomaterials following cargo delivery,<sup>9,10</sup> and only a few studies report on their whole

\* Address correspondence to c.tortiglione@cib.na.cnr.it.

Received for review December 13, 2012 and accepted March 1, 2013.

Published online 10.1021/nn305747e

© XXXX American Chemical Society

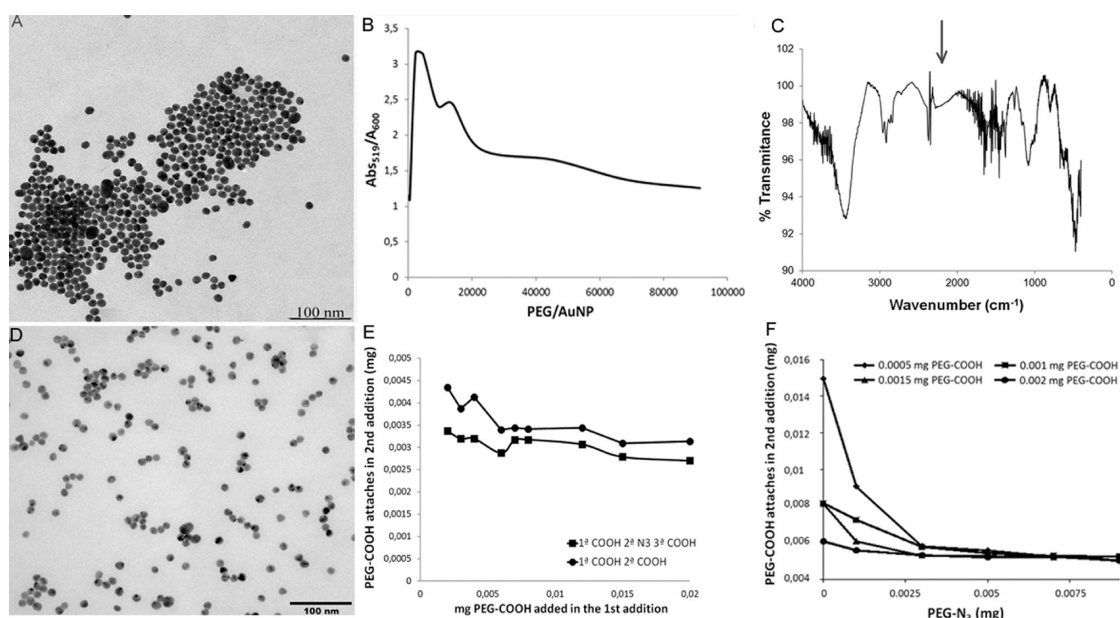


**Figure 1.** Characterization of AuNPs. The high monodispersity of the gold core of AuNP-N<sub>3</sub> (A) and AuNP-siRNA (D) was confirmed by transmission electron microscopy (TEM, T20 200KeV; FEI) showing an average size of 14 nm. (B) Analysis of the stability of AuNP-N<sub>3</sub>: the ratio A519 (contribution of stable AuNPs)/A600 (contribution of aggregated AuNPs) was measured by UV-vis. (C) Infrared spectra (FTIR, JASCO FT/IR 4100) confirmed the presence of the azide groups covering the gold cores, showing a characteristic peak at 2100 cm<sup>-1</sup>. Quantification by Ellman's method of the PEG-COOH chains attached in a second addition after (E) increasing amount of PEG-COOH with (circles) and without (squares) PEG-N<sub>3</sub>, (F) increasing amount of PEG-N<sub>3</sub> at constant PEG-COOH added. Data were collected from a single experiment. Whole characterization of AuNP-siRNA is reported elsewhere.<sup>25</sup>

journey into the cell up to external clearance. Gold nanoparticles (AuNPs) hold great interest in this field thanks to properties such as monodispersity, stability, minimal toxicity, excellent contrasting agent properties for transmission electron microscopy (TEM) analysis, which enable to track with unprecedented resolution dynamic of uptake, intracellular sorting, and potential secretion.<sup>11–13</sup> Recent results gathered on the interaction of AuNP with different synthetic lipid membranes<sup>14</sup> or cell lines demonstrated that properties such size, charge, chemical functionalities, but also the arrangement of organic ligands on nanoparticle surface, dictate the internalization route.<sup>15,16</sup> Moreover, surface functionalization may influence the fate of AuNP upon cell uptake: HUVEC cells treated with AuNP coated by different peptides display distinct exocytosis profiles.<sup>9</sup> Here we investigated the inward and outward trafficking of AuNPs at whole animal level using the small invertebrate *Hydra vulgaris* (Cnidaria, Hydrozoa), a recently emerged amenable system to study nanoparticle–cell interactions.<sup>17,18</sup> Shaped like a simple hollow cylinder with a single apical opening (mouth) surrounded by a tentacle crown and a basal foot to anchor a substrate (Figure 1A).<sup>19</sup> *Hydra* is a freshwater polyp successfully used to test diverse nanoparticles, for example, for evaluation of toxicity of CdTe quantum dots,<sup>20,21</sup> to study cell dynamics using fluorescent quantum rods,<sup>22</sup> or to analyze animal behavior in response to nanoparticle exposure.<sup>23</sup> The possibility to uniformly expose the whole animal to any

given substance by simple soaking makes it ideal to study the mechanism of nanoparticle uptake and fate. In fact, the tissue structure, organized as just two cell layers (ectoderm and endoderm) facing respectively the animal external side and the gastric cavity, enables us to finely track NPs interaction with *Hydra* cells upon pulsed or prolonged exposure at any desired time point. We have recently shown that the capability of *Hydra* cells to uptake soluble macromolecules is greatly enhanced by the positive net charge. CdSe/CdS poly(ethylene glycol) (PEG) coated quantum rods, displaying negative zeta potential as-synthesized, under the condition of charge reversal (*i.e.*, acidic pH) acquire positive charge and capability to enter *Hydra* cells at high efficiency.<sup>22</sup> Similarly, short dsRNA, if protonated at acidic pH, are uptaken at a high rate into the cytosol and are able to initiate an RNAi response,<sup>24</sup> showing the pivotal role played by the positive charge in enhancing cell permeability to several structures, chemically unrelated. Our group has recently shown that multifunctional gold nanoparticles, stabilized by PEG and conjugated to several bioactive molecules (siRNA, TAT, charged groups) are capable of cytosol delivery of small interfering RNAs (siRNA) and induction of a specific RNAi process.<sup>25</sup> The selected siRNA targeted the proto-oncogene *c-myc*, a key gene controlling disparate aspects of cell physiology including cell growth, cell cycle progression, biosynthetic metabolism, and apoptosis and, as expected, found deregulated in the majority of human cancers. Remarkably, these multifunctional



myc-siRNA AuNPs induced specific and efficient RNAi in three different biological systems (human cell culture, *Hydra*, and mouse) thus representing a broadly valid nanotool to achieve gene silencing. In *Hydra* the downregulation of the myc gene (previously isolated by Hartl *et al.*<sup>26</sup>) mediated by myc-siRNA-AuNP induced 80% downregulation<sup>25</sup> and the same effects caused by free siRNA,<sup>24</sup> confirming the specificity of the new approach. Briefly, *Hymec1* inhibition caused increased proliferation of interstitial stem cells, suggesting a role in maintaining the balance between stem cells self-renewal and differentiation, as found in other systems. Ultrastructural analysis by TEM showed the capability of myc-siRNA nanostructures to directly penetrate *Hydra* cell membranes,<sup>25</sup> while in human cells and mouse lungs classic endocytic routes were found. Considering the broad potential of the new nanotool to enter RNAi-based clinical trials, basic knowledge of the rule governing the interaction of such smart nanoparticles with a cell membrane is of fundamental importance, together with the understanding of kinetics of the gold clearance following siRNA delivery. To get deep insights on these mechanisms, here we used an ultrastructural approach to analyze all steps of AuNP cell/interaction using the *Hydra* model. By comparing different chemical functionalities (siRNA and positively charged groups), administration dose, and incubation times we identified novel inward and outward routes, capturing for the first time at whole animal level AuNP exocytosis. The strong evolutionary conservation of the endocytic/secretory machinery in the animal kingdom makes our findings of broad value not only for nanomedicine/pharmacological aims, but also to unravel, *in vivo*, basic mechanisms and parameters regulating cell portals of entry, negotiation, and secretion.

## RESULTS AND DISCUSSION

### Synthesis and Surface Modification of Gold Nanoparticles.

Two types of AuNPs were employed in this study: surface-modified by azide group (AuNP-N<sub>3</sub>) and by siRNA targeting the c-myc gene (AuNP-siRNA). AuNPs used as starting material for both functionalizations were synthesized following the straightforward methodology reported.<sup>27</sup> The obtained AuNPs had an average size of 14 nm (Figure 1A,D). Citrate protective layer was exchanged by a hepta-ethylenglycol spacer including a thiol and an azide functional groups. Thiol moiety was used to react with Au atoms of the AuNP and to establish a strong Au–S pseudo-covalent bond. The azide group was incorporated for further functionalization of the nanoparticles by “click chemistry” reactions with alkyne moieties (data not shown). Moreover, surface modification with PEG resulted in prolonged stability of the nanoparticles in the animal growing media, minimizing unwanted aspecific protein interactions and decreased toxicity of the nanoparticles. Removal of citrate groups from the surface of the

**TABLE 1. Quantification of the PEG Chains, and siRNA Strands for AuNP-N<sub>3</sub> and AuNP-siRNA Bioconjugates, Together with the Z-Potential and Dynamic Light Scattering (DLS) Measurements**

AuNP conjugate	PEG chains/NP	siRNA strands/NP	zeta potential (mV)	DLS (nm)
AuNP-N <sub>3</sub>	~2600		+21	15.5
AuNP-siRNA	1250.5 ± 279.8	41.3 ± 0.8	−25.5 ± 1.2	138.7

nanoparticle caused changes of Z potential changes, from −38 mV to +21 mV, which could drastically modify the cellular uptake. The best conditions for obtaining stable and derivatized AuNPs were obtained by adding different AuNP/PEG-N<sub>3</sub> ratios. The most stable nanoparticles were obtained with AuNP/PEG-N<sub>3</sub> ratios between 1:2000 and 1:5000, and around 2600 PEG-N<sub>3</sub> chains/AuNP were estimated at the maximum point. The addition of higher or lower amounts of PEG-N<sub>3</sub> decreased drastically the stability of nanoparticles (Figure 1B). The presence of N<sub>3</sub> moieties on the AuNP surface was proved by FTIR analysis (Fourier transform infrared spectroscopy), showing a characteristic peak at 2100 cm<sup>−1</sup> (Figure 1C). MALDI TOF of AuNP-N<sub>3</sub> further confirmed the presence of PEG-N<sub>3</sub> (M−H<sup>+</sup> 451.1). In the case of the AuNPs-siRNA, the functionalization was made as previously described,<sup>25</sup> decreasing the total amount of PEG for further incorporation of thiolated siRNAs. To overcome the low stability of partially pegylated nanoparticles using PEG-N<sub>3</sub> chains, 50% of carboxylated PEG chains was added. Quantification of PEG-COOH and PEG-N<sub>3</sub> chains bound to AuNPs was performed as previously reported.<sup>25</sup> Briefly, PEG-COOH chains were measured directly by the determination of the excess of thiol groups on the supernatant by Ellman's method, while in the case of PEG-N<sub>3</sub> chains, an indirect methodology was designed. An accurate description of the quantification of degree of saturation for the PEG chains on AuNP is reported in ref 25, and the results shown in Figure 1E,F. The number of PEG chains on AuNP-siRNA was estimated as 1250.5 ± 279.8. The addition of siRNA also improved the stability of the AuNP due to their negative charge.<sup>28</sup> Quantification of myc siRNA strands following covalent binding to AuNPs (see Material and Methods) led to estimate 41.3 ± 0.8 siRNA strands loaded on AuNPs. The addition of siRNA on NP surface causes a zeta potential switch toward negative values like −25.5 ± 1.2 mV. In Table 1 a summary of the AuNP features is reported, while a scheme of the structure of two nanoparticles is shown in Figure 2 panels A and H.

**Influence of Surface Chemistry on NP Uptake: Biodistribution and Ultrastructural Analysis of AuNP-siRNA and AuNP-N<sub>3</sub>.** A preliminary toxicological evaluation was performed to ensure the absence of harmful effects elicited by AuNPs treatments. Living polytyps were soaked 24 h with

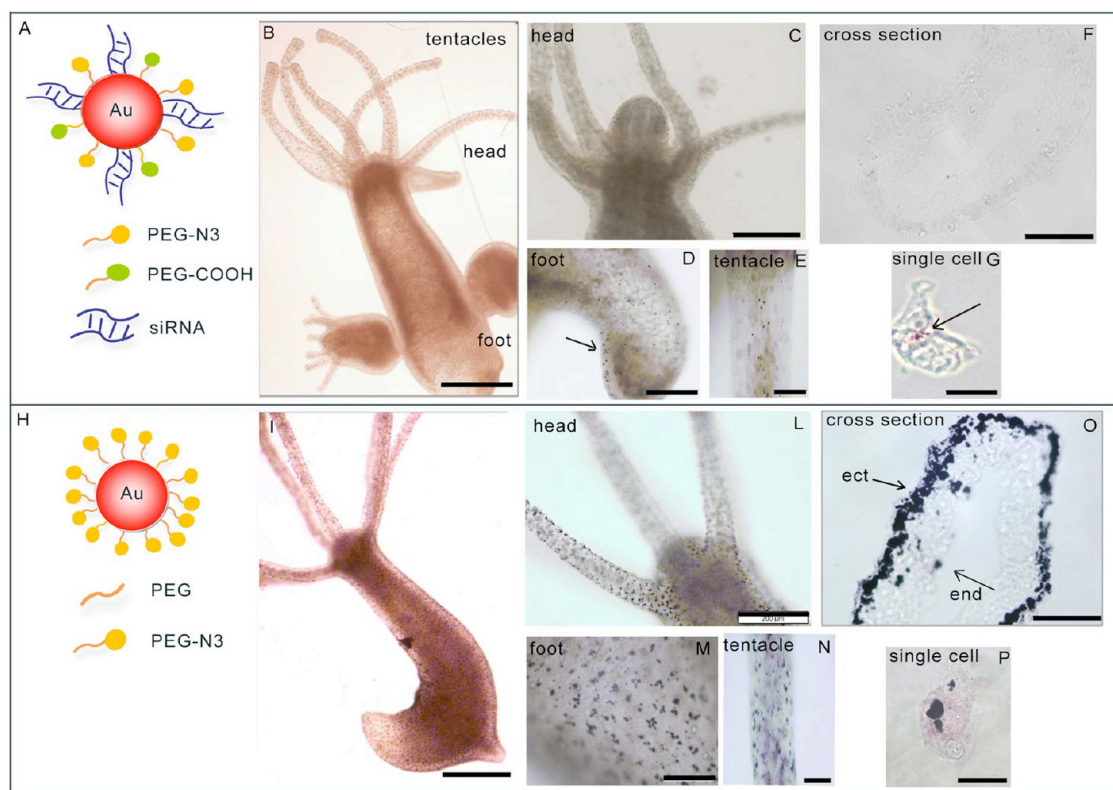


**Figure 2.** *In vivo* uptake and biodistribution of AuNPs in *Hydra*. Upper panel: interaction of *Hydra* with AuNP-siRNA. (A) Schematic illustration of the AuNP-siRNA shows the nanoparticle structure, coated by two different PEG spacers (PEG-COOH, and PEG-N<sub>3</sub>), and functionalized with siRNA molecules.<sup>25</sup> (B) Bright field image of a living *Hydra*, carrying two developing buds, treated 24 h with AuNP-siRNA. Internalized nanoparticles are hardly detectable by whole animal imaging. Zooming into (C) head, (D) foot, and (E) tentacle regions shows nanoparticles as dark granules located on ectodermal cells; (F) tissue cryosections prepared from treated animals. AuNPs are not detectable on such preparation, while (G) single cells preparations AuNPs are visible (arrowed) into the cytosol of ectodermal cells. Scale bars: (B) 500  $\mu$ m; (C,F,D) 200  $\mu$ m; (E) 100  $\mu$ m; (G) 50  $\mu$ m. Lower panel: Interaction of *Hydra* with AuNP-N<sub>3</sub>. (H) Nanoparticle scheme illustrating the homogeneous PEG-azide coating the Au core. (I) A strong punctuated dark labeling is present uniformly all over animal. The pattern is clearly evident on separate imaging of (L) head, (M) foot, and (N) tentacles of treated polyps. (O) Cryosections from labeled polyps show massive AuNP-N<sub>3</sub> accumulation into the ectoderm (ect) and the endoderm (end). (P) Fixed single cell suspension reveals AuNP-N<sub>3</sub> location into vesicle-like structures of different sizes. Scale bars: (I) 500  $\mu$ m; (L,O,M) 200  $\mu$ m; (N) 100  $\mu$ m; (P) 50  $\mu$ m.

70 nM AuNP-siRNA, a concentration previously shown to induce efficient gene silencing<sup>25</sup> and with the same amount of AuNP-N<sub>3</sub>. Polyp morphology was not affected by NP exposure, neither their reproductive capability, as shown by the growth rates of treated animals, not significantly different from control untreated animals (Supporting Information, Figure S1). The bright field images of Figure 2 show a weak punctuated labeling pattern over the body and tentacles (Figure 2D,E), confirming a low rate of internalization of AuNP-siRNA. These NPs were not detectable on cryosections prepared from treated polyps (Figure 2F) while on single cell suspensions a pink colored labeling was found on a small percentage of cells (Figure 2G). Polyp treatment with AuNP-N<sub>3</sub>, by contrast, produced a strong punctuated labeling all over the animals (head, body, and tentacles) (see Figure 2 I–N). Cryosections of treated specimens (Figure 2O) showed internalized AuNP-N<sub>3</sub> both within the ectoderm and few endodermal cells, confirming previous evidence on dynamic processes occurring between the two

cell epithelia, causing displacement or migration of labeled cells or free NPs from the ectoderm to the endoderm.<sup>22</sup> Single cell analysis confirmed the localization of these AuNPs into large cytoplasmic structures (Figure 2P). To investigate the mechanisms underlying this different internalization efficiency, polyps were incubated for increasing periods (5 min, 30 min, and 24 h) with both AuNP types before processing for TEM analysis.

**AuNP-siRNA Cell Uptake Dynamics.** While a short incubation time (5 min) was not sufficient to detect AuNP-siRNA (Figure 3A), the first clear interactions between AuNP-siRNA and the cell membrane was detected after 30 min of incubation. At this time point (Figure 3B,C) AuNP-siRNA are found very close to the cell membrane and also in the act of passing through it, indicating the capability of AuNP-siRNA to directly penetrate the plasma membrane of *Hydra* ectodermal cells. While most of the literature data report on the endocytic-endolysosomal pathway as the main route mediating the entry and fate of NP inside the cells (and often



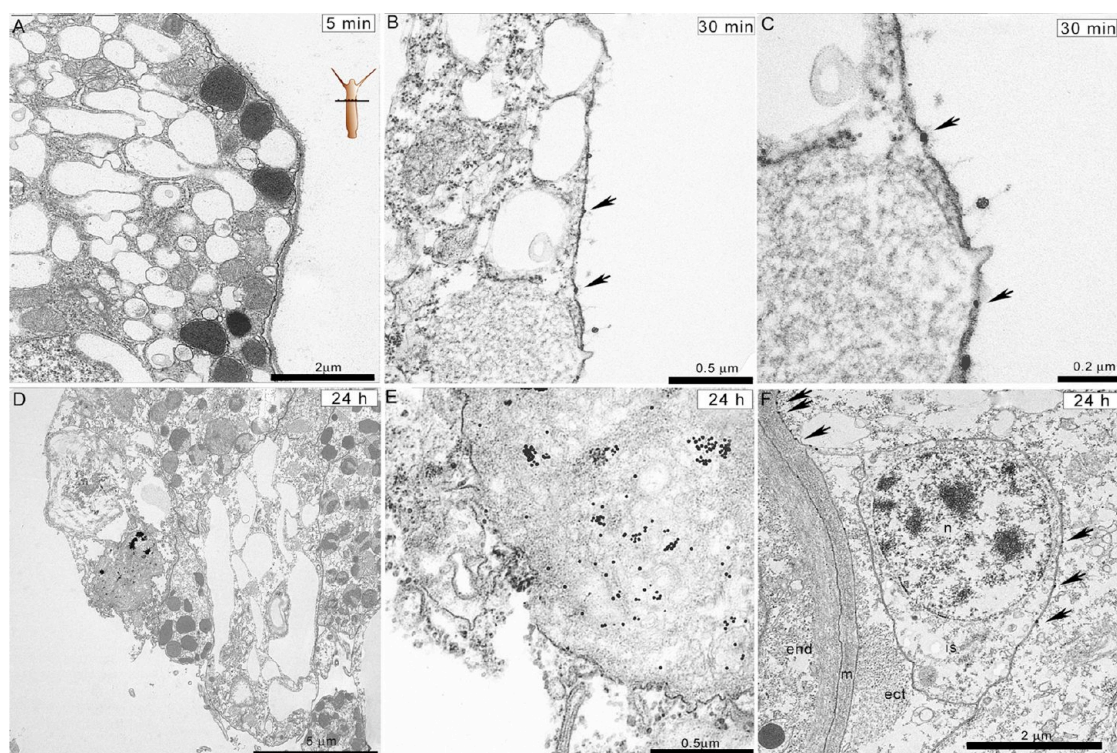


**Figure 3.** Ultrastructural analysis of AuNP-siRNA uptake. Polyps were treated with AuNP-siRNA for (A) 5 min, (B,C) 30 min, (D–F) 24 h, then carefully washed and processed for TEM. Thin sections were obtained cutting the animal at the mid gastric or subhypostomal (below the mouth) level, as shown schematically in the upper part of image A. After 5 min, the first interactions between AuNP and *Hydra* membranes are not detectable, while after 30 min, at higher magnification (B and C), single NPs or clusters of 2–3 units are detected in close proximity of the plasma membrane or within it (indicated by black arrows). In panels D and E images at increasing magnification show AuNP-siRNA located within a dense cytosol region, likely representing a lysosome. In this environment, NPs are not degraded. (F) AuNP-siRNA are detected after 24 h of incubation on the membrane of interstitial cells (is). This single stem cell is located in the interstices between ectodermal cells close to the mesoglea (m), which separates ectoderm (ect) from the endoderm (end). AuNP-siRNA are found also on the mesoglea, indicating the capability of the NP to reach several tissue districts from the original ectodermal delivery. Scale bars: (A) 2  $\mu$ m; (B) 0.5  $\mu$ m; (C) 0.2  $\mu$ m; (D) 5  $\mu$ m; (E) 0.5  $\mu$ m; (F) 2  $\mu$ m.

limiting the cytoplasmic delivery),<sup>29</sup> the direct passage of the gold nanoparticle through the cell membrane has been rarely reported, and in a few cases has been associated to the ordered surface structure.<sup>30,31</sup> TEM analysis performed after 24 h of incubation detected AuNP-siRNA within a dense cytosol region. Figure 3D,E show free nanoparticles or as clusters of a few units within a dense region of an ectodermal cell, likely representing a late endosome. Interestingly, AuNP-siRNA were also found on membranes of interstitial cells, laying in the interstices between ectodermal cells, proving the capability of NP to freely traverse cell layers, delivering their siRNA cargo far from the administration site (Figure 3F).

**AuNP-N<sub>3</sub> Cell Uptake Dynamics.** A different dynamic of internalization emerged from the TEM analysis of AuNP-N<sub>3</sub> incubated over the same periods with *Hydra* polyps (Figure 4) at the same concentration (70 nM). Supporting Information, Figure S2 shows, after 5 min of incubation AuNP-N<sub>3</sub> bound to the glycocalyx, a thick “cuticle layer” composed by glycoproteins and glycosaminoglycans, covering the animal's outer surface (Supporting Information, Figure S3). This molecular

composition of this cuticle layer has been recently identified.<sup>32</sup> The strong interaction between the positive azide group of the AuNP and the negative cuticle components caused in 30 min the massive accumulation of nanoparticles all around the animal tissue. The ectoderm appeared as a typical scalloped surface with branching crypts extending into the epithelium between cells or groups of cells, uniformly labeled by electron dense material (Figure 4A). Interestingly, large vacuoles in the act of fusing/dividing (Figure 4A and Supporting Information, Figure S4) were often found in the apical part of the ectodermal cells, whose probable origin from membrane invagination and fusion (macropinocytosis) is indicated by the presence of the glycocalyx/cuticle lining the inner side of the limiting membrane. Single AuNPs moving through the glycocalyx to reach the cytoplasm revealed the dynamic state of such structures (Figure 4B, arrows). Remarkably, this phenomena has been recently described in HeLa cells incubated with TAT-modified AuNPs: ultrastructural analysis showed NPs to freely negotiate intracellular barriers, moving from vesicles to cytoplasm in either way by direct membrane translocation.<sup>33</sup> Our study

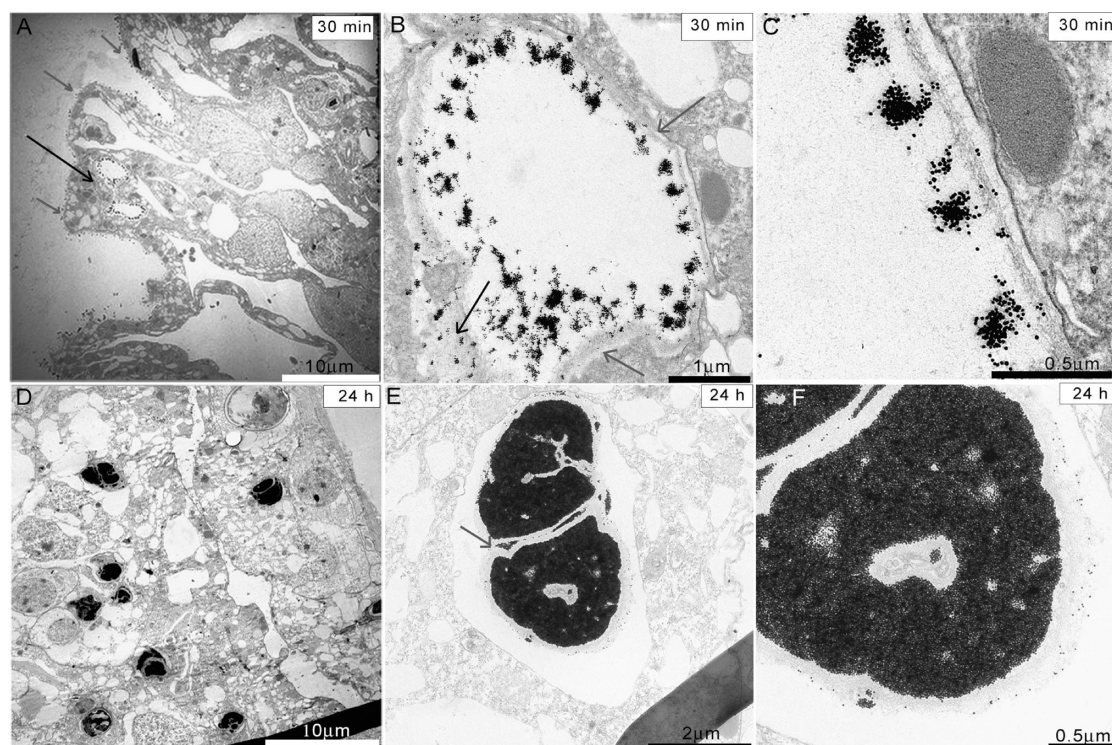


**Figure 4.** Ultrastructural analysis of AuNP-N<sub>3</sub> uptake. *Hydra* polyps were exposed to AuNP-N<sub>3</sub> for (A–C) 30 min, (C–E) 24 h, then extensively washed and processed for TEM. (A) At 30 min time points, AuNP-N<sub>3</sub> were found attached to the glycocalyx, uniformly decorating the animal outer surface (gray arrows), but also inside large vacuoles (black arrow). (B) At higher magnifications the inner side of this structure appears lined by the glycocalyx layer, proving the origin from membrane invagination (gray arrows). AuNP-N<sub>3</sub> are also captured coming out this structure (black arrow) by direct membrane translocation toward the cytosol. (C) A close view of the AuNP-N<sub>3</sub> entrapped into the vacuoles together with the glycocalyx components. (D) At 24 h time point a massive accumulation of AuNP-N<sub>3</sub> into micrometer-sized vesicles is found. In images E and F, higher magnifications of such structures clarify the presence of membrane components in between the packed NPs, suggesting multiple self-fusion and invagination events. Scale bars: (A,D) 10  $\mu$ m; (B) 1  $\mu$ m; (C,F) 0.5  $\mu$ m; (E) 2  $\mu$ m.

also shows AuNP-N<sub>3</sub> directly crossing intracellular or plasma membranes (Supporting Information, Figure S5), as observed with AuNP-siRNA, suggesting multiple mechanisms governing the permeability of cell membrane to AuNPs, and the possibility of identical routes for different chemical functionalities. The most intriguing finding was observed at the 24 h time point analysis (Figure 4D–F), where AuNP-N<sub>3</sub> were found massively packed into micrometer-sized granular structures, mixed to glycocalyx/subcellular debris components. These structures, responsible for the punctuated pattern observed by optical microscopy (see Figure 1I–P), may arise from inward budding of the membrane limiting the endosomal-like structures, as described in mammals.<sup>2</sup> The occurrence of self-folding and fusion events between multiple units may account for the presence of glycocalyx components interspersed between the AuNP aggregates (Figure 4E,F). Similar vesicles densely packed by AuNPs have been described also in HeLa cells,<sup>33</sup> suggesting a conserved mechanism exploited by eukaryotic cells to sort out foreign material. In *Hydra* they may represent storage/garbage vacuoles, possibly due to the saturation of the lysosome machinery unable to sort out high NP concentration. The current view of endosome and lysosomes as dynamic organelles that repeatedly fuse

each other and with cell membrane to either degrade, store, or secrete their content,<sup>34</sup> makes at this stage several hypothesis possible. Our ultrastructural analysis of AuNP-siRNA or AuNP-N<sub>3</sub> uptake indicates that the surface chemistry of the gold nanoparticles controls the efficiency of internalization but not the mechanism itself. The positive surface charge does mediate the intimate contact between the nanoparticles and the cuticle (due to high binding affinity) greatly enhancing, together with the high dose, the uptake. Following this initial interaction, the same mechanisms of entry into the cells can be exploited by both nanoparticle functionalizations, either through endocytosis (including macropynocytosis) or direct membrane translocation. The active/passive nature of the mechanism mediating NP penetration through the membrane and its dependence from the NP surface structure remains to be elucidated.

**Ultrastructural Evidence of AuNP-N<sub>3</sub> Exocytosis.** To get deeper insights into the events characterizing the uptake and fate of AuNP, we focused on AuNP-N<sub>3</sub>, avoiding the potential effect played by additional biomolecules (size, structure, chemistry properties) on the uptake, and also because these NPs represent starting material for further functionalizations. A lower dose of AuNP-N<sub>3</sub>



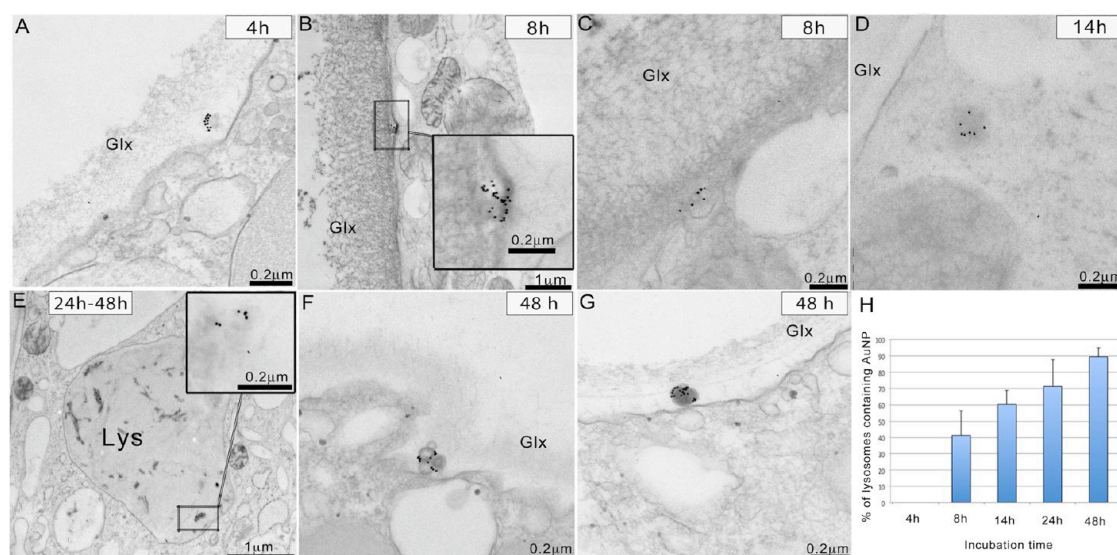


**Figure 5.** High-pressure cryo-TEM reveals additional internalization pathways. Time course analysis of AuNP-N<sub>3</sub> interaction with *Hydra vulgaris*. Polyps were incubated for the indicated periods with 25 nM AuNP-N<sub>3</sub>. (A) Single distinguishable AuNP-N<sub>3</sub> appear attached to nanosized vesicles outside the cell membrane, within the glycocalyx (Glx). (B) Later on the vesicles are found traversing the cell membrane (B,C) to reach (D) the cytoplasm. (E) At 24 and 48 h time point most of the AuNP-N<sub>3</sub> are detected inside lysosomes (Lys). (F,G) At 48 h nanosized vesicles loaded by NPs are also found outside the cell membrane. (H) An estimation of the lysosome containing NPs (expressed as percentage  $\pm$  SE) show that they increase from 8 to 24 h of incubation, when most of uptaken NPs are delivered to lysosomes for degradation. The estimation was done at each time point on 20 TEM images collected from three different animals. Scale bars: (A,C,D,F,G) 0.2  $\mu$ m; (B,E) 1  $\mu$ m.

was employed for animal treatment (25 nM) and the analysis, extended along a wider temporal window, performed by mean of high-pressure cryo-TEM, which avoids ice-crystal formation and potential fixative artifacts, enabling ultrastructural description as close as possible to the living state. In Figure 5, representative TEM images of a time course analysis (4–48 h) show after 4 h incubation the selective binding of the nanoparticles to dense material within the inner glycocalyx layer, lining the round-shaped surface of a vesicle-like structure (Figure 5A). At 8 h these NP-decorated vesicles are found crossing the cell membrane (Figure 5B,C), reaching at 14 h time point the cytosol (Figure 5D). The cytosolic location of AuNP-N<sub>3</sub> decreases after longer incubation times. Indeed, at 24 and 48 h time points AuNP-N<sub>3</sub> were mainly found inside morphologically distinguishable lysosomes, as single units or small clusters (Figure 5E), indicating the lysosomal pathway as the main intracellular fate. By counting the NP-containing lysosomes, their percentage was found directly correlated to the increase of the incubation time, reaching 90% of the total analyzed lysosomes at 48 h (Figure 5H). Surprisingly, the finding at 48 h of nanosized vesicles loaded with NPs outside the cell membrane (Figure 5F) opened the possibility that beside their role as carriers of AuNP from the external medium inside the cell, they could also represent endosome recycled material brought back to the cell membrane. In mammals the fusion of multivesicular bodies with the cell membrane may induce the release of 30–100 nm sized exosomes into the extracellular space.<sup>35,36</sup> Extensive investigations at this time point performed on at

least five different animals (and an average of 20 observations) confirmed AuNP-N<sub>3</sub> associated to dense nanovesicles laying just outside the plasma membrane. This material appears secreted by ectodermal cells, as indicated by the frequent presence of empty vesicles of identical size on the cytosolic side of the cell membrane (Figure 5G and Supporting Information, Figure S6). The occurrence of secretory events is suggested also by the cell membrane morphology, appearing interrupted at different sites due to the external release of nanovesicles (see Figure S6). To further confirm the exocytosis pathway, a “pulse and chase” experiment was carried out. Living animals were incubated for 24 h with AuNP-N<sub>3</sub>, extensively washed, and incubated in fresh medium for a further 24 h and 48 h before processing for TEM and elemental analysis. TEM images in Figure 6 clearly reveal, 24 h postincubation, vesicles containing NP in the apical part of the cell (Figure 6A), on the glycocalyx layer (Figure 6B), and in the act of being released outside the cell (Figure 6C). Other images captured exocytosis by the shedding of vesicles densely packed with AuNPs or mediated by multiple vesicle release through larger membrane areas (Figure 6D–F). As the lysosome content can be directly released outside the cells (Supporting Information, Figure S7A), we conclude that multiple pathways may be employed for AuNPs secretion. A hypothetical scheme summarizing our experimental findings is presented in Figure 7.

**Elemental Analysis Confirms Kinetic of Uptake and Clearance of AuNP.** To quantitatively estimate the amount of AuNP-N<sub>3</sub> internalized by *Hydra* and possibly the extent

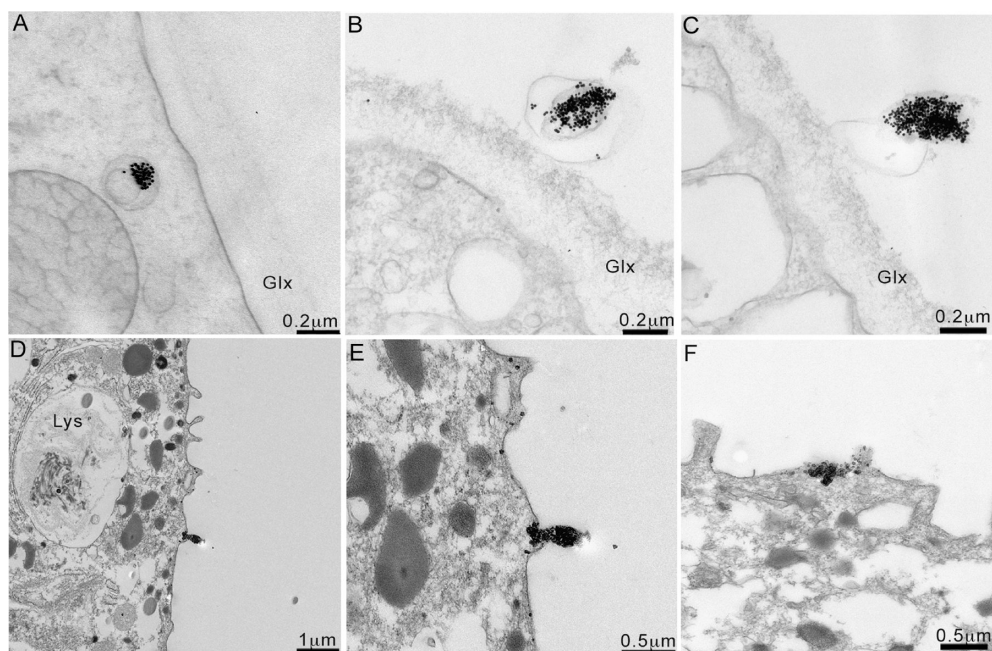


**Figure 6.** Exocytosis of AuNP-N<sub>3</sub>. Polyps were “pulsed” 24 h with AuNP-N<sub>3</sub>, extensively washed, and “chased” by incubation for additional 48 h in fresh medium, before processing for TEM analysis. (A) AuNP-N<sub>3</sub> are found on the apical part of the cell, entrapped into nanosized vesicles that are released out of the animal (B,C). In image D a low magnitude image shows the whole animal tissue section in the act of AuNP-N<sub>3</sub> clearance. Other similar membrane shedding without NP are present on the animal surface, proving the normal occurrence of this phenomena. The same region at higher magnification is shown in image E. (F) Other tissue regions showing NP clearance. In this case a larger membrane area is involved, probably reflecting lysosome exocytosis. Scale bars: (A–C) 0.2  $\mu$ M; (D) 1  $\mu$ M; (E,F) 0.5  $\mu$ M.

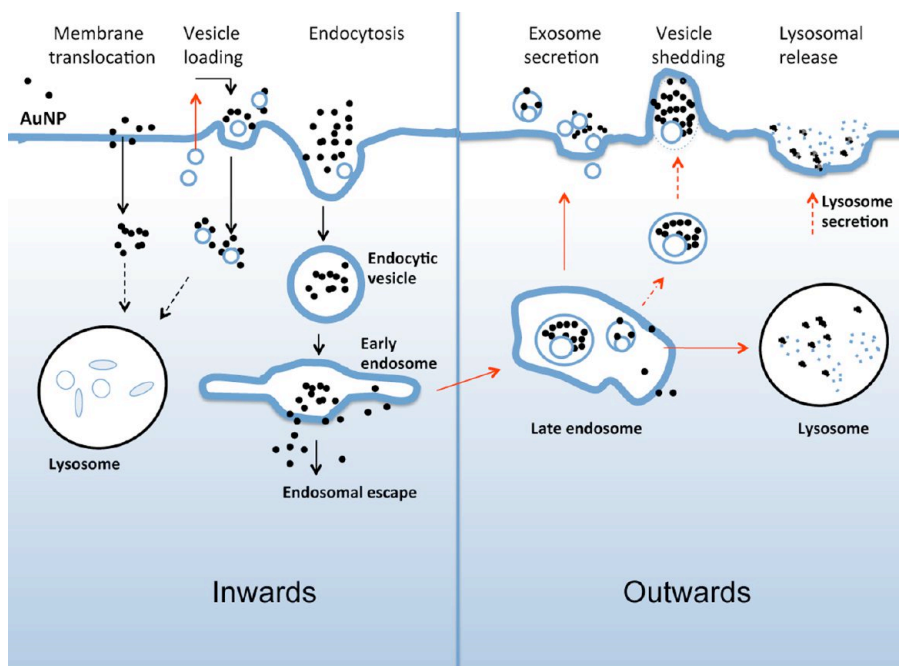


**Figure 7.** Schematic representation summarizing inward and outward trafficking routes of AuNPs. Following AuNP exposure to *Hydra*, several inward routes may be exploited by ectodermal cells, leading to AuNP internalization, illustrated on the left panel: (i) direct membrane translocation, (ii) loading on nanovesicles, (iii) endocytosis (macropinocytosis) through large membrane invaginations. These processes occur within 30 min to 24 h, when a massive recruitment of particles from different cytoplasmic districts into vesicle/vacuole structures is observed. From 24 to 48 h a dynamic exchange of particles between different cell compartments (late endosome/phagosome-lysosome) takes place and AuNPs appear also to move out of vesicle membranes. After 48 h of incubation AuNPs are found at a great extent in lysosomes, but also on exosome-like vesicles. We suggest that following endosomal recruitment several outward routes may take place: (i) through exosomes (possibly derived by late endosomes), (ii) direct membrane exocytosis of NP-loaded vesicles, (iii) fusion of lysosomes with cell membrane. In the scheme the black and red arrows indicate the inward and outward routes, respectively, the dotted arrows indicate possible intracellular trafficking.



**TABLE 2. ICP-AES (Inductively Coupled Plasma Atomic Emission Spectroscopy) Results<sup>a</sup>**

time (h postwashing)	intracellular Au content ( $\mu\text{g}$ )	extracellular Au ( $\mu\text{g}$ )
0	93,74 $\pm$ 1.55	0
24	26,14 $\pm$ 1.20	0.819 $\pm$ 0.012
48	23,14 $\pm$ 0.42	0

<sup>a</sup> ICP-AES was performed on animals pulsed 24 h with 25nM AuNPs (corresponding to 1.25 mg), then washed and chased in fresh medium for 24 and 48 h. At each time point 150 animals (and 1 mL of their incubation medium) were collected and processed for ICP-AES. Experiments were performed in duplicate. Values are indicated as micrograms  $\pm$  SE.

of the exocytosis, elemental analysis by mean of ICP-AES (inductively coupled plasma atomic emission spectroscopy) was performed on animals pulsed 24 h with 25 nM AuNPs (corresponding to 1.25 mg), then washed and chased in fresh medium for 24 and 48 h. The Au content (calculated on 150 treated animals) at the end of the pulse (24 h) was estimated as 93.7  $\mu\text{g}$ , namely 7.5% of the total dose used for treatment. Following washing, the Au content decreased down to 26.1 and 23.1  $\mu\text{g}$ , respectively at 24 and 48 h time points, indicating a 75% release of the internalized material. Interesting, this massive release occurred within the first 24 h of chasing, as after 48 h a quite similar Au value was measured. From analysis of the supernatants collected during the "chase" phase, low but detectable Au amounts (0.8  $\mu\text{g}$ ) were found only at 24 h postwashing, confirming AuNP exocytosis mainly occurring within this temporal window (see Table 2). Although the number of animals employed for the ICP was elevated (150), and the experiments were run in duplicate, the measure of Au content by ICP-AES produces an estimation of the general trend of the endocytosis/exocytosis, and the calculated gold amounts should not be considered as absolute to calculate the real extent of these processes. Overall these findings confirm the kinetics of AuNP entry/exit suggested by the TEM images: AuNPs are moderately recruited into vesicles within the first 24 h of incubation, and then sorted out (1) to lysosomes for external release during the following 24 h, (2) to more stable structures, possibly representing storage vacuoles, discharging their content over a longer period. The unavailability of molecular markers specific for *Hydra* storage/garbage vesicles makes it impossible to further characterize the nature of such structures.

## CONCLUSIONS

The complexity of the molecular interactions underlying the endocytosis suggests that a great evolutionary effort has been spent to regulate the cellular response to a variety of different environmental stimuli. In multicellular organisms the endocytic and secretory pathways evolved to control all aspects of cell physiology and intercellular communication (immune response,

development, hormone-mediated signal transduction, neurotransmission). Nanoparticles, being crystalline solids, can have inherently different properties from other molecules, which might dictate different mechanisms regarding transmembrane transport, intracellular sorting and excretion. While much of the knowledge regarding the cellular uptake and fate of gold nanoparticles has been acquired through *in vitro* cell culture studies, and relies on the response of single cells to AuNPs, here we captured these dynamics *in vivo*, on a simple animal structured as a living bilayered tissue, presenting physiological connections among all cells exposed to NPs. We present direct TEM evidence of several ongoing mechanisms underlying inward and outward trafficking of AuNP tailored with different molecules. The positive surface charge does control the early interaction with the cells, greatly enhancing the efficiency of uptake of AuNP-N<sub>3</sub> compared to AuNP-siRNA, while the mechanisms of uptake are shared by the two different functionalizations. Interestingly, beside expected endocytosis and macropinocytosis (trapping of large fluid pockets by formation and enclosure of membrane invaginations), we showed at least two unusual internalization routes: (1) direct membrane translocation for both AuNP-N<sub>3</sub> and AuNP-siRNA; (2) cell entry mediated by nanovesicles, enabled by the combination of the HP-TEM technique and the low AuNP concentrations. The nanovesicles may represent glycocalyx structural components externally released (and thus NPs passively bind and follow the fate of such structures) or, alternatively, considering their size and morphology, they may represent exosomes, that is, endosomal-derived vesicles shipping extracellular messages, which may entrap AuNPs. The role of the exosomes in cell and animal physiology (immune response, cell signaling) has recently emerged,<sup>35</sup> thus their labeling with AuNPs may provide a unique tool to elucidate their biogenesis and fate. TEM imaging performed at 24 and 48 h time points showed several cell compartments containing the NPs, spanning from early- to late-endosomes, to lysosomes. In addition, AuNPs were found in the act of endosome escaping and traversing intracellular membranes (*i.e.*, AuNP-siRNA present on membranes of interstitial cells), depicting multiple highly dynamic processes elicited in response to AuNPs, over the first 24 h. The elemental analysis confirmed the kinetic of internalization and in addition showed that within 48 h, most of the internalized gold was cleared out the animal.

The dynamic and kinetic of the whole journey of gold nanoparticles within an animal, is here reported for the first time. On one hand, they perfectly mirror previous data obtained in mammalian cells, showing the conservation of such mechanisms throughout the animal kingdom, but, on the other hand, they extend the knowledge of new inward and outward mechanisms negotiating the entrance, trafficking,

and clearance of gold nanoparticles in animal cells.  
This may have a profound impact in the design of

nanodevices for biomedical application and in basic  
cell biology.

## MATERIALS AND METHODS

**Nanoparticle Synthesis.** Hydrogen tetrachloroaurate (III) hydrate ( $\text{HAuCl}_4$ ) was supplied by Strem Chemicals, and *O*-(2-aminoethyl)-*O'*-(2-azidoethyl)pentaethylene glycol was supplied by Iris Biotech. Citrate,  $\gamma$ -tiobutylolactone, triethylamine, dimethyl sulfoxide, sodium dodecyl sulfate, and sodium hydroxide were purchased from Sigma-Aldrich.

**Synthesis of Citrate-Gold Nanoparticles (Au NPs).** Gold nanoparticles with an average diameter of  $\sim 14$  nm were synthesized by the citrate reduction method as described.<sup>26</sup> Briefly, hydrogen tetrachloroaurate (III) hydrate (Strem Chemicals) (0.2 g; 0.589 mmol) was dissolved in 500 mL of Milli-Q water, heated, and stirred under reflux. When the solution boiled, sodium citrate dihydrate (0.598 g; 2.03 mmol) was added resulting in a red solution. The solution was kept under ebullition and protected from light for 30 min, and then cooled down and kept protected from light. The synthesized AuNPs were characterized by UV–vis due to its surface plasmon resonance ( $\lambda_{\text{max}}$ , 519 nm) and by transmission electron microscopy.

**Synthesis of *N*-(20-azido-3,6,9,12,15,18-hexaoxoicosane)-4-mercaptoputanamide ( $\text{HS}-(\text{CH}_2)_3\text{-CONH-EG}(6)\text{-(CH}_2)_2\text{-N}_3$ ).** For the synthesis, 0.6 mmol of  $\alpha$ -amine- $\omega$ -azido hepta(ethylene glycol) were added to 12.5 mL of dimethylsulfoxide under argon atmosphere in a poly(ethylene glycol) bath at 50 °C and under continuous stirring. Subsequently, 0.63 mmol of  $\gamma$ -tiobutylolactone and 5.7 mmol of triethylamine were added. After 5 h, the mixture was cooled down and lyophilized obtaining yellow oil. The yield of the reaction was 93%, without any further purification step. The product was characterized by FT-IR: 3301  $\text{cm}^{-1}$  (NH st), 2870  $\text{cm}^{-1}$  (–CH st), 2530  $\text{cm}^{-1}$  (SH st), 2106  $\text{cm}^{-1}$  ( $\text{N}_3$  st), 1663  $\text{cm}^{-1}$  (C=O st).  $^1\text{H-RMN}$  300 MHz ( $\delta$ ): 2.00 (m, 2H); 2.25 (t, 2H,  $J = 7.30$  Hz); 2.65 (t, 2H,  $J = 7.00$  Hz); 3.01 (s, 1H, SH); 3.32 (t, 4H,  $J = 5.00$  Hz); 3.37 (t, 2H,  $J = 5.22$  Hz); 3.59 (s, 22H); 6.60 (t, 1H,  $J = 4.76$  Hz), and mass spectroscopy [ $\text{M} + \text{H}^+$ ], 451.1.

**Functionalization of AuNPs/AuNP- $\text{N}_3$ .** A AuNP solution (10.7 nM) and  $\text{HS}-(\text{CH}_2)_3\text{-CONH-EG}(6)\text{-(CH}_2)_2\text{-N}_3$  (28  $\mu\text{M}$ ) was prepared the presence of SDS (0.028% v/v). NaOH was further added to a final concentration of 25 mM, and the mixture was incubated for 16 h at room temperature with strong stirring (it is important to follow this order of addition in order to avoid aggregation). The excess of PEGylated chain was washed away by centrifugation at 14000 rpm at 4 °C for 30 min times three. Z potential values for this sample provided a value of +21 mV (pH 7, 1 mM KCl). MALDI-TOF analysis confirmed the presence of PEG- $\text{N}_3$  [ $\text{M} + \text{H}^+$ ], 451.1. The DLS measurement of AuNP- $\text{N}_3$  was 15.5 nm. AuNP-siRNA. AuNPs functionalized with  $\text{HS}-(\text{CH}_2)_3\text{-CONH-EG}(6)\text{-(CH}_2)_2\text{-N}_3$ ,  $\text{HS-EG}(8)\text{-(CH}_2)_2\text{-COOH}$ , and siRNA were prepared following the protocols previously published.<sup>25</sup> Briefly, a mixture of 10 nM of citrate–gold nanoparticles, 7  $\mu\text{M}$   $\text{HS-EG}(8)\text{-(CH}_2)_2\text{-COOH}$  and 7  $\mu\text{M}$   $\text{HS}-(\text{CH}_2)_3\text{-CONH-EG}(6)\text{-(CH}_2)_2\text{-N}_3$ , and 0.028% SDS were prepared. NaOH was further added to a final concentration of 25 mM and the mixture was incubated for 16 h at room temperature. The excess of PEG chains was removed by centrifugation at 14,000 rpm for 30 min at 4 °C, and the supernatant was discarded. This washing process was repeated three times, and the pellet of AuNPs was dissolved in pure water.

For siRNA functionalization, the HS-siRNA previously treated with DTT and purified was incubated at a constant concentration of 5 nmol/mL with RNase free solution of AuNP previously functionalized with PEG (10 nM) containing 0.028% SDS (w/v). Subsequently, the salt concentration was increased to 0.1 M NaCl with brief ultrasonication following each addition to increase the coverage of oligonucleotides on the nanoparticle surface. Following 16 h incubation at 4 °C, the particles were purified by centrifugation at 14000 rpm 30 min at 4 °C and resuspended in DEPC-water 3 times.

The siRNA attached to the AuNP-siRNA was determined by quantification of the excess with the nucleic acid intercalator

GelRed (Biotium), measuring its fluorescence at 602 nm. It was found that  $41.3 \pm 0.8$  strands/AuNP were bound.

The sequence of the siRNA used targeting the *Hydra* myc 1 gene (Accession No. GQ856263) is as follows. Sense: 5'-thiol AAGAUGCACGCGUCAAGAAUU-3'. Antisense: 5'-UUCUUGA-CGCGUGAGCAUCUU-3'.

**Animal Culturing and *in Vivo* Experiments.** *Hydra vulgaris* (strain Zurich, originally obtained by P. Tardent), were cultured in *Hydra* medium (SolHy) comprising 1 mM  $\text{CaCl}_2$ , 0.1 mM  $\text{NaHCO}_3$ , pH 7.0, fed on alternate days with *Artemia nauplii* at 18 °C with 12:12 h light. Polyps from homogeneous populations, three weeks old, were selected for experiments, performed in an air-conditioned environment at 22 °C. The tests were initiated by collecting groups of 10 animals in plastic multiwells, followed by the addition of 70 nM AuNP (either AuNP- $\text{N}_3$  or AuNP-siRNA) in 300  $\mu\text{L}$  of SolHy to each well and incubation for the necessary time periods. Nanoparticle uptake was monitored *in vivo* by a stereomicroscope (Olympus ZSXRL2). Following extensive washes, *in vivo* imaging was accomplished by an inverted microscope (Axiovert 100, Zeiss) equipped with a digital color camera (Olympus, DP70). For imaging acquisition and analysis the software system Cell F (Olympus) was used. At the time indicated above, animals were taken and processed for TEM analysis.

**Hydra Cell and Tissue Analysis.** *Hydra* polyps were macerated into a suspension of fixed single cells as reported.<sup>37</sup> Animals were anaesthetized in 2% urethane in SolHy for 2 min. The relaxed and elongated *Hydra* were fixed with Lavdowsky's fixative (ethanol/formaldehyde/acetic acid/water as 50:10:4:40), rehydrated, and mounted on microscope slides in glycerol 50% in PBS (8 g/L NaCl; 0.2 g/L KCl; 1.44 g/L  $\text{Na}_2\text{HPO}_4 \cdot 7\text{H}_2\text{O}$ ; 0.24 g/L  $\text{KH}_2\text{PO}_4$ ).

Tissue sectioning: Treated animals were soaked overnight in 30% sucrose in PBS and then embedded in the frozen section medium Neg-50 (Richard-Allan Scientific). Cryosections of 10  $\mu\text{m}$  thickness were obtained by a cryostat (Leitz, digital 1760), collected on adhesion microscope slides (SuperFrost Plus, Menzel) mounted in DAKO mounting medium (DAKO) or dehydrated in ethanol, equilibrated in xylene and mounted in D.P.X (Sigma) before imaging.

**Transmission Electron Microscopy Analysis.** Following exposure to nanoparticles, animals were extensively washed, then treated with 2% urethane in SolHy to prevent contraction and fixed for 2 h in 2% glutaraldehyde in SolHy. Samples were washed at least four times with SolHy and postfixed for 45 min with 1% buffered  $\text{OsO}_4$ . After a series of four washes in SolHy, animals were dehydrated in a graded ethanol series (30%, 50%, 70%, 90%, 100%), incubated  $3 \times 15$  min with propylene oxide and then overnight in a 1:1 mixture of propylene oxide/Epon 12 resin. Before they were flat embedded, the animals were incubated  $2 \times 2$  h in Epon 12 resin. Serial thin sections (70 nm) prepared from animal tentacles and body regions below the head level were cut with a diamond knife and mounted onto 150–200 mesh Hex grids. Thin sections were stained with uranyl acetate and lead citrate. Ultrathin sections were examined with a Leo 912 AB transmission electron microscope operating at 80 kV.

**Sample Preparation for High-Pressure Freezing Procedure (HPF).** *Hydra* polyps immersed in SolHy were dissected into appropriate pieces to fit into cup-shaped HPF specimen carriers. Tissue pieces were pipetted with SolHy into a 0.2- or 0.3-mm deep carrier and covered with an additional carrier. Finally, the obtained sandwiches were cryo-immobilized by HPF. Frozen sandwiches were transferred into appropriate containers for storage in liquid  $\text{N}_2$  for later use or subjected to freeze substitution (FS). The frozen samples were transferred under liquid  $\text{N}_2$  into cryovials containing frozen FS cocktails (anhydrous acetone plus 1%  $\text{OsO}_4$  and 0.1–0.2% uranyl acetate). Subsequently, the lids were screwed loosely onto the vials to permit safe evaporation of excess  $\text{N}_2$  gas. The vials were placed into the precooled

FS device, and after about 1 h the lids were tightened and FS was performed for at least 8 h at  $-80$  to  $-90$  °C; warming up to  $-55$  °C at a rate of  $5-10$  °C per hour, subsequent postfixation and staining at  $-55$  °C for 6 h, followed by warming up to  $-30$  °C at a rate of  $5-10$  °C per hour where samples were left for an additional 3 h.<sup>38</sup> Finally the samples were washed 3× with acetone (10 min each), 16 h in 10% epoxy resin (Epon) in acetone, 6 h in 30% Epon in acetone, 16 h in 70% Epon in acetone, 6 h in 100% Epon in acetone, and finally 16 h in 100% Epon in acetone. Then the samples were placed in fresh resin and placed in an oven at 60 °C overnight.

Sample serial thin (70 nm) sections of tentacles and body regions were cut with a diamond knife and mounted onto 150–200 mesh Hex grids. Ultrathin sections were examined with transmission EM Libra 120 EFTEM (Zeiss, Oberkochen, Germany) at 80 eV.

**Elemental Analysis by Inductively Coupled Plasma Atomic Emission Spectroscopy (ICP-AES).** To estimate the extent of endocytosis and exocytosis of AuNP-N<sub>3</sub> in *Hydra*, living polyps were treated 24 h with AuNP, washed, and processed for elemental analysis to evaluate the amount of Au present inside the animals and released in the medium. A total of 1500 *Hydra* polyps were incubated in 3 mL of SolHy with 25 nM AuNP-N<sub>3</sub> for 24 h. At this time point 150 polyps were extensively rinsed and homogenized for ICP-AES. The remaining animals were kept in fresh medium and saved at 24 and 48 h postwashing. For each time point the same amount of polyps (150) and incubation media were saved. Experiments were done in duplicate. For ICP-AES measurements, all the samples were treated with 400  $\mu$ L of aqua regia overnight and then diluted with Milli-Q water to 20 mL to reach a final concentration of acid 2% (v/v).

**Conflict of Interest:** The authors declare no competing financial interest.

**Acknowledgment.** For financial support the authors thank FP7- NanoSciEraNet project NANOTRUCK, and ARAID (Spain). A.A. and V.M. were granted by NANOTRUCK. Moreover, the authors thank G. Marino for technical support with *Hydra* culturing, Stazione Zoologica Anton Dohrn (Napoli) for access to TEM facilities; Michael W. Hess (Division of Histology and Embryology, Innsbruck Medical University) for providing the cryo-EM facility, and Karin Gutleben for excellent technical assistance.

**Supporting Information Available:** Long-term toxicity effects of AuNP in *Hydra*, additional TEM images supporting the mechanisms proposed for endocytosis, intracellular trafficking, and exocytosis of gold nanoparticles. This material is available free of charge via the Internet at <http://pubs.acs.org>.

## REFERENCES AND NOTES

- Conner, S. D.; Schmid, S. L. Regulated Portals of Entry into the Cell. *Nature* **2003**, *422*, 37–44.
- Piper, R.; Katzmann, D. Biogenesis and Function of Multivesicular Bodies. *Annu. Rev. Cell Dev. Biol.* **2007**, *23*, 519–566.
- Farokhzad, O.; Langer, R. Nanomedicine: Developing Smarter Therapeutic And Diagnostic Modalities. *Adv. Drug Delivery Rev.* **2006**, *58*, 1456–1465.
- Hu, Y.; Fine, D. H.; Tasciotti, E.; Bouamrani, A.; Ferrari, M. Nanodevices in Diagnostics. *Wiley Interdiscip. Rev.* **2011**, *3*, 11–32.
- Wang, A.; Langer, R.; Farokhzad, O. Nanoparticle Delivery of Cancer Drugs. *Annu. Rev. Med.* **2012**, *63*, 185–283.
- de la Fuente, J. M.; Berry, C. C. TAT Peptide as an Efficient Molecule to Translocate Gold Nanoparticles into the Cell Nucleus. *Bioconjugate Chem.* **2005**, *16*, 1176–1180.
- Ruoslahti, E. Peptides as Targeting Elements and Tissue Penetration Devices for Nanoparticles. *Adv. Mater.* **2012**, *24*, 3747–3756.
- Child, H. W.; Del Pino, P. A.; de la Fuente, J. M.; Hursthouse, A. S.; Stirling, D.; Mullen, M.; Mcphee, G. M.; Nixon, C.; Jayawarna, V.; Berry, C. C. Working Together: The Combined Application of a Magnetic Field and Penetratin for

the Delivery of Magnetic Nanoparticles to Cells in 3D. *ACS Nano* **2011**, *5*, 7910–7919.

- Bartczak, D.; Nitti, S.; Millar, T. M.; Kanaras, A. G. Exocytosis of Peptide Functionalized Gold Nanoparticles in Endothelial Cells. *Nanoscale* **2012**, *4*, 4470–4472.
- Jiang, X.; Rocker, C.; Hafner, M.; Brandholt, S.; Dorlich, R. M.; Nienhaus, G. U. Endo- and Exocytosis of Zwitterionic Quantum Dot Nanoparticles by Live HeLa cells. *ACS Nano* **2010**, *4*, 6787–6797.
- Chithrani, D. B. Intracellular Uptake, Transport, and Processing of Gold Nanostructures. *Mol. Membr. Biol.* **2010**, *27*, 299–311.
- Giljohann, D. A.; Seferos, D. S.; Daniel, W. L.; Massich, M. D.; Patel, P. C.; Mirkin, C. A. Gold Nanoparticles for Biology and Medicine. *Angew. Chem., Int. Ed.* **2010**, *49*, 3280–3294.
- Kim, C.-k.; Ghosh, P.; Rotello, V. Multimodal Drug Delivery Using Gold Nanoparticles. *Nanoscale* **2009**, *1*, 61–68.
- Lin, J.; Zhang, H.; Chen, Z.; Zheng, Y. Penetration of Lipid Membranes by Gold Nanoparticles: Insights Into Cellular Uptake, Cytotoxicity, and Their Relationship. *ACS Nano* **2010**, *4*, 5421–5429.
- Verma, A.; Stellacci, F. Effect of Surface Properties on Nanoparticle–Cell Interactions. *Small* **2010**, *6*, 12–21.
- Oh, E.; Delehanty, J.; Sapsford, K.; Susumu, K.; Goswami, R.; Blanco-Canosa, J.; Dawson, P.; Granek, J.; Shoff, M.; Zhang, Q.; et al. Cellular Uptake and Fate of PEGylated Gold Nanoparticles Is Dependent on Both Cell-Penetration Peptides and Particle size. *ACS Nano* **2011**, *5*, 6434–6448.
- Tortiglione, C. An ancient model organism to test in vivo novel functional nanocrystals In *Biomedical Engineering: From Theory to Application*; Fazel-Rezaei, R., Ed.; InTech—Open Access Publisher: New York, 2011; Chapter 10.
- Ambrosone, A.; Tortiglione, C. Methodological Approaches for Nanotoxicology Using Cnidarian Models. *Toxicol. Mech. Methods* **2013** (in press) doi:10.3109/15376516.2012.747117).
- Bottger, A.; Hassel, M. *Hydra*, a Model System to Trace the Emergence of Boundaries in Developing Eumetazoans. *Int. J. Dev. Biol.* **2012**, *56*, 583–91.
- Ambrosone, A.; Mattera, L.; Marchesano, V.; Quarta, A.; Susa, A. S.; Tino, A.; Rogach, A. L.; Tortiglione, C. Mechanisms Underlying Toxicity Induced by CdTe Quantum Dots Determined in an Invertebrate Model Organism. *Biomaterials* **2012**, *33*, 1991–2000.
- Tino, A.; Ambrosone, A.; Mattera, L.; Marchesano, V.; Susa, A.; Rogach, A.; Tortiglione, C. A New in Vivo Model System to Assess the Toxicity of Semiconductor Nanocrystals. *Int. J. Biomater.* **2011**, 792854.
- Tortiglione, C.; Quarta, A.; Malvindi, M. A.; Tino, A.; Pellegrino, T. Fluorescent Nanocrystals Reveal Regulated Portals of Entry into and between the Cells of *Hydra*. *PLoS One* **2009**, *4*, e7698.
- Malvindi, M. A.; Carbone, L.; Quarta, A.; Tino, A.; Manna, L.; Pellegrino, T.; Tortiglione, C. Rod-Shaped Nanocrystals Elicit Neuronal Activity in Vivo. *Small* **2008**, *4*, 1747–1755.
- Ambrosone, A.; Marchesano, V.; Tino, A.; Hobmayer, B.; Tortiglione, C. Hymc1 Downregulation Promotes Stem Cell Proliferation in *Hydra Vulgaris*. *PLoS One* **2012**, *7*, e30660.
- Conde, J.; Ambrosone, A.; Sanz, V.; Hernandez, Y.; Marchesano, V.; Tian, F.; Child, H.; Berry, C. C.; Ibarra, M. R.; Baptista, P. V.; Tortiglione, C.; De La Fuente, J. M. Design of Multifunctional Gold Nanoparticles for in Vitro and in Vivo Gene Silencing. *ACS Nano* **2012**, *6*, 8316–8324.
- Hartl, M.; Mitterstiller, A. M.; Valovka, T.; Breuker, K.; Hobmayer, B.; Bister, K. Stem Cell-Specific Activation of an Ancestral Myc Protooncogene with Conserved Basic Functions in the Early Metazoan *Hydra*. *Proc. Natl. Acad. Sci. U.S.A.* **2010**, *107*, 4051–4056.
- Turkevich, J.; Stevenson, P. C.; Hillier, J. A Study of the Nucleation and Growth Processes in the Synthesis of Colloidal Gold. *Discuss. Faraday Soc.* **1951**, *11*, 55–75.
- Ojea-Jimenez, I.; Puentes, V. Instability of Cationic Gold Nanoparticle Bioconjugates: The Role of Citrate Ions. *J. Am. Chem. Soc.* **2009**, *131*, 13320–13327.

29. Krpetic, Z.; Porta, F.; Caneva, E.; Dal Santo, V.; Scari, G. Phagocytosis of Biocompatible Gold Nanoparticles. *Langmuir* **2010**, *26*, 14799–14805.
30. Verma, A.; Uzun, O.; Hu, Y.; Han, H. S.; Watson, N.; Chen, S.; Irvine, D. J.; Stellacci, F. Surface-Structure-Regulated Cell-Membrane Penetration by Monolayer-Protected Nanoparticles. *Nat. Mater.* **2008**, *7*, 588–95.
31. Ding, H. M.; Ma, Y. Q. Interactions between Janus Particles and Membranes. *Nanoscale* **2012**, *4*, 1116–1122.
32. Bottger, A.; Doxey, A. C.; Hess, M. W.; Pfaller, K.; Salvenmoser, W.; Deutzmann, R.; Geissner, A.; Pauly, B.; Altstatter, J.; Munder, S.; *et al.* Horizontal Gene Transfer Contributed to the Evolution of Extracellular Surface Structures: The Freshwater Polyp *Hydra* Is Covered by a Complex Fibrous Cuticle Containing Glycosaminoglycans and Proteins of the PPOD and SWT (Sweet Tooth) Families. *PLoS One* **2012**, *7*, e52278.
33. Krpetic, Z.; Saleemi, S.; Prior, I.; See, V.; Qureshi, R.; Brust, M. Negotiation of Intracellular Membrane Barriers by TAT-Modified Gold Nanoparticles. *ACS Nano* **2011**, *5*, 5195–5396.
34. Andrews, N. Regulated Secretion of Conventional Lysosomes. *Trends Cell Biol* **2000**, *10*, 316–321.
35. Keller, S.; Sanderson, M.; Stoeck, A.; Altevogt, P. Exosomes: From Biogenesis and Secretion to Biological Function. *Immunol. Lett.* **2006**, *107*, 102–108.
36. Record, M.; Subra, C.; Silvente-Poirot, S.; Poirot, M. Exosomes as Intercellular Signalosomes and Pharmacological Effectors. *Biochem. Pharmacol.* **2011**, *81*, 1171–1182.
37. David, C. N. A Quantitative Method for Maceration of *Hydra* Tissue. *Wilhelm Roux Arch. Entw. Mech. Org.* **1973**, *171*, 259–268.
38. Holstein, T.; Hess, M.; Salvenmoser, W. Preparation Techniques for Transmission Electron Microscopy of *Hydra*. *Methods Cell Biol.* **2010**, *96*, 285–591.



# Design of Multifunctional Gold Nanoparticles for *In Vitro* and *In Vivo* Gene Silencing

João Conde,<sup>†,\*,¶</sup> Alfredo Ambrosone,<sup>§,¶</sup> Vanesa Sanz,<sup>†</sup> Yulan Hernandez,<sup>†</sup> Valentina Marchesano,<sup>§</sup> Furong Tian,<sup>‡</sup> Hannah Child,<sup>||</sup> Catherine C. Berry,<sup>||</sup> M. Ricardo Ibarra,<sup>†</sup> Pedro V. Baptista,<sup>‡</sup> Claudia Tortiglione,<sup>§,\*</sup> and Jesus M. de la Fuente<sup>†,\*</sup>

<sup>†</sup>Instituto de Nanociencia de Aragon, University of Zaragoza, C/Mariano Esquillor s/n Zaragoza, Spain, <sup>‡</sup>CIGMH, Departamento de Ciências da Vida, Faculdade de Ciências e Tecnologia, Universidade Nova de Lisboa, Campus de Caparica, 2829-516 Caparica, Portugal, <sup>§</sup>Istituto di Cibernetica "E. Caianiello", Consiglio Nazionale delle Ricerche (CNR), Via Campi Flegrei 34, Pozzuoli, Italy, <sup>‡</sup>Comprehensive Pneumology Center, Institute of Lung Biology and Disease, Helmholtz Zentrum München, Munich, Germany, and <sup>||</sup>Centre for Cell Engineering, University of Glasgow, Joseph Black Building, University Place, Glasgow, United Kingdom. <sup>¶</sup>These authors contributed equally to this work.

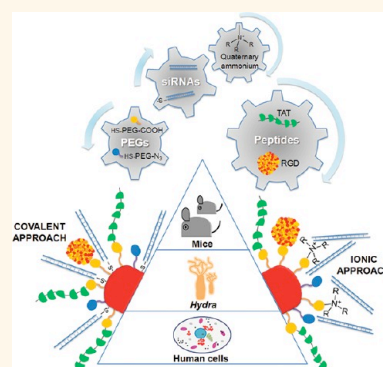
Nanoparticles exhibit excellent physicochemical properties for application in drug delivery, namely, their reduced sizes, rendering them capable of interacting with biomolecules in a one-to-one scale, and the high surface-to-volume ratio allowing for surface functionalization with a plethora of molecules for specific targeting and drug payloads.<sup>1,2</sup> Among the numerous nanoparticle formulations designed to improve siRNA<sup>3,4</sup> delivery and efficiency, those based on gold nanoparticles (AuNPs) have been extensively investigated without undesirable immune response or off-target effects.<sup>5–15</sup> To our knowledge, with the exception of one report on AuNPs for systemic administration of siRNA in humans,<sup>16</sup> over the last 6 years, formulations using AuNP-siRNA have solely been tested in cell cultures targeting reporter genes, such as luciferase or green fluorescence protein.<sup>17</sup> However, as with any drug treatment, gene therapy vehicles need extensive testing in archetypal animal models before translation into the clinics, and this requires the coordinated effort of interdisciplinary research groups.<sup>18</sup>

Here we used a functional comparative approach to assist the smart design, synthesis, and testing of a library of multifunctional nanodevices for RNAi, resulting in a nanocarrier based on AuNPs as the delivery system, with demonstrated functionality both *in vitro* and *in vivo* for RNAi-based therapy. Several biochemical moieties, cell penetrating and cell adhesion peptides were selected to enhance cellular recognition and uptake and confer specific downregulation

**ABSTRACT** Over the past decade, the capability of double-stranded RNAs to interfere with gene expression has driven new therapeutic approaches. Since small interfering RNA (siRNAs, 21 base pair double-stranded RNA) was shown to be able to elicit RNA interference (RNAi), efforts were directed toward the development of efficient delivery systems to preserve siRNA bioactivity throughout the delivery route, from the administration

site to the target cell. Here we provide evidence of RNAi triggering, specifically silencing c-myc protooncogene, via the synthesis of a library of novel multifunctional gold nanoparticles (AuNPs). The efficiency of the AuNPs is demonstrated using a hierarchical approach including three biological systems of increasing complexity: *in vitro* cultured human cells, *in vivo* invertebrate (freshwater polyp, *Hydra*), and *in vivo* vertebrate (mouse) models. Our synthetic methodology involved fine-tuning of multiple structural and functional moieties. Selection of the most active functionalities was assisted step-by-step through functional testing that adopted this hierarchical strategy. Merging these chemical and biological approaches led to a safe, nonpathogenic, self-tracking, and universally valid nanocarrier that could be exploited for therapeutic RNAi.

**KEYWORDS:** gold nanoparticles · RNA interference · animal models · biofunctionalization · c-myc · cancer



of gene expression. The c-myc protooncogene, a key gene playing a pivotal role in cell cycle and tissue homeostasis,<sup>19</sup> was selected as RNAi target; poly(ethylene glycol) (PEG) molecules were incorporated to guarantee nanoparticle stability and avoid unspecific interactions, and three *in vitro/in vivo* model systems were selected: human cells (HeLa), freshwater polyps (*Hydra vulgaris*), and

\* Address correspondence to c.tortiglione@cib.na.cnr.it, jmfuente@unizar.es.

Received for review July 6, 2012 and accepted August 12, 2012.

Published online August 12, 2012 10.1021/nn3030223

© 2012 American Chemical Society

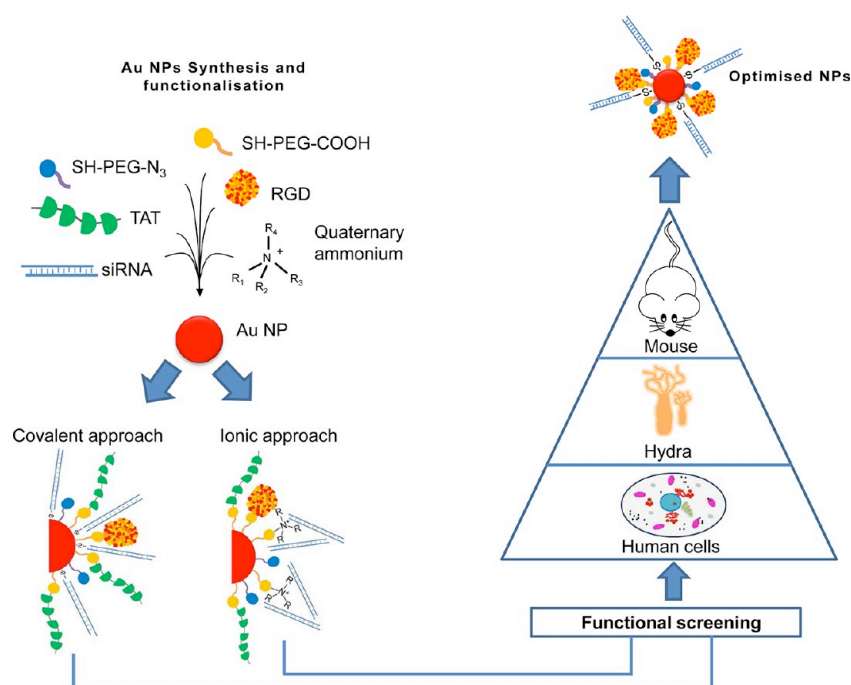


**Figure 1.** *In vivo* gene silencing through nanoparticle-mediated RNAi. The nanocarrier is a AuNP functionalized with multiple biomolecules: PEG, cell penetration and cell adhesion peptides, and siRNA. Two different approaches were employed to conjugate the siRNA to the AuNP: (1) covalent approach, use of thiolated siRNA for gold–thiol binding to the nanoparticle; (2) ionic approach, interaction of the negatively charged siRNA to the modified surface of the AuNP through ionic interactions. A hierarchical scheme employed three biological systems of increasing complexity: cultured cells (HeLa), freshwater polyp (*Hydra vulgaris*), and mouse (C57BL/6j) to screen the synthesized nanocarrier library and select the ideal engineered AuNP for the delivery of siRNA to block gene function.

mouse (C57BL/6j) (Figure 1). This chemical and biological strategy allowed us to compare the effect of the siRNA linkage to the NPs and the effect of cell penetration and adhesion peptides, finally leading to an optimally designed nanocarrier for RNAi therapeutic purposes.

## RESULTS AND DISCUSSION

Stable AuNPs with an average diameter of  $14 \pm 1$  nm were synthesized by reduction of sodium tetrachloroaurate(III) hydrate with sodium citrate dehydrate (Figure S1 of Supporting Information). To increase the stability, biocompatibility, and grant chemical functionality, AuNPs were functionalized with two types of thiolated poly(ethylene glycol) (PEG) spacers: a commercial carboxylated spacer, SH-EG(8)-(CH<sub>2</sub>)<sub>2</sub>-COOH, and an azide-containing spacer custom synthesized in our lab, SH-(CH<sub>2</sub>)<sub>3</sub>-CONH-EG(6)-(CH<sub>2</sub>)<sub>2</sub>-N<sub>3</sub>. The carboxylated spacer provides the anchoring moieties for the covalent binding of amine-containing molecules through carbodiimide chemistry, while the azide-containing spacer confers positive Z-potential values, which is a crucial factor for cell uptake. Combined functionalization of the AuNPs with both spacers was finely tuned by controlling both specific spacer composition and degree of saturation (Figure S2). In order to elucidate the most efficient strategy to bond siRNA to AuNPs, two types of AuNPs stabilized by different degrees of PEG saturation were selected: (i) NP-ion with

100% coverage (25% azide-containing spacer and 75% carboxylated spacer); (ii) NP-cov with 25% coverage (50% of either spacer). These AuNP formulations represented the basic nanoparticles for downstream functionalization with c-myc siRNA, using either ionic interaction (ION) or covalent binding (COV). Both were initially tested for biocompatibility and toxicity in two human cancer cell lines (MCF-7 and HeLa). Cell survival rates following AuNP exposure were determined *via* MTT, with no cytotoxicity detected up to 48 h of incubation with either NP-ion or NP-cov (Figure S5). Further functionalization of these nontoxic AuNPs with c-myc siRNA and the HIV-derived TAT peptide was performed.<sup>20</sup> In the ION method, quaternary ammonium groups (R<sub>4</sub>N<sup>+</sup>) were bound to AuNPs through carbodiimide chemistry between the carboxylated spacer and (2-aminoethyl)trimethylammonium hydrochloride. Ionic interactions between the negatively charged siRNA backbone and both the azide and quaternary ammonium positively charged groups ensured binding of siRNA onto the NP surface for the whole pH range. In the COV method, thiolated siRNA was bound *via* a thiol bond to AuNPs with a nonsaturated PEG layer. The TAT peptide was bound to NP-ion and NP-cov by EDC/NHS coupling between the carboxylated spacer and the amine terminal group of the KKKGRKKRRQRRR (KKK-TAT) peptide. The binding efficiency of each functional group was determined by Bradford assay, alongside detailed



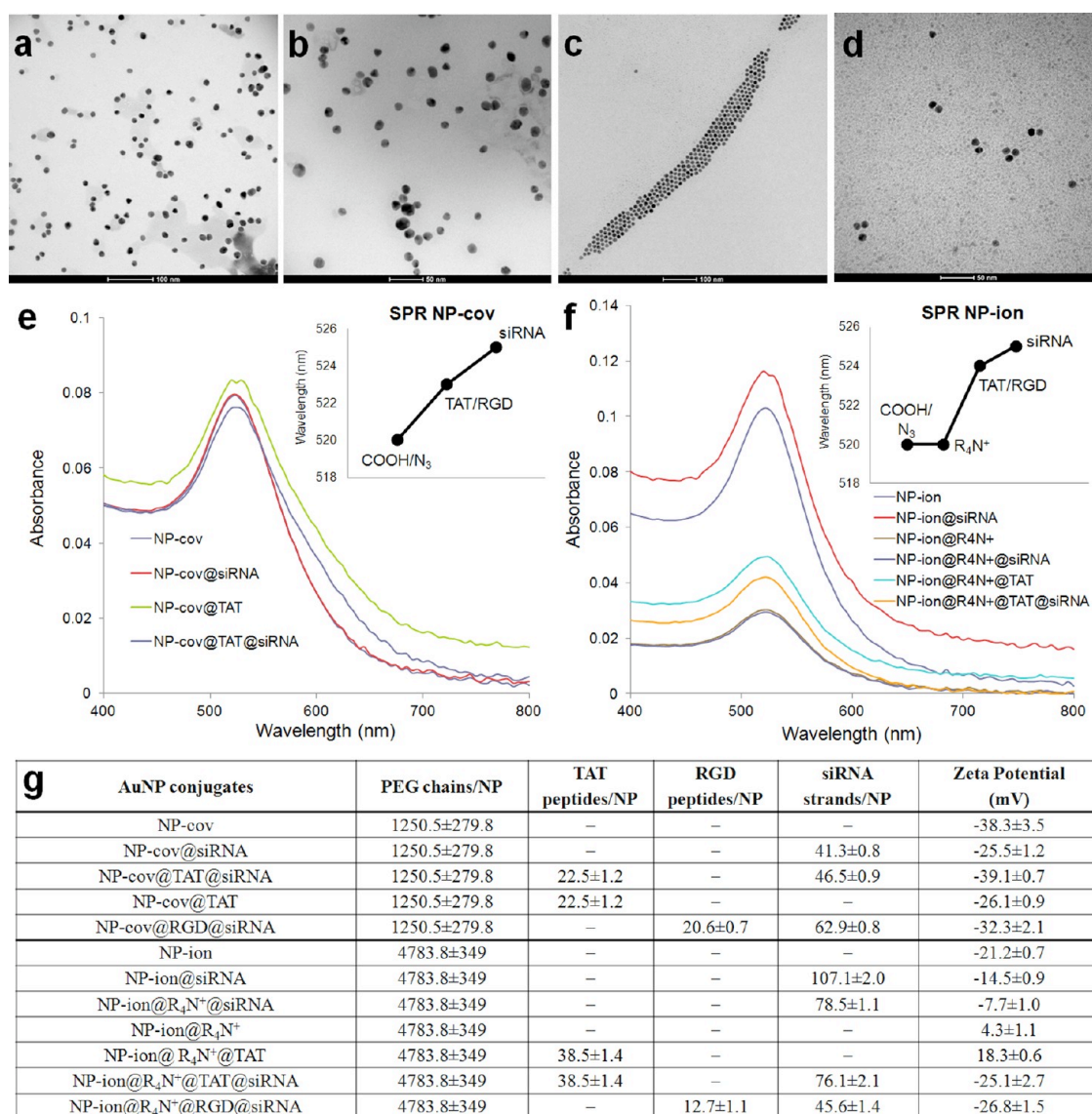


**Figure 2.** Physicochemical characterization of AuNPs. TEM analysis of (a) NP-cov@myc-siRNA, (b) NP-cov@TAT@myc-siRNA, (c) NP-ion@R<sub>4</sub>N<sup>+</sup>@myc-siRNA, (d) NP-ion@R<sub>4</sub>N<sup>+</sup>@TAT@myc-siRNA. The stabilization effect of the different functional groups on the multifunctional AuNPs can be observed via examination of the optical properties by UV-vis spectroscopy (e,f): absorption band of the resulting AuNPs appeared at  $\pm 520$  nm due to the surface plasmon resonance (SPR) of the AuNPs. The spatial arrangement of AuNP can be inferred by measuring the shift of a characteristic SPR band dependent from size, shape, aggregation state, and medium polarity. The SPR of the AuNPs shown in e and f insets exhibited a red shift from 520 to 525 nm: a 3 nm shift for TAT/RGD peptides binding and a 5 nm shift for siRNA binding indicating successful binding of several groups. (g) Quantification of the PEG chains, TAT and RGD peptides, and siRNA strands is shown for all bioconjugates, together with the Z-potential measurements.

AuNP assay characterization (Supporting Information). All AuNP bioconjugates presenting at the surface siRNA and/or TAT/RGD and/or quaternary ammonium groups (R<sub>4</sub>N<sup>+</sup>) in various combinations were characterized by transmission electron microscopy (TEM), UV/vis spectroscopy, surface plasmon resonance (SPR) shift, and zeta-potential (see Figure 2). To determine cell uptake and intracellular fate, HeLa cells were incubated with the functionalized AuNPs for 18 h and processed for TEM analysis. Results show that both NP-ion and NP-cov conjugates were found isolated or as small aggregates in the cytoplasm (Figure 3b,c).

To permit rapid screening of the large variety of functionalized AuNPs in terms of c-myc RNAi, the c-myc gene sequence was cloned into a psiCHECK-2 vector downstream of the Renilla luciferase reporter (Figure S4). This construct was stably expressed in HeLa cells, and the decrease in luciferase activity, as consequence of RNAi, was quantified by a luminescence assay. Figure 3d shows normalized luciferase activity of each AuNP conjugate, where both synthetic approaches used to bind siRNA onto the AuNP (ION versus COV) show comparable silencing efficiency, matching that attained via the transfection of naked siRNA with lipofectamine. Control experiments utilized

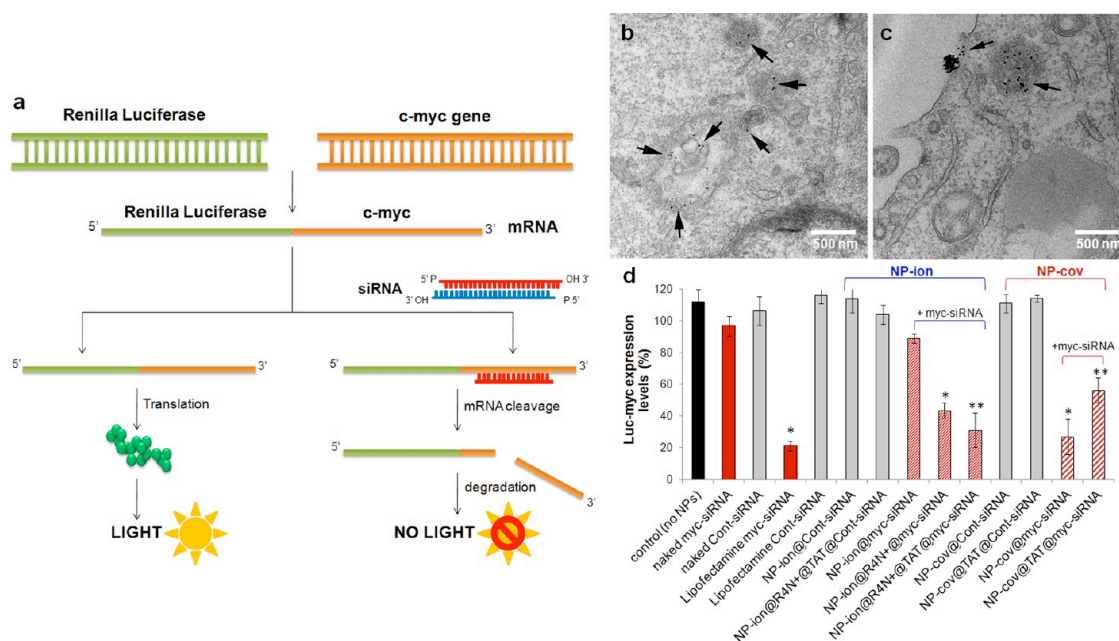


**Figure 3.** Internalization and efficiency of c-myc RNAi induced by functionalized AuNP in HeLa cells. (a) Renilla luciferase was used as the primary reporter gene, and the c-myc gene was cloned into a multiple cloning region located downstream of the Renilla gene. Initiation of the RNAi process by synthetic myc-siRNAs results in cleavage and subsequent degradation of the fusion mRNA. Measuring decreases in Renilla activity provides a convenient way of monitoring the RNAi effect. This vector also contains a second reporter gene, Firefly luciferase, which functions as an internal control for reporter gene activity (scheme adapted from Promega psiCHECK vectors). (b,c) TEM images of cells treated with NP-cov@myc-siRNA (b) and NP-ion@myc-siRNA (c) show NPs present in the cytoplasm as single units, supporting the correct delivery of siRNA to initiate RNAi. (d) Quantitative assessment of RNAi efficiency. HeLa cells were transfected with the recombinant vector psiCHECK-2, encoding for the fusion protein Renilla luciferase-myc. Decrease of Renilla luciferase activity induced by c-myc-siRNA was expressed as percentage of normal luciferase activity. Unrelated siRNA (cont-siRNA) bound on the AuNPs; naked or lipofectamine delivered siRNA were included as negative and positive RNAi controls, respectively. Data marked with asterisks are statistically significant relative to the corresponding NP-ion/cov with control siRNA as calculated by paired Sample *t* test (\*\*,  $P \leq 0.0001$ ; \*,  $P \leq 0.001$ ).

a nonrelated siRNA (cont-siRNA) that does not induce downregulation of luciferase or c-myc. These results clearly show the effective capability of the functionalized AuNPs to specifically and selectively silence c-myc gene expression. With regard to NP-ion design, Figure 3d depicts the importance of including  $R_4N^+$  moiety to introduce ionic interactions between the positively charged NPs and the negatively charged siRNA. Absence of  $R_4N^+$  did not induce any silencing, suggesting a possible proton-sponge effect played by the carboxylic and quaternary ammonium groups, which could be responsible for endosome rupture and release of the trapped materials (siRNA) into the cytoplasm.<sup>21</sup> Also, addition of the TAT peptide branched on NP-ion@ $R_4N^+$ @myc-siRNA showed negligible effects when compared to the same NP without TAT, probably due to steric hindrance of siRNA. Concerning the NP-cov@myc-siRNA, their efficiency in achieving RNAi might result from increased stability of the siRNA covalently bound to the gold core compared to their stability when adsorbed by electrostatic interaction on the NP surface. However, the possibility that the strong efficiency of this adduct might depend on cytoplasmic release of the siRNA (due to the reducing environment of the cytoplasm acting on the thiol bonds) and prompt availability to trigger the RNAi

machinery cannot be excluded. When branched on NP-cov@myc-siRNA, the TAT peptide again decreased the RNAi efficiency from  $73 \pm 11$  to  $43 \pm 7\%$ . These data support the hypothesis that the TAT peptide may act as a suppressor of the RNAi response, as previously reported,<sup>22</sup> which might be related to the fact that this virally derived peptide has evolved to naturally bypass cell defense mechanisms. In summary, despite the low AuNP concentration used (2.1 nM AuNPs, 2 pM siRNA), following confirmed cell uptake *via* TEM (Figure 3b,c), it was able to trigger a very efficient RNAi, likely due to the amplification of the siRNA signal *in vivo*, as elsewhere reported.<sup>23</sup>

Prior to testing the efficiency of the multifunctional nanocarrier for c-myc RNAi on an archetypal animal model, we used a simpler and more singular invertebrate model, *Hydra vulgaris* (Cnidaria, Hydrozoa), to allow for further fine-tuning of the nanocarrier. Thus, following successful silencing in the cell model, the efficiency of both NP-ion and NP-cov were evaluated in the *Hydra in vivo* model. The increase in complexity of the animal model, in fact, could enable us to select the more appropriate nanocarrier to test in mouse. *Hydra* is a freshwater polyp whose structural anatomy reflects a tissue grade of organization (body composed of two cell layers; absence of either proper organs, or central



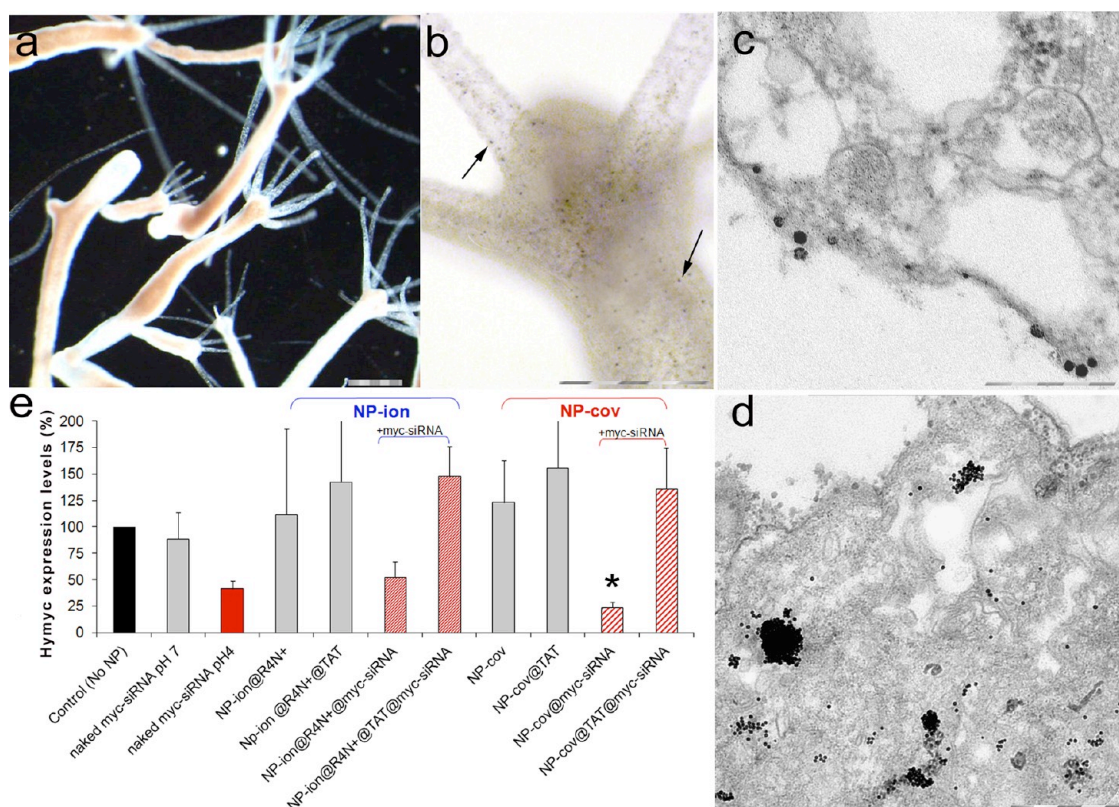


**Figure 4.** Hymyc RNAi in *Hydra vulgaris*. (a) Representative images of living polyps of *Hydra vulgaris* (scale bar 0.5 mm). (b) Bright-field image of *Hydra* treated 24 h with NP-cov@myc-siRNA (scale bar 200  $\mu$ m). Nanoparticles appear as dark spots on the *Hydra* ectodermal cells. Same uptake was observed for NP-ion@myc-siRNA (Supporting Information Figure S3). (c,d) TEM images of *Hydra* tissues, prepared from polyps treated with 15 nM of NP-cov@myc-siRNA for 30 min (c) and 24 h (d). NPs are detected as single unit or small clusters into the cytoplasm for correct delivery of siRNA. Scale bar: 0.2  $\mu$ m (c) and 0.5  $\mu$ m (d). (e) Molecular assessment of RNAi efficiency by qRT-PCR using 15 nM AuNPs and 25 polyps in 100  $\mu$ L of *Hydra* medium. Hymyc relative expression upon incubation with NP-ion and NP-cov was compared to naked siRNA. Relative gene expression changes from NPs not carrying c-myc siRNA are shown as gray bars, while those induced by Hymyc siRNA functionalized NPs are colored red. Data are means of three independent experiments from three biological replicates; error bars show standard deviation. Data marked with asterisk are statistically significant relative to the corresponding NP-ion/cov without siRNA as calculated by paired sample *t* test (\*,  $P \leq 0.005$ ).

nervous system), but exhibiting behavior and physiology proper of animals (Figure 4a and Figure S6 of Supporting Information). Reliable methods have been developed for a comprehensive analysis of nanoparticle impact in *Hydra*, spanning from *in vivo* analysis induced by nanoparticle treatments (structural morphological changes, impact on reproductive rate, efficiency of regeneration) to *in vitro* approaches of cell biology, microscopy, and molecular biology to investigate the internalization routes and the genotoxic effects.<sup>24,25</sup>

Moreover, the *Hydra c-myc* (Hymyc) homologue gene function has been recently identified,<sup>26,27</sup> allowing to functionally test the RNAi efficiency. NP-ion and NP-cov were initially tested for biocompatibility and toxicity by measuring the impact on population growth rate,<sup>25</sup> showing the absence of toxic effects (Figure S7). Optical microscopy showed that both NP-ion and NP-cov were internalized at low rate by ectodermal cells, facing the animal outer plane (Figure 4b and Figure S3), and TEM analysis was necessary for subcellular localization of AuNPs. In

Figure 4c, TEM images on thin sections from animals incubated 30 min with NP-cov@myc-siRNA show nanoparticles bound to the membrane glycolyx, as single units or small clusters passing through the bilayer structure of the cell membrane. After 24 h of incubation, AuNPs were found in the cytoplasm, clustered or monodispersed, demonstrating their capability to cross biological membranes and shuttle siRNA into the cytoplasm (Figure 4d). Hymyc silencing efficiency was assessed using the AuNPs recommended following HeLa silencing (NP-ion@R<sub>4</sub>N<sup>+</sup>@myc-siRNA, NP-ion@R<sub>4</sub>N<sup>+</sup>@TAT@myc-siRNA, NP-cov@TAT@myc-siRNA, NP-cov@myc-siRNA). The qRT-PCR results in *Hydra* further restricted the selection of bioactive AuNP conjugates previously identified in HeLa cells: only two of those nanoparticles induced Hymyc gene silencing, NP-ion@R<sub>4</sub>N<sup>+</sup>@myc-siRNA and NP-cov@myc-siRNA, which rise up to 80% of gene downregulation in the case of the covalent conjugate (Figure 4e). TAT peptide (initially employed to enhance the cell permeability), but causing a decrease in the RNAi efficiency of the NP-cov conjugates in HeLa cells, completely inhibited

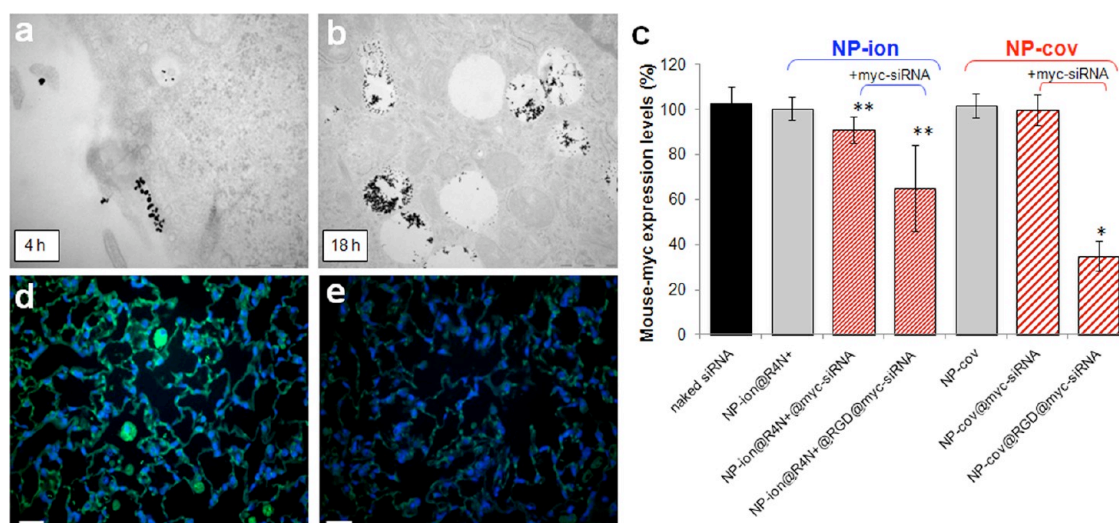


**Figure 5.** c-myc RNAi in mouse. (a,b) TEM images of lung epithelial cells. Mice (C57BL/6j strain) were treated with 16 nM of NP-cov@RGD@myc-siRNA by intratracheal instillation. At 4 h (a) after instillation, NPs are located in ruffles of lung epithelial cell membranes and a few NPs are in the vesicles. At 18 h (b), huge amounts of NPs are found in vesicles or free in cytoplasm (scale bars 500 nm). (c) Molecular assessment of RNAi efficiency. To quantify efficiency of silencing, total RNAs from lung tissue (four mice treated with each NP type) were extracted after 48 h and analyzed by qRT-PCR. The c-myc expression levels were determined using  $\beta$ -actin as reference gene. Data marked with asterisks are statistically significant relative to the corresponding NP-ion/cov without siRNA as calculated by paired sample *t* test (\*,  $P \leq 0.001$ ; \*\*,  $P \leq 0.01$ ). (d,e) c-myc protein expression on alveolar epithelial cells in lung tissue after 48 h treatment. (d) Mice instilled with 16 nM NP-cov@RGD@myc-siRNA. The c-myc protein was detected by Alexa-488-conjugated anti-c-myc antibody (green), and cell nuclei were DAPI stained (blue). Scale bars 200  $\mu$ m.

the RNAi process in *Hydra*, further suggesting that TAT RNAi suppressor activity may be conserved throughout the animal kingdom.<sup>22</sup> Those AuNPs unable to induce gene silencing in cells were also ineffective in *Hydra*, confirmed by analysis of gene expression (Figure 4e).

Finally, the two AuNPs identified as inducing c-myc silencing in both HeLa and *Hydra*, NP-ion@R<sub>4</sub>N<sup>+</sup>@myc-siRNA and NP-cov@myc-siRNA, were tested in the more complex *in vivo* mouse model. Both AuNPs were administered to 10–12 week aged female mice ( $n = 6$ –8 animals) by intratracheal instillation. While intravenous administration is the most popular choice in clinical studies, an oral route inhalation or intratracheal instillation mode, together with intranasal drug delivery, convection-enhanced diffusion, and intrathecal/intraventricular drug delivery systems has been gaining considerable attention. Intratracheal instillation of nanoparticles becomes an important criterion of consideration to overcome the physiological barriers of the lung and to achieve locally high drug concentrations for pulmonary diseases. In our case, the choice was also dictated by the siRNA loaded on the AuNP, targeting the c-myc gene. As this oncogene is deregulated in lung cancer, in a future study of lung cancer treatment, this administration mode might allow proper deliver of therapeutic siRNA to the target organ. After 7 days from instillation, mice were dissected for bronchoalveolar lavage (BAL cells) and lung tissue extraction. In general, NPs of size <100 nm and different zeta-potential display toxic effects, due to trade-off between drug potency and immunologic

surveillance.<sup>28,29</sup> In fact, the influence of size, solubility, and surface modification on the biocompatibility of nanoparticles and their use in biological applications is well-known. NPs have a proclivity *in vivo* and *in vitro* to bioaccumulate within various types of cells with a special affinity for macrophage-type cells and reticuloendothelial cells throughout the body. In order to select safe material for drug delivery, toxicity studies of both NP-cov and NP-ion sets were performed in mice following 1, 3, and 14 days of treatment by the evaluation of the number of macrophages, neutrophils, and lymphocytes, in which an increase indicates an inflammation process. Results showed negligible adverse effects using a low instillation dose (16 nM) (Supporting Information, Figure S8). However, the qRT-PCR performed on four lung samples of each groups, instilled with this dose of NPs, showed very low gene downregulation (Figure 5c), probably due to a lack of NPs' selectivity to the target cells. The functional studies performed in *in vitro* cell culture and in living *Hydra* provided feedback for improving the design and synthesis of AuNPs@siRNA targeting mouse. To this aim, the cell adhesion peptide RGD was incorporated on the AuNP to reinforce cell–NP interaction and drive lung-specific uptake. RGD integrin ligand is well-known for its capability to bind to the integrin  $\alpha_v\beta_3$  receptor family,<sup>30</sup> involved in a wide range of cell–extracellular matrix and cell–cell interactions. Previous studies have demonstrated RGD efficiency to promote NP–cell adhesion events.<sup>31</sup> RGD-containing peptides were conjugated to both NP-ion and NP-cov,

in the presence or absence of c-myc siRNA, by EDC/NHS coupling between the carboxylated spacer and the primary amine in the RGD peptide (Supporting Information). Mice were treated as previously indicated. TEM analysis on lung epithelial cells revealed the efficient uptake of NPs conjugated with RGD with sufficient cytoplasmic availability (Figure 5a,b) to initiate RNAi. The qRT-PCR results showed a  $65.2 \pm 6.7\%$  c-myc downregulation induced by NP-cov@RGD@myc-siRNA and  $34.9 \pm 19\%$  c-myc silencing by NP-ion@R<sub>4</sub>N<sup>+</sup>@RGD@myc-siRNA. These results confirm the specificity of the RNAi approach. Immunolocalization of the MYC protein on alveolar epithelial cells in lung tissue from mice treated with NP-cov@RGD@myc-siRNA confirmed decreased MYC protein accumulation in lung tissue, unequivocally demonstrating the bioactivity of the multifunctional NP (Figure 5d,e).

Remarkably, the same NP-cov@siRNA adduct was shown to elicit highest RNAi in HeLa cells, *Hydra vulgaris*, and mouse, with the only exception of the RGD presence when testing on mouse, as it is not expressed in *Hydra*. From an evolutionary point of view, having found that gene silencing in this primitive animal is accomplished by the same nanocarrier working on human cell cultures and mouse, underlines not only the conservation of key molecular pathways throughout animal evolution but also the conservation of the basic chemicophysical interactions between nanoparticle and the living world, *Hydra* bridging the gap between cell cultures and complex models.

## METHODS

We divided the methods into similar parts for each system (except for the synthesis). Full description of methods can be found in Supporting Information.

**Synthesis and Functionalization of Gold Nanoparticles.** AuNPs with a diameter of  $14 \pm 1$  nm were synthesized by the citrate reduction method described by Lee and Meisel.<sup>32</sup> A mixture of AuNPs, 0.028% SDS, and SH-EG(8)-(CH<sub>2</sub>)<sub>2</sub>-COOH (Iris-Biotech) and SH-(CH<sub>2</sub>)<sub>3</sub>-CONH-EG(6)-(CH<sub>2</sub>)<sub>2</sub>-N<sub>3</sub> in the adequate ratio for NP-ion and NP-cov was mixed under basic conditions for 16 h. PEGylated AuNPs were obtained after purification by centrifugation. Number of PEG molecules was carried out by Ellman's method. Further chemical functionalization with quaternary ammonium ((2-aminoethyl)trimethylammonium chloride hydrochloride), TAT, and RGD peptides was carried out by EDC (1-ethyl-3-(3-dimethylaminopropyl)carbodiimide) (Sigma) and sulfo-NHS (sulfo-hydroxysuccinimide) (Sigma) chemistry at pH 6.1 (25 mM MES). Quantification of TAT peptides was obtained by Bradford assay (CA). AuNP functionalization with siRNA (Thermo Scientific Dharmacon) was taking place using unmodified siRNA for NP-ion by mixing them with NP-ion@R<sub>4</sub>N<sup>+</sup>@TAT during 16 h at 4 °C. For NP-cov, thiolated siRNA was incubated with NP-cov@TAT containing 0.028% SDS and 0.1 M NaCl. Excess siRNA was removed by centrifugation at 4 °C. siRNA quantification was carried out by fluorescence measurement (Perkin-Elmer LS55) using a GelRed (Biotium) acid nucleic intercalator (see Supporting Information, Table 1, for siRNA sequences).

**Hydra Culturing.** *Hydra vulgaris* (strain Zurich, originally obtained by P. Tardent) were asexually cultured in Hydra medium

## CONCLUSION

In this study, we show that two balanced formulations (ionic and covalent approaches), in terms of stability/electrostatic interactions, designed to produce smart multifunctional nanostructures succeeded to generate new innovative and versatile tools for efficient RNA interference in eukaryotic systems. Using three biological models of increasing complexity (cultured cells, invertebrate, and mammal), both design and validation of multifunctional nanocarriers capable of selectively and specifically delivering siRNA *in vivo* were demonstrated. This functional screening approach allowed us to finely tune concentrations, bonding, and the combination of different chemical groups on the nanoparticle surface, addressing current ethical issues on unnecessary, cost-effective, and time-consuming vertebrate testing. These multifunctional nanocarriers are robust enough to preserve stability without showing acute toxicity or cell viability impairment while simultaneously able to bypass biological barriers to perform RNAi activity without off-target effects. Our universal nanocarrier represents a valid gene delivery platform that can be exploited for clinical application in the near future. While treatment of a lung cancer mouse model might represent the first therapeutic test of the nanocarrier developed here, the simple change of the siRNA sequence might target the same device to a huge range of diseases, strengthening the way to clinical application of RNAi.

(1 mM CaCl<sub>2</sub>, 0.1 mM NaHCO<sub>3</sub>, pH 7). The animals were kept at  $18 \pm 1$  °C and fed three times per week with freshly hatched *Artemia salina* nauplii. *In vivo* imaging was accomplished at several magnifications by using both a stereomicroscope and an inverted microscope (Axiovert 100, Zeiss).

**Transmission Electron Microscopy.** To visualize the cellular uptake of NPs, HeLa cells were incubated with all NPs for 18 h. Mice were treated with NPs for 4 and 18 h. Mice were sacrificed and mice lungs fixed in 2.5% glutaraldehyde for TEM. For *Hydra*, polyps were treated with 2% urethane in Hydra medium and then fixed for 2 h in 2% glutaraldehyde in Hydra medium. Samples were postfixed in 1% buffered OsO<sub>4</sub> followed by 0.5% uranyl acetate for 1 h and then taken through alcohol dehydration increments and left in resin (propylene oxide Epon 812 resin mix (1:1) for cells and propylene oxide/Epon 12 resin mix (1:1) for *Hydra*) overnight. Cell layers were captured in pure resin and cured overnight in an oven. *Hydra* were incubated  $2 \times 2$  h in Epon 12 resin. Blocks were then cut into ultrathin sections, stained with 2% methanolic uranyl acetate and Reynolds lead citrate, and viewed under a Leo 912 AB TEM (120 kV for cells and 80 kV for *Hydra*).

**Toxicity.** Cellular cytotoxicity was assessed by standard MTT assay (Invitrogen). *Hydra* growth rate was calculated to monitor NP toxicity, as previously described.<sup>25</sup> Toxicity in mice was assessed by enumeration of total differential cells in bronchoalveolar lavage cells. Several nanomaterials studied in the size range from ca. 5 to 20 nm (TiO<sub>2</sub>, Fe, Cu, Ag) induced higher neutrophil recruitment in BAL fluid, compared to control.<sup>33</sup> Low amounts of neutrophils and lymphocytes indicate minimal inflammatory response or toxicity.



**Assessment of RNAi in HeLa Cells.** c-myc RNAi was evaluated by using the psiCHECK Vector system (Promega), which allows one to monitor change in expression of a reporter gene (Luciferase) fused to a target gene. **MYC-Luciferase vector construction:** the whole human v-myc myelocytomatosis viral oncogene homologue (c-myc) gene was PCR amplified from cDNA retrotranscribed from HeLa cells total RNA (see Supporting Information) and the resulting product cloned in frame with Luciferase reporter gene contained into the vector psiCHECK-2, and maintained in *Escherichia coli* DH5 $\alpha$  strains. **Cell culture:** HeLa cells were grown in Dulbecco's modified Eagle's medium (DMEM, Lonza) with 10% heat inactivated fetal bovine serum, 2 mM glutamine, 100 U/mL penicillin, and 100  $\mu$ g/mL streptomycin and maintained at 37 °C in 5% CO<sub>2</sub>. Cells were seeded at a density of  $5 \times 10^3$  cells/well in 96-well plates and grown for 1 day prior to transfection of the MYC-Luciferase vector (0.125  $\mu$ g per well) using Lipofectamine 2000 (Invitrogen) and Opti-MEM reduced serum medium (Invitrogen) according to the manufacturer's recommendations. RNAi efficiency of different NP conjugates (2.1 nM AuNPs, 2 nM siRNA) was tested by treating the cells for 48 h and by quantification of luciferase expression using a dual-luciferase reporter assay (Promega) assay according to the manufacturer's protocols. Data are average ( $\pm$ SD) of three experiments.

**RNAi Experiments in Hydra.** Groups of 10 animals, collected in plastic multiwells, were incubated in 100  $\mu$ L of Hydra medium in the presence of AuNPs (15 nM), and the treatment was renewed after 24 h to account for possible siRNA degradation. At 48 h, animals were washed and processed for RNA extraction and qRT-PCR. Animals interfered by naked siRNA, nonfunctionalized NP, or untreated were used as controls. Briefly, total RNAs were purified using Trizol (Invitrogen), retrotranscribed using SuperScript II retrotranscriptase (Invitrogen), and used for qRT-PCR analysis (see Supporting Information for detailed methods and primers employed).

**RNAi Experiments in Mouse.** C57BL/6J mice were anesthetized by intraperitoneal injection of a mixture of Medetomidin (0.5 mg/kg body mass), Midazolam (5.0 mg/kg body mass), and Fentanyl (0.05 mg/kg body mass). The animals were then intubated by a nonsurgical technique. Using a cannula inserted 10 mm into the trachea, a suspension containing 16 nM AuNP in 50  $\mu$ L of pyrogen-free distilled water was instilled, followed by 100  $\mu$ L of air. After instillation, animals were antagonized by subcutaneous injection of a mixture of Atipamezol (2.5 mg/kg body mass), Flumazenil (0.5 mg/kg body mass), and Naloxon (1.2 mg/kg body mass) to guarantee their awakening and well-being. Animals were treated humanely and with regard for alleviation of suffering; experimental protocols were reviewed and approved by the Bavarian Animal Research Authority.

**Preparation of BAL Cells/Fluid.** BAL fluid was obtained by injecting and recovering of two 0.5 mL aliquots of PBS via a tracheal cannula. Cells in the lavage fluids were counted using a hemocytometer, and the differentials were determined by utilizing light microscopy to count 200 cells on cytospin preparations.

**Molecular Analyses of Gene Expression in Mouse.** Immunolocalization: Lung tissues were sliced and blocked by adding 1% BSA in PBS for 30 min. Mouse anti-c-myc (Molecular Probes) was added (dilution 1:1000) for 1 h, washed in PBS with agitation for 5 min three times, and incubated with goat anti-mouse IgG coupled with Alexa-488 (Molecular Probes) at 2  $\mu$ g/mL for 30 min. Nuclei were DAPI stained before slide mounting with 50  $\mu$ L of fluoromount mounting medium. Total RNAs were extracted from mouse lungs, retrotranscribed, and analyzed by qRT-PCR (see Supporting Information for detailed methods and primers employed).

**Conflict of Interest:** The authors declare no competing financial interest.

**Acknowledgment.** Authors thank ERANET-NANOSCIERA NANOTRUCK project for financial support. We thank A. Tino, G. Estrada, V. Grazu, and P. del Pino for fruitful discussions. Authors thank I. Echaniz, S. Rivera, and G. Marino for technical support. J.M.F. thanks ARAID for financial support. P.V.B. thanks CIGMH. J.C. acknowledges FCT Grant SFRH/BD/62957/2009. A.A., V.M., and F.T. were granted by NANOTRUCK.

**Supporting Information Available:** Synthesis, physicochemical characterization, and functionalization of AuNPs; internalization of AuNP conjugates; evaluation of RNAi efficiency by functional reporter gene assay; evaluation of toxicity. This material is available free of charge via the Internet at <http://pubs.acs.org>.

## REFERENCES AND NOTES

1. Sperling, R. A.; Parak, W. J. Surface Modification, Functionalization and Bioconjugation of Colloidal Inorganic Nanoparticles. *Philos. Trans. R. Soc. A* **2010**, *368*, 1333–1383.
2. Dreaden, E. C.; Alkilany, A. M.; Huang, X.; Murphy, C. J.; El-Sayed, M. A. The Golden Age: Gold Nanoparticles for Biomedicine. *Chem. Soc. Rev.* **2012**, *41*, 2740–2779.
3. Fire, A.; Xu, S.; Montgomery, M. K.; Kostas, S. A.; Driver, S. E.; Mello, C. C. Potent and Specific Genetic Interference by Double-Stranded RNA in *Caenorhabditis elegans*. *Nature* **1998**, *391*, 806–811.
4. Elbashir, S. M.; Harborth, J.; Lendeckel, W.; Yalcin, A.; Weber, K.; Tuschl, T. Duplexes of 21-Nucleotide RNAs Mediate RNA Interference in Cultured Mammalian Cells. *Nature* **2001**, *411*, 494–498.
5. Pecot, C. V.; Calin, G. A.; Coleman, R. L.; Lopez-Berestein, G.; Sood, A. K. RNA Interference in the Clinic: Challenges and Future Directions. *Nat. Rev. Cancer* **2011**, *11*, 59–67.
6. Shahzad, M. M.; Mangala, L. S.; Han, H. D.; Lu, C.; Bottsford-Miller, J.; Nishimura, M.; Mora, E. M.; Lee, J. W.; Stone, R. L.; Pecot, C. V.; *et al.* Targeted Delivery of Small Interfering RNA Using Reconstituted High-Density Lipoprotein Nanoparticles. *Neoplasia* **2011**, *13*, 309–319.
7. Giljohann, D. A.; Seferos, D. S.; Daniel, W. L.; Massich, M. D.; Patel, P. C.; Mirkin, C. A. Gold Nanoparticles for Biology and Medicine. *Angew. Chem., Int. Ed.* **2010**, *49*, 3280–3294.
8. Giljohann, D. A.; Seferos, D. S.; Prigodich, A. E.; Patel, P. C.; Mirkin, C. A. Gene Regulation with Polyvalent siRNA Nanoparticle Conjugates. *J. Am. Chem. Soc.* **2009**, *131*, 2072–2073.
9. Guo, S.; Huang, Y.; Jiang, Q.; Sun, Y.; Deng, L.; Liang, Z.; Du, Q.; Xing, J.; Zhao, Y.; Wang, P. C.; *et al.* Enhanced Gene Delivery and siRNA Silencing by Gold Nanoparticles Coated with Charge Reversal Polyelectrolyte. *ACS Nano* **2010**, *4*, 5505–5511.
10. Lee, Y.; Lee, S. H.; Kim, J. S.; Maruyama, A.; Chen, X.; Park, T. G. Controlled Synthesis of PEI-Coated Gold Nanoparticles Using Reductive Catechol Chemistry for siRNA Delivery. *J. Controlled Release* **2011**, *155*, 3–10.
11. Song, W. J.; Du, J. Z.; Sun, T. M.; Zhang, P. Z.; Wang, J. Gold Nanoparticles Capped with Polyethyleneimine for Enhanced siRNA Delivery. *Small* **2010**, *6*, 239–246.
12. Oishi, M.; Nakaogami, J.; Ishii, T.; Nagasaki, Y. Smart PEGylated Gold Nanoparticles for the Cytoplasmic Delivery of siRNA To Induce Enhanced Gene Silencing. *Chem. Lett.* **2006**, *35*, 1046–1047.
13. Moon, J. H.; Mendez, E.; Kim, Y.; Kaur, A. Conjugated Polymer Nanoparticles for Small Interfering RNA Delivery. *Chem. Commun.* **2011**, *47*, 8370–8372.
14. Lee, S. H.; Bae, K. H.; Kim, S. H.; Lee, K. R.; Park, T. G. Amine-Functionalized Gold Nanoparticles as Noncytotoxic and Efficient Intracellular siRNA Delivery Carriers. *Int. J. Pharm.* **2008**, *364*, 94–101.
15. Lee, J. S.; Green, J. J.; Love, K. T.; Sunshine, J.; Langer, R.; Anderson, D. G. Gold, Poly( $\beta$ -amino ester) Nanoparticles for Small Interfering RNA Delivery. *Nano Lett.* **2009**, *9*, 2402–2406.
16. Davis, M. E.; Zuckerman, J. E.; Choi, C. H.; Seligson, D.; Tolcher, A.; Alabi, C. A.; Yen, Y.; Heidel, J. D.; Ribas, A. Evidence of RNAi in Humans from Systemically Administered siRNA via Targeted Nanoparticles. *Nature* **2010**, *464*, 1067–1070.
17. Lytton-Jean, A. K.; Langer, R.; Anderson, D. G. Five Years of siRNA Delivery: Spotlight on Gold Nanoparticles. *Small* **2011**, *7*, 1932–1937.
18. Lares, M. R.; Rossi, J. J.; Ouellet, D. L. RNAi and Small Interfering RNAs in Human Disease Therapeutic Applications. *Trends Biotechnol.* **2010**, *28*, 570–579.

19. Vita, M.; Henriksson, M. The Myc Oncoprotein as a Therapeutic Target for Human Cancer. *Semin. Cancer Biol.* **2006**, *16*, 318–330.
20. de la Fuente, J. M.; Berry, C. C. Tat Peptide as an Efficient Molecule To Translocate Gold Nanoparticles into the Cell Nucleus. *Bioconjugate Chem.* **2005**, *16*, 1176–1180.
21. Yezhelyev, M. V.; Qi, L.; O'Regan, R. M.; Nie, S.; Gao, X. Proton-Sponge Coated Quantum Dots for siRNA Delivery and Intracellular Imaging. *J. Am. Chem. Soc.* **2008**, *130*, 9006–9012.
22. Qian, S.; Zhong, X.; Yu, L.; Ding, B.; de Haan, P.; Boris-Lawrie, K. HIV-1 Tat RNA Silencing Suppressor Activity Is Conserved Across Kingdoms and Counteracts Translational Repression of HIV-1. *Proc. Natl. Acad. Sci. U.S.A.* **2009**, *106*, 605–610.
23. Sijen, T.; Fleenor, J.; Simmer, F.; Thijssen, K. L.; Parrish, S.; Timmons, L.; Plasterk, R. H.; Fire, A. On the Role of RNA Amplification in dsRNA Triggered Gene Silencing. *Cell* **2001**, *107*, 465–476.
24. Tortiglione, C. An Ancient Model Organism to Test *In Vivo* Novel Functional Nanocrystals. In *Biomedical Engineering: From Theory to Application*; Fazel-Rezai, R., Ed.; InTech Publisher, 2011; pp 225–252.
25. Ambrosone, A.; Mattera, L.; Marchesano, V.; Quarta, A.; Sussha, A. S.; Tino, A.; Rogach, A. L.; Tortiglione, C. Mechanisms Underlying Toxicity Induced by CdTe Quantum Dots Determined in an Invertebrate Model Organism. *Biomaterials* **2012**, *33*, 1991–2000.
26. Hartl, M.; Mitterstiller, A. M.; Valovka, T.; Breuker, K.; Hobmayer, B.; Bister, K. Stem Cell-Specific Activation of an Ancestral myc Protooncogene with Conserved Basic Functions in the Early Metazoan Hydra. *Proc. Natl. Acad. Sci. U.S.A.* **2010**, *107*, 4051–4056.
27. Ambrosone, A.; Marchesano, V.; Tino, A.; Hobmayer, B.; Tortiglione, C. Hymec1 Downregulation Promotes Stem Cell Proliferation in *Hydra vulgaris*. *PLoS One* **2012**, *7*, e30660.
28. Semmler-Behnke, M.; Kreyling, W. G.; Lipka, J.; Fertsch, S.; Wenk, A.; Takenaka, S.; Schmid, G.; Brandau, W. Biodistribution of 1.4- and 18-nm Gold Particles in Rats. *Small* **2008**, *4*, 2108–2111.
29. Bhaskar, S.; Tian, F.; Stoeger, T.; Kreyling, W.; de la Fuente, J. M.; Grazú, V.; Borm, P.; Estrada, G.; Ntziachristos, V.; Razansky, D. Multifunctional Nanocarriers for Diagnostics, Drug Delivery and Targeted Treatment Across Blood-Brain Barrier: Perspectives on Tracking and Neuroimaging. *Part. Fibre Toxicol.* **2010**, *7*, 1–25.
30. Brooks, P. C.; Montgomery, A. M.; Rosenfeld, M.; Reisfeld, R. A.; Hu, T.; Klier, G.; Cheres, D. A. Integrin  $\alpha_v\beta_3$  Antagonists Promote Tumour Regression By Inducing Apoptosis of Angiogenic Blood Vessels. *Cell* **1994**, *79*, 1157–1164.
31. de la Fuente, J. M.; Berry, C. C.; Riehle, M. O.; Curtis, A. S. G. Nanoparticle Targeting at Cells. *Langmuir* **2006**, *22*, 3286–3293.
32. Lee, P. C.; Meisel, D. Adsorption and Surface-Enhanced Raman of Dyes on Silver and Gold Sols. *J. Phys. Chem.* **1982**, *86*, 3391–3395.
33. Adamcakova-Dodd, A.; Thorne, P. S.; Grassian, V. H. *In Vivo* Toxicity Studies of Metal and Metal Oxide Nanoparticles. In *Handbook of Systems Toxicology*; Cascinao, D. A., Sahu, S. C., Eds.; John Wiley & Sons, Ltd.: New York, 2011; pp 803–834.

# *Hymyc1* Downregulation Promotes Stem Cell Proliferation in *Hydra vulgaris*

Alfredo Ambrosone<sup>1</sup>, Valentina Marchesano<sup>1</sup>, Angela Tino<sup>1</sup>, Bert Hobmayer<sup>2</sup>, Claudia Tortiglione<sup>1\*</sup>

<sup>1</sup> Istituto di Cibernetica "E. Caianiello," Consiglio Nazionale delle Ricerche, Pozzuoli, Italy, <sup>2</sup> Zoological Institute and Center for Molecular Biosciences, University of Innsbruck, Innsbruck, Austria

## Abstract

*Hydra* is a unique model for studying the mechanisms underlying stem cell biology. The activity of the three stem cell lineages structuring its body constantly replenishes mature cells lost due to normal tissue turnover. By a poorly understood mechanism, stem cells are maintained through self-renewal while concomitantly producing differentiated progeny. In vertebrates, one of many genes that participate in regulating stem cell homeostasis is the protooncogene *c-myc*, which has been recently identified also in *Hydra*, and found expressed in the interstitial stem cell lineage. In the present paper, by developing a novel strategy of RNA interference-mediated gene silencing (RNAi) based on an enhanced uptake of small interfering RNAi (siRNA), we provide molecular and biological evidence for an unexpected function of the *Hydra myc* gene (*Hymyc1*) in the homeostasis of the interstitial stem cell lineage. We found that *Hymyc1* inhibition impairs the balance between stem cell self renewal/differentiation, as shown by the accumulation of stem cell intermediate and terminal differentiation products in genetically interfered animals. The identical phenotype induced by the 10058-F4 inhibitor, a disruptor of c-Myc/Max dimerization, demonstrates the specificity of the RNAi approach. We show the kinetic and the reversible feature of *Hymyc1* RNAi, together with the effects displayed on regenerating animals. Our results show the involvement of *Hymyc1* in the control of interstitial stem cell dynamics, provide new clues to decipher the molecular control of the cell and tissue plasticity in *Hydra*, and also provide further insights into the complex *myc* network in higher organisms. The ability of *Hydra* cells to uptake double stranded RNA and to trigger a RNAi response lays the foundations of a comprehensive analysis of the RNAi response in *Hydra* allowing us to track back in the evolution and the origin of this process.

**Citation:** Ambrosone A, Marchesano V, Tino A, Hobmayer B, Tortiglione C (2012) *Hymyc1* Downregulation Promotes Stem Cell Proliferation in *Hydra vulgaris*. PLoS ONE 7(1): e30660. doi:10.1371/journal.pone.0030660

**Editor:** Laszlo Tora, Institute of Genetics and Molecular and Cellular Biology, France

**Received:** August 4, 2011; **Accepted:** December 20, 2011; **Published:** January 23, 2012

**Copyright:** © 2012 Ambrosone et al. This is an open-access article distributed under the terms of the Creative Commons Attribution License, which permits unrestricted use, distribution, and reproduction in any medium, provided the original author and source are credited.

**Funding:** This work was supported by the NanoSci-ERA net project NANOTRUCK (2009–2012). The funders had no role in study design, data collection and analysis, decision to publish, or preparation of the manuscript.

**Competing Interests:** The authors have declared that no competing interests exist.

\* E-mail: c.tortiglione@cib.na.cnr.it

## Introduction

Despite its simple body plan and structural anatomy, the Cnidaria *Hydra*, a diploblastic animal at the base of metazoan evolution, is an excellent model system to investigate the mechanisms controlling stem cell proliferation and differentiation and the balance between the two phenomena. While in most of animals the self-renewing property is confined to one or more tissues, in *Hydra* most of the cells continuously divide and are displaced towards the animal extremities where terminal differentiation occurs before cell loss. The constant growth process requires a homeostatic regulation within and between different cell lineages and a steady state of production and loss of cells [1–4]. The polyp is composed of two epithelial layers, an outer ectoderm and an inner endoderm, shaping a tube-like body, with a single opening (mouth) at one end and a foot to anchor to a substrate at the opposite end. Each layer, which is a single cell deep, comprises a cell lineage. All other cell types are lodged in the interstices among the epithelial cells of both layers, and are part of the interstitial cell lineage (see Figure S1). Interstitial cells occur singly (1 s) or in clusters of 2, 4, 8 and 16 cells (2 s, 4 s, 8 s, 16 s). All these classes are actively proliferating, with a cell cycle length of about 1 day [5]. Single interstitial cells or clusters of 2 form

neurons (sensory and ganglion cells) and secretory cells (zymogen and mucous cells), while clusters of 4, 8 and 16 interstitial cells (nematoblasts) differentiate different types of nematocytes. Multipotent interstitial stem cells, which do not differentiate but simply proliferate, must exist to provide for growth of the interstitial cell population and to provide a continuing supply of differentiating nematocytes, nerve cells, gland cells and gametes [6]. Clearly, a variety of control mechanisms are needed to maintain steady state levels of mature cells, as well as to stimulate the rapid production of specific cell types as needed. This might requires the participation of many factors, including positive and negative regulators of growth and differentiation, which determine survival, growth stimulation, growth arrest, differentiation.

In vertebrates, one of many genes that participate in regulating cell homeostasis is the protooncogene *c-myc*. The *MYC* family of transcription factors controls disparate aspects of cell physiology including cell growth, cell cycle progression, biosynthetic metabolism, and apoptosis [7–9] and, as expected, its deregulated expression occurs in the majority of human cancers. Recently, in *Hydra magnipapillata*, a *c-myc* homologue (*Hymyc1*) has been isolated and fully characterized [10], and by *in silico* genomic analysis three additional *myc*-like or -related genes have been predicted. Among them, HyMYC1 and HyMYC2 deduced protein sequences

display the principal topography of MYC proteins, i.e. bHLH- Zip domains and MYC boxes I to III, and are clearly orthologues of vertebrate *myc*, while the predicted proteins of the two others (HyMYC3 and HyMYC4) present bHLH-Zip domains but are highly divergent in the N-terminal regions, suggesting *myc*-related roles. *Hymyc1* is expressed in proliferating fractions of the interstitial stem cell system, namely single and pairs of interstitial stem cells, proliferating nematoblasts, gland cells. Recombinant hybrid proteins between *Hymyc1* and viral *myc* genes displayed, in assays of cell transformation, oncogenic potential, suggesting structural and functional conservation of *HyMYC1* protein domains. By contrast, the functional role played in the interstitial stem cell lineage in *Hydra* is unknown. To this aim, we have developed a new RNA interference (RNAi) approach to downregulate *Hymyc1* expression. By using small interfering RNAs (siRNA) [11] specifically designed to target *Hymyc1*, we overcome the main issue of their delivery to target tissues by modifying their highly negative charge towards positive values. We have previously shown the capability of *Hydra* to actively uptake positively charged nanoparticles suspended in the culture medium [12]. Here we show that acidic condition enhances the entry of siRNA duplexes into the polyps triggering the *Hydra* RNAi response and leading to specific post transcriptional *Hymyc1* inhibition. Under normal feeding regime and physiological culturing condition, a large scale screening of RNAi phenotype was possible, while avoiding previously used invasive delivering methods to alter gene expression, such as electroporation [13–15]. We provide molecular evidence of *Hymyc1* reduced expression level, while analysis at cellular level led to decipher an unexpected function in the homeostasis of interstitial stem cells. *Hymyc1* inhibition impairs the balance between stem cells self-renewal/differentiation, as shown by the accumulation of intermediate and terminal differentiation products (nematoblasts, nematocytes and secretory cells). The biochemical repression of *Hymyc1* activity achieved by using 10058-F4 inhibitor, a disruptor of c-MYC/MAX dimerization, produced similar effects on *Hydra* polyps, confirming the specificity and the validity of our RNAi approach.

The kinetic of *Hymyc1* RNAi was also evaluated, together with the effect displayed on the regenerative capability of the polyp. Together with the establishment of a reliable loss of function assay to analyse gene function in *Hydra*, the specific *myc* silencing opens new avenues to decipher the molecular control of the cellular plasticity underlying growth and proliferation in *Hydra*, providing further insights into the complex *myc* network also in higher organisms.

## Results

### *Hymyc1* downregulation through siRNA

In a previous study [12] we showed that at acidic pH fluorescent semiconductor nanoparticles, showing positive surface charge, are actively internalized by *Hydra* ectodermal cells, while negatively charged nanoparticles are not uptaken. With the aim to downregulate *Hydra myc1* gene we tested the possibility to perform RNA interference mediated by small interfering RNAs. 21 bp long RNA oligonucleotides with symmetric 2 nt 3' overhangs targeting the coding region of the *Hymyc1* gene (*myc*-siRNA) were designed according to specific rules found to enhance the silencing effect of siRNA [16–18] and chemically synthesized. An estimation of their surface net charge was achieved by zeta potential measurements, a method widely used to quantify the electrokinetic potential in colloidal systems [19]. Zeta potential measurement of siRNA duplexes as function of pH showed that they present positive net charge at pH 4 in *Hydra* culture medium (see Figure S2 of

Supporting Information), while at physiological pH, as expected, they are negatively charged. The silencing properties of *myc*-siRNA were thus tested at pH 4, by soaking the animals in their culture medium in presence of 70 nM *myc*-siRNA, a concentration comparable to that used in other studies of siRNA mediated gene silencing [20], while lower doses were found ineffective. The use of Alexa fluor 488 end labelled *myc*-siRNA enabled us to track *in vivo*, by fluorescence microscopy, the capability of naked siRNAs to cross *Hydra* cell membranes at pH 4 (Figure 1A–1B), with a greater efficacy compared to pH 7 (Figure 1C–1D), indicating that the effective delivery of the siRNA *in vivo* was enhanced by the acidic condition. Analysis of single cell suspensions shows delivery of labelled *myc*-siRNA to both epitheliomuscular and interstitial cells (Figure 1H–1M), while confocal microscopy analysis confirmed the localization within nests of nematoblasts (Figure 1E–1G), where *Hymyc1* is expressed. The silencing effect was evaluated at molecular level by quantitative Real Time PCR (qRT-PCR). Treatment with *myc*-siRNA for two days (2 d) caused a significant reduction of *Hymyc1* transcript levels at pH 4, but not at pH 7 (Figure 2A) suggesting that enhanced acidic-mediated uptake of RNA duplexes is required to induce specific gene silencing. The post-transcriptional silencing induced by *myc*-siRNA was confirmed at protein level by Western Blot analysis. Following preliminary semi-quantitative RT-PCR analysis (Figure 2B, upper panel), polyclonal antibodies raised in rabbit against HyMYC1 recombinant protein detected a drastic decrease of HyMYC1 protein in *myc*-siRNA treated animals by 2 d, compared to endogenous levels of *Hydra* actin (Figure 2B, lower panel). The specificity of the RNAi approach was assessed by testing unrelated siRNAs, such as *Luciferase* siRNA (*luc*-siRNA), designed on the firefly luciferase *GL2* gene. Results showed that *Hymyc1* transcription and translation were unaffected in *luc*-siRNA treated animals (Figure 2B). By qRT-PCR the potential adverse effects played by the acidic pH on gene expression were also analysed. As it might be argued that the acidic condition could play adverse effects on gene expression, we analysed the endogenous *Hymyc1* expression level in animals incubated at pH 4 for increasing periods, and compared them to expression levels in physiological condition (pH 7). The graph of Figure S3-A (Supporting Information) shows similar levels of *Hymyc1* transcripts both at pH 4 and pH 7, indicating that *Hymyc1* endogenous expression was unaffected by the acidic environment. Morphological analysis of treated animals further confirmed the absence of adverse effects played by the low pH on polyp viability (Figure S3-B of Supporting Information).

The efficiency of RNAi as function of the duration of treatment is shown in Figure 2C. Specific gene inhibition was detected in *myc*-siRNA treated animals by 2 d of treatment, when a 60% decrease in the *Hymyc1* mRNA amount was measured. Increasing the period of treatment up to 9 d did not further increase the silencing efficiency, probably due to fast cell turnover of the interstitial stem cells, continuously replacing the interfered cells or to the animal adaptation to the treatment. The long lasting effect of the RNAi was then investigated by performing a 4 d RNAi treatment followed by RNAi suspension and culturing in physiological condition, under normal feeding regime, over different periods. The graph of Figure 2D shows that *Hydra* polyps could recover from the RNAi treatment, restoring physiological levels of *Hymyc1* transcripts over the following five days. Thus the observed downregulation depends upon the continuous presence of siRNA oligonucleotides and indicates the reversibility of the siRNA mediated RNAi, similarly to other invertebrates RNAi knockdown models [21].

The efficiency of the new developed RNAi approach was tested on an additional gene,  $\beta$ -catenin ( $\beta$ -cat), a key gene involved in



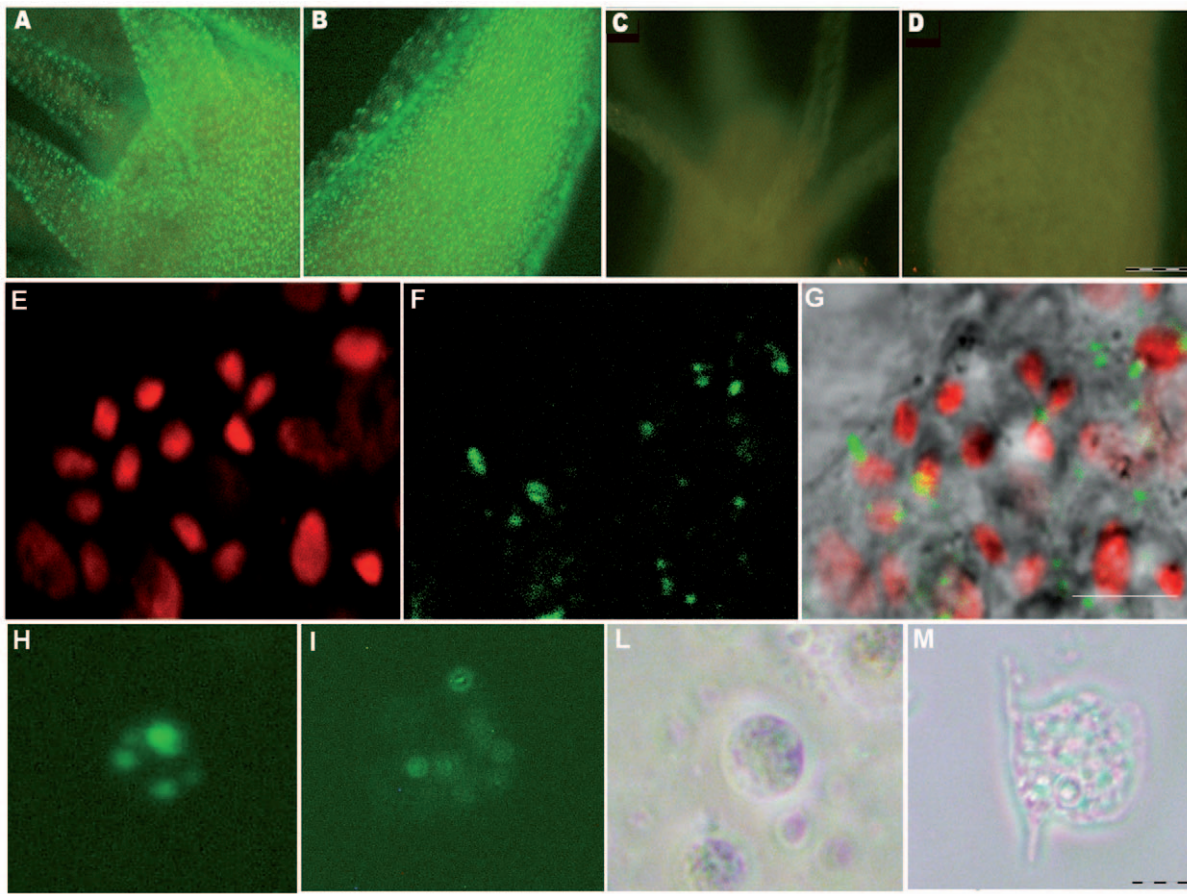


**Figure 1. *In vivo* RNAi mediated by siRNA.** Fluorescence imaging of *Hydra vulgaris* exposed to *myc*-siRNA at different pHs. Living polyps were challenged with 70 nM Alexa488-end labelled *myc*-siRNA, in *Hydra* medium either at pH 4 (A, B) or at pH 7 (C, D). After 24 hr of continuous incubation with siRNA a strong punctuated fluorescence labels uniformly the whole animal, from the head (A) along the body (B) of animals treated at acidic pH, indicating the uptake of siRNA. In (C) and (D) are shown the body regions corresponding to A and B, respectively, of animals treated with the same siRNA at neutral pH. The absence of fluorescence signals indicates that the acidic pH enhances siRNA delivery in *Hydra*. Scale bar 200  $\mu$ m. Confocal laser scanning imaging (E–G) of living *Hydra* treated 24 hr with Alexa488-labelled *myc*-siRNA revealed localization of oligonucleotides into interstitial cells. In (E), nuclear staining of interstitial cell nest with TOPO3; in (F) siRNA green fluorescence appears as faint staining or more evident granules; in (G), the overlay of bright field and fluorescence images revealed that siRNAs localize prevalently into the cytoplasm of interstitial cells. Scale bars: 10  $\mu$ m. Fluorescence microscopy analysis of single cells suspensions prepared from treated dissociated animals shows intracellular localization of siRNA into interstitial (H) and epitheliomuscular (I) cells, as a punctuated pattern. The same cells were observed by phase contrast microscopy, respectively in (L) and (M). Scale bar 10  $\mu$ m.  
doi:10.1371/journal.pone.0030660.g001

setting up the head organizer in *Hydra*.  $\beta$ -cat is an armadillo repeat-containing protein expressed weakly and uniformly throughout the polyp and at higher level in developing buds [22–23]. *Hydra* polyps treated for 2 d with specifically designed  $\beta$ -cat-siRNA revealed a strong and significant reduction (more than 50%) of the target mRNA (Figure S4), confirming the validity and the reproducibility of our RNAi strategy.

### Hymyc1 gene silencing promotes proliferation of single and pairs of interstitial stem cells

In order to detect differences in the expression pattern of *myc*-siRNA interfered animals whole mount *in situ* hybridizations using a Digoxigenin-labelled *Hymyc1* RNA probe were performed. Despite the decreased *Hymyc1* expression detected by qRT-PCR, differences in the signal distribution pattern between healthy and interfered animals (analysed at 2 d, 4 d and 9 d of continuous siRNA treatment) could not be appreciated, due to the Digoxigenin detection technique, not allowing quantitative measurements. As shown by stained specimens both whole

mounted and cryo-sectioned (Figure 3A–3D) *Hymyc1* residual transcripts were detected in *myc*-siRNA treated animals in single and pairs of interstitial cells (1 s, 2 s), nests of nematoblasts (4 s–16 s), accordingly to previous reports [10]. The same expression pattern was detected in *luc*-siRNA treated animals, confirming the absence of aspecific effects due to the siRNA treatment (data not shown). A quantitative evaluation of the *Hymyc1* positive cells confirmed the absence of significant differences between interfered (by *myc*-siRNA and *luc*-siRNA) and control animals (Figure S5). This result suggests that the activation of the RNAi machinery occurred throughout the targeted cells, rather than on limited patches of cells where the siRNA could be selectively delivered.

Since the multipotent interstitial cells, their differentiation intermediates, and their product cells are all closely related (Figure 3E), changes in their relative population sizes may yield clues as to how these populations are controlled. A morphological analysis both at cellular level and in intact animals was then performed to investigate potential effects induced by *Hymyc1*



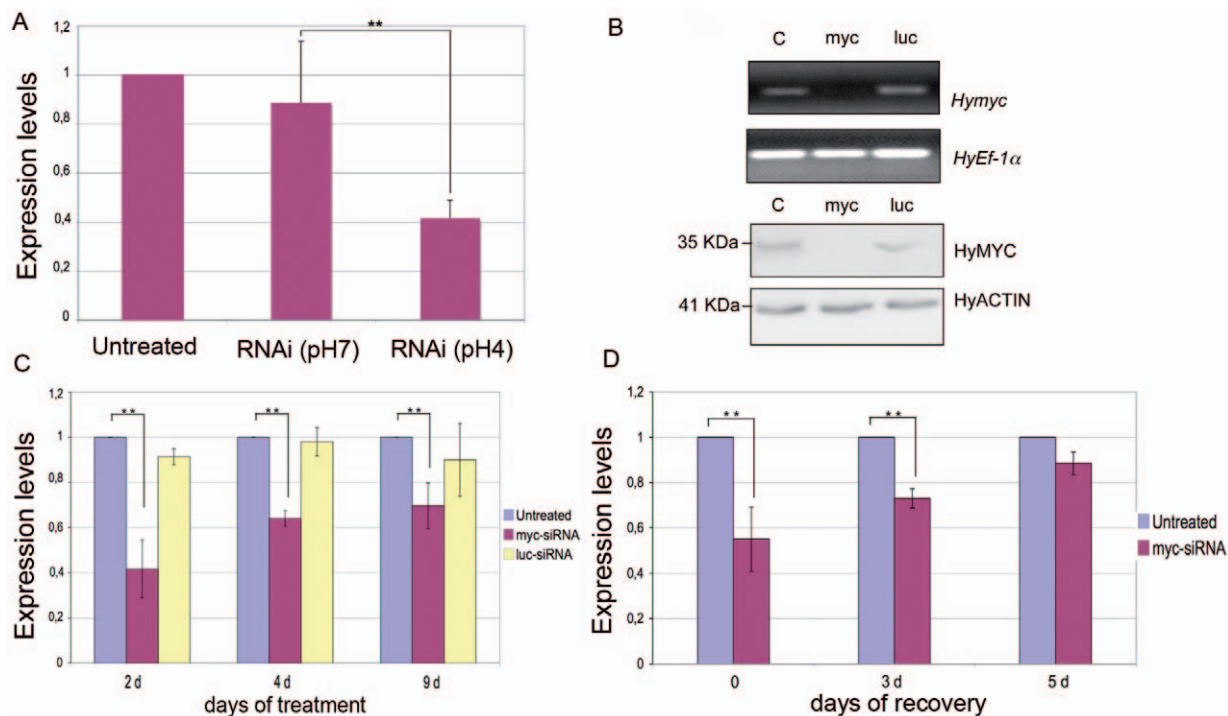


**Figure 2. Molecular characterization of *Hymyc1* RNAi.** (A) quantitative RT-PCR showing *Hymyc1* downregulation enhanced by acidic condition. Animals treated by *myc*-siRNA at pH 4 showed 60% decrease in *Hymyc1* transcription levels compared to *Hydra* Elongation factor *HyEF1α* mRNA, used as internal control (two asterisks,  $p < 0.01$  according to t-Student test). (B) Upper panel: semi-quantitative RT-PCR showing *Hymyc1* downregulation induced specifically by *myc*-siRNA (lane myc) and not by *luc*-siRNA (lane luc), or in untreated animals (lane C) used as controls. Lower panel: *Hymyc1* RNAi affects also MYC protein levels. Lane labels are as in the upper panel. MYC protein levels were detected using anti-HyMYC1 antibody (1:500, kindly provided by K.Bister, University of Innsbruck) and compared to actin proteins, using an anti-actin primary antibody (1:100, Sigma) to probe an identical blotted gel. HyMYC1 shows an apparent mol. weight of 35 kDa, as elsewhere reported [10]. (C) Kinetics of *Hymyc1* downregulation. qRT-PCR was performed on total RNA extracted from 25 animals either untreated (namely incubated at pH 4, in absence of siRNA) or incubated with the indicated siRNA for different periods. The most effective downregulation is detected at the beginning of the treatment, and it is specifically induced by *myc*- and not *luc*-siRNA duplexes (two asterisks,  $p < 0.01$  according to t-Student test). (D) Reversible effect of RNAi. Animals were treated with *myc*-siRNA for 4 d (time  $t = 0$ ) and then cultured in physiological condition for the indicated periods of time (3 days, 5 days), when total RNAs were extracted for qRT-PCR analysis. Suspension of RNAi treatment restored in five days *myc* mRNA transcript levels up to physiological values. Error bars in A, C and D indicate standard deviations calculated from three independent experiments, each performed in triplicate. doi:10.1371/journal.pone.0030660.g002

silencing on the cell proliferation activity and cell type relative distribution.

As *Hydra* epithelial cells proliferate with a cell cycle of about 3,5 d [24–25] and interstitial cells much faster with a cell cycle of about 1 d [26], the cycling activity of the epithelial and interstitial cells was assayed by continuous BrdU-labeling, over 3 and 2 d, respectively. Figure 4A shows that the proliferation rate of epithelial cells was not affected by *myc* RNAi, thus this cell type could be used to normalize relative cell type distribution. By contrast, proliferation of single and pairs of interstitial cells (1 s+2 s) was enhanced in *myc*-RNAi animals, indicating an effect of *myc* downregulation on the stem cell cycling activity (Figure 4B). The estimation of cell proliferation rate by mean of BrdU was carried out also in differentiating nematoblasts (4 s) and gland cells. Results reported in Figure S6 showed that *Hymyc1* RNAi does not affect proliferation rate of these cell types, suggesting a *Hymyc1* role played specifically on 1 s+2 s cells.

To gain insight into the possible effects of *Hymyc1* RNAi on the cell cycle, mitotic index and DNA content of 1 s+2 s cells were assessed. Counts of DAPI-stained cells by phase contrast microscopy combined with nuclear DNA staining revealed that the fractions of cells undergoing mitosis in *myc*-siRNA treated animals were 3,7% and 3,4% upon 3 and 4 d of treatment, respectively ( $n = 1000$ , for each treatment). Conversely, these

fractions in untreated animals were 2,7% and 2,3% after 3 d and 4 d, respectively, indicating an increase of more than 40% of the mitotic index of 1 s+2 s cells as effect of RNAi. To check whether or not *Hymyc1* silencing controls specific cell cycle checkpoints, the DNA content of 1 s+2 s cells from RNAi animals was determined. We found no significant differences in the nuclear DNA profile between untreated and *Hymyc1* RNAi animals, suggesting that *Hymyc1* does not act as a regulator of one specific cell cycle checkpoint (Figure S7 of Supporting Information).

To investigate the effects of *Hymyc1* downregulation on all interstitial cell lineage, cell type distribution was analysed in macerates at two time points, 4 d and 9 d, and the cells counted relative to epithelial cells, as not affected by *Hymyc1* RNAi (Figure 4A). After 4 d of siRNA treatment, the observed increased ratio 1 s+2 s/EPI was consistent with the boost of mitotic index and BrdU labelling previously reported (see above text and Figure 4B). Furthermore, we found in *myc*-siRNA treated animals an increase in the population of nematoblasts (4 s–16 s), zymogen and mucous cells, more pronounced at 9 d (Figure 4C, 4D), while nerve cells were not affected, suggesting a *Hymyc1* specific role in nematocyte and gland cell differentiation pathways. The population of mature nematocytes embedded in the battery cells was analysed in tentacles of intact fixed animals. *Hydra* tentacles are structured as cell bilayers, as the rest of the animal body, but

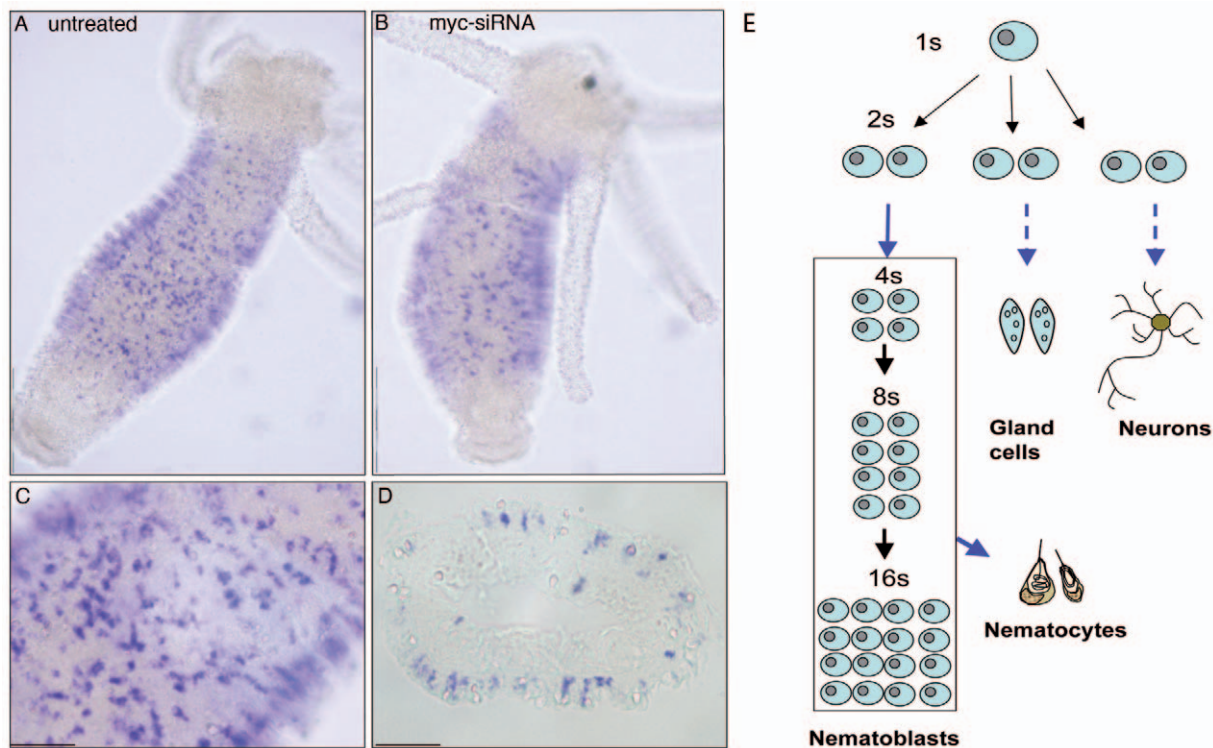


**Figure 3. *Hymec1* expression pattern is not affected by *Hymec1* downregulation.** A comparison of whole mount *in situ* hybridization performed on A) healthy animals and B) *myc*-siRNA treated animals (2 d) shows residual *Hymec1* transcripts in the RNAi targeted cells. As previously reported [10] *Hymec1* is expressed in proliferating interstitial cells, distributed along the gastric region, shown at higher magnification in (C). A cross section of stained animals confirms this expression pattern (D). Scale bars: 1 mm in A and B; 200  $\mu$ m in C and D. A scheme of the differentiation pathways in the interstitial stem cell system is shown in (E). Interstitial stem cells include multipotent stem cells (1 s) and committed stem cells (2 s) that differentiate three major cell types in *Hydra* (nematoblasts, secretory cells, neurons, and gametes). Nematocytes, the phylum representative cells arming the tentacles and used for prey capture, originate from nematoblasts, i.e. committed cells that after several mitotic divisions (generating nests of 4, 8 and 16 cells connected by cytoplasmic bridges) finally differentiates into several types of nematocytes (stenoteles, desmonemes, isoriza, depending on the nematocyst morphology). 2 s cells committed toward either nematocyte, nerve or secretory cells, are morphologically indistinguishable. While single interstitial stem cells (1 s) continuously self renew, among the daughter cells (2 s) 60% remain stem cells, whereas 40% become committed to different cell types. doi:10.1371/journal.pone.0030660.g003

contain specialized ectodermal cells, the battery cells (Figure S1) [27–28]. These tentacle specific cells arise from terminal differentiation of ectodermal cells, including the mitosis arrest and the inclusion into the cytoplasm of neuronal cells and several nematocytes, the stinging cells involved into the prey capture. This complex system, the battery cell, is recognizable by phase contrast optical microscopy. Results of Figure 5A show that *myc*-siRNA interfered animals, both at 4 d and 9 d, presented an increased ratio of mature nematocytes/battery cells, compared to relative control sets of animals and a representative battery cell is reported in Figure 5B. This effect was induced by *myc*-siRNA treatment in almost all individuals, as shown by the distribution of the ratios among ten animals (Figure S8).

The specificity of the phenotype induced by *myc*-siRNAi was tested by treating animals with a biochemical c-MYC inhibitor, the thioxothiazolidinone10058-F4 [29], which blocks c-MYC/MAX heterodimer formation through molecular mechanisms poorly understood so far, and it affects as well the *myc* gene transcription level [30–31]. Treatment of living polyps with 10058-F4 for 2 d induced 50% reduction of *Hymec1* expression levels, as assayed by qRT-PCR (Figure 6A), while analysis of cell proliferation rate showed an effect on 1 s+2 s cells (Figure 6B), but not on other cell types (Figure S6 of Supporting Information). Cell type distribution analysis also revealed increased proliferation

of 1 s+2 s stem cells, and increased amounts of intermediates and terminal differentiation products (nematoblasts, nematocytes, secretory cells) (Figure 6C). As detected in *Hymec1* RNAi polyps, also the phenotype of the battery cells was affected, containing an abnormal number of nematocytes (Figure 6D), indicating unequivocally the specificity of the *Hymec1* downregulation effects, and indirectly the structural and functional conservation of the HyMYC1/HyMAX complex. Taken together, these findings suggest that genetic and biochemical repression of *Hymec1* activity affects in the same way the interstitial cell lineage homeostasis: *Hymec1* conditional elimination enhanced stem cell proliferation, and in turn unbalances the differentiating products.

As *Hymec1* is expressed in proliferating stem cells of the interstitial cell lineage, we also evaluated its expression profile during regeneration, a complex phenomena involving extensive cell reprogramming, proliferation and differentiation processes to rebuild a new organism from an amputated moiety [32].

Quantitative analysis of *Hymec1* expression performed over the first 24 h post amputation indicates that *Hymec1* expression levels were not specifically modulated during the early stages of the regenerative process of healthy animals (Figure 7A). When analysing *myc* RNAi regenerating animals, similar *Hymec1* expression levels were found (Figure 7B) indicating that the RNAi effect was maintained during the regeneration and it could

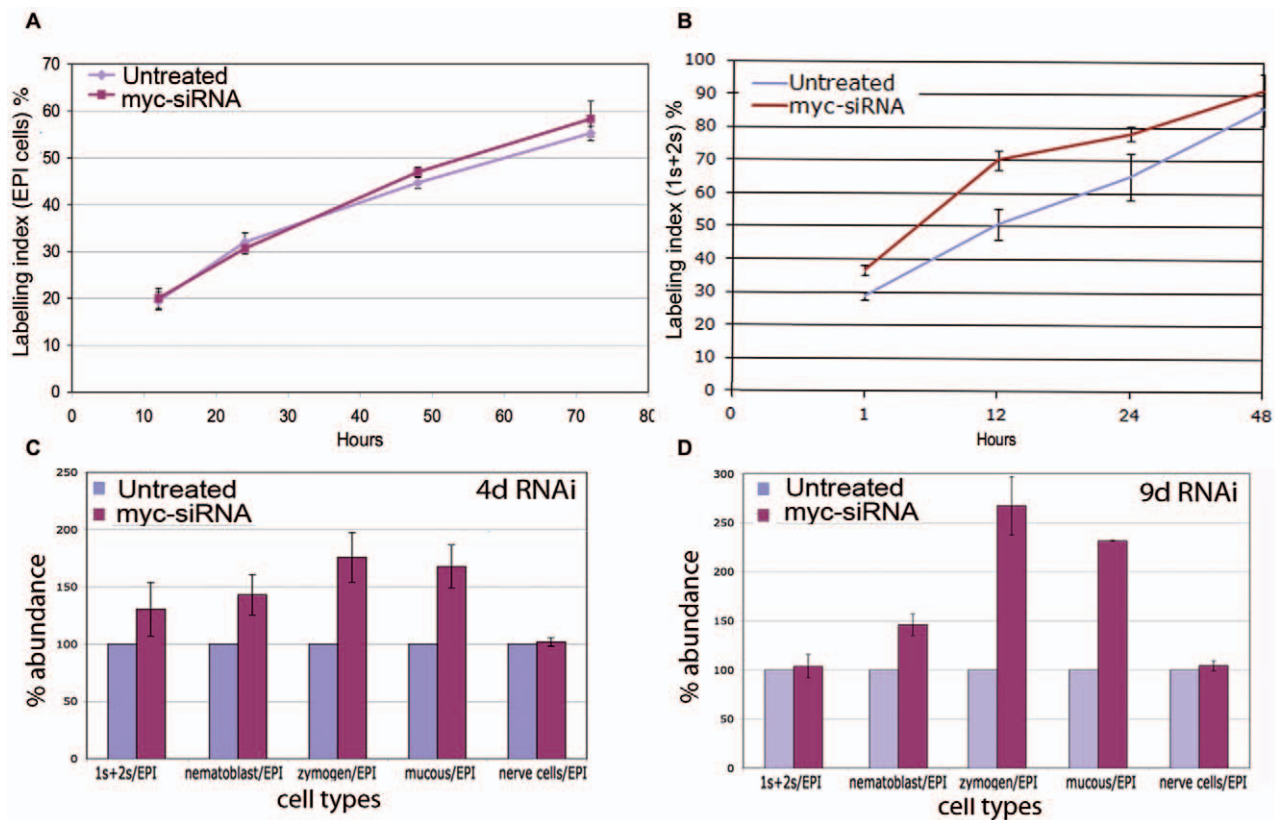


**Figure 4. Effect of *myc* RNAi on cell cycling activity and cell type distribution.** Cell cycling activity of epithelial cells (A) and 1 s+2 s stem cells (B) were obtained in control and treated animals by continuous incubation with BrdU, followed by maceration of ten animals at the indicated time points and fluorescence immunostaining. Data represent the average of three different experiments. In (C) and (D) the distribution of different cell types was assayed after 4 d and 9 d of *myc* RNAi, respectively. Five test animals were randomly selected from a pool of twenty five treated animals, and macerated for cell counting. The data represent the average of five independent RNAi experiments. Bars indicate standard errors. 1 s+2 s = single and pairs of interstitial cells; nematoblasts = nests of 4 s–16 s proliferating and differentiating nematoblasts; EPI = epithelial cells. doi:10.1371/journal.pone.0030660.g004

possibly affect cell type distributions. To this aim, the phenotype of the regenerating animals was analysed in more detail. *In situ* hybridization on *Hymec1* interfered regenerating animals, similarly to what observed on intact animals, did not reveal quantitative differences in the *Hymec1* expression pattern (data not shown), while a clear morphological phenotype was detected in the regenerated tentacles: the average tentacle length and nematocyte content per battery cells were significantly increased (Figure 7D–7F) indicating that *Hymec1* RNAi effect persists throughout the regenerative process and affects tentacle morphogenesis. These results substantiate the view of a role of *Hymec1* in the control of proliferation/differentiation rate in *Hydra*.

## Discussion

The possibility to perform gain- or loss- of function approaches to analyse gene function may add new values to the widespread use of *Hydra* as a genomic model organism with a pivotal position in the evolutionary tree. The generation of transgenic polyps by embryo microinjection is a well-established technique [33] and several methods have been successfully used to do RNAi in adults. The published RNAi methods rely on long dsRNA delivered through different techniques, spanning from whole animal electroporation [13] to localized electroporation [15], and used successfully for functional analysis of genes involved in head regeneration [15–34–35]. In order to reduce major side effects as tissue necrosis and lethality, a milder strategy for dsRNA delivery

through feeding of dsRNA producing bacteria has been developed and used for silencing of both endodermal and ectodermal expressed genes [36–37], while the soaking method using long dsRNA has been employed for efficient RNAi of key developmental genes in the marine hydroid *Hydractinia echinata* [38]. We developed in this paper a novel approach of RNAi in *Hydra*, based on siRNA oligonucleotides. First discovered in plants and in the nematode *Caenorhabditis elegans* [16–39–40] the production of siRNAs that bind to and induce also systemically [41] the degradation of specific endogenous mRNAs is now widely employed to inhibit gene function and holds great potentials in the therapeutic treatment of several diseases [42–44]. At cellular level, duplex siRNAs are negatively charged polymers and so cannot easily penetrate hydrophobic cellular membranes without assisting carriers such as cationic polymers, liposomes or nanoparticles. We succeeded in our delivering method by working in acidic conditions, which resulted in siRNA charge reversal and great enhancement of siRNA intracellular delivery. Alexa 488 labelled *myc*-siRNAs were found into the cytoplasm of *Hydra* ectodermal cells, within both epitheliomuscular and interstitial cells, as granular structures with different sizes, not excluding the presence of single units, undetectable by confocal microscopy analysis (Figure 1). The experimental conditions used for siRNA delivery confirm previous data on the importance of the positive surface charge of delivery vehicles in promoting cell uptake [12–45–46]. In *Drosophila* an active and specific pathway that involves clathrin-mediated endocytosis has been found responsible for



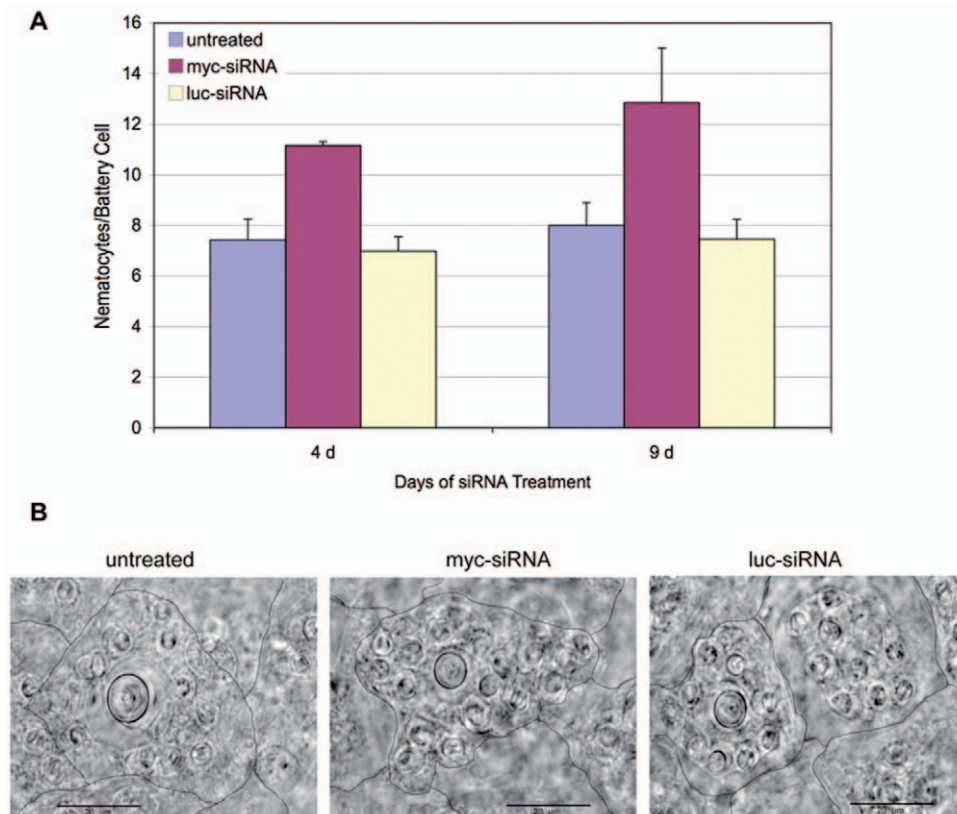


**Figure 5. *Hymec1* RNAi induces an increase in the nematocyte content of battery cells.** (A) At time 4 d and 9 d of treatment with the indicated siRNA, animals were fixed and the number of nematocytes embedded in the battery cells, observed under the same focus plane, was scored. Data represent the average of measures from ten animals  $\pm$  standard deviation. (B) Representative battery cells imaged from normal (left), *myc*-siRNA (middle) and *luc*-siRNA (right) treated animals, on whole mounts. Hand drawn black lines indicate the battery cell membranes. *Hymec1* downregulation induces nematocyte differentiation and accumulation into battery cells. Scale bar: 20  $\mu$ m. doi:10.1371/journal.pone.0030660.g005

siRNA uptake [47] and accumulation in vesicles, while the mechanism of cytoplasmic release to enter the RNAi machinery has not been identified to date. Although it might be argued that by our approach siRNA delivery occurs more into ectodermal cells rather than into interstitial cells, the strong molecular downregulation observed suggests that the RNAi response results from both direct delivery to interstitial cells and spreading effect of the RNAi response, similarly to other invertebrates [41–47]. This hypothesis is supported by the presence in the *Hydra* genome of predicted genes encoding for components required for amplification and systemic spread of an RNAi signal, i.e. RNA-dependent RNA polymerase (RdRP) and SID proteins (Hma1.117083 and Hma1.114101 respectively). Moreover, the cytoplasmic bridges present among nematoblasts might provide direct passage of siRNA signals through connected cells to enable RNAi. We targeted our RNAi approach to *Hymec1* gene and showed the specificity of our method including luciferase- and  $\beta$ -catenin-siRNA as negative and positive controls, respectively. While  $\beta$ -cat silencing proved the robustness and reproducibility of our RNAi method, *luc*-siRNA ineffectiveness in *Hymec1* downregulation demonstrated the absence of harmful sequence independent side effects elicited by the siRNA treatment: phenotypical, cellular and molecular analysis showed that *luc*-siRNA did not alter *Hymec1* expression, nor interfered with proliferative/differentiating processes leading to abnormal phenotypes.

*Hymec1* is homologue of the *c-myc* protooncogene, a key gene conserved throughout the animal kingdom [48], controlling

several fundamental processes of the cell cycle, both intracellular functions (cell growth, proliferation, apoptosis) and extracellular processes that coordinate cell proliferation with the microenvironment (the stem cell niche) [49]. Although the molecular, biochemical and functional analyses of *Hymec1* has highlighted structural conservation in the featuring domains (i.e. bHLH-Zip domain and *myc*-boxes I to III) and functional similarities to the vertebrate derivatives [10], its physiological role in *Hydra* has not been elucidated so far. By challenging living *Hydra* with *myc*-siRNAs, we specifically downregulated *Hymec1* mRNA and protein levels. The inhibition was achieved after 2 d of treatment, while continuous incubation up to 9 d, under normal feeding regime, did not cause cumulative effects, probably due to saturation of the RNAi machinery, or to other mechanisms of animal adaptation. Our experimental conditions ensured animal health all along the treatment period and the absence of stressing condition (such as starvation or chemical/physical compounds required for efficient delivery of nucleic acids), which can complicate the interpretation of the phenotypical effect of gene silencing. Despite the presence of an additional *myc* orthologue gene in the *Hydra* genome database (*Hymec2*) which could possibly interfere with *Hymec1* downregulation, a clear phenotypical effect was detected in *myc*-siRNA treated animals. At cellular level, an extensive analysis of single cells prepared by maceration revealed abnormal distribution ratios between cellular types of the interstitial cell lineage. As the density of the stem cell population (i.e. 1 s+2 s/EPI) is species-specific and dependent upon environ-

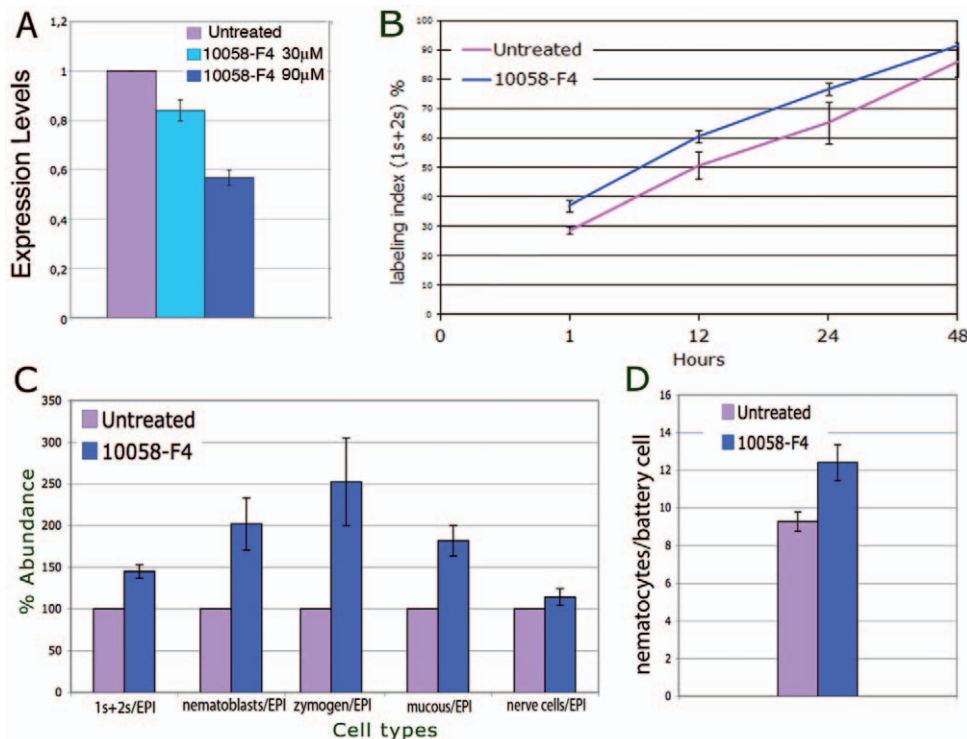


**Figure 6. Molecular and morphological alteration induced by the *c-myc* inhibitor 10058-F4.** A) Living polyps were treated with the *c-myc* inhibitor 10058-F4 for 48 h at two different concentrations (30 μM and 90 μM) before RNA extraction for qRT-PCR analysis. Expression levels, relative to *HyEF1α*, indicate *Hymc1* silencing in a dose dependent manner, reaching 47% downregulation at the higher dose tested. Error bars indicate standard deviations calculated from three independent experiments, each performed in triplicate. B) Cell cycling activity of 1 s+2 s stem cells were obtained in control and treated animals (as above, 10058-F4 90 μM) by continuous incubation with BrdU, followed by maceration of ten animals at the indicated time points and fluorescence immunostaining. Labelling indexes of 4 s and gland cells are reported in Figure S6 of Supporting Information. C) Single cell suspensions were prepared from polyps treated as in A and the relative cell types counted by phase contrast microscopy. Treatment with 10058-F4 enhances stem cell proliferation and determines the accumulation of intermediate and terminal differentiation products. D) Polyps treated with the *c-myc* inhibitor as in A were fixed and whole mounted for analysis of the nematocyte content into the tentacles (as described in Figure 5). The small molecule myc inhibitor induces an increase in the nematocyte content of battery cells, identical to the effect induced by *myc*-siRNA.

doi:10.1371/journal.pone.0030660.g006

mental stimuli, such as the feeding regime [6–25–26], we did not report the absolute values, but pointed out to their changes relatively to control animals. While not affecting the epithelial cell proliferation rate, *Hymc1* downregulation induced a moderate increase in the stem cell proliferation rate and density, which produced dramatic effects on the related cell population sizes. These results are in line with previous studies relating stem cell self-renewal to the cell density, and showing that nematocyte commitment increases as stem cell concentration increases [15–24–26]. The abnormal numbers of mature nematocytes embedded in the tentacle battery cells confirmed the burst in the nematocyte differentiation. Although we cannot exclude an effect on nerve cell commitment, the measure of mature nerve cells, found unaffected by *Hymc1* repression, ruled out an enhancement in nerve cell differentiation. By contrast, the secretory cell differentiation pathway was profoundly activated, as shown by the doubled numbers of both zymogen and mucous cells. Interestingly, at 9 d of treatment, the stem cell density was restored to physiological levels, suggesting a negative feedback between stem cells, as elsewhere proposed [6]. The specificity of the effects produced by *Hymc1* inhibition was confirmed using a chemical inhibitor of the MYC/MAX interaction, 10058-F4 [29]. Treatment of living polyps with this inhibitor induced *Hymc1* downregulation, as well as increased 1 s+2 s stem cell proliferation and enhanced differentiation of nematoblasts, secretory cells and nematocytes.

A schematic model of the effects of both the genetic and biochemical *Hymc1* inhibition on the proliferation/differentiation rates is shown in Figure 8. Altogether these results suggest a role of *Hymc1* in the negative regulation of the stem cells where it is expressed: the decreased expression enhances stem cell proliferation and in turn the differentiation of intermediates and terminal derivatives. The increase in stem cell density may finally inhibit the stem cell self-renewal capability over long periods.

Of intriguing interest is the effect displayed by *Hymc1* RNAi on *Hydra* regeneration. qRT-PCR showed that, 24 h post amputation *Hymc1* transcription levels are similar to pre-amputation. Regenerated heads also presented morphological traits similar to the pre-amputated animals, i.e. longer tentacles armed with an abnormal number of nematocytes, suggesting the persistence of the RNAi response. Consistent with this hypothesis are evidences from *C.elegans*, in which effective interference is observed in the progeny of dsRNA injected animals at early larval stages [21], and from the planarian flatworm *Schmidtea mediterranea*, where gene inhibition persists throughout the process of regeneration [50].

The involvement of *c-myc* in controlling cell proliferation and differentiation processes has been shown in several systems, by both gain and loss of function approaches. In murine hematopoietic stem cells (HSC) the group of Trumpp showed that *c-myc* conditional elimination resulted in the accumulation of HSCs in



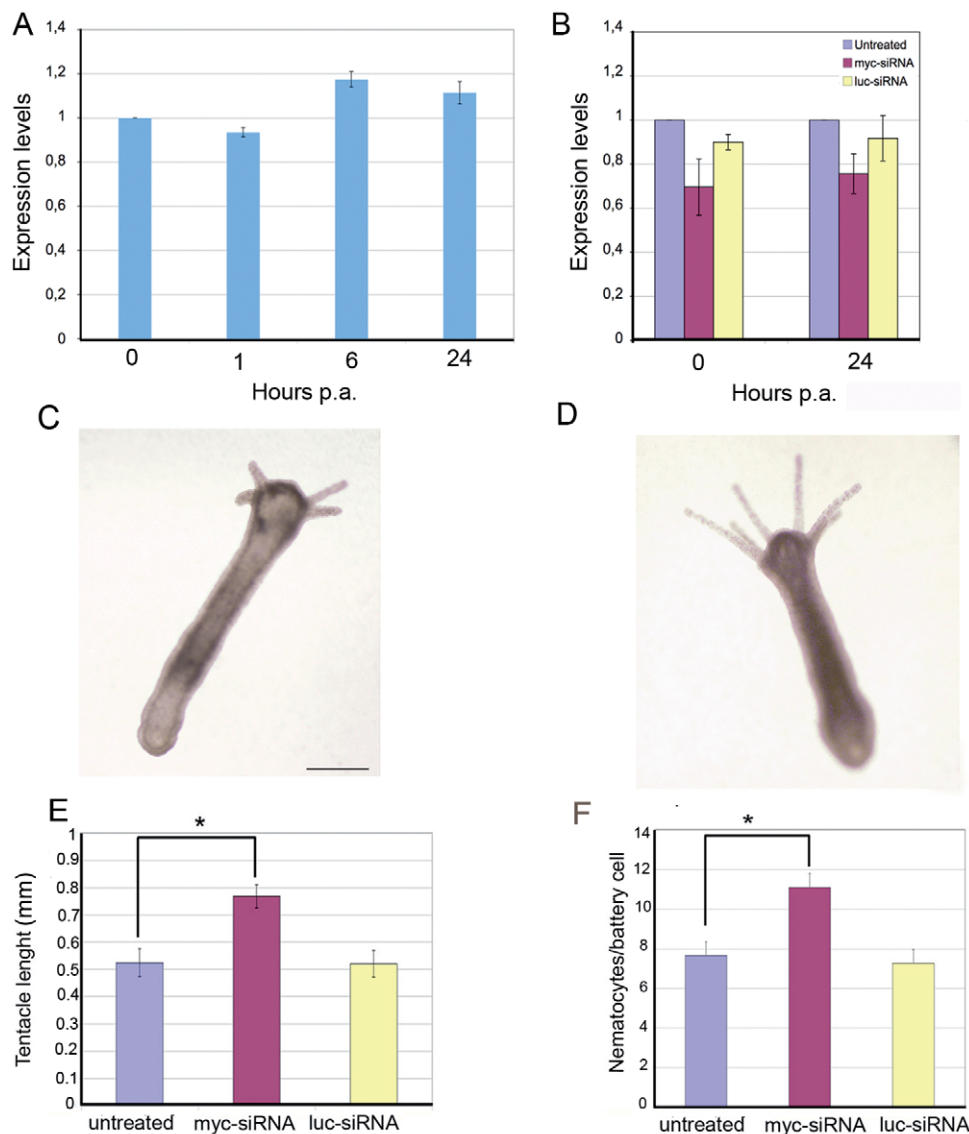


**Figure 7. Effect of *Hymc1* RNAi on regeneration.** A) Healthy animals were bisected at time  $t=0$  and allowed to regenerate for the indicated period, expressed in hours. At different times post amputation (p.a.) total RNA was extracted and analysed by qRT-PCR. Not significant differences in *Hymc1* expression levels were detected during the regenerative process. B) *myc*-siRNA treatment (4 d) caused a reduction of *myc* mRNA levels. At this point (time  $t=0$ ) animals were bisected and allowed to regenerate for the indicated hours. Downregulation effects persist during regeneration. Each error bar indicates standard deviation calculated from triplicates. C–D) *myc*-siRNA treated animal present abnormal tentacle morphogenesis. Representative phenotypes of head regeneration at 72 hr post amputation are shown. A *myc*-siRNA treated animal (D) presents tentacles of increased length compared to untreated (C) or *luc*-siRNA treated polyps (not shown). Scale bars: 500  $\mu$ m. E) The average of tentacle length, calculated on a subset of 20 animals/condition, indicates the faster tentacle development induced by *myc*-RNAi. Asterisk indicates  $p<0.05$ , according to t-Student test). F) The average nematocyte content of the battery cells was scored on tentacles of regenerating animals at 96 hr post amputation. *myc*-RNAi promotes nematocyte differentiation. doi:10.1371/journal.pone.0030660.g007

*situ* due to their failure to initiate normal stem cell differentiation [51–52]. In human pancreatic endocrine cell lines *c-myc* down-regulation by RNAi induces cells to exit the cell cycle and enter the differentiation pathway, thus *c-myc* plays a role in the switch mechanism that controls the inverse relationship between proliferation and differentiation [53]. In *Drosophila* mutation of the *Drosophila myc* gene results in small flies due not to fewer cells but to their cells which are smaller in size [54], suggesting that *dmec* participates in the regulation of cell mass. Although *myc* and the members of the *myc* “network” are encoded in the genomes of most metazoan phyla and many aspects of its biology may arise

from comparative analysis, the disparate cellular events seeing its involvement make it difficult to evaluate *myc*’s function in its entirety due to redundancy among family members, tissue specificity, and complex phenotypes.

In Cnidaria, the molecular mechanism underlying RNAi have not been elucidated so far. We show the capability of siRNA to enter *Hydra* cells and to trigger a RNAi response, similarly to many metazoans. Many other aspects of the *Hydra* RNAi response need to be addressed now, from the systemic long range character of the RNAi response, to the mechanisms underlying the uptake of siRNA, to the deviation from standard endocytic uptake at some

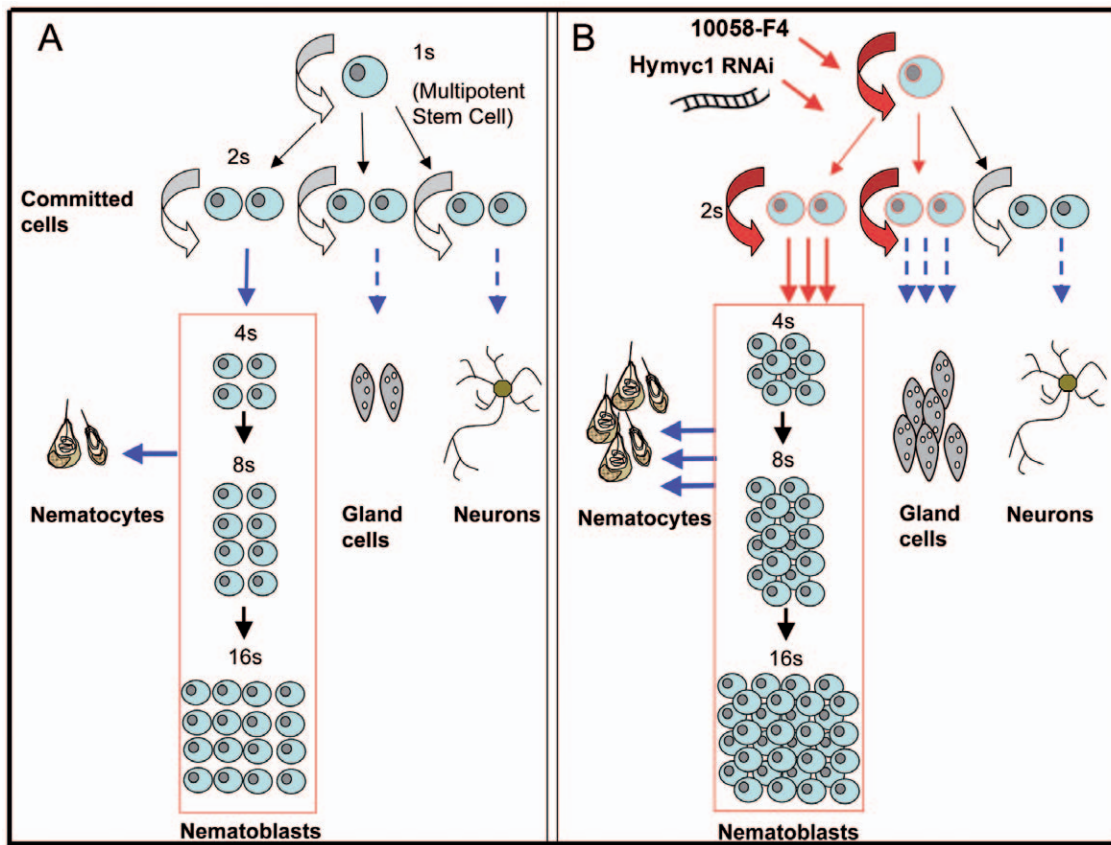


**Figure 8. Interstitial cell differentiation pathways.** Schematic representation of the multiple differentiation pathways of the interstitial stem cells in homeostatic condition (A) and the effects on stem cell proliferation/differentiation induced by genetic or biochemical *Hymyc1* downregulation (B). *myc*-siRNA treatment or *myc* biochemical inactivation induce a moderate increase in the 1 s and 2 s stem cell self-renewal and proliferation activity (red arrows). This in turn generates a higher number of both differentiating intermediates (nematoblasts) and terminal differentiated products such as nematocytes and gland cells (blue arrows). Dashed arrows indicate the absence of morphological distinct cellular intermediates. *Hymyc1* downregulation does not affect the nerve differentiation pathway, consistent with the absence of *Hymyc1* expression in this cell type.

doi:10.1371/journal.pone.0030660.g008

point to deliver dsRNA to the cytoplasm, to date unknown in any model of RNAi. The current design in our group of nanocarriers to improve siRNA delivery, self-tracking and specificity will surely provide in the near future new tools to decipher the mechanisms of RNA interference in *Hydra*.

In conclusion, this study focuses on *Hymyc1* silencing, through an innovative RNAi strategy enhancing siRNA uptake in the polyp, and describes how *Hymyc1* knockdown affects the developmental dynamics of stem and interstitial cell lineage in *Hydra*. In particular, our results add significant value to fundamental studies on the stem cell biology addressing the mechanisms by which these cells maintain the balance between self-renewal and differentiation. As *myc* deregulated expression occurs in the majority of human cancers, understanding the ancient roots of *myc* biology may be of interest for the wide scientific community targeting *c-myc* for therapeutic purposes. For scientists working on cnidarians this paper opens new avenues to decipher the molecular control of the cellular plasticity underlying growth and proliferation in *Hydra*.

Finally, the establishment of a RNAi method which avoids invasive procedures while ensures effective delivery of siRNA under normal culturing condition, lays the foundations of a comprehensive analysis of the RNAi response in *Hydra* allowing to track back in the evolution the origin of the RNAi response.

## Materials and Methods

### Culture of animals and regeneration experiments

*Hydra vulgaris* (strain Zurich, originally obtained by P.Tardent) were asexually cultured in *Hydra* medium (1 mM  $\text{CaCl}_2$ , 0.1 mM  $\text{NaHCO}_3$ , pH 7) by the method of Loomis and Lenhoff with minor modifications. The animals were kept at  $18 \pm 1^\circ\text{C}$  and fed three times per week with freshly hatched *Artemia salina* nauplii. Polyps from homogeneous populations, three-weeks-old and carrying one or two buds, were selected for the experiments. For regeneration experiments, treated polyps (4 d of treatment) were bisected in the upper gastric region and monitored at various time points post amputation.

### In vivo RNA interference through small interfering RNAs

For RNA interference groups of 25 animals were collected in plastic multiwells, allowed to equilibrate at room temperature in 1 ml of *Hydra* medium at pH4. The test was initiated by adding 70 nM siRNA to each well containing the animals, since then continuously exposed to the siRNA oligonucleotides, under normal feeding regime. After the washing procedures new siRNA oligonucleotides were supplied. 21 bp long siRNA targeting *Hymyc1* were designed using on line siRNA design services and purchased by QIAGEN. Both unlabelled and 3'- Alexa fluor 488

siRNA were designed on the *Hymyc1* DNA target sequence: 5'-AAGATGCTCACGCGTCAAGAA-3'. As control of silencing specificity, siRNA oligonucleotides targeting the Luciferase GL2 gene were purchased by QIAGEN (cat no 1022070). Moreover, as positive control to assess the reliability of this RNAi method,  $\beta$ -catenin gene expression was interfered by using a specific 21 bp long siRNA corresponding to nucleotides 750–770 of *Hydra vulgaris*  $\beta$ -catenin mRNA (GenBank Accession no. U38624.1). The myc inhibitor 10058-F4 (5-[(4-Ethylphenyl)methylene]-2-thioxo-4-thiazolidinone) was purchased by Sigma-Aldrich (cat no. F3680). Groups of 25 animals were incubated for 48 h in presence of 10058-F4 (30  $\mu$ M or 90  $\mu$ M), and then used for molecular and cellular characterization, as described in the following sections.

## Imaging

siRNA uptake was monitored *in vivo*, using a Camedia-digital camera (Olympus) connected to a stereomicroscope (Olympus ZSX-RFL2) equipped with fluorescence filter sets (BP460-490/DM505/LP510). Following extensive washes, *in vivo* imaging was accomplished by an inverted microscope (Axiovert 100, Zeiss) equipped with a digital colour camera (Olympus, DP70) and fluorescence filter sets (BP450-490/FT510/LP515). For imaging acquisition and analysis the software system Cell F (Olympus) was used. Confocal images were collected with a Leica TCS SP2 AOBS confocal microscope (Mannheim, Germany) with 40 $\times$  oil immersion optics. Laser lines at 488 nm and 633 nm for excitation of Alexa fluor 488 and TOPO-ETC were provided by an Ar laser and a HeNe laser, respectively. Detection ranges were set to eliminate crosstalk between fluorophores. Tissue imaging of interfered animals was performed under bright field.

Quantification of *in situ* hybridization signal for *Hymyc1* was accomplished as it follows: whole mounted animals were imaged by an inverted microscope (Axiovert 100, Zeiss) equipped with a digital colour camera (Olympus, DP70). Images were taken under the same conditions of acquisition (light and exposure time), saved in tagged-image file format (TIFF) at a size of 1300 $\times$ 1030 pixels, posterized by Adobe Photoshop by setting the same threshold levels and then converted in HSB format for data processing using the Image processing and Analysis software Image J (Version 1.45i).

## Gene and protein expression analyses

Whole-mount *in situ* hybridization using DIG-labelled RNA probe was carried out as described previously [55] using NBT/BCIP (Roche) as substrate for staining. The myc riboprobe was synthesized using the plasmid *Hymyc1* (GenBank Accession no. GQ856263) as template and used at a concentration of 0.1 ng/ml for hybridization. The *Hymyc1* plasmid was produced as described [10].

Total RNAs from treated and untreated animals was purified using Tri Reagent (Molecular Research Center) and its concentration was quantified on the NanoDrop ND-1000 spectrophotometer (Thermo Scientific, USA). The first-strand cDNA synthesis was carried out with the SuperScript II Retrotranscriptase (Invitrogen) and oligo dTs, using 0.5  $\mu$ g of DNA-free RNA in a final volume of 25  $\mu$ l, according to the manufacturer's instructions. Semiquantitative RT-PCR was employed to estimate myc mRNA levels. Each PCR reaction was carried out with Platinum Taq DNA Polymerase kit (Invitrogen) in a total volume of 25  $\mu$ l containing 1  $\mu$ l cDNA and 0.5  $\mu$ M primers for *Hymyc1* (forward: AGGACGAAGTTGATGTAGTTGGA; reverse: 5'-GCGAAGCAACTTTTCAGTATTGTTAC-3') and *Hydra* Elongation factor 1 $\alpha$  (5'-ATGATTGAACCATCCCCAAA-3'; 5'-GCT-TCAATGGCAGGATCATT 3') as reference gene. After initial

denaturing step of 5' at 94°C, cycling steps were as follows: 30 s at 94°C, 30 s 58°C and 30 s at 72°C. For comparative analysis, the experiments were done in triplicate and data were collected at different end point (25, 30 and 35 cycles).

Quantitative Real-Time polymerase chain reaction (qRT-PCR) was performed in 25  $\mu$ l of reaction mixture consisting of 1 $\times$  Platinum SYBR green qPCR SuperMix-UDG with ROX (Invitrogen), serial cDNA dilutions and 0.5  $\mu$ M each primer. The reactions were processed using the StepOne Real-Time PCR system (Applied Biosystem) under the following cycling steps: initial denaturation for 10 min at 94°C, followed by 40 cycles at 94°C for 15 s, 58°C for 30 s, and 72°C for 30 s, and a 20 min gradient from 55°C to 90°C to obtain a melting curve. To normalize RNA levels, *Hydra* Elongation factor 1 $\alpha$  gene (HyEf-1 $\alpha$  GenBank Accession no. Z68181.1) was employed as internal calibrator. Gene-specific primers (HyEf-1 $\alpha$ : forward, 5'-CCAG-GAGACAATGTCTGGTTT 3'; reverse, 5'-GCTTCAATGG-CAGGATCATT 3'; *Hymyc1*: forward, 5'-TACAGAAAGC-GAGGACGAAGTT 3'; reverse, 5'-GCGAAGCAACTTTTCA-GTATTGTTAC 3';  $\beta$ -cat: forward, 5'-GGCGCTCTTCACA-TTTTAGC 3'; reverse, 5'-TGCACCTTCACGCTCAATAG 3') were designed using Primer3 software (<http://frodo.wi.mit.edu/primer3/>); the lengths of *HyEf-1 $\alpha$*  and *Hymyc1* amplicons were 100 bp and 157 bp, respectively. At least three independent repeats for each experiment were carried out. Herein, the delta-delta Ct ( $2^{-\Delta\Delta Ct}$ ) method, for comparing relative expression results between treatments, was applied [56].

For Western blot analysis total proteins were extracted from groups of 25 animals, using the triple detergent buffer according to Sambrook *et al.* [57]. The resulting homogenate was centrifuged for 15 min at 14000 *g* and the proteins contained into the supernatants collected and quantified by the Bradford method using BioRad reagent with BSA as a standard. Equal amounts of proteins were separated on 12% SDS-polyacrylamide gel and transferred onto nylon membranes (BioRad, San Diego, CA). MYC protein levels were detected using anti-HyMYC1 antibody (1:500, kindly provided by K.Bister, University of Innsbruck) and compared to actin proteins, using an anti-actin primary antibody (1:100, Sigma) to probe an identical blotted gel.

## Hydra cell and tissue analysis

Analysis of siRNA treated animals was done both on whole animals and isolated fixed cells. Animals were anaesthetized in 2% urethane in *Hydra* medium for 2 min. The relaxed and elongated *Hydra* were fixed with Lavdowsky's fixative (ethanol: formalin: acetic acid: water-50:10:4:40), rehydrated, and mounted on microscope slides in Glycerol 50% in PBS (8 g/l NaCl; 0.2 g/l KCl; 1.44 g/l Na<sub>2</sub>HPO<sub>4</sub>·7H<sub>2</sub>O; 0.24 g/l KH<sub>2</sub>PO<sub>4</sub>). The tentacles were examined for two types of nematocyst capsules (stenoteles and desmonemes) under an optical microscope. The battery cell structure, indeed, makes it possible to count the nematocytes with phase optics (32 $\times$ ) on the surface of a fixed tentacle facing the objective. Each tentacle was divided into three ideal sections of different length from the base to tip, and the number of nematocytes present in the middle section was counted. The ratio nematocyte/battery cell was calculated on a total of one hundred battery cells, collected on ten different polyps. An estimate of the tentacle length during head regeneration was calculated on images from both untreated and siRNA treated animals using the Cell F software (Olympus). At least 25 animals/condition were analysed.

For analysis of cell type distribution whole animals were macerated into a suspension of fixed single cells as described [58]. Five animals per condition were macerated at the indicated time of treatment and scored for single and pairs of interstitial cells

(1 s+2 s), nests of four –sixteen proliferating or differentiating nematoblasts (4 s–16 s), zymogen and mucous cells, epithelial cells (EPI). An average of 300 EPI cells was counted, per condition. For cell nuclei detection cells were stained with 4',6-diamidino-2-phenylindole dihydrochloride (DAPI) 0.25 mg/L before mounting. For analysis of proliferation rates, intact *Hydra*, untreated or treated for 48 hr with *myc*-siRNA, were continuously incubated with bromodeoxyuridine (BrdU) 5 mmol/l (Sigma) for 1, 12, 24, 48 and 72 hr, immediately fixed, and macerated cells spread on microscope slides as above described. BrdU incorporation in proliferating cells was detected by immunolocalization using mouse anti BrdU monoclonal antibody (1:500, Sigma), and Novolink Polymer detection System (Novocastra Laboratories Ltd.). To further estimate cell proliferation, mitotic index was measured on macerates through phase contrast optical microscopy combined with Hoechst 33342 staining of nuclear DNA by counting the percentage of cells undergoing mitosis ( $n = 1000$  cells for each treatment). To quantify cell cycle distribution, DNA content profiles were determined on Hoechst 33342-stained macerates. Fluorescence intensity of individual nuclei was quantified by using the Fiji program from ImageJ software package.

For tissue sectioning, test animals were soaked over night in 30% sucrose in PBS and then embedded in the frozen section medium Neg-50 (Richard-Allan Scientific). Cryo-sections of 10  $\mu$ m thickness were obtained by a cryostat (Leitz, digital 1760), collected on gelatine coated slides (Superfrost microscope slides, Menzel) and mounted in D.P.X (Sigma) before imaging.

### Statistical analysis

Tentacle length measurements, number of nematocyte per battery cell, relative cell type counting and qRT-PCR results were expressed as means  $\pm$  SD. The statistical significance of the results was determined by analysis of Student's *t* test. *p* values of  $<0.01$  were considered highly statistically significant (two asterisks). *p* values of  $<0.05$  were considered statistically significant (one asterisk).

### Supporting Information

**Figure S1 Structural anatomy of *Hydra vulgaris*.** a) Picture of living *Hydra*. The animal has a simple body plan: it is a tube with a head at the apical end, and a foot, or basal disc at the other. The head is in two parts, the hypostome (mouth) at the apex, and below that the tentacle zone from which a ring of tentacles emerge. Scale bar 200  $\mu$ m b) the bilayered structure of the animal: the body wall is composed of two self renewing cell layers, an outer ectoderm and an inner endoderm, separated by an extracellular matrix, the mesoglea. The arrows on the left side indicate the direction of tissue displacement c) longitudinal sections at level of tentacle (upper figure) and gastric region (lower figure). On the tentacle, the ectodermal cells (ec) are called battery cells and contain embedded several types of nematocytes (nem), one sensory neuron facing the exterior (sn), a ganglial neuron (gn) making connections both with other cells and to myonemes. Along the animal body both ectoderm and endoderm layers are composed of epitheliomuscular cells, while interstitial stem cells and their intermediate and terminal derivatives (neurons, nematocytes and secretory cells) are interspersed among ectoderm and endoderm.

(TIF)

**Figure S2 Zeta potential of siRNA as a function of pH.** The zeta potential of siRNA depends on the pH of the solution: while at neutral pH siRNA show negative zeta potential values due

to the presence of phosphate groups of the RNA backbone, at acidic pH, in *Hydra* culture medium, the presence of calcium divalent ions neutralize the negative charges, conferring a positive net charge to the molecules. The positive charge influences the electrokinetics of the siRNA molecules, promoting their intracellular uptake. Measurements were performed in Hydra medium, at the indicated pH.

(EPS)

**Figure S3 Acidic pH does not affect *Hymyc1* expression levels.** A) Endogenous *Hymyc1* expression levels were measured by qRT-PCR on animals kept for the indicated periods at neutral or acidic pH. Not significant differences were induced by the different conditions. Data are mean of three independent experiments. B) Image of a representative polyp incubated at in *Hydra* medium at pH 4 for 4 days. The polyp appears healthy, with long extended tentacles and presents no signs of toxicity induced by the treatment.

(EPS)

**Figure S4 Efficient silencing of  $\beta$ -catenin gene through siRNA mediated RNAi.** qRT-PCR was performed on total RNA extracted from polyps treated 2 d with *Hydra*  $\beta$ -catenin specific siRNA. A significant reduction of the *Hy* $\beta$ -cat transcript levels (60%), compared to *HyEF1 $\alpha$* , was induced by *Hy* $\beta$ -cat siRNA, showing the reliability and robustness of our approach. Two asterisks,  $p < 0.01$ , according to t-Student test.

(TIF)

**Figure S5 Quantification of *in situ* hybridization signal for *Hymyc1* mRNA.** The Image processing and Analysis software Image J (Version 1.45i) was used to quantify the signal intensity produced by *in situ* hybridization in control, *myc*-siRNA and *luc*-siRNA treated animals, using *Hymyc1* as probe. Not significant differences were detected as effect of siRNA treatment, indicating residual *Hymyc1* transcripts in *myc*-RNAi animals. On the other side, *luc*-siRNA animals were not affected in *Hymyc1* expression, confirming the absence of putative side effects.

(TIF)

**Figure S6 Effect of *Hymyc1* RNAi on nematoblast and gland cell proliferation.** Cell cycling activity of A) nematoblasts (4 s) and B) gland cells. Control untreated animals (incubated at pH 4) and *myc*-siRNA treated animals were continuously incubated with BrdU (red line) and with the *c-myc* inhibitor 10058-F4 (90  $\mu$ M, green line), before maceration at the indicated time points and fluorescence immunostaining. Data represent the average of three different experiments. Not significant differences were observed in the proliferation rates of 4 s and gland cells induced by *myc*-siRNA or 10058-F4 treatments.

(TIF)

**Figure S7 Nuclear DNA content of interstitial stem cells (1 s+2 s) in *myc*-siRNA treated *Hydra*.** A) Hoechst 33342 staining and B) phase contrast image of macerated cells. 1 s and 2 s: large interstitial stem cells (note that 1 s is in mitosis); ecto: ectodermal epithelial cell; endo: endodermal epithelial cell; gc: gland cell. C) After three or four days of siRNA treatment, the nuclear DNA profile of 1 s+2 s shows no significant differences as compared with untreated polyps. Nuclei of 25 nerve cells and differentiated nematocytes, which are terminally arrested in G1, were used to determine the fluorescence intensity of the 2C DNA content. Procedures: Polyps were treated for three or four days with *myc*- siRNA. Then, treated and untreated animals were macerated and spread onto microscope slides. After drying, the maceration preparations were stained with Hoechst 33342.

Fluorescence intensity of individual nuclei was finally quantified by using the Fiji program of the ImageJ software package. (TIF)

**Figure S8 Distribution of the ratio nematocyte/battery cells among different animals.** At time 4 d and 9 d of treatment with the indicated siRNA, animals were fixed and examined under an optical microscope. Under fixed focus plane, the ratio nematocyte/battery cell was calculated on a total of one hundred battery cells, collected on ten different polyps. *myc*-siRNA specifically induces an increase in the nematocytes embedded in the tentacle battery cells. (TIF)

## References

- Askew DS, Ashmun RA, Simmons BC, Cleveland JL (1991) Constitutive c-myc expression in an IL-3-dependent myeloid cell line suppresses cell cycle arrest and accelerates apoptosis. *Oncogene* 6: 1915–1922.
- Bosch TC (2009) Hydra and the evolution of stem cells. *Bioessays* 31: 478–486.
- Bode HR (1996) The interstitial cell lineage of hydra: a stem cell system that arose early in evolution. *J Cell Sci* 109(Pt 6): 1155–1164.
- Watanabe H, Hoang VT, Mattner R, Holstein TW (2009) Immortality and the base of multicellular life: Lessons from cnidarian stem cells. *Semin Cell Dev Biol* 20: 1114–1125.
- Campbell RD, David CN (1974) Cell cycle kinetics and development of Hydra attenuata. II. Interstitial cells. *J Cell Sci* 16: 349–358.
- Holstein TW, David CN (1990) Cell cycle length, cell size, and proliferation rate in hydra stem cells. *Dev Biol* 142: 392–400.
- Amati B, Brooks MW, Levy N, Littlewood TD, Evan GI, et al. (1993) Oncogenic activity of the c-Myc protein requires dimerization with Max. *Cell* 72: 233–245.
- Evan GI, Littlewood TD (1993) The role of c-myc in cell growth. *Curr Opin Genet Dev* 3: 44–49.
- Shi Y, Glynn JM, Guilbert LJ, Cotter TG, Bissonnette RP, et al. (1992) Role for c-myc in activation-induced apoptotic cell death in T cell hybridomas. *Science* 257: 212–214.
- Hartl M, Mitterstiller AM, Valovka T, Breuker K, Hobmayer B, et al. (2010) Stem cell-specific activation of an ancestral myc protooncogene with conserved basic functions in the early metazoan Hydra. *Proc Natl Acad Sci U S A*.
- Elbashir SM, Harborth J, Lendeckel W, Yalcin A, Weber K, et al. (2001) Duplexes of 21-nucleotide RNAs mediate RNA interference in cultured mammalian cells. *Nature* 411: 494–498.
- Tortiglione C, Quarta A, Malvindi MA, Tino A, Pellegrino T (2009) Fluorescent nanocrystals reveal regulated portals of entry into and between the cells of Hydra. *PLoS One* 4: e7698.
- Lohmann JU, Endl I, Bosch TC (1999) Silencing of developmental genes in Hydra. *Dev Biol* 214: 211–214.
- Miljkovic M, Mazet F, Galliot B (2002) Cnidarian and bilaterian promoters can direct GFP expression in transfected hydra. *Dev Biol* 246: 377–390.
- Smith KM, Gee L, Bode HR (2000) HyAlx, an aristaless-related gene, is involved in tentacle formation in hydra. *Development* 127: 4743–4752.
- Elbashir SM, Lendeckel W, Tuschl T (2001) RNA interference is mediated by 21- and 22-nucleotide RNAs. *Genes Dev* 15: 188–200.
- Naito Y, Yoshimura J, Morishita S, Ui-Tei K (2009) siDirect 2.0: updated software for designing functional siRNA with reduced seed-dependent off-target effect. *BMC Bioinformatics* 10: 392.
- Reynolds A, Leake D, Boese Q, Scaringe S, Marshall WS, et al. (2004) Rational siRNA design for RNA interference. *Nat Biotechnol* 22: 326–330.
- Hunter RJ (1988) Zeta Potential in Colloid Science: Principles and Applications. Academic Press, UK.
- Kim D, Rossi J (2008) RNAi mechanisms and applications. *Biotechniques* 44: 613–616.
- Timmons L, Court DL, Fire A (2001) Ingestion of bacterially expressed dsRNAs can produce specific and potent genetic interference in *Caenorhabditis elegans*. *Gene* 263: 103–112.
- Gee L, Hartig J, Law L, Wittlieb J, Khalturin K, et al. (2010) beta-catenin plays a central role in setting up the head organizer in hydra. *Dev Biol* 340: 116–124.
- Hobmayer B, Rentzsch F, Kuhn K, Happel CM, von Laue CC, et al. (2000) WNT signalling molecules act in axis formation in the diploblastic metazoan Hydra. *Nature* 407: 186–189.
- David CN, Campbell RD (1972) Cell cycle kinetics and development of Hydra attenuata. I. Epithelial cells. *J Cell Sci* 11: 557–568.
- Holstein TW, Hobmayer B, David CN (1991) Pattern of epithelial cell cycling in hydra. *Dev Biol* 148: 602–611.
- Sproull F, David CN (1979) Stem cell growth and differentiation in Hydra attenuata. II. Regulation of nerve and nematocyte differentiation in multiclonal aggregates. *J Cell Sci* 38: 171–179.
- Hobmayer B, Holstein T, David C (1990) Tentacle morphogenesis I. Development 109: 887–895.
- Hobmayer B, Holstein T, David C (1990) Tentacle morphogenesis in Hydra II. Development 109: 897–904.
- Yin X, Giap C, Lazo JS, Prochownik EV (2003) Low molecular weight inhibitors of Myc/Max interaction and function. *Oncogene* 22: 6151–6159.
- Huang MJ, Cheng YC, Liu CR, Lin S, Liu E (2006) A small-molecule c-Myc inhibitor, 10058-F4, induces cell-cycle arrest, apoptosis, and myeloid differentiation of human acute myeloid leukemia. *Exp Hematol* 34: 1480–1489.
- Gomez-Curet I, Perkins RS, Bennett R, Feidler KL, Dunn SP, Kruger LJ (2006) c-Myc inhibition negatively impacts lymphoma growth. *J Pediatr Surg* 41: 207–211.
- Galliot B, Miljkovic-Licina M, de Rosa R, Chera S (2006) Hydra, a niche for cell and developmental plasticity. *Semin Cell Dev Biol* 17: 492–502.
- Wittlieb J, Khalturin K, Lohmann JU, Anton-Erxleben F, Bosch TC (2006) Transgenic Hydra allow in vivo tracking of individual stem cells during morphogenesis. *Proc Natl Acad Sci U S A* 103: 6208–6211.
- Cardenas MM, Salgado LM (2003) STK, the src homologue, is responsible for the initial commitment to develop head structures in Hydra. *Dev Biol* 264: 495–505.
- Lohmann JU, Bosch TC (2000) The novel peptide HEADY specifies apical fate in a simple radially symmetric metazoan. *Genes Dev* 14: 2771–2777.
- Chera S, de Rosa R, Miljkovic-Licina M, Dobretz K, Ghila L, et al. (2006) Silencing of the hydra serine protease inhibitor Kazal1 gene mimics the human SPINK1 pancreatic phenotype. *J Cell Sci* 119: 846–857.
- Chera S, Ghila L, Dobretz K, Wenger Y, Bauer C, et al. (2009) Apoptotic cells provide an unexpected source of Wnt3 signaling to drive hydra head regeneration. *Dev Cell* 17: 279–289.
- Duffy DJ, Plickert G, Kuenzel T, Tilmann W, Frank U (2010) Wnt signaling promotes oral but suppresses aboral structures in *Hydractinia* metamorphosis and regeneration. *Development* 137: 3057–3066.
- Fire A, Xu S, Montgomery MK, Kostas SA, Driver SE, et al. (1998) Potent and specific genetic interference by double-stranded RNA in *Caenorhabditis elegans*. *Nature* 391: 806–811.
- Gheysen G, Vanholme B (2007) RNAi from plants to nematodes. *Trends Biotechnol* 25: 89–92.
- Timmons L, Tabara H, Mello CC, Fire AZ (2003) Inducible systemic RNA silencing in *Caenorhabditis elegans*. *Mol Biol Cell* 14: 2972–2983.
- Castanotto D, Rossi JJ (2009) The promises and pitfalls of RNA-interference-based therapeutics. *Nature* 457: 426–433.
- Kim DH, Rossi JJ (2007) Strategies for silencing human disease using RNA interference. *Nat Rev Genet* 8: 173–184.
- Whitehead KA, Langer R, Anderson DG (2009) Knocking down barriers: advances in siRNA delivery. *Nat Rev Drug Discov* 8: 129–138.
- Howard KA (2009) Delivery of RNA interference therapeutics using polycation-based nanoparticles. *Adv Drug Deliv Rev* 61: 710–720.
- Torchilin VP, Levchenko TS, Rammohan R, Volodina N, Papahadjopoulos-Sternberg B, et al. (2003) Cell transfection in vitro and in vivo with nontoxic TAT peptide-liposome-DNA complexes. *Proc Natl Acad Sci U S A* 100: 1972–1977.
- Saleh MC, van Rij RP, Hekele A, Gillis A, Foley E, et al. (2006) The endocytic pathway mediates cell entry of dsRNA to induce RNAi silencing. *Nat Cell Biol* 8: 793–802.
- de la Cova C, Johnston LA (2006) Myc in model organisms: a view from the flyroom. *Semin Cancer Biol* 16: 303–312.
- Wilson A, Laurenti E, Trumpp A (2009) Balancing dormant and self-renewing hematopoietic stem cells. *Curr Opin Genet Dev* 19: 461–468.
- Newmark PA, Reddien PW, Cebria F, Sanchez Alvarado A (2003) Ingestion of bacterially expressed double-stranded RNA inhibits gene expression in planarians. *Proc Natl Acad Sci U S A* 100 Suppl 1: 11861–11865.
- Laurenti E, Wilson A, Trumpp A (2009) Myc's other life: stem cells and beyond. *Curr Opin Cell Biol* 21: 844–854.
- Laurenti E, Varnum-Finney B, Wilson A, Ferrero I, Blanco-Bose WE, et al. (2008) Hematopoietic stem cell function and survival depend on c-Myc and N-Myc activity. *Cell Stem Cell* 3: 611–624.

## Acknowledgments

We thank Dr. Alessandra Quarta from the Italian Institute of Technology (Genova, Italy) for her support with the zeta-potential measurements; Giuseppe Marino from National Research Council (Pozzuoli, Italy) for assistance on animal culturing. We thank Salvatore Arbucci and Rosarita Tatè (Institute of Genetics and Biophysics, CNR of Italy, Naples) for assistance on confocal microscopy.

## Author Contributions

Conceived and designed the experiments: CT AA. Performed the experiments: AA VM AT CT. Analyzed the data: AA AT BH CT. Contributed reagents/materials/analysis tools: BH. Wrote the paper: CT.



53. Demeterco C, Itkin-Ansari P, Tyrberg B, Ford LP, Jarvis RA, et al. (2002) c-Myc controls proliferation versus differentiation in human pancreatic endocrine cells. *J Clin Endocrinol Metab* 87: 3475–3485.
54. Gallant P (2009) *Drosophila* Myc. *Adv Cancer Res* 103: 111–144.
55. Grens A, Gee L, Fisher DA, Bode HR (1996) CnNK-2, an NK-2 homeobox gene, has a role in patterning the basal end of the axis in hydra. *Dev Biol* 180: 473–488.
56. Livak KJ, Schmittgen TD (2001) Analysis of relative gene expression data using real-time quantitative PCR and the  $2^{-\Delta\Delta C_T}$  Method. *Methods* 25: 402–408.
57. Sambrook J, Fritsch EF, Maniatis T (1989) *Molecular Cloning: A Laboratory Manual*, 2nd ed. Cold Spring Harbor Laboratory Press, Plainview, NY.
58. David CN (1973) A quantitative method for maceration of Hydra tissue: Wilhelm Roux Arch. *EntwMech Org*, pp 259–268.

## Research Article

# A New *In Vivo* Model System to Assess the Toxicity of Semiconductor Nanocrystals

Angela Tino,<sup>1</sup> Alfredo Ambrosone,<sup>1</sup> Lucia Mattera,<sup>1</sup> Valentina Marchesano,<sup>1</sup>  
Andrei Sussha,<sup>2</sup> Andrey Rogach,<sup>2</sup> and Claudia Tortiglione<sup>1</sup>

<sup>1</sup>Institute of Cybernetics “E. Caianiello”, National Research Council of Italy, Via Campi Flegrei, 34, 80078 Pozzuoli, Italy

<sup>2</sup>Department of Physics and Materials Science, City University of Hong Kong, Hong Kong SAR, Kowloon, China

Correspondence should be addressed to Claudia Tortiglione, c.tortiglione@cib.na.cnr.it

Received 16 December 2010; Accepted 2 March 2011

Academic Editor: Toshiki Miyazaki

Copyright © 2011 Angela Tino et al. This is an open access article distributed under the Creative Commons Attribution License, which permits unrestricted use, distribution, and reproduction in any medium, provided the original work is properly cited.

In the emerging area of nanotechnology, a key issue is related to the potential impacts of the novel nanomaterials on the environment and human health, so that this technology can be used with minimal risk. Specifically designed to combine on a single structure multipurpose tags and properties, smart nanomaterials need a comprehensive characterization of both chemicophysical properties and adequate toxicological evaluation, which is a challenging endeavour; the *in vitro* toxicity assays that are often employed for nanotoxicity assessments do not accurately predict *in vivo* response. To overcome these limitations and to evaluate toxicity characteristics of cadmium telluride quantum dots in relation to surface coatings, we have employed the freshwater polyp *Hydra vulgaris* as a model system. We assessed *in vivo* acute and sublethal toxicity by scoring for alteration of morphological traits, population growth rates, and influence on the regenerative capabilities providing new investigation clues for nanotoxicology purposes.

## 1. Introduction

During the past decade, advances in synthesis and biofunctionalization of colloidal semiconductor nanocrystals have generated an increasing widespread interest among investigators in the field of biology and medicine. The multitude of successful uses of quantum dots (QDs) as specific markers for cellular structures and molecules, monitoring molecular and physiological events in live cells and animals, is a testimony of their great potential as multipurpose bioprobes [1, 2]. However, there exists an open question regarding whether nanoparticles per se can elicit biological responses, which could interfere with the phenomena they are intended to measure. Evidences are cumulating that nanoparticles play active roles even in the absence of specific ligands and that factors such as size and charge are crucial for the activation of cell responses, internalization, and intracellular trafficking [3, 4]. Thus, it is a priority for the wide scientific community working to develop nanostructured materials for biomedical purposes to relate the physical and chemical characteristics of nanomaterials to their behaviour, *in vivo*.

While most of the published data addressing this important issue rely on cell culture studies and are focussed on the identification of the physicochemical parameters influencing the impact of nanoparticle on living cells [5, 6], we propose a new model system to work at the whole animal level. The small freshwater polyp *Hydra vulgaris* (Cnidaria, Hydrozoa) is a diploblastic animal, at the base of the metazoan evolution, composed of just two epithelial cell layers (an inner endoderm and an outer ectoderm facing the low ionic strength medium) with few interspersed specialised cell types, a neuronal net controlling functions and physiology (Figure 1). This structural complexity, simpler than vertebrates, with central nervous system and specialized organs, but much complex compared to cultured cells, makes *Hydra* comparable to a living tissue whose cells and distant regions are physiologically connected [7].

The feasibility to approach biological issues using *Hydra* as model system has been shown previously by our group. In a pioneer work, we synthesised glutathione functionalised quantum dots (GSH-QDs), studied the biological activity

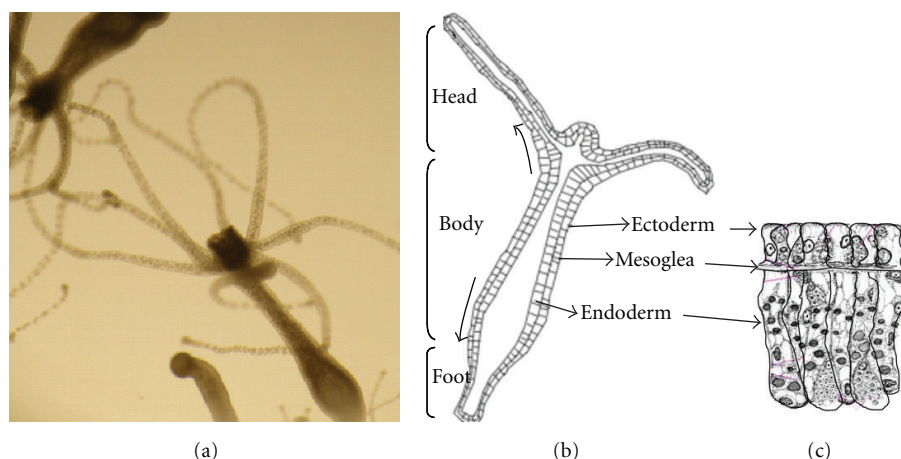


FIGURE 1: (a) Picture of living *Hydra*. The animal has a simple body plan: it is a tube with a head at the apical end and a foot or basal disc at the other. The head is in two parts, the hypostome (mouth) at the apex and below that the tentacle zone from which a ring of tentacles emerge. Scale bar  $200\ \mu\text{m}$ . (b) Schematic representation of the bilayered structure of the animal: the body wall is composed of two self-renewing cell layers, an outer, the ectoderm, and an inner, the endoderm, separated by an extracellular matrix, the mesoglea. The arrows on the left side indicate the direction of tissue displacement. (c) Along the animal body, both ectoderm and endoderm layers are composed of epitheliomuscular cells, while interstitial stem cells and their intermediate and terminal derivatives (neurons, nematocytes, and secretory cells) are interspersed among ectoderm and endoderm.

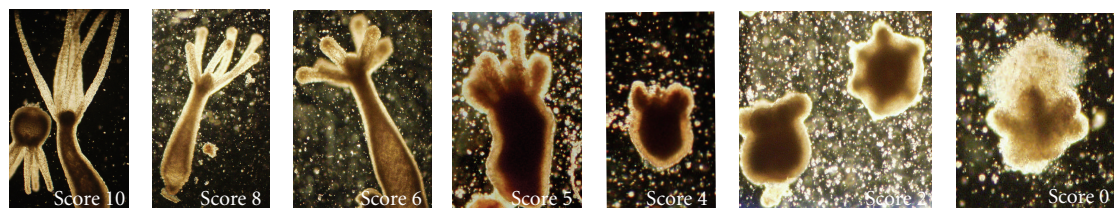


FIGURE 2: Example of morphological alterations induced by the treatment of living *Hydra* with CdTe QDs. Animals were incubated with increasing doses of TGA- and GSH-capped CdTe QDs, from left to right: 50 nM, 100 nM, 200 nM, 300 nM, 500 nM, 750 nM, and  $1\ \mu\text{M}$  over a period of 2 h and then imaged. Progressive morphological changes were scored from 10 down to 1, as previously described in [8].

evoked in living polyps, and identified GSH-targeted cells [9]. In the following studies, we used rod-shaped CdSe/CdS nanocrystals (QRs) not bearing functional groups to identify the mechanisms underlying cell-QR interaction. Unexpectedly, *Hydra* treated with QRs showed a behavioural response, a tentacle writhing activity, which was finely characterized and shown to be calcium dependent and relying on the presence of tentacle neurons. These results indicated that the interactions between living organisms and newly synthesised nanomaterials need to be deeply investigated before employing any new nanostructure for biological purposes, that is, for cell-tracking studies, drug delivery. We have also identified both chemical and biological factors involved in the interaction QR-*Hydra* [4] working both *in vivo*, at the level of whole animal and isolated cells, and *in vitro* on fixed specimens, concluding that the QR internalization is the combined results of QR positive surface charge and membrane trafficking events regulated by the presence of annexin proteins on cell membranes.

A remarkable advantage offered by *Hydra* as a model organism to be targeted by metal-based nanocrystals is the possibility to evaluate the potential toxicity of these

nanoparticles on different aspects of *Hydra* physiology. The availability of new animal models suitable for the assessment of nanotoxicity is currently recognised as a priority. *Hydra* is sensitive to a range of pollutants and has been used as a biological indicator of water pollution [10–12]. Metal pollutants such as copper, cadmium, and zinc have been tested against different *Hydra* species, and the relative toxicity based on the median lethal concentration (LC<sub>50</sub>) for all species was ranked from copper, the most toxic, to cadmium with zinc, the least toxic [13]. Drugs and pharmaceuticals targeted at mammalian receptors have also been shown to adversely affect *Hydra*, showing the feasibility to use this aquatic invertebrate to accurately assess the potential toxicological effect of pharmaceuticals entered into natural waters through sewage effluent and landfill leakages [12]. Several bioassays are available to assess the toxicity of a given compound in terms of acute or sublethal toxicity. Polyps exposure to different drugs may cause (1) alteration of morphological traits and developmental programs, (2) alteration of regeneration or pattern formation; the remarkable regenerative capacity of *Hydra* relies on the presence of mitotically active multipotent stem cells in the gastric

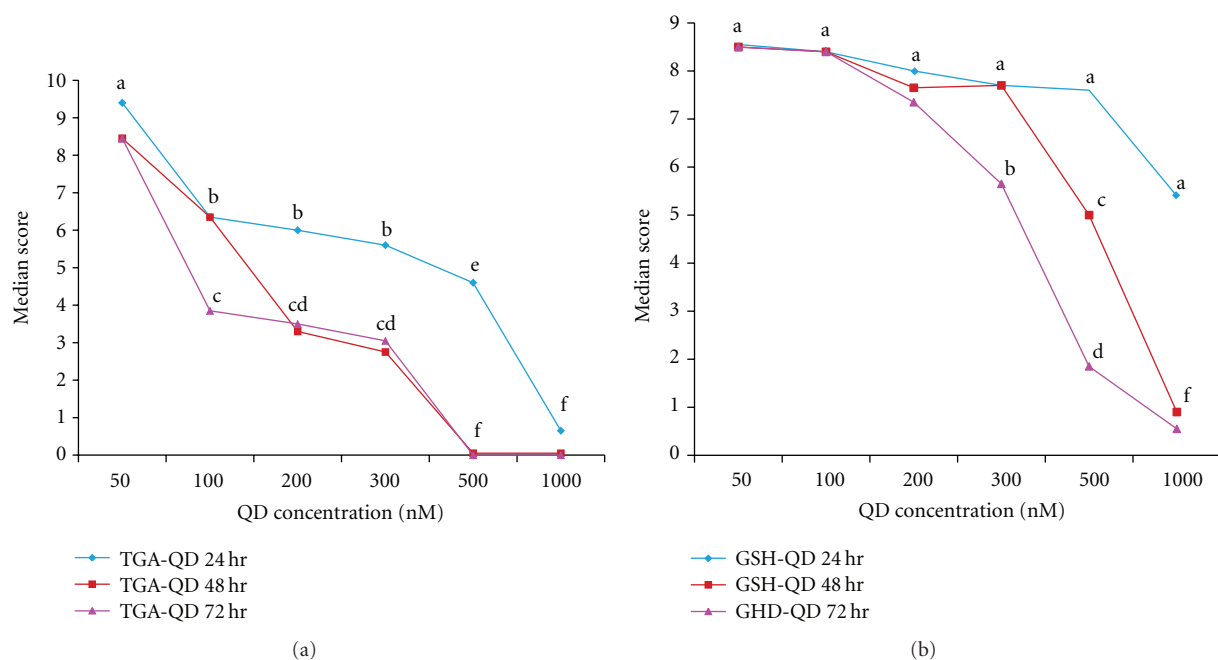


FIGURE 3: Dose response toxicity curves to (a) TGA- and (b) GSH-capped QDs. 20 *Hydra* were treated with the indicated QD at increasing concentrations for 2 hours and then, following extensive washing, allowed to recover in physiological solution for 24 hr (blue line), 48 hr (red line), and, 72 hr (purple line), when morphology was appropriately scored. Median scores of morphological condition were compared by nonparametric Friedman Test; values with a letter in common are not significantly different ( $P < .001$ ). The toxicity of TGA-and-GSH capped QDs on *Hydra* morphology increases with time and concentration.

region, able to regenerate a new organism within 72 hr; as this process is controlled by temporal, positional, and morphogenetic factors, the presence of toxicants in the medium may affect the full process, and (3) alteration of population growth rates; bioassays measuring *Hydra* population growth by asexual reproduction are rapid, sensitive, and precise. Large numbers of *Hydra* can be cultured due to their small size and rapid reproductive rate [14]. The high reproductive rate of *Hydra* enables subchronic toxicity test which assess the population reproductive effects of a toxicant to be done in short time periods.

In the present paper, we evaluated the toxicological effects of fluorescent CdTe QDs, presenting different chemical coatings, on a whole organism, *Hydra vulgaris*. By using different approaches, from *in vivo* evaluation of morphological traits to the impact on growth rate and regeneration, we determined different behaviours and toxicological effects played by CdTe QDs, such as the influence of the surface coating, showing the feasibility of using *Hydra* as fast, low-cost, and reliable tool for nanotoxicology studies.

## 2. Methods

**2.1. Nanocrystals Employed.** The water-soluble CdTe QDs used in this study were surface capped with thioglycolic acid (TGA) or glutathione (GSH) and synthesized as described in [15]. In this work, TGA-QDs (mean diameter of 3.1 nm) present an absorption wavelength of the first electronic

transition at 537 nm, while GSH-QDs (mean diameter of 3.6 nm) at 598 nm.

**2.2. *Hydra* Culture.** *Hydra vulgaris* (strain Zurich, originally obtained by P. Tardent) were asexually cultured in physiological solution (SolHy: 1 mM  $\text{CaCl}_2$ , 0.1 mM  $\text{NaHCO}_3$ , pH 7) by the method of Loomis and Lenhoff with minor modifications [14]. The animals were kept at  $18 \pm 1^\circ\text{C}$  and fed three times per week with freshly hatched *Artemia salina* nauplii.

**2.3. *In Vivo* Experiments with Intact and Regenerating Animals.** Groups of 20 animals were collected in plastic multiwells and allowed to equilibrate at room temperature in 300  $\mu\text{L}$  of physiological solution (SolHy:  $\text{CaCl}_2$  1 mM,  $\text{NaHCO}_3$  0.1 mM, pH 7). The test was initiated by adding test QDs to each well containing 10 polyps and incubating as necessary. QD uptake was monitored *in vivo*, unless otherwise stated, by continuous video recording using a Camedia digital camera (Olympus) connected to a stereomicroscope (Olympus ZSX-RFL2) equipped with fluorescence filter sets (BP460–490/DM505/LP510). Following extensive washes, *in vivo* imaging was accomplished at several magnifications by using both a stereomicroscope and an inverted microscope (Axiovert 100, Zeiss) equipped with a digital colour camera (Olympus, DP70) and fluorescence filter sets (BP4502013490/FT510/LP515). In order to assay acute toxicity, the morphological changes induced by QD treatment were monitored, by using a scoring procedure

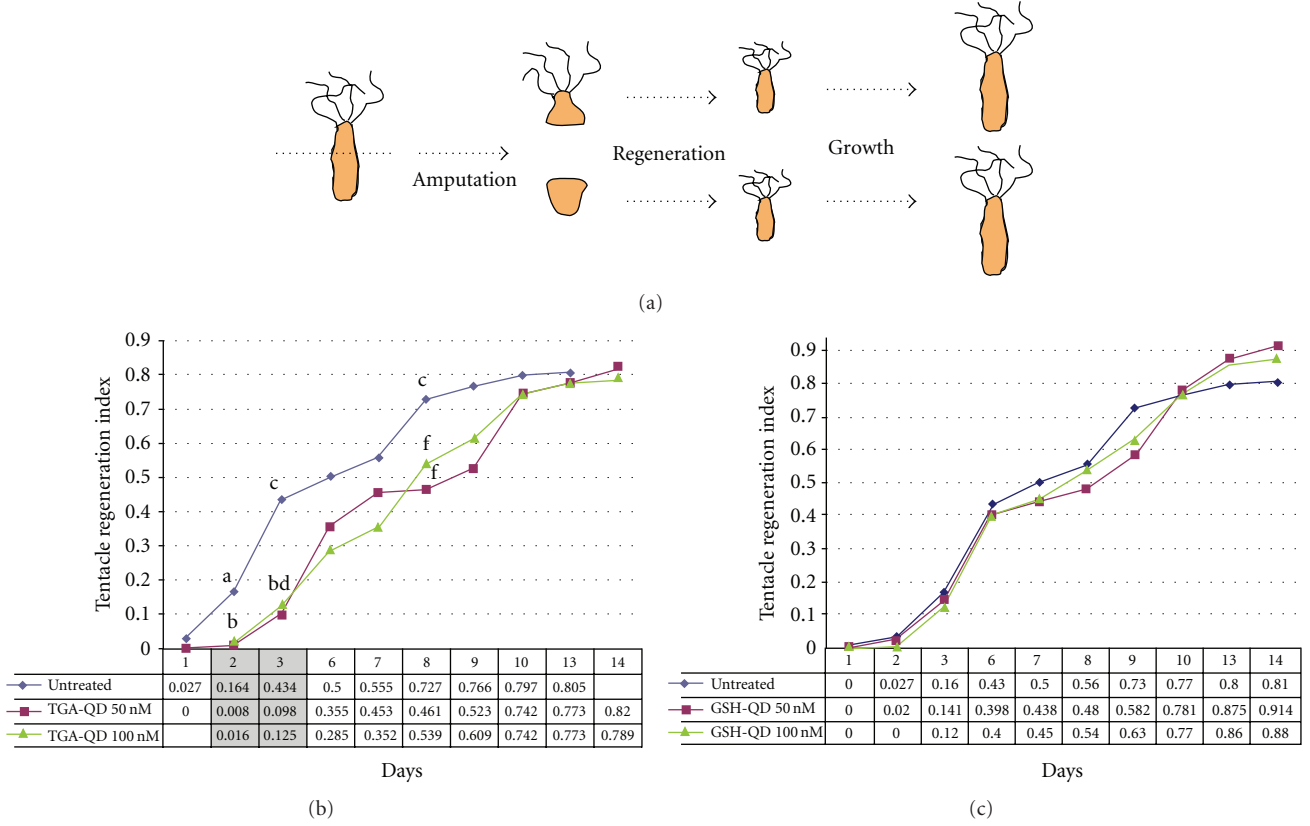


FIGURE 4: Mean tentacle regeneration indices (TRI) plotted against corresponding days of regeneration. In (a), a scheme of the regeneration is illustrated. Groups of 4 *Hydra* treated with TGA-QD (b) or GSH-QD (c) were bisected and allowed to regenerate for 14 days. For each type of QD, two different concentrations were tested (50 nM, purple line, and 100 nM, green line) and compared to untreated regenerating *Hydra*. Mean TRI values with diverse letter are significantly different (unpaired *t*-test ( $P < .001$ )).

of the progressive changes in structure. This procedure allows to examine the ability of animals to recover from QD-induced damage. Every day, using a stereomicroscope, recognizable physical changes in response to different QD ranges were recorded, according to score values (ranging from 1 to 10) described by Wilby [8]. For imaging acquisition and analysis, the software system Cell F (Olympus) was used. For regeneration experiments, treated polyps were bisected in the gastric region and *in vivo* imaged at various time points after amputation. A quantitative method was used for the evaluation of distal regeneration in *Hydra*, based on estimates of tentacle elongation during 14 days of regeneration, determination of a tentacle regeneration index (TRI), and a statistical analysis of profiles obtained from various samples in different experiments [16]. According to this method, for each of the  $N$  polyps, it is possible to calculate at time  $t$  the corresponding Tentacle regeneration index (TRI) as follows:

$$R_j(t) = \sum_{K=1}^5 p_k \cdot \frac{n_k^j(t)}{n_{\max}} \quad j = 1, 2, \dots, N, \quad (1)$$

where  $n$  represents the maximal tentacle number for a single polyp under physiological conditions, that is,  $n_{\max} = 8$ ;  $n_k^j(t)$  represents the number of tentacles of class  $K$  (5 tentacle

classes were set, of length equal to 1/8, 1/4, 1/2, 3/4, and 1) regenerated by the  $j$ th *Hydra* at time  $t$ . The series of TRI values of the  $j$ th polyp, obtained at the fixed observation times, represents the individual regeneration profile of the polyp. Finally, for each group of  $N = 4$  *Hydra*, a mean TRI was calculated at any observation time  $t$  in order to follow the average regeneration rate of the group. Experiments were performed in air-conditioned environment at 22°C and repeated three times for each condition tested. Median lethal concentrations (LC50) and lethal time (LT50) were calculated using the Spearman-Kärber trim method [17].

**2.4. Hydra Growth Rates.** Experimental animals (four *Hydra* with one bud) were treated with the indicated QD, for 4 h, then washed, and the following day placed in 3.5 cm Petri dishes (1 *Hydra*/dish). Control animals at the same developmental stage were not treated. Both experimental and control *Hydra* were fed once daily, and the population doubling time was determined as growth parameter. The growth rate constant ( $k$ ) of an exponentially growing group of animals is defined as  $\ln(n/n_0) = kt$ , where  $n$  is the number of animals at time  $t$  and  $n_0$  the number of animals at  $t_0$ . For  $n/n_0 = 2$ ,  $t = T_2$ , the doubling time of the population  $T_2$  was determined by linear regression [18].



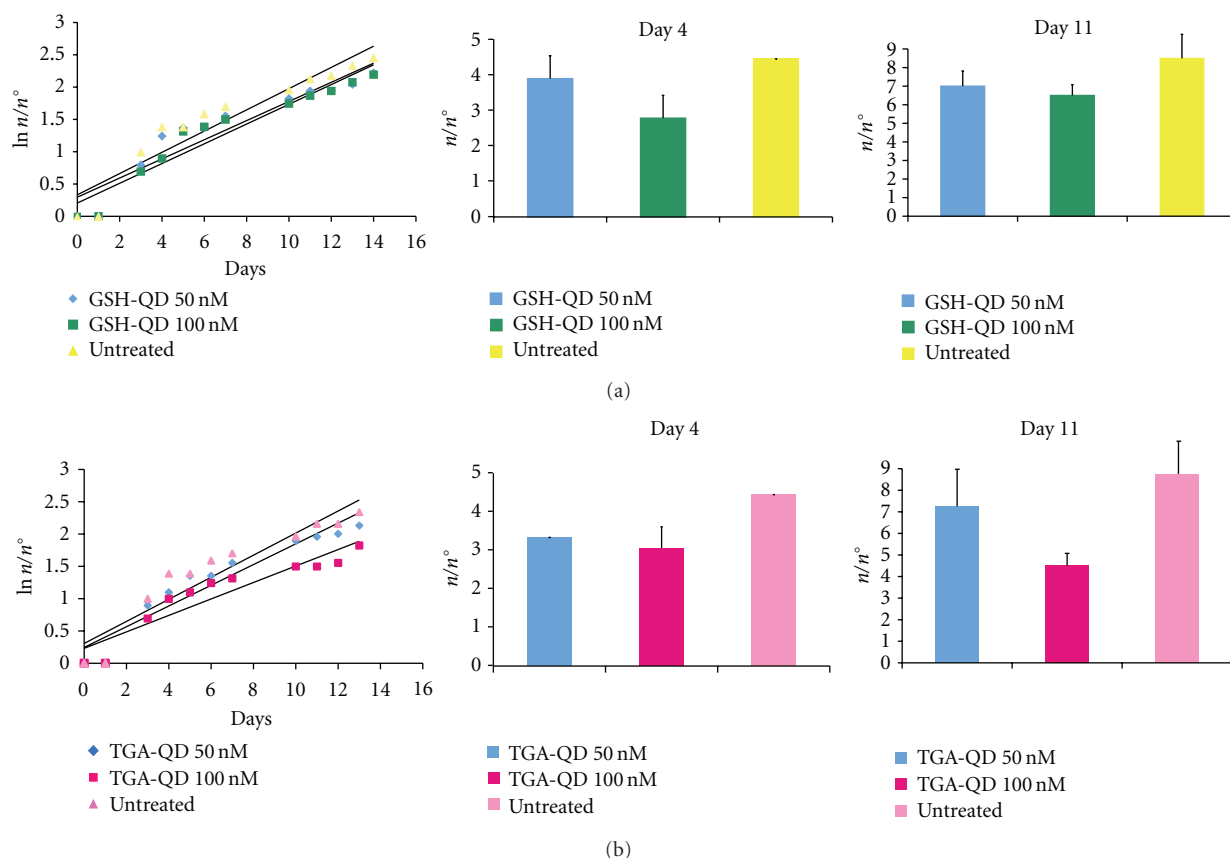


FIGURE 5: Influence of the QD treatment on *Hydra* population growth rate. Population growth test started with a population of four full-grown *Hydra*, incubated 2 h with the indicated QD, washed out, and monitored every day for bud detachment. *Hydra* were treated with GSH-QDs, dark and light green bars, (a), or TGA-QDs, dark and light pink bars, (b), washed, and equilibrated in culture solution or not treated (blue bars). The individuals were inspected daily and counted under a stereomicroscope. The logarithmic growth rate constant ( $k$ ) is the slope of the regression line using the standard equation of logarithmic growth:  $\ln(n/n_0) = kt$ . Significant differences between growth rates of *Hydra* population treated with TGA-QD or untreated were obtained comparing linear regression slopes using ANOVA two-way test ( $P < .005$ ). On the right panel,  $n/n_0$  ratio ( $\pm$ SD) extrapolated from growth curves at days 4 and 11 is indicated.

**2.5. Statistical Analysis.** LC50 and LT50 values were calculated using the Spearman-Kärber trim method [17]. Median scores of morphological condition were compared by nonparametric Friedman analysis [13]. A  $t$ -test ( $P < .001$ ) was used to test for significance between TRI values within treatments. The slope of the regression curves obtained from single population growth rate was tested for significance using a two-way ANOVA ( $P < .001$ ).

### 3. Results

The two types of highly luminescent CdTe QDs were utilised, thioglycolic acid-capped CdTe QD (from here it is indicated as TGA-QDs) [15] and glutathione-capped QDs (from here named GSH-QDs), and the effects on animal behaviour and morphology were investigated over different incubation times. Being *Hydra* a small water living animal, the simple addition of QDs to the culture medium enables us to study the interaction between QD and animals, avoiding delivering methods or invasive procedures. TGA-QDs and GSH-QDs were added at different concentrations to groups of living

polyps which were continuously monitored by fluorescence stereomicroscopy to visually inspect potential QD uptake, localisation, and cell morphology following incubation. By fluorescence microscopy observation, the animals appeared not fluorescently labelled, possibly due to the effect of calcium ions present in *Hydra* culture solution, which have been shown to bleach the QD luminescence [19]. As shown in Figure 2, morphological alterations were induced by the treatment with both CdTe-based QDs and scored according to previous methods [8].

A precise and accurate estimation of the median lethal concentration (LC50) was obtained by applying the trimmed Spearman-Kärber method, which has good statistical properties, is easy to use, and is recommended for accurate and precise calculation of LC50 values and their 95% confidence interval end points [17]. As this method counts the dead animals and *Hydra* can recover the damage, we considered dead animals as those showing scores lower than 4. Median scores recorded at each QD test concentration of treated animals decreased with increasing exposure, concentration, and time, as shown in the graphs of Figure 3.

In Table 1, LC50 and LT50 values calculated using the Spearman-Kärber method are reported for both TGA- and GSH-capped QDs. TGA-QDs are characterized by lower values of both LC50 and LT50 compared to GSH-QDs, indicating a more toxic effect played by the thioglycolic acid surface compared to glutathione capping.

To fully characterize the toxicological impact of CdTe QDs on *Hydra*, two further approaches were followed. The first one is based on the capacity of *Hydra* to regenerate missing parts of the body after amputation. During head regeneration, the development of new tentacles can be monitored by stereomicroscopy, and tentacles numbers and lengths can be scored daily to assess the potential effects played by a toxicant on this controlled process. We used a quantitative method to assay the effect of QD treatment on *Hydra* regeneration [16], calculating every day for each condition the tentacle regeneration index (TRI), which indicates the average tentacle length/*Hydra* (relative to the maximum tentacle length, assumed as 1 when the process is completed).

As shown by the graph of Figure 4, TRI values for TGA-QD-treated animals were significantly lower compared to TRI of untreated animals. These differences were more evident during the first days of tentacle regeneration (gray shaded in the left panel of Figure 4) and less evident during the late stages of tentacle development. GSH-QD-treated animals, by contrast, were characterized by TRI similar to untreated animals, indicating for this QD type the absence of toxic effect on *Hydra* regeneration.

Finally, the potential long-term toxic effects induced by CdTe QDs on *Hydra* reproductive capabilities were assayed. Growth rate of *Hydra* tissue is normally regulated by a balance between epithelial cell cycle length, phagocytosis of ectodermal cell in “excess,” and bud formation [18]. Thus, the population growth rate is an indirect measure of the *Hydra* tissue growth rate and cell viability. The growth rates of QD-treated polyps were calculated and compared to untreated animals, under regular feeding regime. As shown in the graph of Figure 5(a), the growth rate of polyps treated with GSH-QDs (two different sublethal concentrations were used) was similar to untreated animals, indicating the absence of toxic effects. Slight differences were observed only at the beginning of the experiment, as shown by the ratio  $n/n^0$  (number of individuals/number of the founders) at day 4, but not later, that is, at day 11, when the differences were not significant.

Constant growth rates of *Hydra* treated with TGA-QDs (Figure 5(b)), on the opposite, were significantly different from untreated *Hydra*. Differences in the ratio  $n/n^0$  were found all along the period of investigation, indicating an adverse effect displayed by this type of QD on *Hydra* reproductive capability.

#### 4. Discussion

Despite the abundant data accumulated on the toxicity of CdTe QD on cell culture systems [20–23], it is a priority of the scientific community to assess toxicological effects at the

level of whole animal. *Hydra vulgaris* represents an amenable system to study the impact of the new nanomaterials on living organism, as it is very simple; it is structured in only two cell layers, thus it can be compared to a living tissue, but it presents the complex physiology and behaviour of evolved animals. The transparency of the epithelia makes it possible to track fluorescent nanoparticles, while its sensitivity to metals makes it an ideal model for nanotoxicology studies. In this study, we investigated the effect of CdTe QDs on *Hydra*, using three different approaches, that is, assessing the effect on the polyps morphology and regenerating and reproductive capabilities. We quantitatively estimated these effects, calculating LC50 and LT50 values, tentacle regeneration index, and population growth rate, respectively, for each approach. Overall our data show that TGA-capped QDs display toxic effect compared to GSH-capped QD or to untreated animals. As by fluorescence microscopy, we were unable to evaluate the uptake of the fluorescent QDs into *Hydra* cells; at this stage, we cannot assess whether the toxicity is due to an intracellular or extracellular action played by the TGA-QDs. As we have previously shown that the positive surface charge is the crucial factor for nanoparticle internalization into *Hydra* cells [4], the observed toxicity of TGA-QD might be due to an extracellular activity, that is, binding and competing to divalent ions for membrane receptors, and we are currently investigating in to this aspect.

Several studies suggested that the cytotoxic effects of (QDs) may be mediated by cadmium ions ( $\text{Cd}^{2+}$ ) released from the QD cores [24], and indeed *Hydra* has been shown sensitive to free Cd ions [10]. However, we performed similar bioassays using the supernatant of pelleted QD preparation, and we could not detect any induced toxicity, suggesting a potential role of the  $\text{Cd}^{2+}$  ions coordinated by the negative groups of the capping TGA, on the QD surface, rather than a release  $\text{Cd}^{2+}$  from the QD core. Thus, the identification of *Hydra*  $\text{Cd}^{2+}$  responsive membrane proteins would shed light on the potential mechanism of CdTe-QD-induced toxicity. The dose-dependent correlation between animal viability and QD administered further supports the hypothesis that their cytotoxicity depends on the QD actions and not on other ongoing processes, opening the path to future investigations on the intriguing cellular and molecular mechanisms underlying the CdTe-QD response in *Hydra*. Confocal laser microscopy of single-cell preparation from CdTe-QDs-treated animals imaged with organelle-specific dyes might reveal lysosomal damage attributable to the presence of reactive oxygen species (ROS), which can be formed via  $\text{Cd}^{2+}$ -specific cellular pathways and/or via CdTe-triggered photo-oxidative processes involving singlet oxygen or electron transfer from excited QDs to oxygen [20, 25]. Cell biology investigation tools to check for the presence of necrosis processes or for the induction of programmed cell death (apoptosis) will help to unravel the mechanism underlying CdTe QD toxicity, which would be of invaluable help to decipher the basis of semiconductor nanocrystal toxicity also in higher organisms.

In summary, we have shown that, when CdTe QDs interact with *Hydra* cells, this interaction induces progressive changes of cell morphology, leading finally to cell and animal

TABLE 1: Comparison of Mean (SE) lethal concentration (LC50) and lethal time (LT50) for TGA- and GSH-capped QDs.

Time (h)	LC50 (nM)		QD	LT50 (hr)
	TGA-QDs	GSH-QDs	TGA-QDs 300 nM	36
24	687.04 (27.9)	—	TGA-QDs 500 nM	24
48	232.89 (31.5)	629.99 (18.8)	GSH-QDs 500 nM	63
72	153.24 (18.9)	434.29 (15.3)	GSH-QDs 1000 nM	32

death. CdTe-QD-induced cytotoxicity was associated with QD exposure time and concentration and with the surface chemistry and coating of the QD. Animal exposure for 2 hr to nanomolar doses of CdTe QD induced progressive morphological alterations, which were scored up to 72 hrs when the complete death was detected. Anterior-posterior polarity, which is normally established during bud morphogenesis and regeneration, was not affected. The induced toxicity was more pronounced in case of TGA-QD exposure, rather than GSH-QD, as shown by the dose responses curves. By treating the animals with sublethal doses of QDs, both regeneration assay and population growth rate were affected by TGA- and not GSH-capped QD, suggesting either an increased subcellular stability of GSH-QDs or a protective role played by GSH against potential Cd<sup>2+</sup>-induced ROS productions.

As nanoparticles may enter natural waters through sewage effluent and landfill leakages and present unknown risk to aquatic species including freshwater invertebrates, we recommend that invertebrate testing is used not only to advance the level of knowledge in nanoecotoxicology but also for investigating the behaviour and bioavailability of engineered nanoparticles in the aquatic environment through standardized tests. In conclusion, we suggest that our simple model system, up to now used mainly by a niche of biologists to study developmental and regeneration processes, has great potential to inspire many scientists working in the field of nanoscience, from chemists to toxicologists demanding new models to study the impact of nanoparticles on living organisms and their environment and to investigate the molecular basis of the bio-nonbio interactions.

## Acknowledgments

We thank Dr. Giuseppe Nolfé (Institute of Cybernetic CNR, Pozzuoli) for invaluable help in the statistical analysis of the data; Giuseppe Marino for technical assistance; Giovanna De Rosa for assistance on *Hydra* morphology scores. This work was supported by the NanoSci-ERA net project NAN-OTRUCK (2009–2012) and by the Croucher Foundation project 9220054.

## References

- [1] M. Bruchez Jr., M. Moronne, P. Gin, S. Weiss, and A. P. Alivisatos, "Semiconductor nanocrystals as fluorescent biological labels," *Science*, vol. 281, no. 5385, pp. 2013–2016, 1998.
- [2] P. Alivisatos, "The use of nanocrystals in biological detection," *Nature Biotechnology*, vol. 22, no. 1, pp. 47–52, 2004.
- [3] M. A. Malvindi, L. Carbone, A. Quarta et al., "Rod-shaped nanocrystals elicit neuronal activity in vivo," *Small*, vol. 4, no. 10, pp. 1747–1755, 2008.
- [4] C. Tortiglione, A. Quarta, M. A. Malvindi, A. Tino, and T. Pellegrino, "Fluorescent nanocrystals reveal regulated portals of entry into and between the cells of Hydra," *PLoS One*, vol. 4, no. 11, Article ID e7698, 2009.
- [5] W. Jiang, B. Y. S. Kim, J. T. Rutka, and W. C. W. Chan, "Nanoparticle-mediated cellular response is size-dependent," *Nature Nanotechnology*, vol. 3, no. 3, pp. 145–150, 2008.
- [6] R. Minchin, "Nanomedicine: sizing up targets with nanoparticles," *Nature Nanotechnology*, vol. 3, no. 1, pp. 12–13, 2008.
- [7] B. Galliot, M. Miljkovic-Licina, R. de Rosa, and S. Chera, "Hydra, a niche for cell and developmental plasticity," *Seminars in Cell and Developmental Biology*, vol. 17, no. 4, pp. 492–502, 2006.
- [8] O. K. Wilby, "The Hydra regeneration assay," in *Proceedings of Workshop Organised by Association Francaise de Teratologie*, pp. 108–124, 1988.
- [9] C. Tortiglione, A. Quarta, A. Tino, L. Manna, R. Cingolani, and T. Pellegrino, "Synthesis and biological assay of GSH functionalized fluorescent quantum dots for staining Hydra vulgaris," *Bioconjugate Chemistry*, vol. 18, no. 3, pp. 829–835, 2007.
- [10] D. A. Holdway, K. Lok, and M. Semaan, "The acute and chronic toxicity of cadmium and zinc to two hydra species," *Environmental Toxicology*, vol. 16, no. 6, pp. 557–565, 2001.
- [11] C. A. Pollino and D. A. Holdway, "Potential of two hydra species as standard toxicity test animals," *Ecotoxicology and Environmental Safety*, vol. 43, no. 3, pp. 309–316, 1999.
- [12] D. Pascoe, W. Karntanüt, and C. T. Müller, "Do pharmaceuticals affect freshwater invertebrates? A study with the cnidarian Hydra vulgaris," *Chemosphere*, vol. 51, no. 6, pp. 521–528, 2003.
- [13] W. Karntanüt and D. Pascoe, "The toxicity of copper, cadmium and zinc to four different Hydra (Cnidaria: Hydrozoa)," *Chemosphere*, vol. 47, no. 10, pp. 1059–1064, 2002.
- [14] W. F. Loomis and H. M. Lenhoff, "Growth and sexual differentiation of Hydra in mass culture," *Journal of Experimental Zoology*, vol. 132, pp. 555–574, 1956.
- [15] A. L. Rogach, T. Franzl, T. A. Klar et al., "Aqueous synthesis of thiol-capped CdTe nanocrystals: state-of-the-art," *Journal of Physical Chemistry C*, vol. 111, no. 40, pp. 14628–14637, 2007.
- [16] G. Nolfé, P. Pierobon, and S. Piscitelli, "Tentacle regeneration in Hydra: a quantitative methodological approach," *Journal of Biomedical Engineering*, vol. 9, no. 3, pp. 267–272, 1987.
- [17] M. A. Hamilton, R. C. Russo, and R. V. Thurston, "Trimmed Spearman Karber method for estimating median lethal concentrations in toxicity bioassays," *Environmental Science and Technology*, vol. 11, no. 7, pp. 714–719, 1977.
- [18] T. C. G. Bosch and C. N. David, "Growth regulation in Hydra: relationship between epithelial cell cycle length and growth

- rate," *Developmental Biology*, vol. 104, no. 1, pp. 161–171, 1984.
- [19] A. S. Susha, A. M. Javier, W. J. Parak, and A. L. Rogach, "Luminescent CdTe nanocrystals as ion probes and pH sensors in aqueous solutions," *Colloids and Surfaces A*, vol. 281, no. 1–3, pp. 40–43, 2006.
- [20] A. Khatchadourian, K. Krumova, S. Boridy, T. N. An, D. Maysinger, and G. Cosa, "Molecular imaging of lipid peroxy radicals in living cells with a BODIPY- $\alpha$ -tocopherol adduct," *Biochemistry*, vol. 48, no. 24, pp. 5658–5668, 2009.
- [21] B. R. Prasad, N. Nikolskaya, D. Connolly et al., "Long-term exposure of CdTe quantum dots on PC12 cellular activity and the determination of optimum non-toxic concentrations for biological use," *Journal of Nanobiotechnology*, vol. 8, article 7, 2010.
- [22] J. Lovrić, H. S. Bazzi, Y. Cuie, G. R. A. Fortin, F. M. Winnik, and D. Maysinger, "Differences in subcellular distribution and toxicity of green and red emitting CdTe quantum dots," *Journal of Molecular Medicine*, vol. 83, no. 5, pp. 377–385, 2005.
- [23] A. Khatchadourian and D. Maysinger, "Lipid droplets: their role in nanoparticle-induced oxidative stress," *Molecular Pharmacology*, vol. 6, no. 4, pp. 1125–1137, 2009.
- [24] C. Kirchner, T. Liedl, S. Kudera et al., "Cytotoxicity of colloidal CdSe and CdSe/ZnS nanoparticles," *Nano Letters*, vol. 5, no. 2, pp. 331–338, 2005.
- [25] N. Lewinski, V. Colvin, and R. Drezek, "Cytotoxicity of nanoparticles," *Small*, vol. 4, no. 1, pp. 26–49, 2008.

Contents lists available at [SciVerse ScienceDirect](http://www.sciencedirect.com)

## Biomaterials

journal homepage: [www.elsevier.com/locate/biomaterials](http://www.elsevier.com/locate/biomaterials)

# Mechanisms underlying toxicity induced by CdTe quantum dots determined in an invertebrate model organism

Alfredo Ambrosone<sup>a</sup>, Lucia Mattera<sup>a</sup>, Valentina Marchesano<sup>a</sup>, Alessandra Quarta<sup>b</sup>, Andrei S. Sussha<sup>c</sup>, Angela Tino<sup>a</sup>, Andrey L. Rogach<sup>c</sup>, Claudia Tortiglione<sup>a,\*</sup>

<sup>a</sup> CNR-Istituto di Cibernetica "E. Caianiello", Via Campi Flegrei 34, 80078 Pozzuoli, Italy

<sup>b</sup> CNR-Istituto di Nanoscienze, NNL, Via Arnesano km 5, 73100 Lecce, Italy

<sup>c</sup> Department of Physics and Materials Science & Centre for Functional Photonics, City University of Hong Kong, SAR, Hong Kong

## ARTICLE INFO

## Article history:

Received 26 September 2011

Accepted 20 November 2011

Available online xxx

## Keywords:

Animal model

Cytotoxicity

Genotoxicity

In vivo test

CdTe quantum dots

## ABSTRACT

A systematic and thorough quantitative analysis of the *in vivo* effects of inorganic nanoparticles is extremely important for the design of functional nanomaterials for diagnostic and therapeutic applications, better understanding of their non-specificity toward tissues and cell types, and for assessments of their toxicity. This study was undertaken to examine the impact of CdTe quantum dots (QDs) on an invertebrate freshwater model organism, *Hydra vulgaris*, for assessment of long term toxicity effects. The continuous exposure of living polyps to sub-lethal doses of QDs caused time and dose dependent morphological damages more severe than Cd<sup>2+</sup> ions at the same concentrations, impaired both reproductive and regenerative capability, activated biochemical and molecular responses. Of remarkable interest, low QD doses, apparently not effective, caused early changes in the expression of general stress responsive and apoptotic genes. The occurrence of subtle genetic variations, in the absence of morphological damages, indicates the importance of genotoxicity studies for nanoparticle risk assessment. The versatility in morphological, cellular, biochemical and molecular responses renders *Hydra* a perfect model system for high-throughput screening of toxicological and ecotoxicological impact of nanomaterials on human and environmental health.

© 2011 Elsevier Ltd. All rights reserved.

## 1. Introduction

Semiconductor nanocrystals, also known as colloidal quantum dots (QDs), have been widely employed as components of solar cells [1,2] and light-emitting diodes [3,4] and have a great potential as probes for ultrasensitive molecular sensing, diagnostic imaging, and actuators for drug delivery [5–9]. Their unique photophysical properties, such as high brightness, resistance to photobleach, and the ease of functionalization with targeting ligands for site-directed activity are very attractive for several areas of biology and medicine. However, major concerns have been raised regarding the toxicity of heavy metal based QDs, especially for those containing cadmium (Cd) in the core, like CdSe or CdTe QDs encapsulated in various coatings [10–13]. While risks posed on human health by Cd toxicity

have been known and thoroughly investigated for over 50 years and extensive studies on both the genotoxic and cellular effects have been performed on many model systems [14], the large variety of inducible effects, from the intracellular damages, to the induction of oxidative stress, apoptosis, disruption of intracellular calcium signalling still remain separate pieces of a complex puzzle [15,16]. Toxicity evaluation of Cd-based QDs appears rather difficult, and even more if considering several nanoscale depending properties to be taken into account, such as quantum size effects and electronic interactions; particle's size, surface coating and charge; particular synthetic route, etc [17–21]. In the *in vitro* models the cytotoxic effects of Cd-based QDs have been ascribed to the release of Cd<sup>2+</sup> ions from the particle core [22–24], as well as to the Cd<sup>2+</sup> ions present at particle surface [25,26]. Coating of these QDs with an additional inorganic shell (i.e. ZnS) or stabilizing ligands employed during the synthesis (i.e., thioglycolic acid (TGA), glutathione (GSH), mercaptopropionic acid, cysteamine) has been shown to strongly influence the interaction with living cells and the toxicity of QDs [13,26–28]. Depending on the subcellular localization of the internalized QDs, and the local pH and the redox environment they encounter, stabilizing ligands can be removed from

\* Corresponding author.

E-mail addresses: [a.ambrosone@cib.na.cnr.it](mailto:a.ambrosone@cib.na.cnr.it) (A. Ambrosone), [lc.mattera@gmail.com](mailto:lc.mattera@gmail.com) (L. Mattera), [v.marchesano@cib.na.cnr.it](mailto:v.marchesano@cib.na.cnr.it) (V. Marchesano), [alessandra.quarta@nano.cnr.it](mailto:alessandra.quarta@nano.cnr.it) (A. Quarta), [asusha@cityu.edu.hk](mailto:asusha@cityu.edu.hk) (A.S. Sussha), [a.tino@cib.na.cnr.it](mailto:a.tino@cib.na.cnr.it) (A. Tino), [andrey.rogach@cityu.edu.hk](mailto:andrey.rogach@cityu.edu.hk) (A.L. Rogach), [c.tortiglione@cib.na.cnr.it](mailto:c.tortiglione@cib.na.cnr.it) (C. Tortiglione).



the surface via protonation or photooxidation [29,30] resulting in the QD aggregation and/or exposure of their inorganic core to the cytoplasmic biomolecules. Such unprotected QDs may induce the generation of Reactive Oxygen Species (ROS), whose cellular unbalance causes modification and damage of lipids, proteins and DNA, finally leading to cell death [21,28,31]. However, cell death induced by Cd-based QDs has also been associated with apoptotic pathways, as shown both at biochemical and molecular levels by the deregulated expression of anti- and pro-apoptotic genes, i.e. Fas receptor and Jun-N-terminal kinase (JNK) in neuroblastoma cells [32], Bax, Bcl-2 and caspase in human breast cancer cells [33]. Despite the great number of cytotoxicity studies utilizing *in vitro* models, *in vivo* studies of the inorganic nanoparticles have been very limited [34–36]. *In vivo* systems are extremely complicated and interactions of nanomaterials with biological components, such as proteins and cells, could lead to unpredictable effects. Aquatic invertebrates, routinely employed for environmental pollution studies, are valuable organisms for both toxicology and ecotoxicology studies. After release to the aquatic environment nanoparticles can be uptaken by planktonic or sediment dwelling invertebrates, and enter the food chain, representing a hazard for wildlife and humans [37]. Although a few studies have been testing Cd-based QDs in freshwater invertebrates such as *Daphnia magna* [38] and the mussel *Elliptio complanata* [39,40], quantitative data are still rare, and further in-depth studies are highly desirable. Here, we have chosen the cnidarian polyp *Hydra vulgaris*, a well characterized system to test environmental pollution, to assess toxic effects of thiol-capped CdTe QDs, a well known example of light-emitting semiconductor nanoparticles which can be directly synthesized in water [41,42]. *Hydra* is a small freshwater polyp, shaped like a hollow tube with a basal foot and an apical mouth surrounded by tentacles. It can be easily maintained in the lab allowing massive culturing. Polyps exposure to medium suspended toxicants may cause alteration of morphological traits and developmental programs, adversely affect regeneration process, pattern formation, reproductive capabilities, parameters that can be all precisely and accurately estimated and quantified by reliable assays. *Hydra* has been used in the past to study the toxicity of effluents [43] and heavy metals [44,45]. Moreover, owing to its remarkable regenerative capacity, it was employed to examine the teratogenic potential of several chemicals including ethinylestradiol and bisphenol A [46,47], nonylphenol [48] and several pharmaceuticals [49–51]. Furthermore, the molecular tools available, i.e. whole genomic sequence, gain and loss of function techniques, may enable to study at molecular level the mechanisms underlying the toxicity.

In the past few years we have tested the interaction of both quantum dots and quantum rods coated by amphiphilic polymers with *Hydra*, showing their great potential for studies of *in vivo* imaging and cell tracking, as well as behavioural assays [52–55]. More recently we have reported that CdTe QDs (stabilized by either TGA or GSH) induce clear signs of toxicity in acute lethality tests [55]. With the aim to understand the long-term effect of CdTe QDs on *Hydra*, we provide here a comprehensive toxicity study of one specific QD type (TGA capped CdTe QDs), rather than comparing different chemistries of QD coatings. Different organic ligands of QDs exposed at the cell surface may elicit specific responses, which might be difficult to distinguish from the Cd responses, due to the overlapping and cross-talking of defence mechanisms occurring inside the cell. We evaluated the QD toxicity using multiple quantitative approaches, spanning from *in vivo* tests (evaluation of morphological alterations, reproductive and regenerative capabilities), to cell biology approaches (determination of cell proliferation rate, nuclei apoptosis markers), up to the molecular analysis of genes involved in the cell death by controlling apoptosis or cell

stress responses. Our results address multiple aspects of QD induced toxicity offering a valuable scenario of the possible signalling pathways activated, and emphasizing the use of *Hydra* as efficient, cost effective and reliable model system to assess *in vivo* ecotoxicological impact of colloidal nanomaterials.

## 2. Materials and methods

### 2.1. Culture of test organism

*H. vulgaris* were cultured in *Hydra* medium comprising 1 mM calcium chloride, 0.1 mM sodium hydrogen carbonate, pH 7 [56]. Animals were fed on alternate days with *Artemia nauplii* at 18 °C with a 12:12 h light: dark regime. Polyps from homogeneous populations, three-weeks-old and carrying one or two buds, were selected for the experiments.

#### 2.1.1. Toxicity of CdTe QDs to individual polyp

At an early stage, lethal toxicity studies were performed in order to assess the animal tolerance and to accurately set the sub-lethal doses of QDs.

Increasing QD concentrations (from 1 nM to 100 nM, corresponding to 0.04 mg/L–4.0 mg/L Cd equivalent, as determined by elemental analysis) were selected to assess the progressive effects on the morphology and physiology of individual polyps. Toxicity tests were carried out on groups of 25 polyps for 24, 48 and 72 h. The animals were placed into plastic multiwells maintained at a temperature of 18 °C in an incubator with a light regime of 12 h light and 12 h dark, refreshing the medium every 24 h. For comparison, toxicity tests using water-soluble CdCl<sub>2</sub> salt, prepared from 100 mg/L stock solutions using *Hydra* medium as diluent were performed at same time points to study the effects caused by Cd<sup>2+</sup> ions. Effects were recorded by microscopic examination of each polyp at 24 h intervals and a score was assigned ranging from 10 for a normal polyp to 0 if it was disintegrated, as described in the key (Table S1 of Supplementary data) constructed by Wilby [57] and used by many authors [45,50,58]. The median scores were analysed at 24, 48 and 72 h for each concentration of QDs and CdCl<sub>2</sub>.

### 2.2. Estimation of the Cd content per *Hydra* by elemental analysis

Five hundreds polyps were incubated for 12 and 24 h with 1 mg/mL Cd supplied either as QDs (corresponding to 25 nM nanoparticle concentration) or as CdCl<sub>2</sub> salt, then washed and digested by the addition of a HCl/HNO<sub>3</sub> 3:1 (v/v) solution. The intracellular Cd content was measured by means of ICP-AES (Inductively Coupled Plasma Atomic Emission Spectrometer). The data obtained were reported as Cd content per *Hydra*.

### 2.3. *Hydra* growth rates and regeneration

Animals (four *Hydra* with one bud) were treated with 10 and 25 nM of CdTe QDs for 24 h, then washed, and the following day placed in 3.5 cm Petri dishes (1 *Hydra*/dish). Control polyps at the same developmental stage were not treated. Both treated and untreated *Hydra* were fed once daily for 14 days. The growth rate constant (*k*) of an exponentially growing group of animals is defined as  $\ln(n/n_0) = kt$  where *n* is the number of animals at time *t* and *n*<sub>0</sub> the number of animal at *t*<sub>0</sub>. For *n*/*n*<sub>0</sub> = 2, *t* = *T*<sub>2</sub>, the doubling time of the population. *T*<sub>2</sub> was determined by linear regression [59]. For regeneration experiments, groups of 25 polyps were bisected in the upper gastric region and incubated in presence of 10 nM and 25 nM QDs. The regenerating polyps, monitored through a stereomicroscope, were grouped in three stages according to their tentacle morphogenetic process.

### 2.4. BrdU assay

To estimate the cell proliferation rate, intact *Hydra*, untreated or treated for 72 h with 25 nM QDs, were continuously incubated with 5 mmol/L bromodeoxyuridine (BrdU) (Sigma) for 12, 24, 48 and 72 h. Animals were anaesthetized in 2% urethane in *Hydra* medium for 2 min, macerated by heating, immediately fixed with 4% para-formaldehyde and the cells spread on microscope slides. BrdU incorporation in proliferating cells was detected by immunolocalization using mouse anti BrdU monoclonal antibody (1:500, Sigma), and Novolinker polymer detection system (Novocastra) according to the manufacturer's instructions. Epithelial and interstitial BrdU-labelled cells were observed and counted by phase contrast microscopy (Axiovert 100, Zeiss) equipped with a digital colour camera (Olympus, DP70).

### 2.5. RNA extraction and qRT-PCR

Total RNA from treated and untreated animals was purified using Tri Reagent (Molecular Research Center) and its concentration was determined on the NanoDrop ND-1000 spectrophotometer (Thermo Scientific, USA). The first-strand cDNA synthesis was carried out with the SuperScript II Retrotranscriptase (Invitrogen) and oligo dTs, using 0.5 µg of DNA-free RNA in a final volume of 25 µL, according to the manufacturer's instructions. Real-time RT-PCR (qRT-PCR) was performed in 25 µL of

reaction mixture consisting of 1 × Express Sybr® GreenER qPCR SuperMix with premixed ROX (Invitrogen), serial cDNA dilutions and 0.3 μM each primer. The reactions were processed using the StepOne Real-Time PCR System (Applied Biosystem) under the following fast cycling steps: initial denaturation for 2 min at 94 °C, followed by 40 cycles at 94 °C for 2 s, 59 °C for 30 s. In addition, melting curves (20 min; from 59 °C to 90 °C) were generated to check any spurious amplification products. To normalize RNA levels, *Hydra* Elongation factor 1 $\alpha$  gene (HyEf-1 $\alpha$ , GenBank Accession no. Z68181.1) was employed as internal calibrator. Nucleotide sequences and alignments were obtained from *Hydra* genome database (<http://Hydrasome.metazome.net>). Specific primers of *Hydra* homologues genes of Superoxide dismutase (HySOD), Caspase 3 (HyCasp3), c-myc (Hymyc1), FoxO, Hsp70, Bcl-2 (Bcl2-like 4), were designed using Primer3 software (<http://frodo.wi.mit.edu/primer3/>) and are listed in the Table S2 of Supplementary Data. Gene expression was evaluated in QD treated and untreated polyps; at least three technical repeats from three biological replicates were carried out. Herein, the delta–delta Ct (2- $\Delta\Delta$ CT) method, for comparing relative expression results between treatments, was applied [60].

## 2.6. Assessment of apoptosis

Apoptotic cell death was evaluated by 4'-6-Diamidino-2-phenylindole (DAPI) staining and confirmed by Terminal deoxynucleotidyl Transferase-mediated dUTP nick end labeling (TUNEL) assay [61]. Briefly, untreated and QD treated polyps were macerated and the single cell suspension was fixed with 4% paraformaldehyde and spread on slides. After extensive washing in PBS, macerates were stained with DAPI for 2 min and washed in PBS. Slides were observed with phase-contrast fluorescent microscopy to detect picnotic nuclei. More than 300 cells were counted for each treatment and the percentage of apoptotic nuclei was determined. In Situ Cell Death Detection Kit Fluorescein (Roche) was used for TUNEL assay to confirm the nuclear shrinkage in macerates. In particular, fixed cells were permeabilized for 2 min with 0.1% Triton X-100/0.2% sodium citrate solution. Slides were incubated with 50 μl TUNEL reaction mixture in a humid dark chamber for 60 min at 37 °C, extensively washed in PBS and counterstained with DAPI solution. The presence of apoptotic cells was confirmed by counting fluorescein-labelled nuclei by fluorescent microscopy.

## 2.7. Caspase assay

Caspase-3 activity was measured using the Ac-DEVD-AMC (N-Acetyl-Asp-Glu-Val-Asp-7-amino-4-methylcoumarin) fluorogenic substrate (Alexis). Total protein extraction from untreated and QD-treated polyps was carried out in 25 mM HEPES pH 7.5, 5 mM MgCl<sub>2</sub>, 1 mM EGTA, protease inhibitors (leupatin, pepstatin and aprotinin 10 μg/ml each), and 1 mM Pefabloc. Protein content was measured using Bradford assay (Bio-Rad, CA). Standard curves for Caspase-3 substrate were prepared with serial dilution of AMC (aminomethylcoumarin, Calbiochem). Protein extracts for each treatment were incubated with 100 mM Ac-DEVD-AMC substrate in 25 mM HEPES pH 7.5, 0.1% CHAPS, 10 mM DTT and protease inhibitors for 1 h at 37 °C. Caspase-3 activity was measured by monitoring the release of fluorogenic AMC using a microplate reader (Infinite M1000, TECAN).

## 3. Results

### 3.1. *Hydra* exposure to CdTe QDs: impact on the morphology and survival rate

TGA capped QDs (3.2 nm mean diameter with an absorption wavelength of the first electronic transition at 550 nm) were synthesized as previously reported [41]. Living animals were soaked in culture medium supplemented with increasing QD doses (from 1 nM to 100 nM) and monitored at 24, 48 and 72 h of incubation. Progressive physical damages were observed, as shown by representative images of Fig. 1A. Morphological alterations were estimated using a score system ranging from 10 (indicative of healthy condition) to 0 (animal fully disintegrated), as previously reported [57] (Table S1 and Fig. S1 of Supplementary Data). Median scores recorded at each QD test concentration decreased for treated animals with increasing concentration and incubation time (Fig. 1B). Similar toxicity curves were obtained by exposing animals to water-soluble CdCl<sub>2</sub> salt, at concentrations comparable to Cd contained in the QD. According to the ICP-AES analysis, 10 nM and 25 nM concentration of QDs equals to 0.4 mg/L and 1 mg/L Cd, respectively. By comparing statistically the median scores of animals exposed to similar Cd doses, supplied either as CdCl<sub>2</sub> (plane line) or CdTe QDs (dotted line), significant lower values were

produced by QDs at each time point and test concentration relative to Cd salt (Fig. 1C), indicating a more toxic effect of QDs. Mortality data from these experiments were analysed to determine median lethal times (LT50) and median lethal concentrations (LC50), presented in Fig. 1D. These values were calculated by applying the trimmed Spearman-Kärber method, which offers good statistics, is easy to use, and is recommended for accurate and precise calculation of LT50 and LC50 values and their 95% confidence interval end points [62]. The calculated values at 24 h time point, clearly indicated a more toxic effect caused by QDs compared to equivalent CdCl<sub>2</sub> doses, confirming morphological analysis. Overall, the two different methods used to examine toxicity of CdTe QDs, based on structural changes and on mortality, enabled to determinate sub-lethal doses to assess QD long term effects.

Due to the luminescence quenching effect played by the *Hydra* culture medium (containing 1 mM calcium ions) on CdTe QDs [63], we could not observe their internalization into *Hydra* tissues via *in vivo* optical detection. As it has been widely discussed that the primary determinant of CdTe QDs toxicity might be Cd<sup>2+</sup> ions released from QDs [17,23,24], by means of ICP-AES we measured the intracellular Cd concentration of animals treated either with QDs or with equivalent amount of CdCl<sub>2</sub>. Fig. 1E shows the Cd content per *Hydra* measured after 12 and 24 h of incubation: for QD treated polyps most of the uptake occurs over the first 12 h of incubation, as shown by similar Cd amounts found also at 24 h. For CdCl<sub>2</sub> treated animals the measured Cd content was nearly three times higher, suggesting different internalization route and toxicity mechanisms for CdTe QDs and Cd<sup>2+</sup> ions. In order to further assess the stability of CdTe QDs in *Hydra* medium, an estimation of the amount of Cd<sup>2+</sup> ions released into solution was performed following QD centrifugation and analysis of both the QD and the remaining supernatant solution after 12 and 24 h of incubation. Results of these measurements (shown in Fig. S2 of Supplementary Data) indicate that only small percentages of Cd<sup>2+</sup> ions are released into solution at these two time points (12% and 14% of the total measured Cd, respectively), indicating a good stability of QDs in *Hydra* medium. This further confirms that the observed toxicity effects were mostly due to the intact QDs rather than to the small amounts of released Cd<sup>2+</sup> ions. From here onwards the toxicity studies were performed on CdTe QDs, without comparing them to CdCl<sub>2</sub>.

### 3.2. *Hydra* exposure to CdTe QDs: impact on regeneration and reproductive capabilities

The QD toxicity screening *in vivo*, at whole animal level, was completed by the assessment of the impact on the regenerative and reproductive capabilities. *Hydra* polyps are characterized by the remarkable capacity to regenerate amputated body parts: during the first 48 h post-amputation (p.a.) morphogenetic processes take place, followed by cell proliferation to restore adult size. Healthy polyps were bisected and allowed to regenerate in presence of sub-lethal doses of QDs. A clear dose dependent inhibition of regeneration was observed (Fig. 2A): stumps exposure to high QD dose (25 nM) impaired most of polyp head regeneration at stage 0 (stumps with no emerging tentacles) and caused 35% of mortality, while exposure to 10 nM QDs slightly impaired patterning during the first 48 h, but this effect was later completely recovered. The observed differences in the efficiency of regeneration (for the 25 nM treatment) were highly significant as shown by the statistical analysis (Chi-square equal to 73.4, with six degree of freedom,  $P < 0.0001$ ).

Besides the effect on regeneration, the reproductive capability of QD treated polyps was estimated. In *Hydra*, the epithelial cells structuring its body continuously divide, migrate towards the

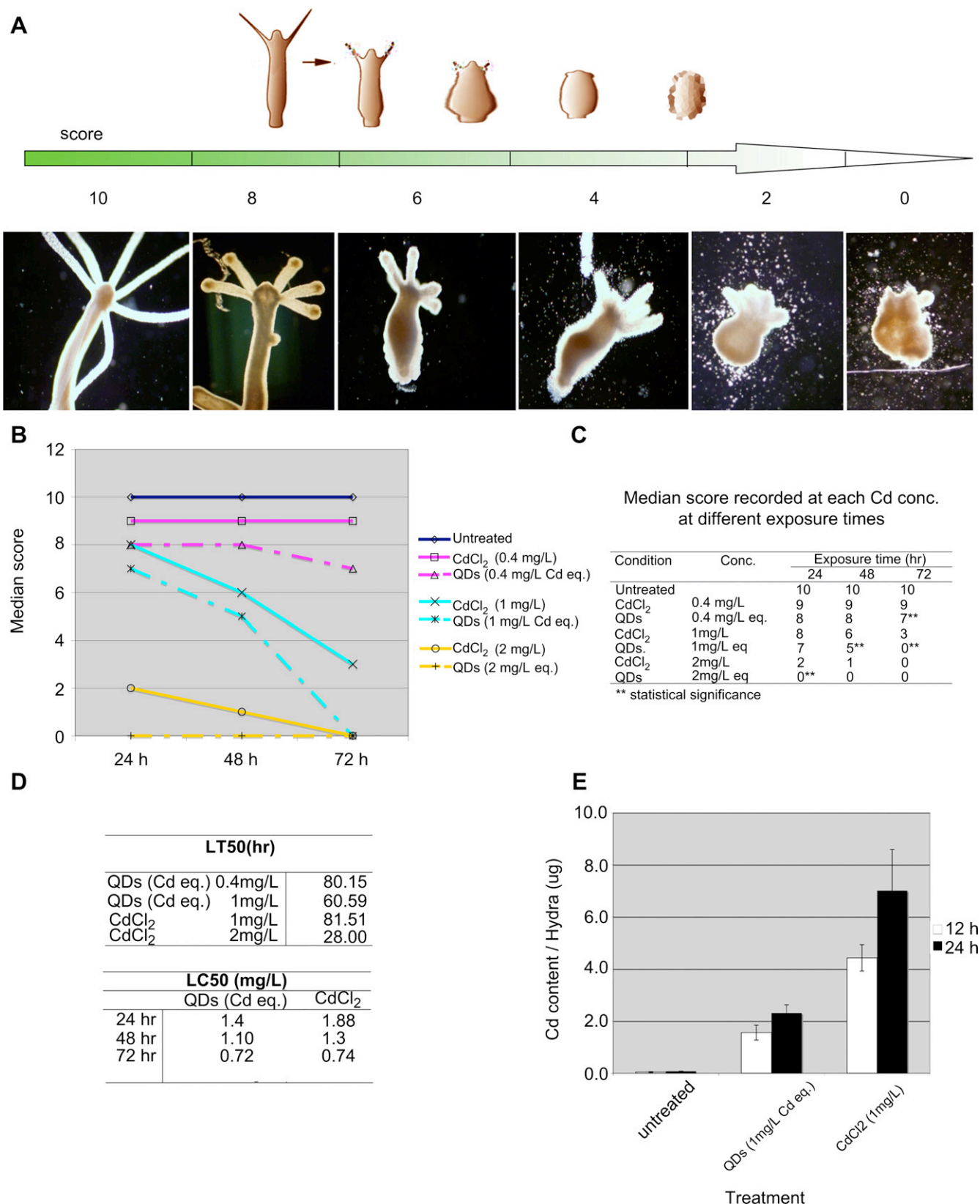


**Fig. 1.** Toxicological impact of CdTe QDs on *Hydra*'s morphology and viability. A) Examples of morphological alterations induced by continuous exposure to CdTe QDs. The green arrow represents the score system [57] used to evaluate progressive morphological changes of polyps exposed to CdTe QDs, ranging from 10 (healthy animals) to 0 (disintegrated polyps). The complete description of the structural changes associated to the numerical score is provided in Table S1 of Supplementary Data. B) Toxicity curves of *Hydra* polyps exposed to different concentrations of Cd in QDs or CdCl<sub>2</sub>. For both treatments, toxicity increases with time and concentration. For each test concentration and time point median values were calculated on groups of 25 animals. A representative experiment from triplicates is shown. C) For each concentration, a statistical analysis of significance between QD and CdCl<sub>2</sub> treatment indicates a higher toxic effect of QDs compared to the same amount of CdCl<sub>2</sub> (Kruskal–Wallis non parametric Anova and Dunn's post hoc tests,  $p < 0.0001$ ). D) Comparison of median lethal concentration (LC50) and median lethal time (LT50) for QDs and CdCl<sub>2</sub>. Scores  $\geq 5$  were reversible and sub-lethal, while scores  $\leq 4$  were considered lethal. As the test is based on mortality data, and CdCl<sub>2</sub> at 0.4 mg/L does not cause mortality, for the CdCl<sub>2</sub> treatment the LT50 were calculated relative to 1 mg/L and 2 mg/L concentration. Data are means ( $\pm$ SD) of three independent experiments ( $n = 60$ ). E) The intracellular Cd amount was evaluated by elemental analysis. *Hydra* polyps were incubated with either QDs or CdCl<sub>2</sub> salt at an equivalent Cd concentration (1 mg/L) for 12 and 24 h. The Cd content is reported as mass per *Hydra*. (For interpretation of the references to colour in this figure legend, the reader is referred to the web version of this article.)



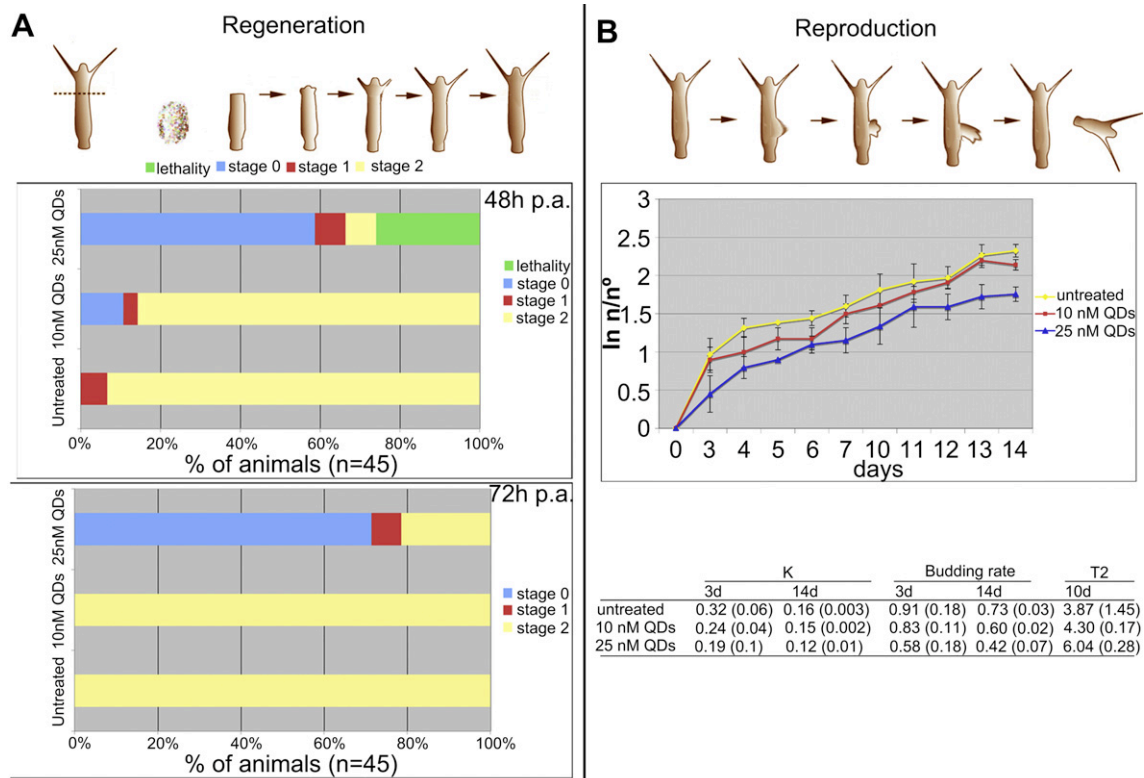


**Fig. 2.** Influence of CdTe QDs on *Hydra* regeneration and reproduction. A) Impact of CdTe QDs on regeneration. Groups of 15 animals were bisected at subhypostomal level and allowed to regenerate (scheme at the top panel) in presence of 10 nM or 25 nM QDs, or in normal medium. At 48 h and 72 h post-amputation animals were inspected for viability and regeneration stage: stage 0 indicates a complete inhibition of regeneration; stage 1 indicates the presence of tentacle buds; stage 2 indicates new emerging tentacles. Animals treated with 25 nM QDs are significantly impaired in the regeneration process. Data are means of three independent experiments. Chi-square equal to 73.4, with six degree of freedom, was highly significant ( $P < 0.0001$ ). The post hoc test indicated that the high QD dose condition (25 nM) determined the significant contribution to the Chi square value. B) Impact of CdTe QDs on reproduction. *Hydra* population growth test started with a population of four full-grown *Hydra*, either untreated or incubated 24 h with 10 nM and 25 nM CdTe QDs, washed out and monitored every day for bud detachment (scheme at the top panel). Different parameters concerning the population growth rate are presented:  $k$  is the logarithmic growth rate constant and represents the slope of the regression line obtained from the standard equation of logarithmic growth:  $\ln(n/n^0) = kt$ .  $T_2$  is the population doubling time, obtained by the standard equation when  $n/n^0 = 2$ . The budding rate was calculated as the average number of buds detached per *Hydra* per day. The graph in the middle panel shows the  $\ln(n/n^0)$  values at each time point. In the lower panel the growth parameters ( $\pm$ SE) at day 3 and day 14 are compared. The 25 nM QD treatment impaired the population growth (see the differences in the  $n/n^0$ ,  $k$  and the budding rate at day 3 at the beginning of the monitoring period), while later on the animals recover (constant growth values similar at 14 day).

animal ends, contributing to the formation of new individuals, budding from the gastric region, and detaching from the mother in about 3 days (Fig. 2B, upper panel) [59]. Environmental factors, such as the presence of pollutants or the feeding regime, can affect this process. Thus, the population growth rate is an indirect measure of the *Hydra* tissue growth rate and cell viability. A group of founder animals ( $n^0$ ) either untreated or incubated for 24 h with 10 nM or 25 nM QDs, were monitored over two weeks, and the total number of individuals ( $n$ ) used to calculate the growth rate constant ( $k$ ) over the duration of the experiment ( $t$ ), was defined by the equation  $\ln(n/n^0) = kt$ . In Fig. 2B the growth rate curve of animals treated with 25 nM QDs was found significantly different from the others (untreated animals, or treated with the 10 nM QDs), over the initial days of monitoring, impacting on the total population along the overall period. Comparing the growth parameters at each inspection time (lower panel of Fig. 2B) significant differences were found in the  $k$  values and in the budding rates at the beginning (day 3) but not at the end (day 14) of the observation period, indicating that the treated population founders were impaired in the budding process. As the QDs were diluted to the progeny, from the second generation onwards, the reproduction process was progressively less affected up to the normal physiological rates ( $k$  values become not significantly different in about one week).

### 3.3. Cytotoxic effects of CdTe QDs: cellular and biochemical evidences

As the growth rate is related to the epithelial cell cycle, we also investigated the potential effect of QDs on cell proliferation activity. *Hydra* polyps were co-incubated with 25 nM QDs (the dose affecting reproduction) and BrdU (see Materials and methods); the proliferation rates of both epithelial and stem cells were calculated over 72 h by BrdU immunodetection. Results presented in Fig. 3A and B show a significant decrease in the cell proliferation activity of epithelial and interstitial cells of treated animals, starting 24 h after QD incubation. This effect on cell division accounts for the decreased population growth observed in Fig. 2B.

As nuclear shrinkage, chromatin condensation and DNA damage are associated with multiple pathways leading to cell death, we analysed by confocal laser scanning microscopy possible effects of QD treatment with nuclear morphology. A quantitative analysis performed on single cell suspensions obtained from treated animals, shows that the nuclear damage is time and dose dependent, as cells treated with 25 nM QDs for 72 h show the highest percentage (20%) of damaged nuclei (Fig. 3C). The presence of apoptotic nuclei also in untreated polyps is due to the physiological role played by the programmed cell death in maintenance of the steady state in continuously renewing tissues, such as all *Hydra*.

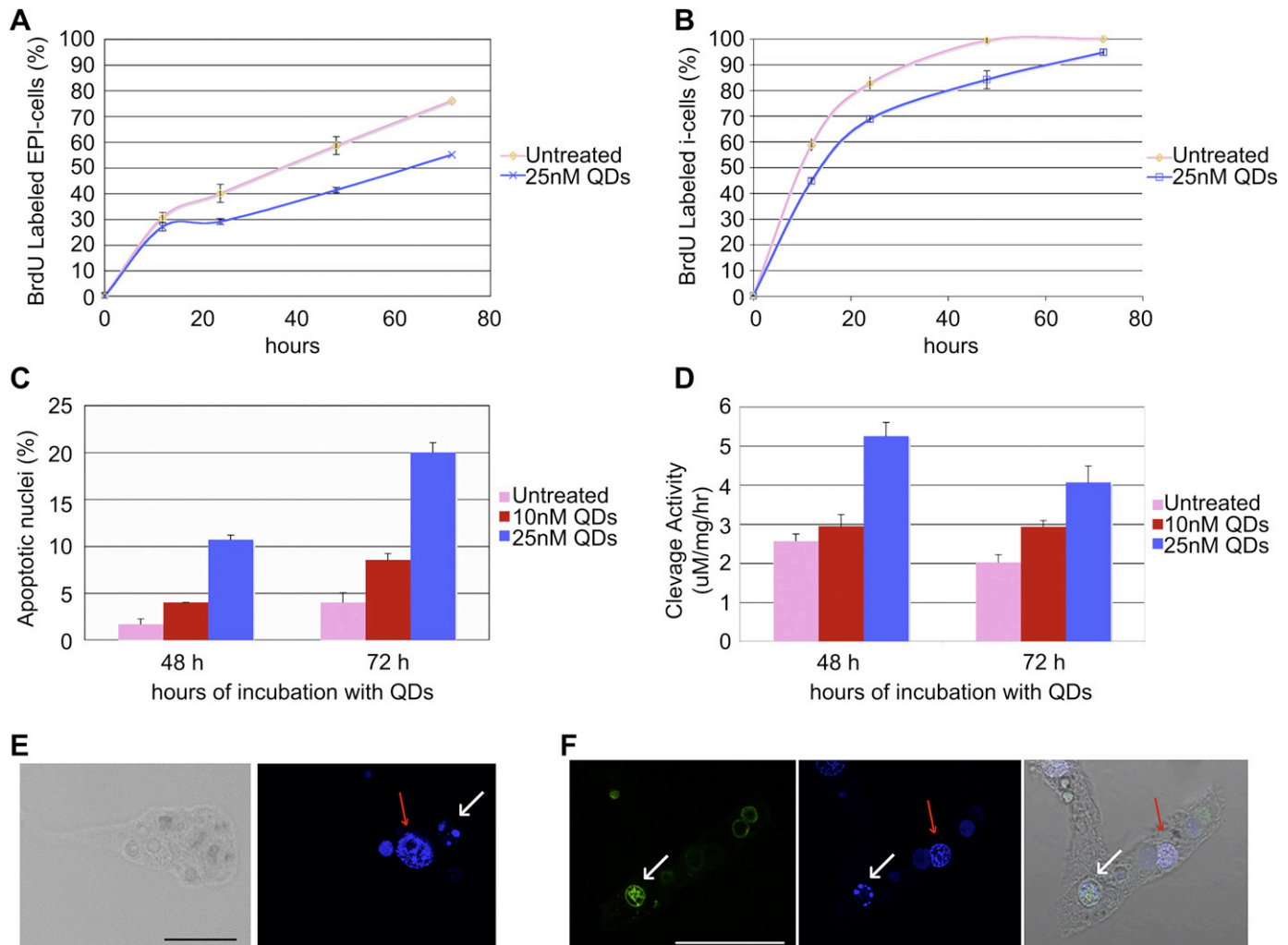


**Fig. 3.** Effect of CdTe QDs on cell proliferation and death A) Cell cycling activity of epithelial cells (EPI) and B) cell cycling activity of interstitial stem cells (i-cells) were estimated in untreated and 25 nM QD treated animals by continuous incubation with BrdU, followed by maceration of ten animals (showing morphological score >6) at the indicated time points and the colorimetric immunostaining (see Materials and Methods). QDs impaired the proliferating activity of both epithelial and interstitial cells, as shown by the lower percentage of BrdU labelled nuclei. Data represent the average of three different experiments. C) Cellular assessment of apoptosis induction by QDs. Following 48 h and 72 h incubation with 25 nM QDs polyps were macerated in single cells and the percentage of apoptotic cells was determined by counting the DAPI-stained fragmented nuclei. D) Biochemical assessment of apoptosis induction by QD. Caspase enzyme activity was measured on extracts of QD-treated (10 nM and 25 nM) and untreated control tissues incubated with the caspase substrates Ac-DEVD-AMC. The enzyme activity was significantly higher in polyps treated with the highest QD dose. E) Confocal microscopy imaging of single cells prepared from QD treated Hydra. The morphology observed by phase contrast indicates an ectodermal epitheliomuscular cell. Fluorescence imaging following DAPI staining shows a normal nucleus (red arrow) and a typical apoptotic picnotic nucleus (white arrow). A digestive vacuole is also DAPI positive, due to the presence of DNA from ingested preys. F) TUNEL assay on single cell suspensions prepared from QD treated Hydra. On fluorescence images the white arrow indicates an apoptotic nucleus, TUNEL positive (left panel, green channel) and fragmented (central panel, DAPI staining, blue channel), while the red arrow indicates a normal nucleus (TUNEL negative, non fragmented). Both nuclei are located inside an endodermal cell, which engulfed an apoptotic cell. Other reacting signals arise from DNA containing digestive vacuoles (abundant in endodermal cells), as shown by merging phase contrast and fluorescence images (right panel). Scale bar in E and F: 20  $\mu$ m. (For interpretation of the references to colour in this figure legend, the reader is referred to the web version of this article.)

tissues, as reported elsewhere [64]. A representative image of a fragmented nucleus (Fig. 3E, white arrow) compared with the normal nucleus (Fig. 3E, red arrow) shows its localization inside an epithelial cell, which indicates that an apoptotic cell has been engulfed by an epithelial ectodermal cell. To gain deep insights into the mechanisms causing the QD induced cell death, we investigated the elicitation of the apoptotic pathways both at the biochemical and cellular level. To test for caspase activity associated with apoptosis, protein extracts were prepared from QD treated and untreated animals and incubated with the fluorogenic substrate Ac-DEVD-AMC, which is specifically cleaved by Caspase 3 in *Hydra* [65]. Fig. 3D shows that extracts of untreated *Hydra* had a lower level of caspase activity compared to QD treated *Hydra* extracts, causing the induction of a twofold increase in Ac-DEVD-

AMC cleavage activity both at 48 and 72 h of the 25 nM QD treatment. At cellular level DNA fragmentation resulting from apoptotic signalling cascades was detected by TUNEL assay. In Fig. 3F, confocal laser scanning imaging of single cell suspensions processed for TUNEL assay and DAPI staining clearly indicate an apoptotic nucleus inside an endodermal cell.

### 3.3.1. Genotoxic effect of CdTe QDs

Recent findings showed the CdTe QD mediated activation of different genetic cascades leading to cell death. General stress responsive genes or more specifically those acting in the apoptosis signalling pathway have been found induced by CdTe QDs in several biological systems [26,33,40,66]. The conservation of key molecular pathways in *Hydra* genome led us to study the



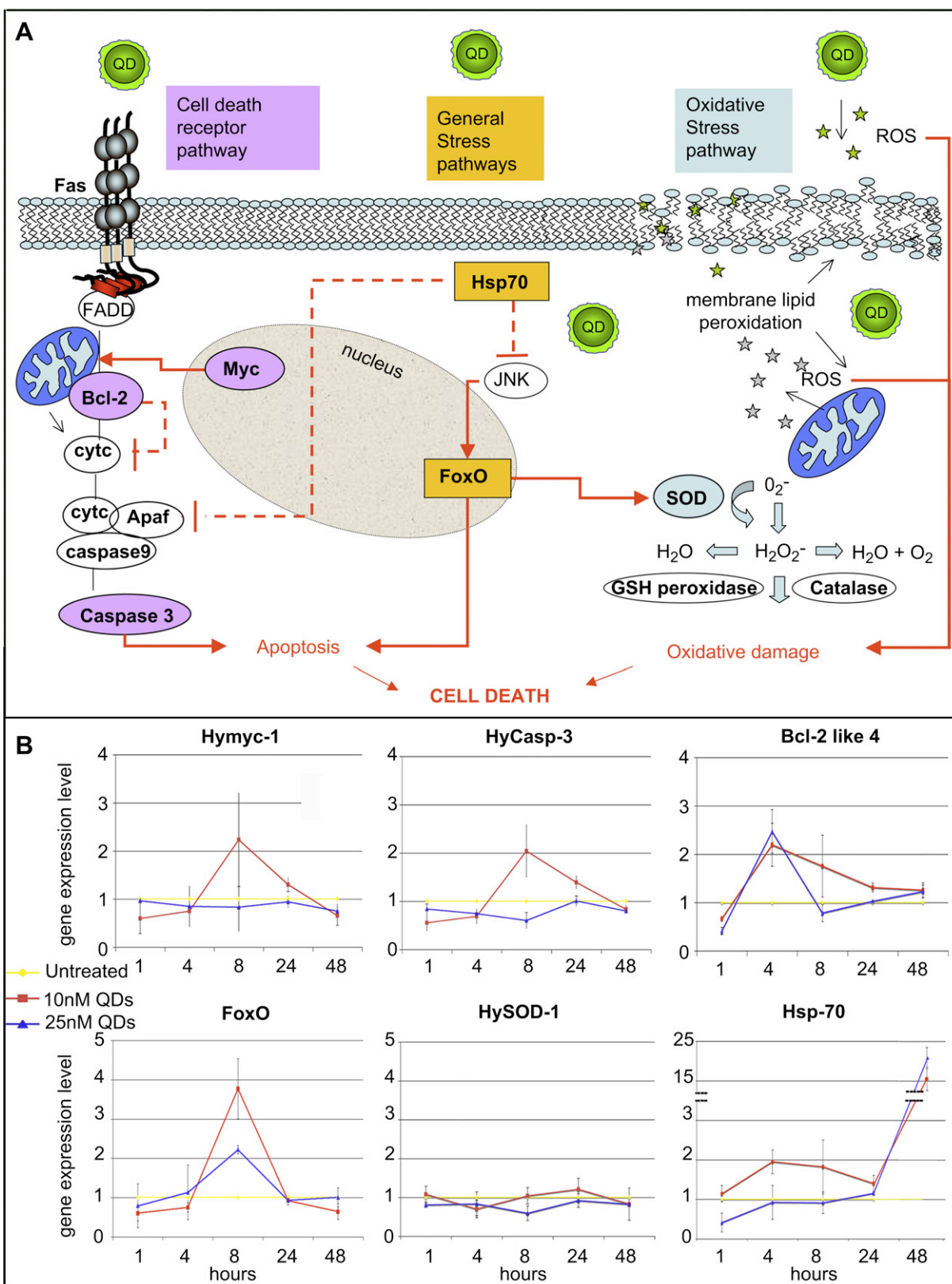


**Fig. 4.** Genotoxic effect of CdTe QDs on *Hydra* A) Schematic representation of molecular pathways involved in the cell response to environmental stimuli. Cell exposure to CdTe QDs may elicit a number of reactions which may lead to death or stress adaptation. These processes are mediated by signaling pathways which induce deregulation of various stress-inducing or protective molecules. Key components of the apoptotic pathways are shown on the left panel and depend on the activation of the death receptor. Genes selected in this study, namely the *c-myc*, *Bcl2* and *caspase 3*, are indicated in violet. Gene accession numbers for the *Hydra* homologues (*Hymyc1*, *Bcl-2 like 4*, and *HyCaspase 3*) are reported in Table S2 of Supplementary data. Selected stress responsive genes are depicted in orange (*Hsp-70*, *FoxO*), together with their relationship with components of other signalling pathways (plain arrowed red line indicates activation, dotted line indicates inhibition). On the right panel key reactions of the oxidative pathways are presented, from the membrane lipid peroxidation to the conversion of oxygen radicals into non-toxic products by the SOD gene (coloured in light blue). B) Temporal expression patterns of selected stress responsive genes in QD treated polyps by qRT-PCR analysis using Elongation factor 1-alpha (*Ef-1α*) as reference gene. Animals were treated with 10 nM and 25 nM QDs for the indicated periods, and processed for RNA extraction and qRT-PCR analysis using specific primers (see Table S2 of Supplementary Data). The general trend is an early (8 h) up-regulation of apoptotic genes induced by the 10 nM QD dose, and a late response (from 24 h) of the protective *Hsp-70* gene, suggesting a possible animal recovery. Data represent mean  $\pm$  SE of three technical repeats from three biological replicates. (For interpretation of the references to colour in this figure legend, the reader is referred to the web version of this article.)

transcriptional modulation possibly played by QD treatment on genes involved in such vital processes as oxidative stress detoxification, apoptosis and cell proliferation. Among the complex gene networks acting independently or cross-talking in response to environmental (chemical, physical, mechanical) stimuli or biological stressors, we focussed our attention on an array of genes already isolated and characterized in *Hydra*: the transcriptional factor *Hymyc1*, involved in stem cell proliferation/differentiation [67,68]; the anti-apoptotic gene *Bcl2-like 4* [69] which controls mitochondrial outer membrane permeabilization; the effector protease *Caspase-3* [65], the stress responsive transcription factor *FoxO* [70], and the detoxifying *Superoxide Dismutase* (SOD) [71]. Their role in the diverse stress responses is schematically shown in Fig. 4A. Animals were incubated with QDs for increasing periods ranging from 1 h up to 48 h, and then processed for qRT-PCR analysis, using specific primers (see Table S2 of Supplementary Data). Results of Fig. 4B show that SOD transcript levels were not affected by the QDs, while all the other genes clearly showed a deregulation over the first 8 h of treatment. In detail, the apoptotic *Hymyc1* and *HyCasp3* genes showed an overlapping expression pattern, being both upregulated after 8 h of exposure to 10 nM QDs. *Bcl2-like 4* expression levels were also enhanced, throughout an extended temporal window (4 h–24 h). *FoxO* was found similarly activated after 8 h of exposure, by both QD doses, although once again the 10 nM QD amount caused the maximum effect. Finally, the anti-apoptotic gene *Hsp-70* showed increased expression along the period 4 h–24 h, and from 24 h onward an extraordinary enhancement. Considering the anti-apoptotic roles played by the *Hsp-70* gene family, this strong upregulation might suggest the cellular shifting from apoptosis pathway to normal cycle for functional recovery. Overall, the general trend of this gene profiling indicates an enhancement of stress responsive genes at 8 h elicited by the lowest investigated QD concentration (10 nM) pointing out on an effect on gene expression even in absence of morphological alterations.

#### 4. Discussion

For the widespread application of QDs in biology and medicine, the understanding of their potential toxicity effects on human and environment is crucial. Due to the presence of Cd in the most common types of QDs like CdSe and CdTe, the obvious concerns regarding their *in vivo* use for human purposes have emerged in many studies focused on elucidation of mechanisms underlying their toxicity [21,23,25,26] and discussed in recent excellent reviews [12,72]. The common conclusion from the different studies, most of them performed *in vitro*, was the finding of QD induced responses similar to the cellular responses to free Cd<sup>2+</sup> ions: depletion of endogenous antioxidants, enhanced production of ROS, lipid peroxidation, DNA damage, induction of apoptosis, disruption of intracellular calcium signalling [15,16]. The differences in QD types, synthetic routes, as well as cell lines or *in vivo* systems tested (molluscs, crustaceans, fish, mouse), make it difficult to assemble the large variety of data available from the literature into a general view. Following our recent study addressing the acute toxicity of *Hydra* to CdTe QDs [55], we present here a comprehensive analysis at animal, cellular, biochemical and molecular levels aimed on the identification of the whole response of *H. vulgaris* chronic exposure to CdTe QDs. Different to the most of higher vertebrate animals where cell stemness is confined, in adults, to a few anatomical districts, in *Hydra* all cell layers structuring the body are continuously dividing, so that a stress stimulus applied for a short period (2 h, as in the acute toxicity treatments) may generate immediate animal recovering after removal of stress, due to the continuous cell renewal. The chronic treatment makes it

possible to constantly expose all renewing cells to the stressor, and to assess the effects over a long time scale.

Progressive structural damages and lethality observed after continuous incubation with increasing doses of CdTe QDs, allowed for accurate estimation of typical LT50 and LC50 toxicity parameters, and for their comparison with those of CdCl<sub>2</sub>. Surprisingly, QDs showed higher toxicity compared to the same amounts of CdCl<sub>2</sub>, in line with some recent reports on bacteria, zebrafish and algae, which suggested nanoscale effects to explain the higher QD toxicity [13,73,74]. As the release of Cd<sup>2+</sup> ions from the QD cores was often considered to be the main cause of CdTe QDs cytotoxicity, we measured the intracellular Cd concentration of polyps treated with either CdCl<sub>2</sub> or CdTe QDs by elemental analysis. Our results showed a lower intracellular amount of Cd supplied as QDs, mostly uptaken over the first 12 h, compared to the amount found in polyps treated with CdCl<sub>2</sub>, uptaken at high rate. These data indicate (i) stability of QDs in *Hydra* medium, because if degradation would occur a high intracellular Cd content would be found, which was not the case; and (ii) higher QD toxicity, because a low intracellular Cd amount found in QD treated animals caused more severe damage than the high dose found in CdCl<sub>2</sub> treated animals, which is also shown by the median scores values at 24 h and 48 h in Fig. 1. They further show that the internalization routes for Cd<sup>2+</sup> ions and CdTe QDs may be different, and possibly rely on specific protein transporters for the former and occur through active membrane transport for the latter [75] and that the mechanisms behind the toxicity to Cd supplied as Cd<sup>2+</sup> ions or as CdTe QDs, although possibly overlapping at some point, are distinct. The sub-lethal doses estimated by morphological analysis were further applied for evaluation of long term effects on physiologically important phenomena, such as development and regeneration of *Hydra*. Interestingly, both *Hydra*'s reproductive rates and regenerating efficiency were impaired by the 25 nM but not 10 nM QD concentration, and were found to depend upon a decreased proliferation activity of all (epithelial and interstitial) *Hydra* cell layers. The decreased cell proliferation rates accounts for the delayed budding process at the beginning of the population growth test, which was slowly recovered until normal rate as the QD containing cells were sloughed off and replaced by new cells, and for the adverse effect on regeneration. This remarkable property relies on the reactivation of developmental programs, including cell division, whose impairment together with other possible ongoing cytotoxic effects may explain the decreased regeneration efficiency. The finding that only the 25 nM dose impacted these phenomena suggested a threshold toxicity value for this kind of QDs. The following cellular and biochemical assays confirmed this hypothesis. The elicitation of the apoptotic pathway was demonstrated by a quantitative analysis of the fragmented nuclei, engulfed by epithelial cells, present in higher percentages in animals treated with the higher QD dose, from 48 h onward. These cells were TUNEL positive, supplying further evidence for the initiation of the apoptotic pathway. A third approach confirmed this hypothesis: caspase 3 enzymatic activity was found enhanced by 25 nM QD treatment condition, thus indicating at the biochemical level the occurrence of apoptosis, as well. Finally, the conservation of the key regulatory genetic pathways in *Hydra*'s genome enabled the molecular characterization of QD treated polyps, through the assessment of transcriptional modulation of general stress responsive and apoptotic genes, which is known to occur as early response to the stimulus. Gene profiling by qRT-PCR from 1 to 48 h of incubation showed, except for SOD-1, enhanced transcript levels for the apoptotic genes *Hymyc1*, *Caspase 3*, *Bcl2*, and for the stress responsive *FoxO* and *Hsp70*. This enhancement, picking mostly at 8 h and for the 10 nM treatment, indicates an early response to a toxic stimulus, leading to a programmed cell death. Interestingly, from 24 h onwards, all gene expression levels were brought back to

normal, except the anti-apoptotic *Hsp70* known to inhibit different stress response pathways (Fig. 4), which showed strong upregulation (about 20 times) at 48 h. Overall this modulation might suggest *Hydra*'s controlled response, whose temporal dynamic can be divided in two phases: an immediate early response, over the first hours of challenging, to enhance the transcription of apoptotic genes, whose products (i.e. effector *caspase 3*) would act later (from 48 h onward), and a late response, from 24 h onward, switching on genes (i.e. *Hsp70*) to enable functional recovery. This interpretation fits well within the morphological scores of the animals sacrificed for gene profiling, ranging from 7 at 24 h (shortened tentacles, body slightly contracted) to 5 at 48 h (totally contracted, tentacles visible), the two stages still allowing animal recovery after stress suspension. The remarkable aspect of this molecular characterization is the gene modulation exerted by the low (10 nm) QD dose, which is consistent with the elicitation of apoptotic genes (*Hymc-1*, *Casp-3*, *FoxO*, *Bcl-2*) early in the treatment. Following continuous QD incubation the animal may shift to adaptation mechanisms, activating maintenance genes, such as *Hsp70*. Higher doses of QDs (25 nm) were not- or less effective in the induction of apoptotic genes, mirroring the cellular need to rapidly cope for the stressors (i.e. activation of necrotic mechanisms), rather than to activate slower genetic responses.

## 5. Conclusion

By using *H. vulgaris* as an aquatic invertebrate model organism, a comprehensive analysis of the effects displayed by CdTe QDs was performed at manifold levels. *Hydra* assays are fast, reliable and less expensive than cell culture systems, and yet provide an extraordinary wide repertoire of responses, *in vivo*, and *in vitro*, which allows us to study factors influencing toxicity of nanoparticles for human and environment health. Moreover, the high sensitivity to heavy metals makes *Hydra* an amenable tool for assessment of inorganic nanoparticle's toxicity in natural ecosystems, modelling biological barriers for their absorption, distribution, and persistency in the food chain. We found clear signs of cytotoxicity for CdTe QDs, resulting in endpoints of toxicity being distinct and even more potent than of dissolved Cd<sup>2+</sup> ions at equivalent doses. QD treatment adversely affected reproduction, regeneration, cell proliferation, and exerted genotoxic effects, such as chromosomal fragmentation, alterations in gene expression profiles. The modulation of gene expression in absence of evident morphological damages underlines the necessity of genotoxicity studies for a thorough examination of QD impact on living systems.

## Acknowledgments

We thank Dr. Angelika Bottger, Ludwig-Maximilians-Universität München, for invaluable help in cell biology approaches to evaluate apoptosis in *Hydra*; Dr. Giuseppe Nofe (CNR-Istituto di Cibernetica "E. Caianiello") for help in the statistical analysis of the data; and Giuseppe Marino (CNR-Istituto di Cibernetica "E. Caianiello") for technical assistance. This work was supported by the NanoSci-ERA net project NANOTRUCK (2009–2012), by the CNR Short Term Mobility Program 2011 awarded to A. Ambrosone, by the European project Magnifyco (Contract NMP4-SL-2009-228622), and by the City University of Hong Kong.

## Appendix. Supplementary material

Supplementary material associated with this article can be found, in the online version, at doi:10.1016/j.biomaterials.2011.11.041.

## References

- [1] Huynh WU, Dittmer JJ, Alivisatos AP. Hybrid nanorod-polymer solar cells. *Science* 2002;295:2425–7.
- [2] Hetsch F, Xu X, Wang H, Kershaw SV, Rogach AL. Semiconductor nanocrystal quantum dots as solar cell components and photosensitizers: material, charge transfer, and separation aspects of some device topologies. *J Phys Chem Lett* 2011;2:1879–87.
- [3] Choi CL, Alivisatos AP. From artificial atoms to nanocrystal molecules: preparation and properties of more complex nanostructures. *Annu Rev Phys Chem* 2010;61:369–89.
- [4] Rogach AL, Gaponik N, Lupton JM, Bertoni C, Gallardo DE, Dunn S, et al. Light-emitting diodes with semiconductor nanocrystals. *Angew Chem Int Ed* 2008;47:6538–49.
- [5] Medintz IL, Uyeda HT, Goldman ER, Mattoussi H. Quantum dot bioconjugates for imaging, labelling and sensing. *Nat Mater* 2005;4:435–46.
- [6] Alivisatos AP, Gu W, Larabell C. Quantum dots as cellular probes. *Annu Rev Biomed Eng* 2005;7:55–76.
- [7] Rogach AL, Ogris M. Near-infrared emitting semiconductor quantum dots for tumor imaging and targeting. *Curr Opin Mol Ther* 2010;12:331–9.
- [8] Pinaud F, Clarke S, Sittner A, Dahan M. Probing cellular events, one quantum dot at a time. *Nat Methods* 2010;7:275–85.
- [9] Michalet X, Pinaud FF, Bentolila LA, Tsay JM, Doose S, Li JJ, et al. Quantum dots for live cells, *in vivo* imaging, and diagnostics. *Science* 2005;28(307):538–44.
- [10] Rivera GP, Oberdorster G, Elder A, Puentes V, Parak WJ. Correlating physicochemical with toxicological properties of nanoparticles: the present and the future. *ACS Nano* 2010;4:5527–31.
- [11] Maynard AD, Aitken RJ, Butz T, Colvin V, Donaldson K, Oberdorster G, et al. Safe handling of nanotechnology. *Nature* 2006;444:267–9.
- [12] Maynard AD, Warheit DB, Philbert MA. The new toxicology of sophisticated materials: nanotoxicology and beyond. *Toxicol Sci* 2010;120:109–29.
- [13] Su Y, Hu M, Fan C, He Y, Li Q, Li W, et al. The cytotoxicity of CdTe quantum dots and the relative contributions from released cadmium ions and nanoparticle properties. *Biomaterials* 2010;31:4829–34.
- [14] Friberg L, Elinder CG, Kjellstrom T, Nordberg GF, editors. Cadmium and health: a toxicological and epidemiological appraisal. Boca Raton: CRC Press; 1986.
- [15] Moulis JM, Thevenod F. New perspectives in cadmium toxicity: an introduction. *Biometals* 2010;23:763–8.
- [16] Thevenod F. Cadmium and cellular signaling cascades: to be or not to be? *Toxicol Appl Pharmacol* 2009;238:221–39.
- [17] Kirchner C, Javier AM, Susha AS, Rogach AL, Kreft O, Sukhorukov GB, et al. Cytotoxicity of nanoparticle-loaded polymer capsules. *Talanta* 2005;67:486–91.
- [18] Fischer HC, Chan WC. Nanotoxicity: the growing need for *in vivo* study. *Curr Opin Biotechnol* 2007;18:565–71.
- [19] Auffan M, Rose J, Bottero JY, Lowry GV, Jolivet JP, Wiesner MR. Towards a definition of inorganic nanoparticles from an environmental, health and safety perspective. *Nat Nanotechnol* 2009;4:634–41.
- [20] Lewinski N, Colvin V, Drezek R. Cytotoxicity of nanoparticles. *Small* 2008;4:26–49.
- [21] Su Y, He Y, Lu H, Sai L, Li Q, Li W, et al. The cytotoxicity of cadmium based, aqueous phase - synthesized, quantum dots and its modulation by surface coating. *Biomaterials* 2009;30:19–25.
- [22] Li KG, Chen JT, Bai SS, Wen X, Song SY, Yu Q, et al. Intracellular oxidative stress and cadmium ions release induce cytotoxicity of unmodified cadmium sulfide quantum dots. *Toxicol In Vitro* 2009;23:1007–13.
- [23] Derfus AM, Chan WCW, Bhatia SN. Probing the cytotoxicity of semiconductor quantum dots. *Nano Lett* 2004;4:11–8.
- [24] Hoshino A, Fujioka K, Oku T, Suga M, Sasaki YF, Ohta T, et al. Physicochemical properties and cellular toxicity of nanocrystal quantum dots depend on their surface modification. *Nano Lett* 2004;4:2163–9.
- [25] Kirchner C, Liedl T, Kudera S, Pellegrino T, Munoz Javier A, Gaub HE, et al. Cytotoxicity of colloidal CdSe and CdSe/ZnS nanoparticles. *Nano Lett* 2005;5:331–8.
- [26] Lovric J, Cho SJ, Winnik FM, Maysinger D. Unmodified cadmium telluride quantum dots induce reactive oxygen species formation leading to multiple organelle damage and cell death. *Chem Biol* 2005;12:1227–34.
- [27] Lovric J, Bazzi HS, Cuie Y, Fortin GR, Winnik FM, Maysinger D. Differences in subcellular distribution and toxicity of green and red emitting CdTe quantum dots. *J Mol Med* 2005;83:377–85.
- [28] Choi AO, Cho SJ, Desbarats J, Lovric J, Maysinger D. Quantum dot-induced cell death involves Fas upregulation and lipid peroxidation in human neuroblastoma cells. *J Nanobiotechnol* 2007;5(1).
- [29] Aldana J, Wang YA, Peng X. Photochemical instability of CdSe nanocrystals coated by hydrophilic thiols. *J Am Chem Soc* 2001;123:8844–50.
- [30] Aldana J, Lavelle N, Wang Y, Peng X. Size-dependent dissociation pH of thiolate ligands from cadmium chalcogenide nanocrystals. *J Am Chem Soc* 2005;127:2496–504.
- [31] Prasad BR, Nikolskaya N, Connolly D, Smith TJ, Byrne SJ, Gerard VA, et al. Long-term exposure of CdTe quantum dots on PC12 cellular activity and the determination of optimum non-toxic concentrations for biological use. *J Nanobiotechnol* 2010;8(7).
- [32] Chan WH, Siao NH, Lu PZ. CdSe quantum dots induce apoptosis in human neuroblastoma cells via mitochondrial-dependent pathways and inhibition of survival signals. *Toxicol Lett* 2006;167:191–200.



- [33] Choi AO, Brown SE, Szyf M, Maysinger D. Quantum dot-induced epigenetic and genotoxic changes in human breast cancer cells. *J Mol Med* 2008;86: 291–302.
- [34] Cheng J, Flahaut E, Cheng SH. Effect of single-walled carbon nanotubes on developing zebrafish (*Danio rerio*) embryos. *Environ Toxicol Chem* 2007;26: 708–16.
- [35] Cheng J, Fernando KAS, Veca LM, Sun YP, Lamond AI, Lam YW, et al. Reversible accumulation of PEGylated single-walled carbon nanotubes in the mammalian nucleus. *ACS Nano* 2008;2:2085–94.
- [36] King-Heiden TC, Wicinski PN, Mangham AN, Metz KM, Nesbit D, Pedersen JA, et al. Quantum dot nanotoxicity assessment using the zebrafish embryo. *Environ Sci Technol* 2009;43:1605–11.
- [37] Cattaneo AG, Gornati R, Chiriva-Internati M, Bernardini G. Ecotoxicology of nanomaterials: the role of invertebrate testing. *Invert Surviv J* 2009;6: 78–97.
- [38] Lee J, Ji K, Kim J, Park K, Lim KH, Yoon TH, et al. Acute toxicity of two CdSe/ZnSe quantum dots with different surface coating in daphnia magna under various light conditions. *Environ Toxicol* 2009;25(6).
- [39] Peyrot C, Gagnon C, Gagné F, Wilkinson KJ, Turcotte P, Sauvé S. Effects of cadmium telluride quantum dots on cadmium bioaccumulation and metallothionein production to the freshwater mussel, *Elliptio complanata*. *Comp Biochem Physiol C Toxicol Pharmacol* 2009;150:246–51.
- [40] Gagne F, Auclair J, Turcotte P, Fournier M, Gagnon C, Sauvé S, et al. Ecotoxicity of CdTe quantum dots to freshwater mussels: impacts on immune system, oxidative stress and genotoxicity. *Aquat Toxicol* 2008;86:333–40.
- [41] Rogach AL, Franzl T, Klar TA, Feldmann J, Gaponik N, Lesnyak V, et al. Aqueous synthesis of thiol-capped CdTe nanocrystals: state-of-the-art. *J Phys Chem C* 2007;111:14628–37.
- [42] Gaponik N, Rogach AL. Thiol-capped CdTe nanocrystals: progress and perspectives of the related research fields. *Phys Chem Chem Phys* 2010;12: 8685–93.
- [43] Pardos M, Benninghoff C, Gueguen C, Thomas R, Dobrowolski J, Dominik J. Acute toxicity assessment of Polish (waste) water with a microplate-based *Hydra attenuata* assay: a comparison with the Microtox test. *Sci Total Environ* 1999;243:141–8.
- [44] Holdway DA, Lok K, Semaan M. The acute and chronic toxicity of cadmium and zinc to two hydra species. *Environ Toxicol* 2001;16:557–65.
- [45] Karntanut W, Pascoe D. The toxicity of copper, cadmium and zinc to four different *Hydra* (Cnidaria: Hydrozoa). *Chemosphere* 2002;47:1059–64.
- [46] Pascoe D, Carroll K, Karntanut W, Watts MM. Toxicity of 17 $\alpha$ -ethinyles-tradiol and bisphenol A to the freshwater Cnidarian *Hydra vulgaris*. *Arch Environ Contam Toxicol* 2002;43:56–63.
- [47] Johnson EM, Gorman RM, Gabel BE, George ME. The *Hydra attenuata* system for detection of teratogenic hazards. *Teratog Carcinog Mutagen* 1982;2: 263–76.
- [48] Pachura S, Cambon JP, Blaise C, Vasseur P. 4-nonylphenol-induced toxicity and apoptosis in *Hydra attenuata*. *Environ Toxicol Chem* 2005;24:3085–91.
- [49] Quinn B, Gagne F, Blaise C. The effects of pharmaceuticals on the regeneration of the cnidarian, *Hydra attenuata*. *Sci Total Environ* 2008;402:62–9.
- [50] Quinn B, Gagne F, Blaise C. Evaluation of the acute, chronic and teratogenic effects of a mixture of eleven pharmaceuticals on the cnidarian, *Hydra attenuata*. *Sci Total Environ* 2009;407:1072–9.
- [51] Pascoe D, Karntanut W, Muller CT. Do pharmaceuticals affect freshwater invertebrates? A study with the cnidarian *Hydra vulgaris*. *Chemosphere* 2003; 51(6):521–8.
- [52] Tortiglione C, Quarta A, Malvindi MA, Tino A, Pellegrino T. Fluorescent nanocrystals reveal regulated portals of entry into and between the cells of *Hydra*. *PLoS One* 2009;4(11):e7698.
- [53] Tortiglione C. An ancient model organism to test in vivo novel functional nanocrystals. In: Fazel-Rezai R, editor. *Biomedical Engineering: from theory to application*. InTech - Open Access Publisher; 2011. p. 225–52.
- [54] Malvindi MA, Carbone L, Quarta A, Tino A, Manna L, Pellegrino T, et al. Rod-shaped nanocrystals elicit neuronal activity in vivo. *Small* 2008;4:1747–55.
- [55] Tino A, Ambrosone A, Mattera L, Marchesano V, Sussha A, Rogach AL, et al. A new in vivo model system to assess the toxicity of semiconductor nanocrystals. *Int J Biomater*; 2011:792854.
- [56] Loomis WF, Lenhoff HM. Growth and sexual differentiation of *Hydra* in mass culture. *J Exp Zool* 1956;132:555–74.
- [57] Wilby OK. The *Hydra* regeneration assay. *Proc Assoc Francaise de Teratologie*; 1988:108–24.
- [58] Karntanut W, Pascoe D. A comparison of methods for measuring acute toxicity to *Hydra vulgaris*. *Chemosphere* 2000;41:1543–8.
- [59] Bosch TC, David CN. Growth regulation in *Hydra*: relationship between epithelial cell cycle length and growth rate. *Dev Biol* 1984;104:161–71.
- [60] Livak KJ, Schmittgen TD. Analysis of relative gene expression data using real-time quantitative PCR and the 2 $^{-\Delta\Delta C_T}$  method. *Methods* 2001;25: 402–8.
- [61] Gavrieli Y, Sherman Y, Ben-Sasson SA. Identification of programmed cell death in situ via specific labeling of nuclear DNA fragmentation. *J Cell Biol* 1992;119: 493–501.
- [62] Hamilton MA, Russo RC, Thurston RV. Trimmed Spearman-Kärber method for estimating median lethal concentrations in toxicity bioassays. *Environ Sci Technol* 1977;11:714–9.
- [63] Sussha A, Munoz Javier A, Parak W, Rogach A. Luminescent CdTe nanocrystals as ion probes and pH sensors in aqueous solutions. *Colloids Surf A* 2006;281: 40–3.
- [64] Lasi M, David CN, Bottger A. Apoptosis in pre-Bilaterians: hydra as a model. *Apoptosis* 2009;15:269–78.
- [65] Cikala M, Wilm B, Hobmayer E, Bottger A, David CN. Identification of caspases and apoptosis in the simple metazoan *Hydra*. *Curr Biol* 1999;9:959–62.
- [66] Xu M, Deng G, Liu S, Chen S, Cui D, Yang L, et al. Free cadmium ions released from CdTe-based nanoparticles and their cytotoxicity on *Phaeodactylum tricornutum*. *Metallomics* 2010;2:469–73.
- [67] Hartl M, Mitterstiller AM, Valovka T, Breuker K, Hobmayer B, Bister K. Stem cell-specific activation of an ancestral myc protooncogene with conserved basic functions in the early metazoan *Hydra*. *Proc Natl Acad Sci U S A* 2010; 107:4051–6.
- [68] Ambrosone A, Marchesano V, Tino A, Hobmayer B, Tortiglione C. Hymc downregulation through small interfering RNA promotes stem cell differentiation in *Hydra vulgaris*. Submitted for publication 2011.
- [69] Lasi M, Pauly B, Schmidt N, Cikala M, Stiening B, Kasbauer T, et al. The molecular cell death machinery in the simple cnidarian *Hydra* includes an expanded caspase family and pro- and anti-apoptotic Bcl-2 proteins. *Cell Res* 2010;20:812–25.
- [70] Bridge D, Theofilis AG, Holler RL, Marcinkevicius E, Steele RE, Martinez DE. FoxO and stress responses in the cnidarian *Hydra vulgaris*. *PLoS One* 2010;5: e11686.
- [71] Dash B, Metz R, Huebner HJ, Porter W, Phillips TD. Molecular characterization of two superoxide dismutases from *Hydra vulgaris*. *Gene* 2007;387:93–108.
- [72] Rzigalinski BA, Strobl JS. Cadmium-containing nanoparticles: perspectives on pharmacology and toxicology of quantum dots. *Toxicol Appl Pharmacol* 2009; 238:280–8.
- [73] Priester JH, Stoimenov PK, Mielke RE, Webb SM, Ehrhardt C, Zhang JP, et al. Effects of soluble cadmium salts versus CdSe quantum dots on the growth of planktonic *Pseudomonas aeruginosa*. *Environ Sci Technol* 2009;43:2589–94.
- [74] Domingos RF, Simon DF, Hauser C, Wilkinson KJ. Bioaccumulation and effects of CdTe/CdS quantum dots on *Chlamydomonas reinhardtii* - nanoparticles or the free ions? *Environ Sci Technol* 2011;45:7664–9.
- [75] Nabiev I, Mitchell S, Davies A, Williams Y, Kelleher D, Moore R, et al. Non-functionalized nanocrystals can exploit a cell's active transport machinery delivering them to specific nuclear and cytoplasmic compartments. *Nano Lett* 2007;7:3452–61.

# Bridging the fields of nanoscience and toxicology: nanoparticle impact on biological models

A. Ambrosone, V. Marchesano, L. Mattera, A. Tino, C. Tortiglione  
Istituto di Cibernetica “E. Caianiello”, Consiglio Nazionale delle Ricerche, Via Campi Flegrei, 34,  
80078 Pozzuoli, Italy

## Abstract

In the emerging area of nanotechnology a key issue is related to the potential impacts of the novel nanomaterials on the environment and human health so that this technology can be used with minimal risk. Specifically designed to combine on a single structure multipurpose tags and properties, nanomaterials need a comprehensive characterization of both chemicophysical properties and toxicological evaluation, which is a challenging endeavor: the *in vitro* toxicity assays that are employed for nanotoxicity assessments do not accurately predict *in vivo* response. To overcome these limitations and gain a deeper understanding of nanoparticle-cell interactions, we have employed cnidarian models, in particular the freshwater polyp *Hydra vulgaris*, not opposed to more complex and evolved systems, but to add valuable information, at an intermediate level between prokaryotes and vertebrates, on both cytotoxicity and on pollution affecting the environment. By testing CdSe/CdS core shell nanocrystals *in vivo*, at whole animal level, we investigated the impact of their properties on uptake, accumulation, biodistribution, elicitation of behavioural responses. Spanning from animal to cell biology, we provide an analysis on metal based and semiconductor NC, discussing the crucial role played by the synthesis route and chemical surface on the toxicity for living organisms.

**Keywords:** model organisms, *Hydra vulgaris*, nanotoxicology, nanocrystals, Quantum Rods

## 1. INTRODUCTION

The intriguing field of bionanotechnology opens promising scenarios in research and clinical practices. In particular, recent advances in synthesis and biofunctionalization of colloidal semiconductor nanocrystals have generated an increasing widespread interest among investigators in biology and medicine. Specifically, due to their unique optical and electronic properties, which have already suggested their use in tunable polarized lasers and organic-inorganic hybrid solar cells, quantum rods (QRs) are expected to have great potential as multipurpose bioprobes in biomedical applications. However, critical issues concerning the effect of nanobiomaterials on cells and living organisms remain to be resolved. Latest evidences are cumulating that nanoparticles plays active roles even in absence of specific ligands and that factors such as size and charge are crucial for activation of cell responses, internalization, and intracellular trafficking [1, 2]. Thus it is a priority for the wide scientific community working to develop nanostructured materials for biomedical purposes to relate the physical and chemical characteristics of nanomaterials to their behaviour, *in vivo*. Increasing data addressing this important question relies on cell culture systems, and are focussed on the identification of the physicochemical parameters influencing the impact of nanoparticle on living cells [3, 4] we propose a new model system to work at whole animal level. The ancient freshwater polyp *Hydra vulgaris*, a member of the Cnidarian, has a tube-like shape, consisting of two epithelial cell layers (an inner endoderm and an outer ectoderm facing the low ionic strength medium) separated by a distinctive extracellular membrane (mesoglea) (Figure 1 A, B). The remaining cell types are lodged in the interstices of the epithelial cells (interstitial cell lineage). Interestingly, this structural complexity, simpler than vertebrates, with central nervous system and specialized organs, but much complex compared to cultured cells, makes *Hydra* comparable to a living tissue which cells and distant regions are physiologically connected [5]. Our previous studies demonstrated *Hydra vulgaris* represents a unique system to study the interaction between nanoparticles and living systems.



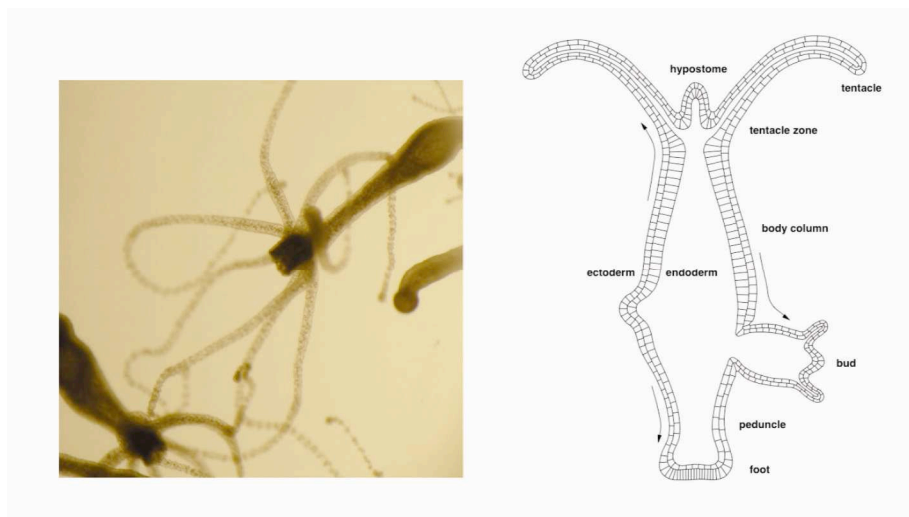


Figure 1. a) A living *Hydra* in culture medium. The animal has a simple body plan: it is a tube with a head at the apical end, and a foot, or basal disc at the other. The head is in two parts, the hypostome (mouth) at the apex, and below that the tentacle zone from which a ring of tentacles emerge. Scale bar 500  $\mu\text{m}$ . b) Cross-section of the bilayered structure of the animal, adapted from [6] : the polyp is composed of two self renewing cell layers, an outer the ectoderm and an inner endoderm, and separated by an extracellular matrix, the mesoglea. The arrows on the left side indicate the direction of tissue displacement. c) Along the animal body both ectoderm and endoderm layers are composed of epitheliomuscular cells, while interstitial stem cells and their intermediate and terminal derivatives (neurons, nematocytes and secretory cells) are interspersed among ectoderm and endoderm.

A remarkable advantage offered by *Hydra* as model organism to be targeted by metal based nanocrystals is the possibility to evaluate the potential toxicity of these nanoparticles on different aspects of *Hydra* physiology. The availability of new animal models suitable for the assessment of nanotoxicity is currently recognised as a priority. *Hydra* is sensitive to a range of pollutants and has been used as a biological indicator of water pollution [6-8]. Metal pollutants such as copper, cadmium and zinc have been tested against different *Hydra* species, and the relative toxicity based on the median lethal concentration (LC50) for all species was ranked from copper, the most toxic, to cadmium with zinc least toxic [7]. Interestingly, interfacing *Hydra* polyps with nanocrystals, we found that the surface charge of nanoparticles determines the efficiency of uptake. In particular, by tuning the number of amino-PEG molecules attached at the rod surface and thus by manipulating the resulting surface charge at different pHs, we tuned the capability of *Hydra* ectodermal cells to internalize QRs, from very high at acidic pH to zero at neutral pH. Only under acidic conditions *Hydra* ectodermal cells bind and sequester into cytoplasmic granular structures positively charged QRs, while at neutral pH this does not occur [2].

In the present paper we evaluated in *Hydra vulgaris* the internalization and toxicological effects of negatively charged fluorescent CdSe/CdS core shell QRs. As the impact of QR administered to *Hydra* by soaking has already been investigated, here we assessed the impact of the same semiconductor nanocrystals (CdSe/CdS) on the digestive cells of *Hydra*, which are often the final target for ecotoxicological purposes. By using different approaches, from *in vivo* evaluation of morphological traits to the evaluation of the growth rate and regeneration mechanisms, we show that QR do not display toxic effects as they are stably accumulated into storage vesicles, and thus they have great potential to be used as markers for cell tracking and biological investigations.

## 2. METHODS

### Nanocrystals employed

Amino-PEG coated CdSe/CdS core/shell QRs were a kind gift of Teresa Pelegrino (National Nanotechnology Laboratory, Lecce, Italy). The QR here used (Length:  $35 \pm 2$  nm; diameter:  $4.2 \pm 0.4$  nm) (Fig. 2 A) were prepared by the seeded growth approach as recently reported [8, 9]. Surface coating with diamino-PEG molecules was achieved by means of EDC crosslinking chemistry as previously described [2]

### Hydra culture

*Hydra vulgaris* (strain Zurich, originally obtained by P. Tardent) were asexually cultured in physiological solution (SolHy: 1mM  $\text{CaCl}_2$ , 0.1mM  $\text{NaHCO}_3$ , pH 7) by the method of Loomis and Lenhoff with minor modifications [10]. The animals were kept at  $18 \pm 1^\circ\text{C}$  and fed three times per week with freshly hatched *Artemia salina* nauplii.

### In vivo experiments with intact,regenerating and macerated animals

Groups of 20 animals were collected in plastic multiwells, allowed to equilibrate at room temperature in 300 $\mu$ l of physiological solution (SolHy:  $\text{CaCl}_2$  1mM,  $\text{NaHCO}_3$  0.1mM, pH 7). The test was initiated by adding test QRs to each well containing 10 polyps and incubating as necessary. QR uptake was monitored *in vivo*, unless otherwise stated, by continuous video recording using a Camedia-digital camera (Olympus) connected to a stereomicroscope (Olympus ZSX-RFL2) equipped with fluorescence filter sets (BP460- 490/DM505/LP510). Following extensive washes, *in vivo* imaging was accomplished at several magnification by using both a stereomicroscope and an inverted microscope (Axiovert 100, Zeiss) equipped with a digital colour camera (Olympus, DP70) and fluorescence filter sets (BP450-490/FT510/LP515). In order to assay acute toxicity, the morphological changes induced by QD treatment were monitored, by using a scoring procedure of the progressive changes in structure. This procedure allows to examine the ability of animals to recover from NP-induced damage. Every day, using a stereomicroscope, recognizable physical changes in response to different NP ranges were recorded, according to score values (ranging from 1-10) described by Wilby (1988) [11]. For imaging acquisition and analysis the software system Cell F (Olympus) was used. For regeneration experiments, treated polyps were bisected in the gastric region and *in vivo* imaged at various time points post amputation. Macerations of *Hydra* polyps were obtained as described in [12]Experiments were performed in air-conditioned environment at  $22^\circ\text{C}$ , and repeated three times for each condition tested.

### Hydra growth rates

Experimental animals (four *Hydra* with one bud) were treated with the indicated NP, for 4 h, then washed, and the following day placed in 3,5 cm petri dishes (1 *Hydra*/dish). Control animals at the same developmental stage were not treated. Both experimental and control *Hydra* were fed once daily and the Population doubling time was determined as growth parameter. The growth rate constant ( $k$ ) of an exponentially growing group of animals is defined as  $\ln(n/n_0)=kt$  where  $n$  is the number of animals at time  $t$  and  $n_0$  the number of animal at  $t_0$ . For  $n/n_0 = 2$ ,  $t = T_2$ , the doubling time of the population.  $T_2$  was determined by linear regression [13].

### Transmission electron microscopy

*Hydra* polyps were treated with 2% urethane in SolHy (1 mM  $\text{CaCl}_2$ , 0.1 mM  $\text{NaHCO}_3$ , pH 7.0) to prevent specimens contraction during fixation and then fixed for 2hrs in 2% glutaraldehyde in SolHy. Samples were then washed at least four times with SolHy and postfixed for 45' with 1% buffered  $\text{OsO}_4$ . After a series of four washes in SolHy, animals were dehydrated in a graded ethanol series (30%-50%-70%-90%-100%). Samples were incubated 2x15' with Propylene oxide and then overnight in a 1:1 mixture Propylene oxide/Epon 12 Resin. Before flat embedding animals were incubated 2x2hr in Epon 12 Resin. Sample serial thin (70nm) section of tentacles and hypostoma were cut with a diamond knife and mounted onto 150-200 mesh Hex grids. Thin sections were stained with uranyl acetate and lead citrate. Ultrathin sections were examined with Leo 912 AB transmission electron microscope operating at 80 k.

### 3. RESULTS

The effects of amino-PEG coated CdSe/CdS quantum rods (from here simply named QRs) on animal behaviour, morphology, growth and regeneration capability was investigated over different incubation times. Being *Hydra* a small water living animal, the simple addition of QRs to the culture medium enables to study the interaction between QR/animal, avoiding delivering methods or invasive procedures. To allow nanoparticle internalization either into the ectoderm or in the endoderm, QRs were added at different concentrations at different pH conditions to groups of living polyps. Treated animals were continuously monitored by fluorescence stereomicroscopy to track QR uptake, localization and morphological alterations. As previously reported, after 24h of incubation in a suspension of QRs at nanomolar concentration (7 nM) at acidic pH conditions, rinsed polyps appeared strongly labelled (Fig 1). In particular, QR uptake by soaking, initially restricted to tentacle battery cells (30 min post incubation), takes place also in the ectodermal producing a homogenous body staining (Fig. 2 B and C) [2]. The tripeptide Glutathione, (GSH) is the physiological stimulator of the *Hydra* feeding response [14]. Thus, in presence of micromolar doses of GSH (within the range 1-10 micromolar) *Hydra* polyps are induced to open their mouth allowing the outer medium to enter the body cavity. Thus, following GSH addition at physiological pH (Fig. 2 D), negatively charged QRs did not enter the ectoderm and were largely ingested, accumulated as aggregates into the body cavity (Fig. E) and internalized exclusively by the endodermal layer ( Fig. 2 F).

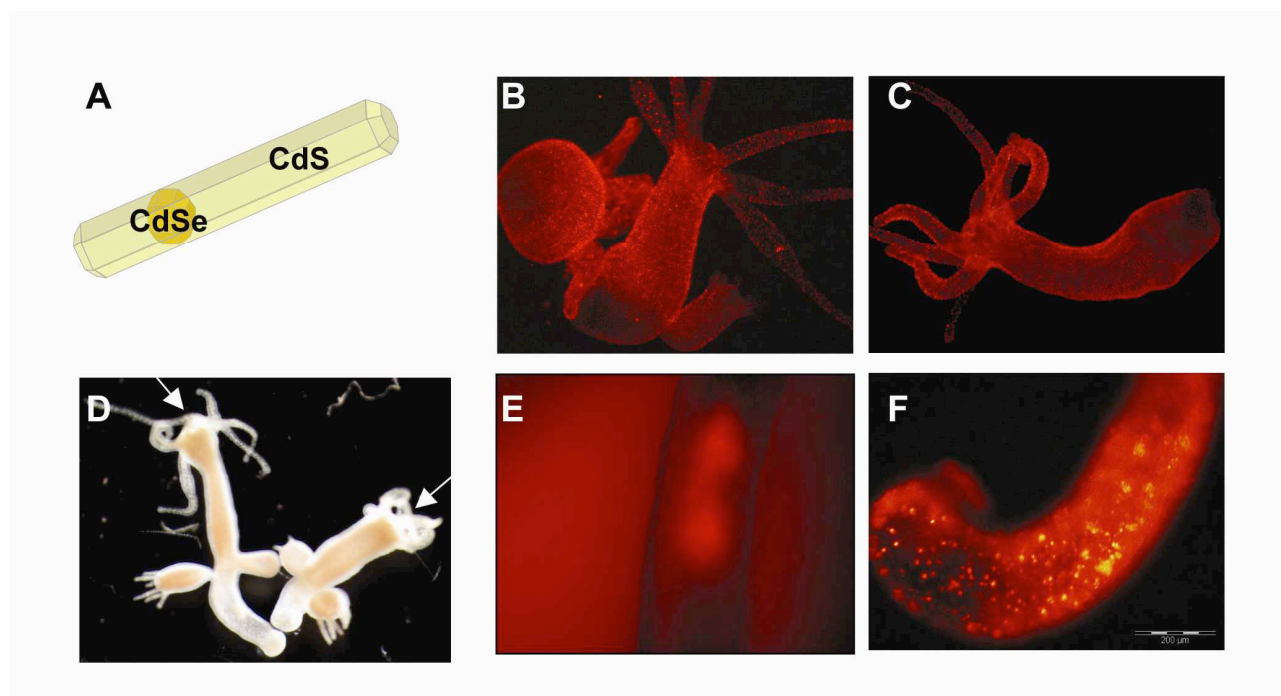


Fig. 2 *In vivo* labelling of *Hydra* polyp with high fluorescent QRs. A) Representative structure of Nanorods. B and C) Pictures of a living *Hydra* after 24 hour incubation with QRs; by soaking, the polyp strongly internalized QRs in the epithelial layer of the body. D) Representative image of GSH-treated *Hydra*. GSH addition on the *Hydra* medium induces a reversible mouth opening (white arrows). E) Aggregation of QRs immediately after Ingestion. F) QRs biodistribution in the endodermal layer of the gastic region at 24h after ingestion. QRs are homogeneously dispersed among the endoderm.

The cross-sections made from fixed treated polyps revealed that the internalization occur rapidly in the endodermal cell layer, facing directly the body cavity that in turn receives the QRs from the culture solution (Figure 3 B and C). Remarkably, 24 h post treatment, fluorescent material migrates through the endoderm cell layer underlying cellular dynamics among the endoderm.

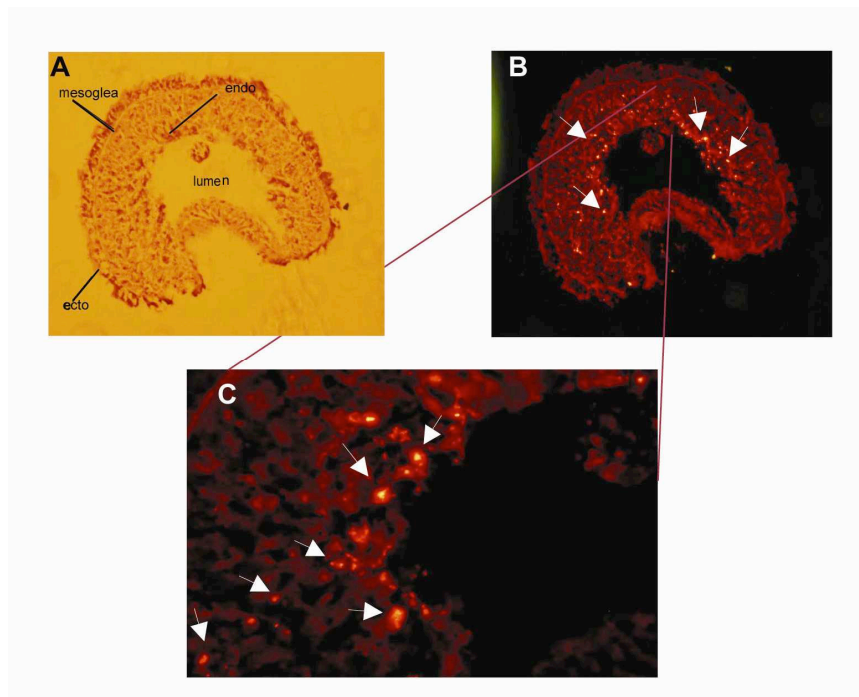


Fig. 3 Biodistribution of QRs in *Hydra* tissue sections after NP ingestion. A) histological cryosection at level of gastric region shows the tissue organization of *Hydra* allowing to distinguish the ectoderm (ecto), the mesoglea, the endoderm (endo) and the body cavity (lumen). B) Fluorescent image of the cryosection; the diffuse red colour is due to tissue autofluorescence, while the red punctuated signals (white arrows) indicates the QR presence. C) A higher magnification of B reveals QRs localize into endodermal cells.

To investigate the intracellular localization of QRs, whole animals were incubated with QRs for 4 h, extensively washed and then macerated. The maceration method permits to rapidly and completely dissociate *Hydra* tissue into individual cells. Each cell type preserves the original shape and is promptly distinguishable by microscopy analysis [12].

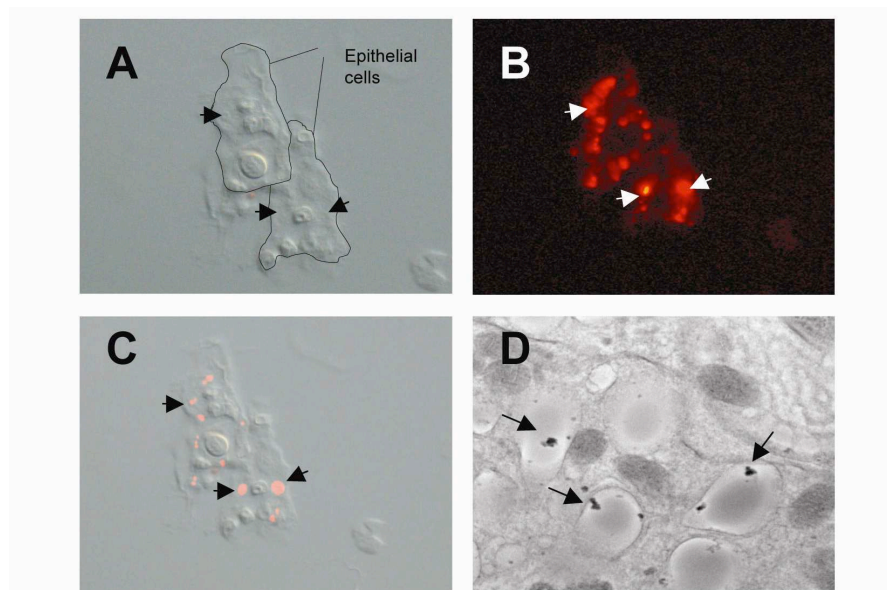


Fig. 4 Cellular localization of QRs in *Hydra*. A) Phase contrast image of intact epithelial cells obtained by maceration; black arrows indicate the presence of different vesicle-like structures. B) Red-fluorescent QRs (white arrows) are accumulated into epithelial cells after 24 h incubation. C) Merged image of A and B indicates that QRs are located in vesicles dispersed in the cytoplasm. D) QRs localization by TEM microscopy. The nanocrystals are dispersed in cellular vesicles of *Hydra* epithelial cells .

As shown in Fig 4 (A, B, C), QRs were dispersed as highly fluorescent spots in the cytoplasm of epithelial cells; in particular QRs appeared to be compartmentalized in vesicle-like structures as indicated by the black arrows in Fig. 4 (A, C). To validate this hypothesis, we further investigated intracellular localization by transmission electron microscopy. As illustrated in Fig. 4 D, rod nanocrystals were retained in cytoplasmatic vesicles of *Hydra* epithelial cells.

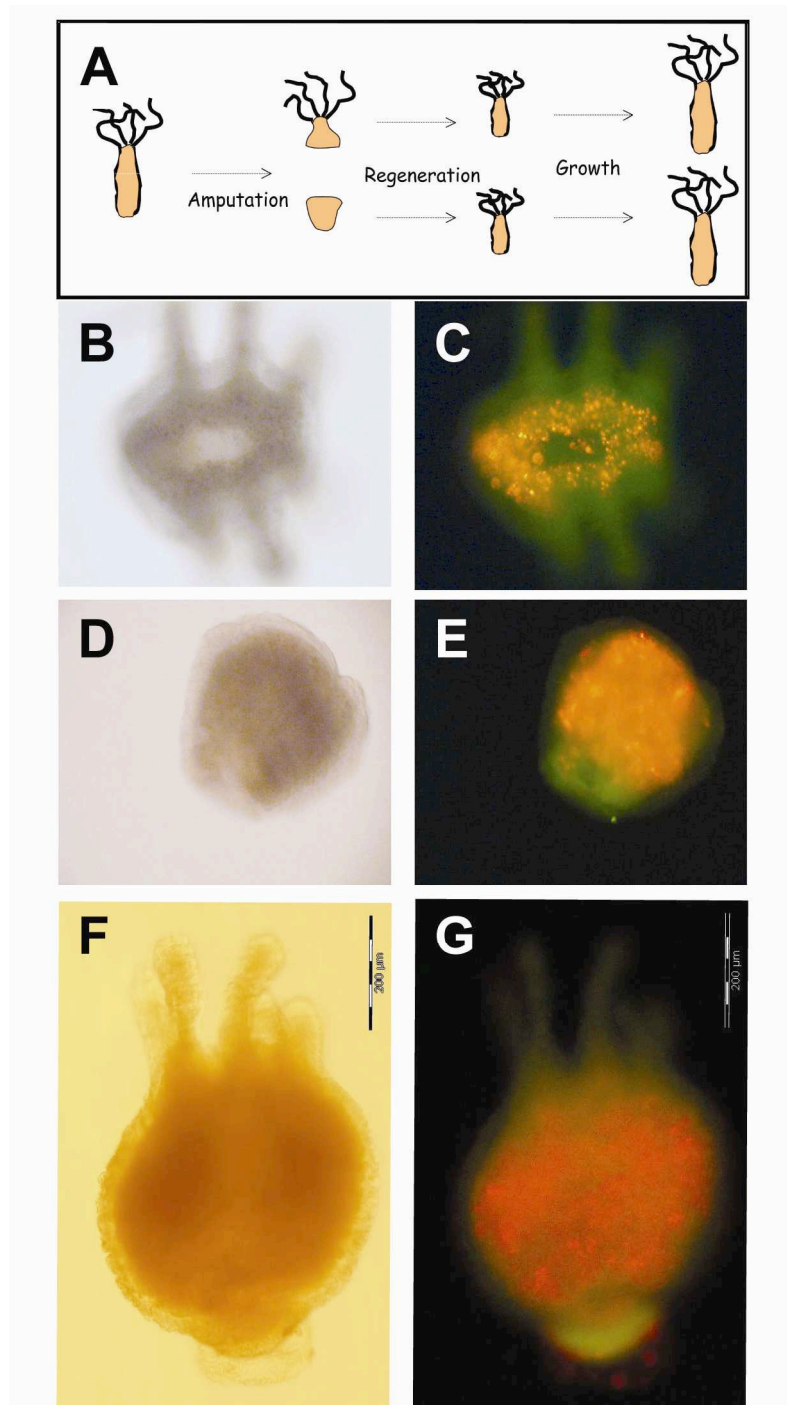


Fig. 5 Regeneration of *Hydra* polyps labelled with fluorescent QRs. A) schematic representation of polyp regeneration. *Hydra* has the ability to regenerate completely the head and the body after bisection. B and C) Bright-field and fluorescent images of a QR labelled *Hydra*'s head after amputation, respectively. D and E) Bright-field and fluorescent images of a QR labelled *Hydra*'s head and foot after amputation, respectively. F and G) Bright-field and fluorescent images of a regenerating *Hydra*. After three days post-amputation, the polyp contains a high concentration of fluorescent QRs.



Finally, to evaluate the toxicity associated with the internalization of QRs, we incubated *Hydra* polyps in presence of different concentration (from 1 nM up to 200nM) of nanoparticles for 24 h, 48 h and 72 h. According to the Wilby's criteria based on phenotypical observations, no significant alterations in the morphology of the animals were found (data not shown), suggesting QRs have no or limited negative effects on *Hydra* after ingestion. To definitely characterize the toxicological impact of rod-shaped nanocrystal on *Hydra*, regeneration and growth rate of polyps were investigated after treatments with 7 nM QRs. Overall, *Hydra* has the capability to regenerate missing parts of the body after amputation (Fig. 5, A). Head regeneration is a critical aspect of *Hydra* biology and the development of emerging tentacles can be monitored by stereomicroscopy to estimate the potential effects of toxicants on this tightly controlled process. As showed in Fig. 5 C and E, after bisection QRs are still present in the treated animal body during the first phases of regeneration. More interestingly, three-day head regenerating *Hydra* appeared highly fluorescent by microscope analysis (Fig. 5 G) indicating that QRs are retained during regeneration processes. Significantly, treated polyps regenerated heads and tentacles similar to the control animals indicating QRs did not produce adverse effects during *Hydra* regeneration.

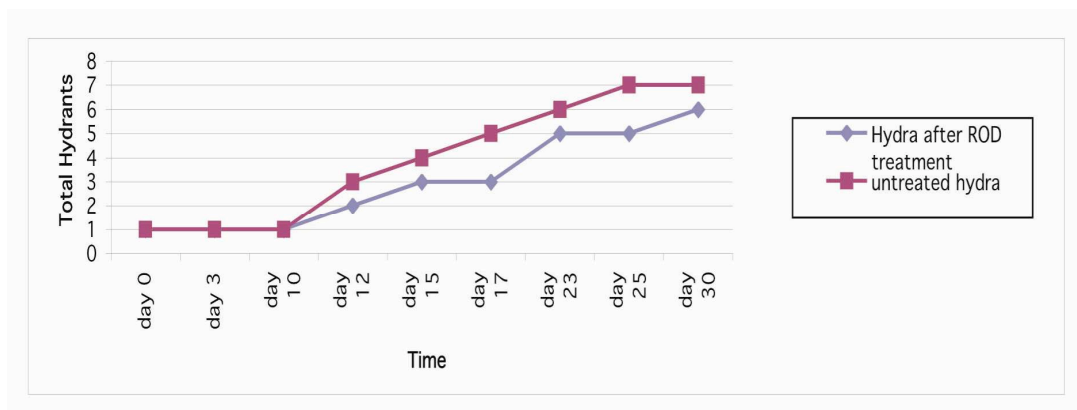


Figure 6. Influence of the QR treatment on *Hydra* population growth rate. Population growth test started with a population of four full-grown *Hydra*, incubated 24 h with 7nM QR, washed out and monitored every day for bud detachment. The individuals were inspected daily and counted under a stereomicroscope. There are not significant differences between treated (blue line) and untreated (red line) population growth rates. The logarithmic growth rate constant ( $k$ ) is the slope of the regression line using the standard equation of logarithmic growth:  $\ln(n/n_0) = kt$ .

In order to assess the potential long-term lethal effects induced by QRs, *Hydra* capabilities to growth and to reproduce were assayed. Growth rate of *Hydra* tissue is normally regulated by a balance between epithelial cell cycle length, phagocytosis of ectodermal cell in “excess”, and bud formation [13]. Thus, the population growth rate is an indirect measure of the *Hydra* tissue growth rate and cell viability. The growth rates of QR treated polyps were estimated and compared to untreated animals, under regular feeding regime. As shown in the graph of Fig. 5 the growth rate of polyps treated with 7 nM QRs was similar to untreated animals, suggesting once again the absence of significant toxic effects in *Hydra* population.

#### 4. DISCUSSION

Due to their unique physicochemical properties, nanocrystals attract increasing interest in a wide range of biomedical applications, from cell biology to medical diagnostic. However, main critical issues regarding the health and environmental effects have to be resolved before employing semiconductor nanocrystals for biomedical purposes. While *in vitro* assays are widely exploited for toxicological studies they do not accurately address the complexity of the *in vivo* response. Alternatively, we have previously proposed as a new model system the freshwater polyp *Hydra vulgaris*, to investigate the *in vivo* response to different nanomaterials. The recent full genome sequencing of *Hydra* will allow to explore this response also at molecular level, disclosing many aspects concerning NP internalization, cellular processes and molecular effectors involved in the detoxification and/or compartmentalization of nanocrystals [15]. We previously studied the uptake of unfunctionalized rod shaped CdSe/CdS nanocrystals, and shown that positively charged QRs are internalized into the ectoderm while the negatively charged ones do not. Growth rates of *Hydra* labelled into ectoderm by QR are similar to growth rates of untreated animals, suggesting that these nanocrystals have no toxic effects on the reproductive capabilities of the animals. Here, we investigated the impact of the negatively charged QRs when they are ingested and showed the kinetics of this response. Following GSH administration and mouth opening, medium suspended QRs were abundantly accumulated in the body cavity of the polyps. The

endodermal cells lining the gastric cavity of the polyps rapidly uptake QRs, probably by the pinocytosis processes typical of the digestive cells [16]. Due to the lack of photostable fluorescent markers, the cellular mechanisms of endocytosis in *Hydra* have not been clarified to date. The kinetics of QR internalization showed that QRs migrate from the body cavity into the endodermal cells. The mechanisms underlying this dynamic might be due to an array of events, from migration of free nanoparticles, or relocation of cells containing nanoparticles among the endoderm, to autophagocytosis events known to regulate tissue and body maintenance of the polyp. The subcellular QR localization was also investigated, by mean of TEM analysis. Our findings demonstrated that nanorods are prevalently located in cytoplasmatic vesicles, stably maintained over the cell divisions to daughter cells, which characterization requires further work.

In ecology, aquatic invertebrates have been largely employed as biological indicators to test the presence of environmental contaminants. In particular *Hydra* is highly susceptible to many toxicants and pollutants [17] and may be a valid biological model to measure the toxicity of metal-based nanomaterials in solution.

In order to evaluate the toxicological impact of QRs on *Hydra*, morphological traits, regeneration capabilities and growth rate were assessed. According to Wilby's score method measuring morphological changes of polyps in presence of toxicants, we did not observe any phenotypical alteration in the tentacles and in the body column after NP internalization, suggesting QRs have no lethal effects either by soaking and ingestion. Moreover, here we have demonstrated that *Hydra* polyps retain QRs during the regeneration, allowing these dynamic processes to be easily tracked without adverse effects. Similarly, QR uptake does not influence the growth rate of *hydra* population, suggesting that the reproductive capabilities of treated animals are not affected by the presence of QRs. In summary, none of the investigated parameters were affected by the QR ingestion, suggesting a protective role of the polymer and PEG chain on the CdSe core, possibly preventing the Cd leakage and the derived toxicity.

In conclusion, our study indicates that the uptake process in the endoderm, as that previously observed into the ectoderm, occurs during the first hours post-incubation. Moreover, low QR dosage (7 nM) ensures a suitable amount of fluorescent nanocrystals to enter *Hydra* cells, enabling cell labelling and tracking. The absence of detectable toxic evidences over short and long periods together with the possibility to be used at low concentrations, make PEG-coated CdSe/CdS QRs an useful and promising tool to be employed for biological application in living organism.

## REFERENCE

1. Malvindi, M.A., et al., Rod-shaped nanocrystals elicit neuronal activity in vivo. *Small*, 2008. 4(10): p. 1747-55.
2. Tortiglione, C., et al., Fluorescent nanocrystals reveal regulated portals of entry into and between the cells of *Hydra*. *PLoS One*, 2009. 4(11): p. e7698.
3. Jiang, W., et al., Nanoparticle-mediated cellular response is size-dependent. *Nat Nanotechnol*, 2008. 3(3): p. 145-50.
4. Minchin, R., Nanomedicine: sizing up targets with nanoparticles. *Nat Nanotechnol*, 2008. 3(1): p. 12-3.
5. Galliot, B., et al., *Hydra*, a niche for cell and developmental plasticity. *Semin Cell Dev Biol*, 2006. 17(4): p. 492-502.
6. Bode, H.R., The interstitial cell lineage of *hydra*: a stem cell system that arose early in evolution. *J Cell Sci*, 1996. 109 ( Pt 6): p. 1155-64.
7. Karntanut, W. and D. Pascoe, The toxicity of copper, cadmium and zinc to four different *Hydra* (Cnidaria: Hydrozoa). *Chemosphere*, 2002. 47(10): p. 1059-64.
8. Carbone, L., et al., Synthesis and micrometer-scale assembly of colloidal CdSe/CdS nanorods prepared by a seeded growth approach. *Nano Lett*, 2007. 7(10): p. 2942-50.
9. Rogach, A.L.F., T.; Klar, T. A.; Feldmann, J.; Gaponik, N.; and V.S. Lesnyak, A.; Eychmuller, A.; Rakovich, Y. P.; Donegan, J. F., Aqueous Synthesis of Thiol-Capped CdTe Nanocrystals: State-of-the-Art. *J Phys Chem C*, 2007. 111: p. 14628-14637.
10. Loomis, W.F., and Lenhoff, H. M., Growth and sexual differentiation of *Hydra* in mass culture. . *J. Exp. Zool.*, 1956. 132: p. 555-574.
11. Wilby, O.K., The *Hydra* regeneration assay. *Proceedings of workshop organised by Association Francaise de Teratologie*, 1988: p. 108-124.
12. David, C.N., A quantitative method for maceration of *hydra* tissue. *Development Genes and Evolution*, 1973. 171: p. 259-268.
13. Bosch, T.C. and C.N. David, Growth regulation in *Hydra*: relationship between epithelial cell cycle length and growth rate. *Dev Biol*, 1984. 104(1): p. 161-71.
14. Lenhoff, H.M., Activation of the feeding reflex in *Hydra littoralis*. I. Role played by reduced glutathione and quantitative assay of the feeding reflex. *J Gen Physiol*, 1961. 45: p. 331-44.
15. Chapman, J.A., et al., The dynamic genome of *Hydra*. *Nature*. 464(7288): p. 592-6.

16. McNeil, P.L., Mechanisms of nutritive endocytosis. I. Phagocytic versatility and cellular recognition in *Chlorohydra* digestive cells, a scanning electron microscope study. *J Cell Sci*, 1981. 49: p. 311-39.
17. Karntanut, W. and D. Pascoe, A comparison of methods for measuring acute toxicity to *Hydra vulgaris*. *Chemosphere*, 2000. 41(10): p. 1543-8.